

**Vector meson production in p+Nb reactions  
and statistical particle production  
in Ar+KCl collisions**

Dissertation  
zur Erlangung des Doktorgrades  
der Naturwissenschaften

vorgelegt beim Fachbereich Physik  
der Johann Wolfgang Goethe-Universität  
in Frankfurt am Main

von  
**Manuel Lorenz**  
aus Frankfurt

Frankfurt 2012  
(D30)

vom Fachbereich Physik der  
Johann Wolfgang Goethe-Universität als Dissertation angenommen.

**Dekan:**

Prof.Dr. Huth

**Gutachter:**

Prof.Dr. Stroth

Prof.Dr. Blume

**Datum der Disputation:**

17.07.12

## Abstract

For this thesis, data taken in two measuring campaigns of the HADES spectrometer located at the GSI in Darmstadt were analyzed.

In Ar+KCl collisions at 1.76A GeV an efficiency correction based on simulation was performed for the charged kaons. For their identification the energy loss information of the drift chambers and the time of flight wall are essential. Comparisons of the simulated and experimental distributions showed deviations in both, widths and positions, leading to wrongly estimated efficiencies. Therefore a method was developed to adjust the cut applied in the simulation in order to make it act in the same way on simulated data as the corresponding cut on real data.

Furthermore, the dielectron identification in Ar+KCl is based for the first time on a neural network developed in [Lan08]. Comparisons to the standard method showed a low efficiency for electrons and positrons in the TOF region. By adjusting the input variates on which the algorithm bases its identification decision, the efficiencies could be improved by a factor larger than three for electron momenta  $>0.5$  GeV/c.

The hadron yields obtained in several analysis campaigns and thesis are compared to a statistical hadronization model fit and discussed with respect to the amount of thermalization of the system and the strong deviation observed for double strange particles.

A fair agreement, except for the  $\Xi^-$ , in a strangeness-canonical approach is achieved. This underlines the assumption that a unique freeze out of all particles occurs to some extent.

The linear dependence of the  $T_{eff}$  of non strange particles as a function of the particle mass suggests a radial expansion velocity  $\langle \beta \rangle$  of  $\approx 0.39 \pm 0.1$ . The obtained kinetic freeze out temperature for non strange particles  $T_{kin} = 72 \pm 6$  MeV nicely agrees with the chemical freeze out temperature obtained from the SHM fit  $T_{chem} = 73 \pm 3$  MeV. The kinetic freeze out temperature of strange particles seems to be higher and shows a rather flat behavior with increasing mass.

It could be shown by a PLUTO simulation, that the difference between the slope of the  $K^-$  and  $K^+$  can be explained by feed down corrections of  $\phi$  meson decays.

Additionally to the observed excess of low mass dielectron pairs [eaHC11a], the  $\phi$  to  $\omega$  ratio, which shows no indication of any suppression due the OZI rule, and the  $\Xi^-$  yield which is one magnitude higher as expected from thermal production, show a strong enhancement over the expectation values indicating effects of the strongly interacting medium.

The main part of this thesis deals with the analysis of dielectron radiation from p+Nb reactions at 3.5 GeV recorded in September 2008. Technical challenges were to adapt the multivariate analysis to the low multiplicity environment and to do a careful comparison to the standard electron identification method, in order to reduce systematic uncertainties and to learn more about the advantages and disadvantages of both methods. It could be clearly shown that already in the low multiplicity environment of p+Nb reactions the MVA has on average 20% higher efficiencies compared to the standard method of hard cuts, while the signal to background ratio in the final dielectron spectra showed no differences between the two methods. The focus on the interpretation of the data is put on the modification of the vector meson line shape by comparing the p+Nb dielectron spectra to data from elementary p+p collisions. Furthermore emphasis is put on the additional effects for a nuclear modification of the cross section, like particle production in secondary reactions.

The best theoretical description of the p+p data is achieved by introducing a coupling of the  $\rho$  to baryonic resonances, leading to modifications of the  $\rho$  meson line shape due to phase space restrictions of the resonance decays. These modifications in elementary p+p collisions complicate the extraction of additional modifications of the line shape in the p+Nb data.

## IV

Comparing the line shape of the p+p with the p+Nb invariant mass spectra, normalized to the number of neutral pions, no significant difference is visible. The situation changes dramatically if one applies a selection on the pair momenta. While for pair momenta larger than 0.8 GeV/c the spectra still agree, for smaller momenta a strong modification in the vector meson region, where modification due to the nuclear medium are predicted by hadronic models, is observed.

The nuclear modification factor  $R_{pA}$  shows a rise for all regions of the invariant mass for small momenta, giving hints for strong contribution from secondary reactions, also indicated by a shift in rapidity. The value for identified  $\omega$  stays flat over the whole region, pointing to no large contribution from secondary reactions to the  $\omega$  yield. This could be explained by an increase of its in-medium width resulting in a massively reduced partial branching ratio to dielectrons.

Comparing the presented results to other experiments we find good agreement on the nuclear suppression of  $\omega$  mesons. The hints for a flat behavior of this modifications as a function of the momentum, reported recently by the CBELSA-TAPS collaboration can be confirmed. Moreover the modification of the line shape in the vector meson region for slow pairs represents the first measurement sensitive to the momentum region where the modification are expected to be most pronounced.

## Inhaltsangabe

In dieser Arbeit werden Daten zweier Messkampagnen des an der GSI in Darmstadt installierten HADES Spektrometers analysiert.

Für Ar+KCl Kollisionen bei einer kinetischen Strahlenergie von 1.76A GeV werden Effizienzkorrekturen, basierend auf Simulationen, für geladene Kaonen durchgeführt. Um diese zu identifizieren ist die Energieverlustinformation in den Driftkammern und den Flugzeitwänden essentiell. Im Vergleich der simulierten mit den experimentell gemessenen Verteilungen zeigten sich jedoch Abweichungen, die eine Anpassung der für die Simulation verwendeten Auswahlsschnitte erforderten. Sie wurden derart angepasst, dass sie auf simulierte Daten genauso wirken wie die entsprechenden Auswahlsschnitte auf echte Daten.

Weiter wurde die Dielektronen-Identifizierung, die in dieser Strahlzeit zum ersten Mal auf einem neuronalen Netzwerk basierte [Lan08], im Bezug auf Effizienz verbessert. Durch Änderung der als Eingabe in das neuronale Netzwerk verwendeten Detektorinformationen, konnte diese um mehr als einen Faktor drei in der TOF-Region des Detektors für Impulse größer als 0.5 GeV/c verbessert werden.

Die verschiedenen gemessenen Hadronen-Raten werden mit einem "Statistical Hadronization Model" (SHM) Fit verglichen und in Bezug auf den Grad der erreichten Thermalisierung des Systems und der starken Abweichung für Teilchen mit zweifachem Strangeness-Inhalt diskutiert. Alle Teilchenraten, bis auf die des  $\Xi^-$ , werden zufriedenstellend beschrieben, was auf einen hohen Thermalisierungsgrad des Systems hindeutet.

Die lineare Abhängigkeit von  $T_{eff}$  von der Masse für Teilchen ohne Strangeness-Inhalt ist mit einer radialen Expansionsgeschwindigkeit von  $\langle \beta \rangle \approx 0.39 \pm 0.1$  erklärbar. Die ermittelte kinetische Ausfrieretemperatur  $T_{kin} = 72 \pm 6$  MeV stimmt sehr gut mit der chemischen Ausfrieretemperatur von  $T_{chem} = 73 \pm 3$  MeV, bestimmt mittels des SHM-Fits, überein. Die kinetischen Ausfrieretemperaturen der Teilchen mit Strangeness-Inhalt zeigen keinen starken Anstieg zu höheren Massen.

Anhand einer PLUTO-Simulation konnte gezeigt werden, dass die beobachteten unterschiedlichen inversen Steigungsparameter der geladenen Kaonen durch Korrektur der Beiträge aus Zerfällen des  $\phi$  Mesons erklärt werden können.

Zusätzlich zu der beobachteten Erhöhung in der Dileptonen-Rate, zeigt das  $\phi$  zu  $\omega$  Verhältnis keinerlei Anzeichen für eine Unterdrückung aufgrund der OZI-Regel, sowie die Rate der  $\Xi^-$  eine starke Überhöhung über der SHM Vorhersage. Alle drei Beobachtungen deuten auf Mediumeffekte hin.

Der Hauptteil der Arbeit behandelt die Analyse von Dielektronenstrahlung aus p+Nb Reaktionen bei einer kinetischen Strahlenergie von 3.5 GeV. Die technische Herausforderung bestand darin, die multivariate Analyse an die geringe Spurdichte der p+Nb Umgebung anzupassen. Weiter wurden systematische Vergleiche zur Standard-Elektronen-Identifizierung Methode durchgeführt, mit dem Ziel mehr über die Eigenarten der beiden Methoden zu lernen und sie so verbessern zu können. Es konnte gezeigt werden, dass die multivariate Analyse eine um mehr als 15% bessere Effizienz für Elektronen und Positronen bei vergleichbarem Signal zu Untergrundverhältnis erzielt.

In der Interpretation der Daten wird der Fokus auf die Modifikation der Dielektronen-Linienform im Vergleich mit elementaren p+p Reaktionen gelegt. Darüber hinaus wird die nukleare Modifikation der Raten diskutiert.

Es zeigt sich, dass die theoretisch beste Beschreibung der p+p Daten erzielt wird, indem man eine Kopplung der  $\rho$  Mesonen an baryonische Resonanzen einführt. Als Konsequenz aus den Phasenraumbeschränkungen dieser Resonanzzerfälle wird allerdings die Linienform schon in elementaren Reaktionen verändert. Dieser Umstand kompliziert die Isolierung von Modifikationen der Linienform

aufgrund zusätzlicher Medium-Effekte in p+Nb Reaktionen.

Trotz dieser Problematik zeigt sich im Vergleich der Linienform für langsame Paare in der Vektormeson-Massenregion eine starke Modifikation. Der nukleare Modifikationsfaktor  $R_{pA}$  zeigt einen Anstieg zu niedrigen Impulsen in allen Massenbereichen. Zusammen mit der beobachteten Verschiebung der Rapiditätsverteilungen deutet dies auf starke Beiträge von Teilchenproduktion in sekundären Reaktionen hin. Im Gegensatz dazu verhalten sich die Werte für identifizierte  $\omega$ -Mesonen flach. Dies kann zum Beispiel durch eine starke Verbreiterung des  $\omega$ -Mesons im Medium und daraus resultierendem verringertem Verzweigungsverhältnis zu Dielektronen erklärt werden.

Im Vergleich mit vorangegangenen Experimenten zeigt sich eine gute Übereinstimmung in Bezug auf die nukleare Unterdrückung der totalen  $\omega$  Produktionsraten. Weiter konnte deren flacher Verlauf als Funktion des Impuls, wie kürzlich von der CBELSA-TAPS Kollaboration gemessen, bestätigt werden. Die beobachtete Modifikation der Dielektronenlinienform für niedrige Impulse stellt die erste Messung dieser Impulsregion, in der man aufgrund hadronischer Modelle die stärksten Mediumeffekte erwartet, da.

*„Fear is the true enemy, the only enemy“*  
Sun Tzu



# Contents

<b>Contents</b>	<b>1</b>
<b>List of Figures</b>	<b>5</b>
<b>List of Tables</b>	<b>9</b>
<b>1 Introduction</b>	<b>11</b>
1.1 The generation of hadron masses . . . . .	12
1.1.1 The strong interaction and QCD . . . . .	13
1.1.2 Chiral Symmetry . . . . .	13
1.1.3 Melting of the condensates and modification of hadron properties . . . . .	13
1.1.4 Experimental observable . . . . .	15
1.2 Experimental access I: cold nuclear matter . . . . .	15
1.2.1 Results . . . . .	15
1.3 Experimental access II: The QCD phase diagram and HIC . . . . .	22
1.3.1 Observables of heavy-ion collisions . . . . .	24
1.3.2 Experimental results . . . . .	24
1.4 Structure and goal of the thesis . . . . .	29
<b>2 The HADES detector system</b>	<b>31</b>
2.1 Physics goal and detector requirements . . . . .	31
2.1.1 Configuration . . . . .	32
2.2 Ring Imaging Cherenkov detector (RICH) . . . . .	33
2.2.1 Ring reconstruction and quality assessment . . . . .	34
2.3 Tracking system . . . . .	35
2.3.1 Magnet . . . . .	36
2.3.2 Multiwire Driftchambers (MDCs) . . . . .	36
2.3.3 Track reconstruction and momentum determination . . . . .	38
2.4 Time of flight measurement . . . . .	40
2.4.1 Diamond counter . . . . .	40
2.4.2 Scintillator time of flight wall (TOF) . . . . .	41
2.4.3 Scintillator time of flight wall (TOFino) . . . . .	41
2.5 Pre-SHOWER detector . . . . .	42
2.6 Trigger and data acquisition . . . . .	43
2.7 Analysis framework . . . . .	44
2.7.1 Toolkit for Multivariate Data Analysis with ROOT . . . . .	44

<b>3</b>	<b>Analysis of the p+<i>Nb</i> data</b>	<b>47</b>
3.1	Choice of the collision system . . . . .	47
3.2	Specifications of the p+ <i>Nb</i> run . . . . .	48
3.3	Electron identification . . . . .	49
3.3.1	MVA PID . . . . .	50
3.3.2	RICH-Track matching . . . . .	57
3.3.3	Track sorting . . . . .	57
3.3.4	Overview of the selections and purity estimation . . . . .	58
3.4	Di-electron analysis . . . . .	61
3.4.1	Physical combinatorial background sources . . . . .	62
3.5	Efficiency corrections . . . . .	66
3.5.1	Self consistency check and opening angle correction . . . . .	69
3.6	Comparison between MVA and HCA . . . . .	70
3.7	Normalization . . . . .	74
3.8	Error estimation . . . . .	75
3.8.1	Total error of the measurement . . . . .	75
3.9	The HADES acceptance filter . . . . .	75
<b>4</b>	<b>Discussion of the p+<i>Nb</i> data compared to the p+p reference</b>	<b>77</b>
4.1	Establishing a reference cocktail for p+ <i>Nb</i> . . . . .	77
4.1.1	The p+p dielectron spectrum . . . . .	77
4.1.2	Long-lived sources . . . . .	78
4.1.3	Short-lived sources . . . . .	78
4.1.4	Bremstrahlung . . . . .	81
4.1.5	Reaction kinematics and particle threshold . . . . .	82
4.2	The p+ <i>Nb</i> data . . . . .	83
4.2.1	Scaling of the p+p data . . . . .	83
4.2.2	Differential analysis . . . . .	87
4.2.3	Momentum dependent comparison of the spectral shape . . . . .	90
4.2.4	Momentum dependence of the nuclear modification . . . . .	94
4.2.5	Modification of .. . . . .	95
4.2.6	Comparison to other experiments . . . . .	97
4.3	Summary and conclusion . . . . .	97
4.3.1	... and what about chiral symmetry? . . . . .	98
<b>5</b>	<b>Finalizing the Ar+<i>KCl</i> data</b>	<b>99</b>
5.1	Specifications of the Ar+ <i>KCl</i> run and status of the data analysis . . . . .	99
5.2	Efficiency correction for charged kaons . . . . .	100
5.2.1	Transverse mass spectra and total production yields . . . . .	106
5.3	Refinement of the MVA settings . . . . .	109
5.3.1	Choice of variates . . . . .	111
5.3.2	Impact of the refinement . . . . .	112
5.3.3	$\omega$ yield . . . . .	115

<b>6</b>	<b>Interpretation of the Ar+KCl data</b>	<b>117</b>
6.1	Particle yields . . . . .	117
6.1.1	Strangeness balance . . . . .	117
6.2	Comparison with statistical hadronization . . . . .	119
6.2.1	Ensemble theory and particle production in heavy-ion collisions . . . . .	119
6.2.2	SHM fit to Ar+KCl yields . . . . .	120
6.2.3	The $\phi$ meson and OZI suppression . . . . .	121
6.2.4	The $\Xi^-$ hyperon and catalytic strangeness production . . . . .	123
6.3	Chemical vs. kinetic freeze-out . . . . .	124
6.3.1	The different freeze out criteria of charged kaons . . . . .	125
6.4	Summary and conclusions . . . . .	125
<b>7</b>	<b>Summary and outlook</b>	<b>127</b>
7.1	The upgraded HADES . . . . .	130
<b>8</b>	<b>Zusammenfassung</b>	<b>133</b>
<b>A</b>	<b>Abbreviations register</b>	<b>139</b>
	<b>Bibliography</b>	<b>141</b>



# List of Figures

1.1	Additional contributions to the in-medium particle self energy . . . . .	14
1.2	In-medium transverse amplitude of the $\rho$ meson spectral function . . . . .	14
1.3	Acceptance of the KEK-E325 experiment . . . . .	15
1.4	E325: dielectron invariant mass spectra . . . . .	16
1.5	E325: $\phi$ signal . . . . .	17
1.6	Dielectron acceptance of the CLAS spectrometer . . . . .	18
1.7	CLAS: dielectron invariant mass spectra . . . . .	19
1.8	Transparency ratio of $\omega$ mesons . . . . .	20
1.9	Transparency ratio of different particles . . . . .	22
1.10	Phase diagram of strongly interacting matter . . . . .	23
1.11	The liquid-gas phase transition . . . . .	24
1.12	NA60: $\rho$ meson contribution in heavy-ion collisions . . . . .	26
1.13	Comparison of DLS data to transport calculation. . . . .	26
1.14	PHENIX: Dielectron spectrum from Au+Au collisions . . . . .	27
1.15	Dielectron data from the CERES experiment . . . . .	28
1.16	Comparison of inverse slope parameters of charged kaons . . . . .	29
1.17	Ratio of charged kaons as a function of the centrality . . . . .	30
2.1	Elongated view of the HADES detector . . . . .	31
2.2	Layer structure of modern particle detectors . . . . .	32
2.3	Cross section of the HADES detector . . . . .	33
2.4	Cross section of the Ring Imaging Cherenkov detector . . . . .	34
2.5	RICH cathode layer . . . . .	34
2.6	Quality parameter of reconstructed RICH rings . . . . .	35
2.7	Super conducting magnet . . . . .	36
2.8	MDC drift cell . . . . .	37
2.9	Time over threshold distribution and resolution of the MDCs . . . . .	37
2.10	MDC dE/dx distribution as a function of the momentum . . . . .	38
2.11	Wire-cluster in the drift chambers . . . . .	39
2.12	Momentum resolution . . . . .	40
2.13	Diamond start and veto counter . . . . .	40
2.14	Beta vs. momentum distribution in TOF region . . . . .	41
2.15	Energy loss vs. momentum distributions of the TOF detectors . . . . .	42
2.16	Cross section of a Pre-SHOWER cell . . . . .	42
2.17	Shower signal . . . . .	43
2.18	Trigger system . . . . .	44

2.19	Concept of the multivariate analysis . . . . .	45
2.20	Architecture of a neural network . . . . .	46
3.1	Reconstructed vertex distribution . . . . .	48
3.2	Matching radius between RICH and Tracking detectors . . . . .	50
3.3	Variates in the TOF region . . . . .	53
3.4	Variates in the TOFino region . . . . .	54
3.5	Correlation matrix in the TOF region . . . . .	55
3.6	Correlation matrix in the TOFino region . . . . .	55
3.7	Answering value of the neural network . . . . .	56
3.8	Effect of the MVA PID on single tracks . . . . .	56
3.9	2-dimensional RICH-MDC correlation . . . . .	57
3.10	Topology of reconstructed tracks used in the final pair spectra . . . . .	60
3.11	Purity of single lepton tracks . . . . .	61
3.12	Physical background sources . . . . .	62
3.13	Relative rates of electrons and positrons . . . . .	63
3.14	Distribution of pair tracks over the 6 sectors . . . . .	63
3.15	Uncorrected invariant mass spectra . . . . .	65
3.16	Signal to background ratio . . . . .	66
3.17	Spread between initial and reconstructed momentum . . . . .	66
3.18	Efficiency matrix . . . . .	68
3.19	Projected efficiency . . . . .	68
3.20	Opening angle distribution . . . . .	69
3.21	Self consistency of dielectrons originating from direct $\omega$ decays. . . . .	70
3.22	Comparison of the signal to background ratio . . . . .	71
3.23	Comparison of projected efficiencies . . . . .	72
3.24	Ratio MVA to HCA: invariant mass . . . . .	72
3.25	Ratio MVA to HCA: kinematical observables . . . . .	73
3.26	Difference between initial and reconstructed momentum . . . . .	76
4.1	Comparison of p+p data to calculated dielectron cocktail . . . . .	80
4.2	Diagram of resonance decay via VMD . . . . .	80
4.3	Comparison of p+p invariant mass to GiBUU (including resonances) . . . . .	81
4.4	Systematics of dielectron emission from p+p and p+d collisions . . . . .	82
4.5	Comparison of dielectron cross sections as a function of the invariant mass . . . . .	84
4.6	Comparison of the dielectron invariant mass spectra normalized to the neutral pion cross section . . . . .	86
4.7	Comparison of transverse momentum distributions . . . . .	88
4.8	Comparison of rapidity distributions . . . . .	89
4.9	Fraction of inside to outside the medium decays . . . . .	90
4.10	Momentum coverage for dielectron pairs . . . . .	91
4.11	Comparison of the invariant mass spectra for fast pairs . . . . .	92
4.12	Comparison of the invariant mass spectra for slow pairs . . . . .	93
4.13	Nuclear modification factor $R_{pA}$ . . . . .	94
4.14	Difference in the vector meson region for slow pairs . . . . .	96
5.1	Uncorrected invariant mass spectra . . . . .	101

5.2	Efficiencies of the cut in the energy loss vs. momentum plane for the drift chambers . . . . .	102
5.4	Total efficiency for charged kaons . . . . .	104
5.6	Transverse mass spectra . . . . .	106
5.7	Rapidity distributions . . . . .	108
5.8	Systematics of $K^-/K^+$ ratio . . . . .	109
5.9	Comparison of the MVA and HCA electron efficiency . . . . .	110
5.10	Positron MVA efficiencies in for the different detector system . . . . .	110
5.11	Variates distribution . . . . .	113
5.12	Comparison of the improved MVA setting efficiency to the original one. . . . .	114
5.13	Comparison of the improved MVA setting efficiency to the HCA. . . . .	114
5.14	Invariant mass of dielectrons in the vector meson region . . . . .	115
6.1	Freeze-out points in the QCD phasediagram . . . . .	121
6.2	Comparison of particle yields to the SHM values . . . . .	122
6.3	$\phi$ to $\omega$ ratio as a function of the $\phi$ excess energy . . . . .	123
6.4	Effective temperature as a function of the particle mass . . . . .	124
6.5	Simulated $K^-$ spectra and rapidity distribution . . . . .	126
7.1	Comparison of dielectron radiation from HIC to an elementary reference . . . . .	128
7.2	p+Nb: Charged kaon invariant mass spectra . . . . .	130
7.3	Comparison of DAQ rates of different HIC experiments . . . . .	130
7.4	Facility for antiproton and ion research (Fair) . . . . .	131



# List of Tables

1.1	Overview of results on vector mesons in the medium . . . . .	21
3.1	Beam and target specifications of the p+ $\text{Nb}$ run . . . . .	48
3.2	Data taking specifications . . . . .	49
3.3	Allowed ranges of variates . . . . .	51
3.4	Overview of event and single track selections . . . . .	59
4.1	Elementary production thresholds . . . . .	85
4.2	Comparison of the mean values of the kinematical observables . . . . .	87
5.1	Beam and target specifications of the Ar+ $\text{KCl}$ run . . . . .	99
5.2	Overview of analyzed particle species . . . . .	100
5.3	Overview of the charged kaon results . . . . .	107
6.1	Particle yields . . . . .	118



# Chapter 1

## Introduction

At the end of the 19th century and the beginning of the 20th century the field of physics was believed to be a nearly solved discipline, with only a few high-precision measurements to be done. The spirit of this time is nicely underlined by a citation of the well known American physicist Albert Michelson: "The most important fundamental laws and facts of physical science have all been discovered, and these are now so firmly established that the possibility of their ever being supplemented by new discoveries is exceedingly remote."

What we today call classical physics consists of Newton's laws of the motion of matter, Maxwell's theory of electromagnetic waves, optics and thermodynamics. Based on these theories the common view of the world was that of a static, causal and deterministic universe, embedded into an absolute reference frame. This implied that by gathering all initial information on a system, its exact evolution in time could be predicted, which in principle would allow to predict the future, if one had all relevant information.

But this view of the world could not keep up for long, due to two big revolutions which changed everything: Albert Einstein's special relativity and general relativity theory, both relevant for cosmological scales, broke with the concepts of an absolute reference frame and a static universe <sup>1</sup>, while the determinism and to some extent causality could no longer be held up in quantum mechanics, which is used to describe microscopic systems on the atomic scale and below.

Quantum mechanic differs strongly from classical physics in both, its mathematics, as well as in its fundamental principles, which are often absolutely not intuitive, such as quantized energy states, particle wave duality and the uncertainty relation, within which energy and momentum conservation can be disabled. The deeper scientists investigated the theory, the more curiosities they found, like quantum entanglement brought up the first time by Einstein, Podolski and Rosen <sup>2</sup> and later confirmed by several sophisticated experimental setups [Bell11]. These observations keep the interpretation of the theory and the deduced view of the world challenging until today.

Following the pioneering scattering experiments by Rutherford, experiments at ever increasing energies disentangled step by step a complete zoo of new particles. The obtained systematics are the basis for the so-called Standard Model of particle physics, which includes the strong, weak and electromagnetic interaction. It arranges particles in two main groups, leptons and quarks, each consisting of three generations. In addition, four particles are included as carriers of the different interaction forces.

Although phenomenologically the model is very successful, it has several draw backs, e.g. missing

---

<sup>1</sup>After Einstein realized this, he introduced an additional term to his equations in order to allow static solutions, the cosmological constant.

<sup>2</sup>Known in literature as the EPR-effect.

inclusion of the gravitational force, no underlying reason for the mass ordering etc.

On the other hand, on very large scales, Einstein's general relativity theory describes the gravitational force no longer as a force field but rather as a curvature of the 4-dimensional space-time. Together with the cosmological principle, which postulates a homogenous and isotropic universe, and the Olbers' paradox, which excludes an infinitely old universe from the fact that the universe is not in chemical equilibrium<sup>3</sup>, it serves as the basis for the big bang theory.

In recent years, striking experimental constraints could be made on cosmological parameters, e.g. the results of the WMAP satellite allowed to constrain the age of the universe to  $13.8 \cdot 10^9$  years and the composition of matter in the universe to 4.5% baryonic, while the rest consists to 22.6% of dark matter and 72.9% of dark energy [eaWC11].

Up to now, both theories are used separately to describe the smallest and largest scales independently of each other, but as soon as the energy density from an object approaches the value of the Planck-mass ( $1.2 \cdot 10^{19} \text{ GeV}/c^2$ ), its Compton wave length is at the order of its Schwarzschild radius<sup>4</sup> and a quantum gravitation theory would be needed. The search for such a grand unified theory is one of the biggest challenges in theoretical physics nowadays.

Another big challenge of modern physics, concerning both microscopic (e.g hadrons) and macroscopic (e.g. neutron stars) objects, is the understanding of the generation of hadron masses and will be discussed in more details in the following. For popular science reviews about modern physics see [Gre05, Wil10].

## 1.1 The generation of hadron masses

In our current belief quarks are the smallest components of matter. Since they have never been observed directly, their free (current) masses can be extracted from their influence on hadron properties, only. For a review on the extraction of the current quark masses see [qua]. However, meanwhile the masses of the two lightest flavors, the up (u) and down (d) quarks, have been extracted with good precision and have values smaller than  $10 \text{ MeV}/c^2$ <sup>5</sup>. Three of these light objects combine together to a roughly 50 times heavier object: the nucleon.

This generation of mass can be understood on a phenomenological level, in the following way: the strong force, theoretically described by **Quantum Chromo Dynamics (QCD)**, is responsible for the interaction among the quarks. The charge of this interaction is called color. QCD allows only the existence of color neutral objects, which are either realized by the combination of three quarks with different colors or by a combination of a quark and an antiquark carrying color and the corresponding anticolor. Accordingly, in nature the quarks which form a color neutral object will be arranged as close as possible to each other, in order to disturb color neutrality as low as possible. On the other hand according to Heisenberg's uncertainty relation:

$$\Delta x \Delta p \geq \hbar, \quad (1.1)$$

such a localization demands large momenta and amounts of energy. With the help of Einsteins famous relation:

$$E = \sqrt{(pc)^2 + (mc^2)^2}, \quad (1.2)$$

<sup>3</sup>If so, there should be no black regions in the night sky.

<sup>4</sup>The Schwarzschild radius is the event horizon of a black hole and defined as  $R = \sqrt{3/2} \left( \frac{c^2}{GM} \right)^2$ .

<sup>5</sup>For a detailed discussion about the extraction of the free quark masses see [qua].

this energy can be directly related to the observed particle masses. If one assumes the radius of a nucleon to be of the order of 1 fm one can estimate the lower limit of the uncertainty on the momentum  $\Delta p$  to be 200 MeV/c, with the help of formula 1.1 by putting  $\hbar c = 200 \text{ MeV fm}$ . Neglecting the current quark masses one can estimate the total energy of the nucleon to be 600 MeV with the help of formula 1.2, and explain already about 2/3 of the actual hadron mass by dynamical generation. Following this line of argumentation, the observed hadron masses can be understood as nature's compromise between the disturbances of the vacuum due to the violation of color neutrality on the one hand and the cost of localization on the other hand.

### 1.1.1 The strong interaction and QCD

QCD is a relativistic field theory, which is formulated in close analogy to the theory of electromagnetic interactions, the **Quantum Electro Dynamics** (QED). The characteristics of the theory is that unlike the photons in QED, the force carriers of the strong interaction, the gluons, carry the strong charge (color) themselves, which allows them to interact among themselves. This implies that the coupling strength  $\alpha_s$  of the strong interaction is strongly depending on the 4-momentum transfer. While it becomes small for large momentum transfers and can be treated with perturbation theory, this is not the case for small momentum transfers and one has to rely on effective models for the description of the interactions.

It is the special character of QCD which prevented us from a deeper understanding of phenomena like the generation of mass and the confinement of quarks. Therefore, since over 40 years the phases of QCD matter are systematically investigated in heavy ion collisions (HIC), section 1.3 and cold nuclear matter experiments, section 1.2.

### 1.1.2 Chiral Symmetry

The helicity of a particle is defined to be right handed if the spin of the particle points into the same direction as its motion and left handed otherwise. For massless particles helicity and chirality are equal. For massive ones however it is possible for an observer to move into a reference frame, where he or she overtakes the particle, which is then moving in the opposite direction, which obviously changes the helicity. Chirality is defined in a more abstract way in order to be invariant under the Lorentz transformation.

In the Lagrangian formulation of a field theory symmetries of the Lagrangian lead to conserved quantities. According to QCD the spontaneous breaking of chiral symmetry due to a non-vanishing expectation value of the two quark condensate  $\langle \bar{q}q \rangle$  is responsible for the degeneracy of chiral partners like the  $\pi$  and the  $\sigma$  and for the creation of hadron masses.

The small current quark masses on the other hand are due to an explicit breaking of the chiral symmetry due the Higgs field and is investigated in elementary collisions at the highest possible energies at the **Large Hadron Collider** (LHC).

### 1.1.3 Melting of the condensates and modification of hadron properties

One of the order parameters of chiral symmetry is the scalar two quark condensate  $\langle \bar{q}q \rangle$ , which is expected to vanish if the symmetry is restored. According to model calculations, for instance by the Nambu-Jona-Lasino model [MLW92], the expectation value of the condensate is expected to decrease

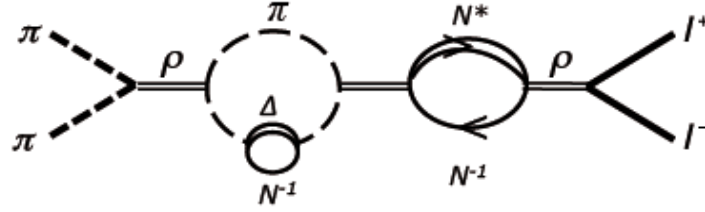
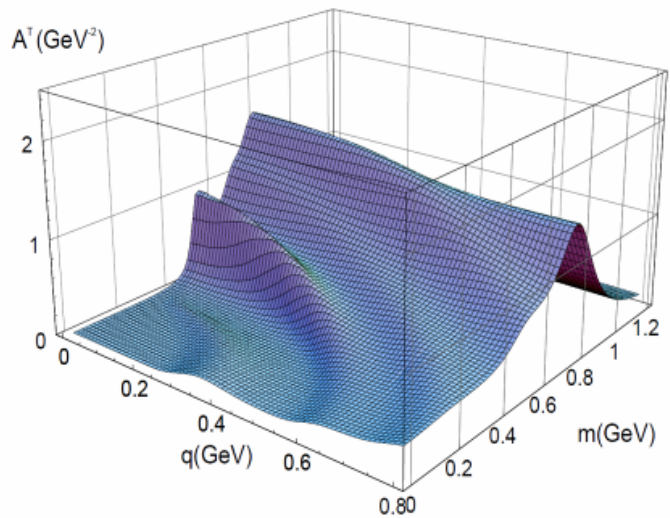


Figure 1.1: Additional contributions to the in-medium  $\rho$  self energy due to dressed pion loops (first part) and resonance hole excitations (second part).

with increasing temperature and/or density. According to the model, already at nuclear ground state density  $\rho_0$ , the scalar two quark condensate is decreased to  $\approx 80\%$  of its initial value.

Unfortunately the  $\langle \bar{q}q \rangle$  expectation value is not a direct observable and can only be determined indirectly. It can be linked with the help of QCD sum rules [HL92b] to the energy weighted integral over hadronic spectral functions. Implying that the hadronic spectral functions are constrained, but not determined, and effective models are needed to predict specific hadron properties inside the medium. Various models predict relatively strong changes of particle masses and/or widths already at normal nuclear matter density  $\rho_0$  [HL92a, BM88, ea97]. Early models suggested a shift of the particle masses of the light vector mesons  $\rho$  and  $\omega$ , proportional to the reduction of the  $\langle \bar{q}q \rangle$  condensate [BR91]. More recent hadronic model calculations [MPM04] take additional contribution to the in-medium self energy, due to couplings to resonance hole excitations inside the medium, shown in Feynman graph in Fig. 1.1, into account. The resulting spectral function develops additional structures, shown in Fig. 1.2 for the transverse amplitude of the  $\rho$  meson spectral function as a function of the particle mass and the relative momentum to the surrounding medium. The calculations are done for different densities, shown is the one for two times nuclear ground density. It should be stated here that according to this model calculation, the effects are most pronounced for relative momenta smaller  $0.8 \text{ GeV}/c$ .

Figure 1.2: Plotted is the transverse amplitude of the  $\rho$  meson spectral function as a function of the particle mass and the relative momentum to the surrounding medium calculated for a density of two times nuclear ground density using a hadronic model [MPM04]. According to this model calculation the effects are most pronounced for relative momenta smaller  $0.8 \text{ GeV}/c$ .



### 1.1.4 Experimental observable

In order to measure directly a modification of a particle line shape, two conditions have to be fulfilled:

- The particle lifetime has to be sufficiently short, so that the decay can take place inside the medium.
- The decay products should not be affected by final state interaction while propagating to the detectors.

Therefore, penetrating probes like dilepton pairs are a promising probe. As the short lived vector mesons ( $\rho/\omega$ ) couple via a virtual photon to a dilepton pair, their line shape can be reconstructed undistorted by final state interactions. Drawbacks are however the small branching ratio at the order of  $10^{-5}$ , due to a double electromagnetic suppression and the question how one can distinguish a broadened  $\omega$  from a vacuum  $\rho$ , since both mesons have comparable pole masses and the same quantum numbers apart from their isospin I and their G-parity.

## 1.2 Experimental access I: cold nuclear matter

Photon, pion or proton induced reactions on heavy nuclei offer a possible access to medium modifications. Although the expected effects are only on the order of 20% [MLW92], characteristics of the collision, like no density and temperature evolution of the system and the small combinatorial background, are clear advantages.

Apart from direct line shape measurements the nuclear modification of the production cross sections is another promising observable specific for cold matter experiments. As the particle rate in cold nuclear matter reactions is proportional to the life time of the meson, strong broadening of hadrons inside the medium would lead to a reduced partial decay branch to dielectrons and hence to a reduced production cross section. The nuclear modification can then be connected via phenomenological models to the total width of the hadron inside the medium, see section 4.2.5 for details.

### 1.2.1 Results

#### Direct line shape

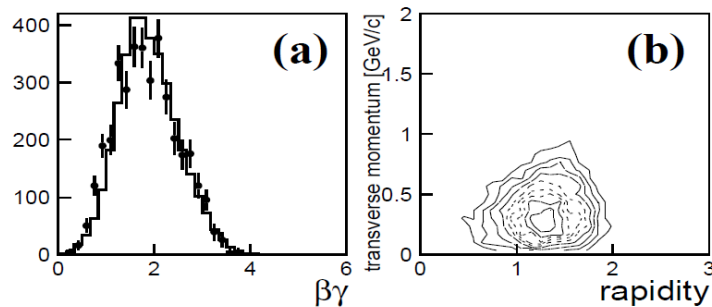
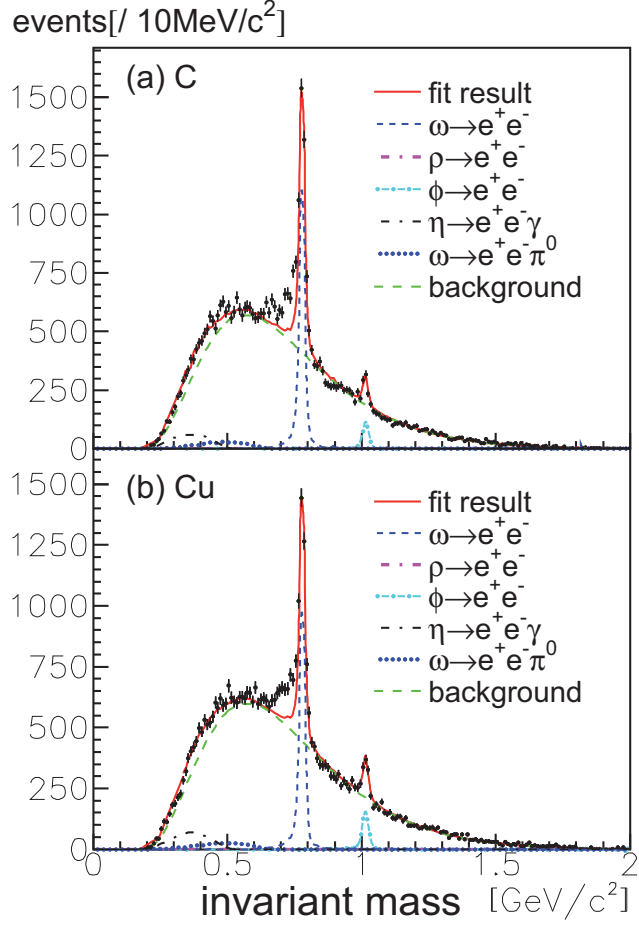


Figure 1.3: Acceptance of the KEK-E325 experiment: pair momentum distribution (left side) and rapidity coverage of the setup (right side) [eaKPEC07].

Direct line shape measurements of the  $\rho/\omega$  mesons in the dielectron channel have been investigated by the CLAS experiment in photon induced reactions at Jefferson Lab [eaCC07] and by the

Figure 1.4: Dielectron invariant mass spectra measured by the E325 experiment, for C (upper part) and Cu targets (lower part), compared to a cocktail assuming vacuum spectral functions and fitted simultaneously with the combinatorial background, the shape of which is obtained from event mixing [eaEC06]. The excess on the left side of the  $\omega$  peak is attributed to a shift of the  $\rho/\omega$  meson mass inside the medium consistent with a decrease by 9%, see text for details.



E325 experiment at the KEK proton synchrotron in proton induced interactions [eaEC06].

The E325 experiment measured dielectron production on C, and Cu targets, induced by a proton beam with a kinetic beam energy of 12 GeV. The apparatus is a two arm spectrometer with 3 drift chambers used for tracking. The initial beam energy increases the production cross sections for vector mesons compared to beam energies of a few GeV but leads to high average momenta of the produced particles and consequently a high fraction of decays taking place outside the medium ( $c\tau_\rho=1.3$  fm,  $c\tau_\omega=23$  fm) and less pronounced modifications, according to the previously discussed hadronic model [MPM04]. The pair momentum distribution and rapidity coverage of the setup is displayed in Fig. 1.3.

The measured dielectron invariant mass spectra for the two targets, together with a calculated dielectron cocktail and the combinatorial background (CB) estimated by event mixing, are displayed in Fig. 1.4. The excess on the left side of the  $\omega$  peak structure is attributed to a shift of the  $\rho/\omega$  meson mass inside the medium consistent with a decrease by 9%.

It should be critically remarked, that the background subtraction using the mixed event method, may introduce systematical effects in the high invariant mass region, due to the missing energy conservation in mixed events compared to same events in elementary reactions. Indeed the calculated background describes the data on the right side of the  $\omega$  peak, without any additional contribution of the  $\rho$  meson, which should be at least present in case of its vacuum decays.

Furthermore the E325 collaboration investigated the line shape of  $\phi$  mesons for three different pair

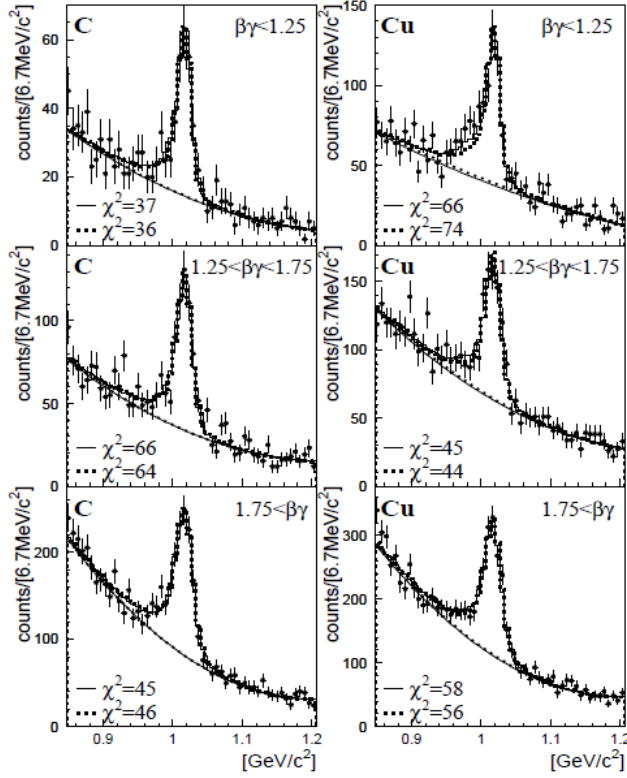


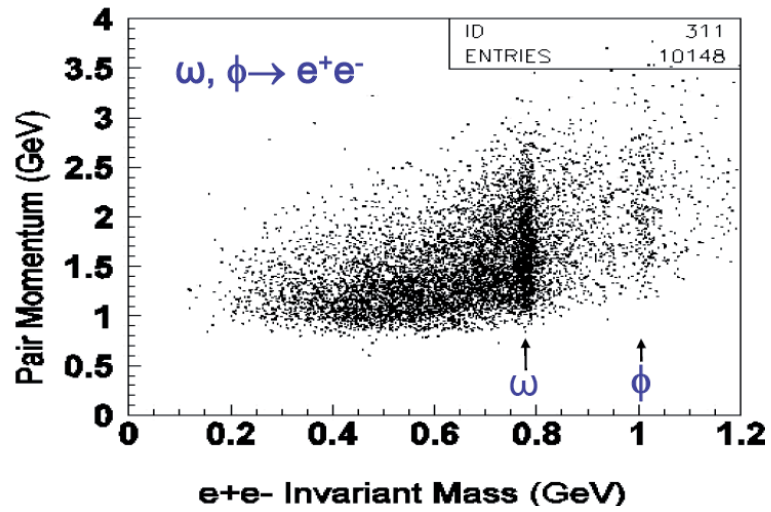
Figure 1.5: E325  $\phi$  signal in the dielectron invariant mass spectra for C (left side) and Cu targets (right side), for three different momentum regions. For the lowest momentum bin ( $\beta\gamma < 1.25$ ) of the Cu-target a broadening of the signal is observed, from which a decrease of the vacuum mass of 3% and a broadening of a factor 3.6 compared to the nominal values are deduced [eaKPEC07].

momentum regions, see Fig.1.5. Although the lifetime of the  $\phi$  meson ( $c\tau_\phi=46$  fm) is a factor two higher compared to the  $\omega$ , for the low momentum bin ( $\beta\gamma < 1.25$ ) of the Cu-target a broadening of the signal is observed. From this observation a decrease of the vacuum mass of 3% and a broadening of a factor 3.6 ( $\Gamma_\phi^{med} \approx 16$  MeV) compared to the nominal values are deduced.

The CLAS experiment on the other hand measured dielectron production in photon induced reactions on D, C, and Fe-Ti targets. The incident photon beam was produced from a primary electron beam at kinetic beam energies of 3-4 GeV. The acceptance of the setup is restricted to pairs with momenta larger than 0.8 GeV/c, as displayed in Fig. 1.6. The corresponding invariant mass spectra for the 3 different targets are displayed in Fig. 1.7, together with the CB contribution estimated via same event positive and negative like sign pairs. The increasing yield at low invariant masses with increasing size of the target nucleus is attributed to a broadening of the  $\rho$  contribution, deduced by comparing a dilepton cocktail consisting only of the vacuum contributions of the three light vector mesons to the data. The collaboration states, that observed broadening is consistent with model expectations of simple nuclear many body effects [eaCC07].

Although there are small differences between the two experimental setups, e.g. the induced particle, the acceptance and the kinetic beam energy, the difference in interpretation between the two presented results should be attributed rather to underestimated systematics, especially in extracting the  $\rho$  signal than to different initial conditions. Apart from the problem of the correct background subtraction, several effects especially related to baryonic resonances have to be at least considered, like the contribution from Dalitz decays of baryonic resonances and the modification of the line shape due to secondary reactions, proceeding via these baryonic resonances, see section 4.1.1 for details.

Figure 1.6: Dielectron acceptance of the CLAS spectrometer. Only pairs with momenta larger than 0.8 GeV/c can be reconstructed. Picture taken from [SL10]



### Indirect measurements: nuclear modification

As mentioned earlier, the nuclear modification of the cross section is another promising observable. Strong broadening of hadrons inside the medium lead to a reduced partial decay branch and hence to a reduced measured production cross section of the meson. Thus the nuclear suppression can be connected via phenomenological models to the total width of the hadron inside the medium. If the low density approximation is valid, the imaginary part of the medium self-energy of the meson can be directly related to the additional width in the medium  $\Gamma_{coll}$ , for details see section 4.2.5.

Systematics on the nuclear suppression of  $\omega$  mesons are provided by the already introduced CLAS experiment and the CBELSA-TAPS experiment located in Bonn. Both setups use a secondary photon beam, at energies of 0.6-3.6 GeV (CLAS) and 0.7-2.6 GeV (CBELSA-TAPS). Compared to CLAS the CBELSA-TAPS setup reconstructs the  $\omega$  meson not in the dielectron channel, but via the decay:  $\omega \rightarrow \pi^0\gamma$ . The  $\omega$  reconstruction is done in two steps: the photon of the  $\omega$  decay is combined with the neutral pion, which is reconstructed via double photon conversion. The characteristic of reconstructing the  $\omega$  meson in this decay channel is, besides the large branching ratio of  $\approx 0.09$ , that the  $\rho$  meson is not contributing (branching ratio= $6 \cdot 10^{-4}$ ), thus any medium-modification can clearly be attributed to the  $\omega$  meson (apart from  $\omega$  interference effects before the decay). The disadvantage is the strong final state interaction of the neutral pion which might distort the initial information to some extent. The collaboration tries to minimize the effect by applying a selection on the kinetic energies of the pions. The nuclear modification ratio is traditionally called transparency ratio in photon induced reactions, which is misleading since it implies that only effects of absorption and no particle production in secondary reactions influence the ratio. In order to avoid that isospin effects and Fermi motion modify the ratio additionally, the data are usually normalized to the production cross section on the carbon nucleus [eaCTC08].

The obtained systematics on the  $\omega$  transparency ratio by CBELSA-TAPS [eaCTC08] are compared to those obtained by CLAS [eaCC10b], in Fig. 1.8. The CLAS data suggest a much stronger broadening as expected due to the CBELSA-TAPS data, however for the heaviest nucleus no significant  $\omega$  signal could be reconstructed and therefore the last point corresponds strictly speaking to an upper limit.

Further complication arises from the model dependence of extracted in-medium cross sections: e. g.

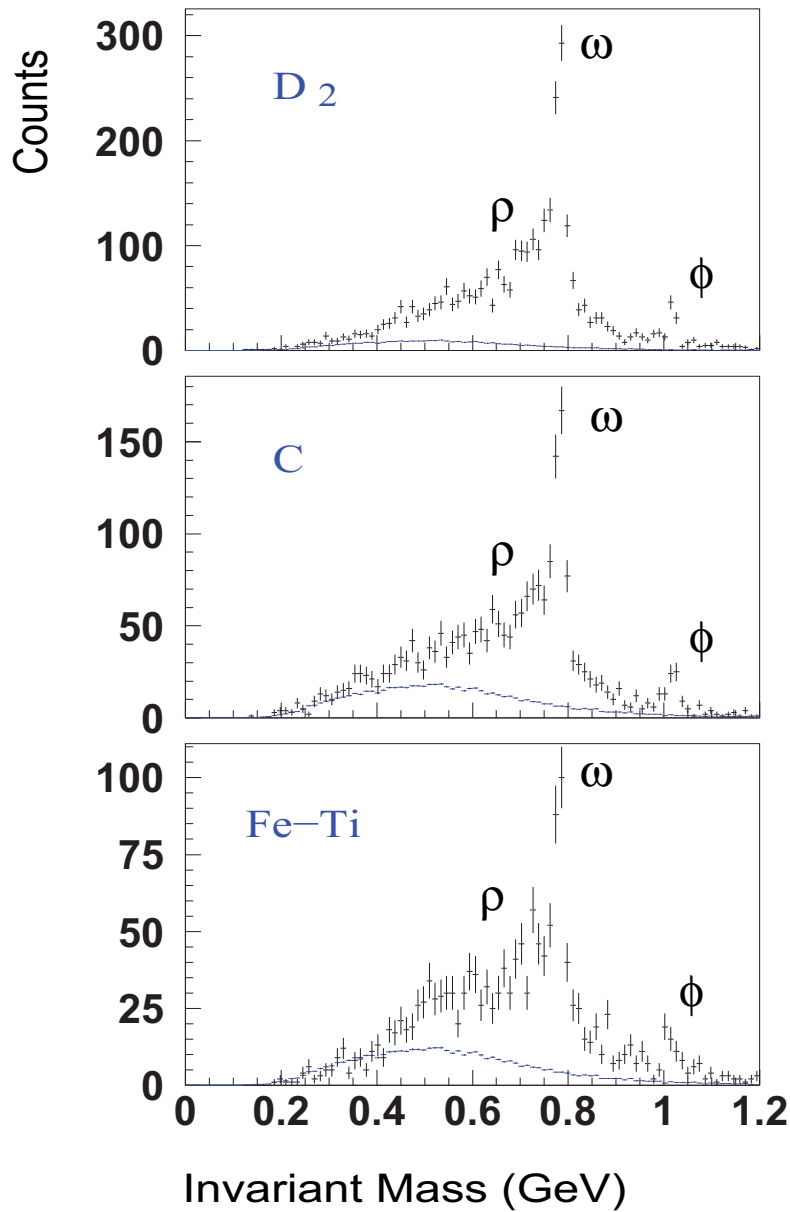
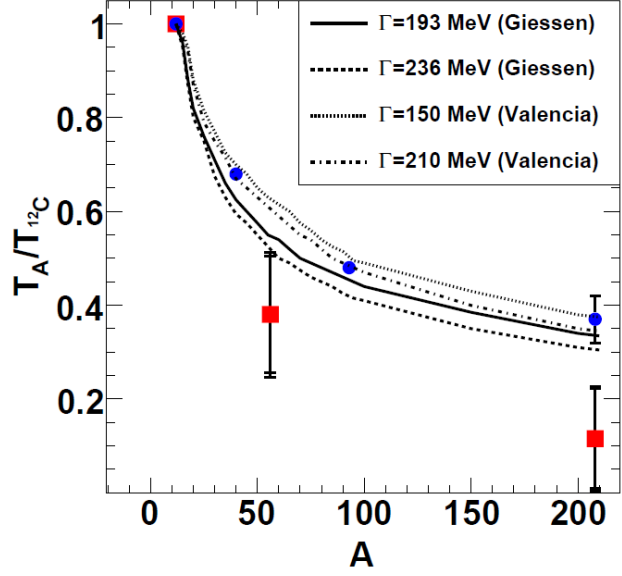


Figure 1.7: Invariant dielectron mass spectra for the three different targets D (top), C (middle) and Fe-Ti (bottom). The increasing yield at low invariant masses with increasing size of the target nucleus is attributed to a broadening of the  $\rho$  contribution, which is consistent with model expectations of simple nuclear many body effects [eaCC07].

Figure 1.8: Systematics of the transparency ratio of  $\omega$  mesons, obtained from the CLAS (red squares) and CBELSA-TAPS (blue points) experiments. The CLAS data seem to suggest a stronger broadening of the mesons inside the medium [eaCC10b].



the recent analysis of [RAN11] led to a significantly different width of the  $\omega$  meson inside the medium as extracted in [eaCTC08]. The previously mentioned complication due to the feeding by secondary particle production is investigated in a preliminary work from CBELSA-TAPS, [PCN11] by applying selections on the kinetic energy of the particles. As can be seen from Fig. 1.9 the  $\eta$  yield experiences a strong feeding by secondary production, while the yields of  $\omega$  and  $\eta'$  mesons seem not to be affected. The data on the nuclear modification obtained by the previously discussed KEK-PS E325 experiment [ea06], agree within errors with the results of the CBELSA-TAPS collaboration. Moreover the nuclear modification of the  $\phi$  meson production cross section was investigated by the SPring-8 [ea05] and ANKE [APea11] experiments. Both results point to a strong broadening of the  $\phi$  meson inside the medium, the extracted medium widths from the SPring-8 data corresponds to  $\Gamma_{\phi}^{med} \approx 60$  MeV at average  $\phi$  momenta of  $\langle P_{\phi} \rangle = 1.7$  GeV/c and the one from the ANKE data to  $\Gamma_{\phi}^{med} \approx 33-50$  MeV at  $\langle P_{\phi} \rangle = 1.1$  GeV/c. Both results are in contradiction with the value observed from the direct line shape measurement of the KEK-E325 experiment, described above.

The measurements are complemented by recent results of the NA60 collaboration in the dimuon channel [eaNC11].

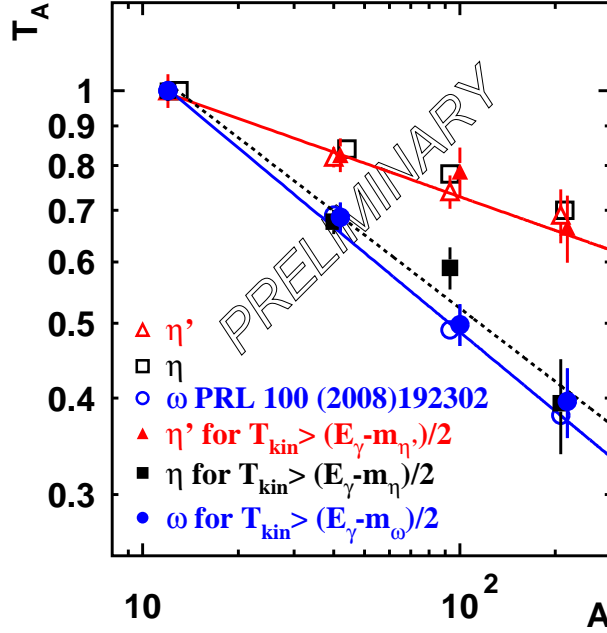
### Summary on results obtained from cold nuclear matter

All presented results on in-medium properties of vector mesons, including the one from heavy-ion collisions are summarized in Tab. 1.1. As the fraction of the inside to outside decays and the strength of the expected modification depend strongly on the average momentum, the presented overview must be interpreted with care. However, the dispersion of extracted results, point to underestimated systematics and more experimental data are needed to get a converging picture. For a review on the status on medium modifications of mesons see [SL10].

experiment	reaction	momentum [GeV/c]	$\rho$	$\omega$	$\phi$
			$\Delta\Gamma$ [MeV] $\Delta m$ [%]	$\Delta\Gamma$ [MeV] $\Delta m$ [%]	$\Delta\Gamma$ [MeV] $\Delta m$ [%]
SPring-8	$\gamma$ +A 1.5-2.4 GeV	$p > 1.0$			$\Delta\Gamma \approx 56$
ANKE	p+A 2.83 GeV	$p > 0.6$			$\Delta\Gamma \approx 29-46$
KEK -E325	p+A 12 GeV	$p > 0.5$	$\Delta\Gamma=0$ $\Delta m \approx -9$	$\Delta\Gamma=0$ $\Delta m \approx -9$	$\Delta\Gamma \approx 12$ $\Delta m \approx -3$
CLAS	$\gamma$ +A 0.6-3.6 GeV	$p > 0.8$	$\Delta\Gamma \approx 70$ $\Delta m=0$	$\Delta\Gamma > 130$	
CBELSA -TAPS	$\gamma$ +A 0.7-2.5 GeV	$p > 0.0$		$\Delta\Gamma \approx 130$ $\Delta m=0$	
CERES	Au+Pb 158A GeV	$p_t > 0.0$	broadening favored		
NA60	In+In 158A GeV	$p_t > 0.0$	$\Delta\Gamma$ : central. dep. $\Delta m=0$		

Table 1.1: Overview of the discussed results on vector mesons in the medium. The presented table has been taken to large extent from [Met11].

Figure 1.9: Transparency ratio for  $\eta$ ,  $\eta'$  and  $\omega$  mesons, corrected for the feed down from secondary particle production. Compared to the yield of the  $\eta$  meson the  $\omega$  and  $\eta'$  seem not to be affected by secondary particle production [PCN11].



### 1.3 Experimental access II: The QCD phase diagram and HIC

In contrast to reactions in cold nuclear matter the particle rate in a heavy-ion collision (HIC) is not proportional to the lifetime of the particle but rather to the lifetime of the collision zone (fireball), due to continuous absorption and recreation. If the lifetime and the interaction rate in such collisions is sufficient to reach chemical equilibrium, the collision can be described by a thermodynamical ansatz, characterizing the generated matter as a function of the temperature  $T$  and the baryochemical potential  $\mu_B$ . HIC allow then to probe systematically the phase diagram of strongly interacting matter, displayed in Fig. 1.10.

However, in its time evolution the system created in HIC runs through different stages, from the initial first chance collisions, through a hot and dense phase, to an expansion phase leading to chemical and kinetic freeze out. As particles are continuously produced and emitted throughout all phases, it is quite challenging to reconstruct the conditions reached in the different phases of the collision. Moreover, much of the information on the early phases might be lost due to strong final-state interactions.

Although the phenomenologies of HIC are meanwhile well characterized over a wide energy range, difficulties in disentangling the different effects and in tracing them back to their origin, have prevented us from answering the big questions about the properties of the different QCD phases and the origin of hadron masses.

At low  $\mu_B$  and high temperatures a phase of free quarks and gluons, the quark gluon plasma (QGP), is expected to exist. Solving QCD equations on a fixed lattice indicate that at a critical temperature  $T_c \approx 160 \text{ MeV}$  [YAS06, ABea11] a cross over between the phase of hadrons and deconfined quarks occurs rather than a real phase transition. These calculations have the advantage that QCD can be di-

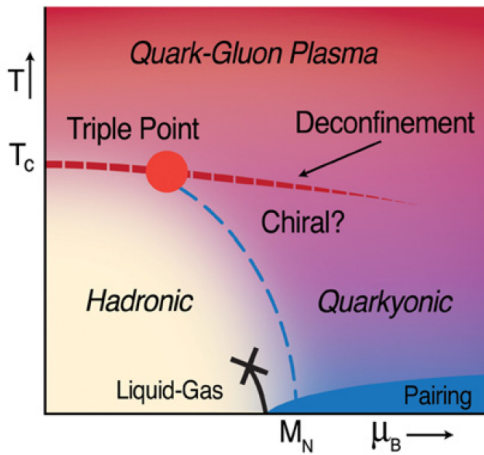


Figure 1.10: The phase diagram of strongly interacting matter [ea10a]. At low baryon chemical potential  $\mu_B$  and high temperatures  $T$ , lattice calculations predict a cross over to a phase of free quarks, which is supported by data. At large  $\mu_B$  the situation is not settled and leaves room for speculations, like the hypothetical phase of quarkyonic matter. Experimentally well confirmed however is the liquid-gas phase transition at temperatures smaller 10 MeV and close to nuclear ground state density.

rectly solved in a regime where the interaction is strong. However, besides time consuming computer calculations several essential operations like the extrapolation from finite lattice size to the continuum introduces systematic uncertainties and resulted in significant differences between the different research groups in the past. Furthermore, calculations at larger  $\mu_B$  cause additional problems.

Experimentally, plenty of observables for the onset of deconfinement have been investigated but, due to the discussed general difficulties in characterizing a HIC, none is fully established yet. Most of the observables, e.g. jet suppression, can not be tested easily at lower initial energies, where no formation of the QGP is expected, due to the steep excitation function of their production cross section. However, new information on the disappearance of possible QGP signals are expected to be available from the RHIC <sup>6</sup> beam energy scan program, soon. Furthermore, new data on heavy ion collisions at the highest possible energies at the LHC <sup>7</sup> might help to understand the characteristics of the deconfined phase better. For a review on the experimental results, see [eaSC05].

At higher  $\mu_B$  the situation is even less clear. One expects that the cross over to the QGP changes at some point to a phase transition of higher order. The end of this transition is marked by a critical point. It is not clear whether the phase boundary falls together with the transition to a phase of chiral symmetric matter in this region. The critical point is one of the major goals of the RHIC beam energy scan program and could manifest itself in fluctuations of the net baryon number, or higher orders of the net baryon number distribution [eaSC].

Besides the nature and location of the transition to the QGP, it is also not clear whether between the hadronic and the quark phase a third phase of still confined but effectively free percolating quarks, called quarkyonic matter, exists, as it has been proposed in the limit of unlimited color charge  $n_c$  in [LMS09].

Although it was conjectured, that in the region of high baryo-chemical potential, the universal freeze-out curve, obtained from statistical hadronization model fits to measured hadron yields, might mark the boundary between a hadron gas and the quarkyonic phase [ea10a], the excitement about this new phase of matter seems to have decreased recently.

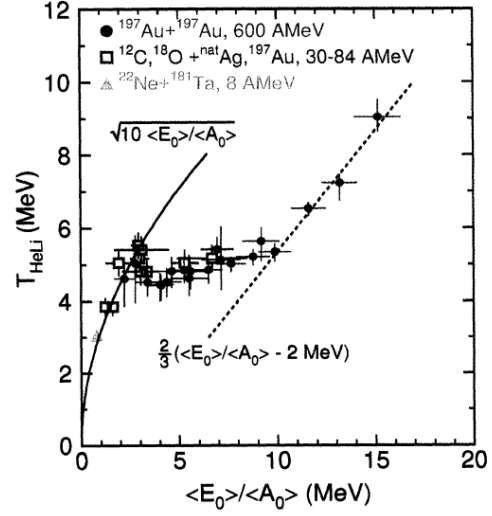
At even higher  $\mu_B$  and zero temperature neutron stars are located and a phase of color superconductivity is expected to form from some point on [MGAW98].

Experimentally best known is the liquid-gas phase transition located at temperatures below 10 MeV near nuclear ground state density  $\rho_0$ . It was probed by fragment distributions from Au+Au collisions

<sup>6</sup>Relativistic Heavy Ion Collider

<sup>7</sup>Large Hadron Collider

Figure 1.11: The fragment temperatures from Au+Au collisions show a discontinuous behavior as a function of the excitation energy per nucleon, giving a clear hint for a phase transition [JPea95].



[JPea95]. The fragment temperature as a function of the excitation energy per nucleon shows a clear discontinuous behavior, as seen in Fig.1.11.

### 1.3.1 Observables of heavy-ion collisions

The reconstruction of the conditions and moreover the evolution of a HIC represent a correlated many body problem which is extremely challenging.

In order to clearly trace an observation back to a specific effect, it is important to be able to explain as many observations as possible with the same model. Therefore a lot of the experimental effort should be put to measure as many observables as possible.

These observables can be divided into those characterizing global parameters of the reaction, like yields of particles and such describing the dynamics, like phase space distributions. Both categories can again be divided into bulk observables e.g. charged particle distribution and rare probes like dileptons and in the 1-2A GeV energy regime, particles containing strangeness. While the quality of dileptons has already been discussed in section 1.2, particles containing strangeness are of great interest at these energies, due to their steep excitation function, which makes them very sensitive to the conditions reached inside the fireball. As it will be shown in chapter 6, particles containing two or more strange particles are even more sensitive to the production and propagation of strangeness inside the medium.

### 1.3.2 Experimental results

As discussed, in order to characterize a HIC many observables have to be considered and experiments have collected data over a wide energy range, where totally different phases of matter are expected to be realized. The presented results, except for the dileptons, focus on the energy regime of a few GeV.

#### Bulk observables

The compression phase of a HIC is characterized by the transparency of the two colliding nucleons, the baryon stopping. If the baryons are fully stopped and thermalized, one expects no difference in the widths of the rapidity distributions in longitudinal and transverse directions with respect to the

beam axis. Systematic investigations of proton and cluster distributions from Au+Au collisions in the kinetic beam energy range of 0.2-1.5A GeV by the FOPI collaboration [eaFC10] showed that the widths of the transverse rapidity distributions are in good agreement with values expected for thermal distributions and always narrower than the ones in the longitudinal direction. The differences increase with increasing beam energies, thus less stopping occurs. Comparing the data to the transport model IQMD [CHA] an overestimation of the transparency in the model is observed, the differences increase with increasing beam energies.

The expansion phase is characterized by the radial expansion velocity  $\langle \beta \rangle$ . It can be extracted, e.g. from the increase of the inverse slope of the particle energy spectra, as a function of the particle mass. The data of the FOPI collaboration show a strong dependence of  $\langle \beta \rangle$  on the kinetic beam energy and the system size. For central Au+Au collisions the values of  $\langle \beta \rangle$  rise from  $\approx 0.15$ -0.4 by increasing the energy from 0.2 to 1.5A GeV. The corresponding radial flow energy decreases by varying the system size from central Au+Au collisions with  $\approx 400$  participants to peripheral collisions of  $\approx 50$  participants by roughly a factor three [CHA]. An extrapolation to Ar+KCl collisions at 1.76A GeV, which are investigated in this work, gives  $\langle \beta \rangle$  values of  $\approx 0.2$ .

The conditions at the chemical freeze out can be estimated by statistical hadronization model (SHM) fits to the measured particle yields. These models characterize matter by two main parameters, the temperature T and the baryochemical potential  $\mu_B$ . Using these models, systematics on the freeze out points in the T- $\mu_B$  plane are obtained [JCW06, ea10a]. In the investigated energy regime heavier and especially strange particles are rarely produced and thus their yields are poorly known. Hence, in the past only few particle yields with small statistical errors were available as input to the fit procedure resulting in uncertainties. The Ar+KCl data collected by HADES allow for the first time in this energy range to adapt a SHM fit to 13 different particle species providing a unique possibility to test the SHM and the amount of equilibration reached, see chapter 6 for details.

## Dileptons

Concerning medium modifications of vector mesons in ultra-relativistic HIC an important fact has to be considered: If the main source of dileptons is two pion annihilation the relative contribution of the three light vector mesons are given by their partial decay width  $\Gamma_{e^+e^-}$ <sup>8</sup> resulting in a ratio  $\rho/\omega/\phi$  of  $\approx 10:1:2$ .

Direct line shape measurements of the  $\rho$  meson in HIC have been performed in the dimuon channel by the NA60 experiment at the European Organization for Nuclear Research CERN. This setup was equipped with a hadron absorber providing a clean dimuon signal on the one hand, but requiring a careful normalization of the yield to the reaction cross section on the other hand. The acceptance for dimuon pairs starts from very low transverse momenta.

In order to interpret the data a dimuon cocktail consisting of the light vector mesons as well as the  $\eta$  meson is adjusted to peripheral events. The collaboration subtracted then the  $\eta$ ,  $\omega$  and  $\phi$  sources, assuming no modification of the line shape of these contributions due to the longer lifetime of these sources and the dominance of the  $\rho$  contribution in two pion annihilation. The data is divided into four different centrality regions and the remains are attributed to the  $\rho$  meson. The resulting spectra are displayed in Fig. 1.12. A centrality dependent broadening of the  $\rho$  meson, but no indication for a mass shift is deduced [eaNC06].

Apart from direct line shape measurements, an apparent omni-present low mass dilepton excess

<sup>8</sup>Probability that the two pions annihilate into the given state ( $\Gamma_{tot}$ ) times the probability to decay to  $e^+e^-$  final state ( $BR_{e^+e^-}$ ).

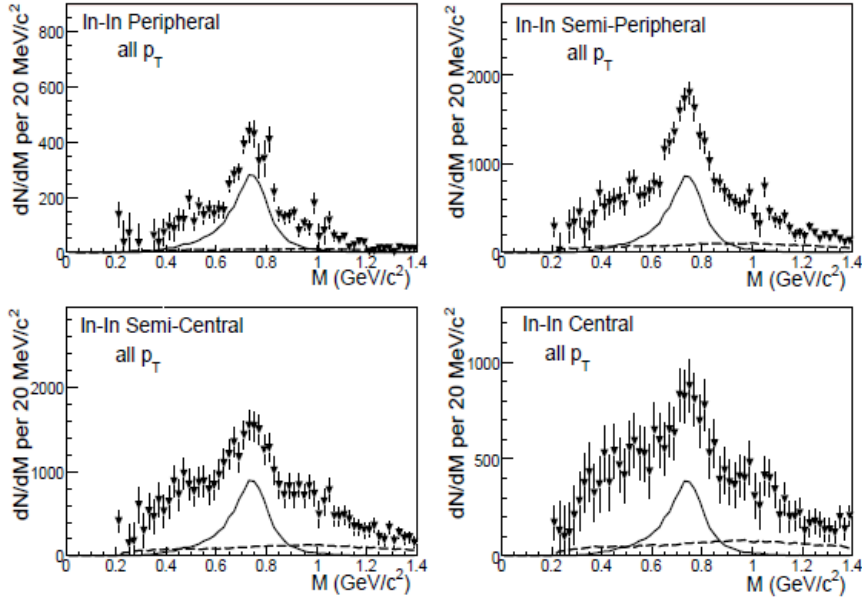


Figure 1.12:  $\rho$  meson contribution after subtracting the other cocktail components (see text for details) reconstructed in the dimuon channel for 4 different centrality bins. The solid line represents the unmodified  $\rho$  contribution, while the dashed line uncorrected charm decays. The data give evidence for a centrality dependent broadening but no indication for a shift of the pole mass[eaNCO6].

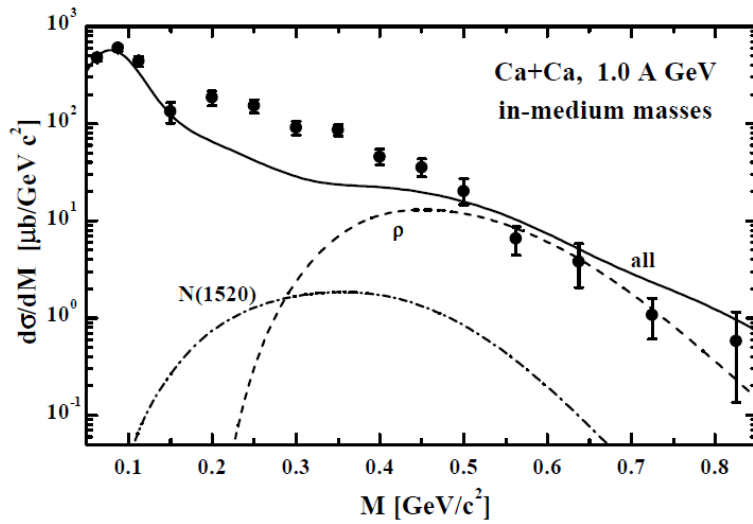


Figure 1.13: Comparison of DLS Ca+Ca dielectron data at 1A GeV to transport calculation including in-medium modifications [BK99]. In the low mass region a clear excess over the calculation represented by the solid line is visible.

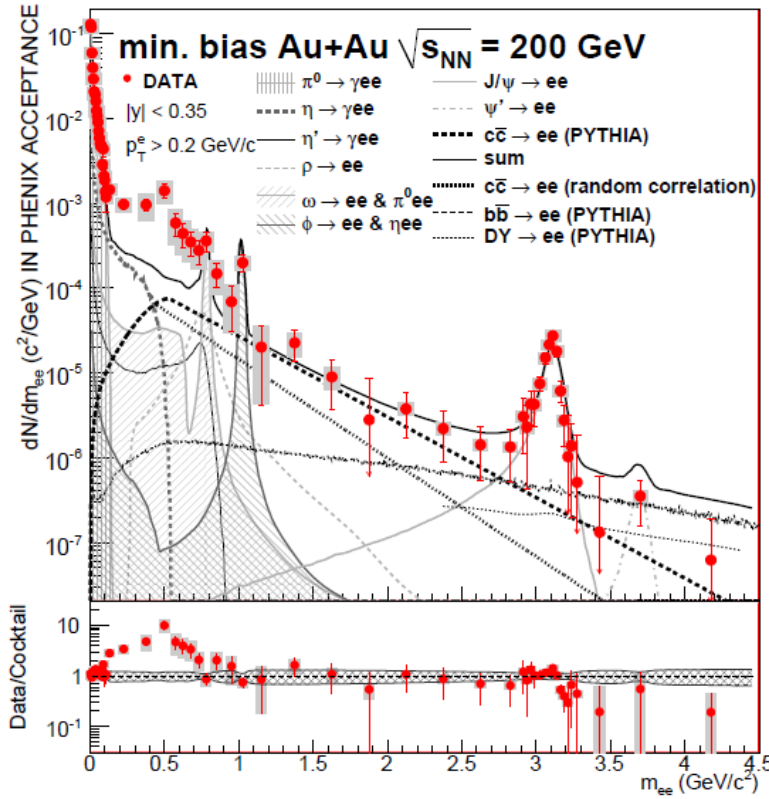


Figure 1.14: Di-electron spectrum radiated from Au+Au collisions at the top RHIC energy of  $\sqrt{s} = 200 \text{ GeV}$  measured with the PHENIX detector. At low invariant masses a clear excess over the dilepton cocktail is visible, see insert below.

is reported by experiments from kinetic beam energies in the few GeV regime up to the top RHIC energies.

The DLS collaboration published dielectron data from C+C and Ca+Ca collisions at energies of 1-2A GeV [eaDC97]. Transport models were for a long time not able to explain the high yield in the low mass region [BK99], compare Fig. 1.13. The situation became known as the "DLS puzzle". Recently it could be shown by HADES that part of the unexplained excess is resulting from an insufficient treatment of elementary p+n collisions in the models [eaHC10c], see also chapter 7 for more details.

At top RHIC energies ( $\sqrt{s} = 200 \text{ GeV}$ ) the PHENIX collaboration reports on a very strong low mass dielectron excess in Au+Au collisions [eaC10], see Fig. 1.14. The obtained signal to background ratio in the region of interest is at the order 0.01<sup>9</sup>. The excess increases with increasing centrality and decreasing transverse momentum  $p_t$ . Up to now this excess can not be explained by any modulations even including radiation off the QGP.

The low mass dilepton excess and the modifications of the line shape of the  $\rho$  meson are connected in [DAea08], where dielectron data of the CERES experiment from Pb+Au collisions at 158 A GeV are presented. The data are compared to  $\rho$  in-medium broadening and mass shift scenarios [vHR06] (see right side of Fig. 1.15) and to a vacuum cocktail (see left side of Fig. 1.15). The in-medium broadening scenario describes the data best.

<sup>9</sup>Note that, if one requires an accuracy of 10% at a given signal to background ratio of 0.01, the precision on the background calculation must be on the per mil level.

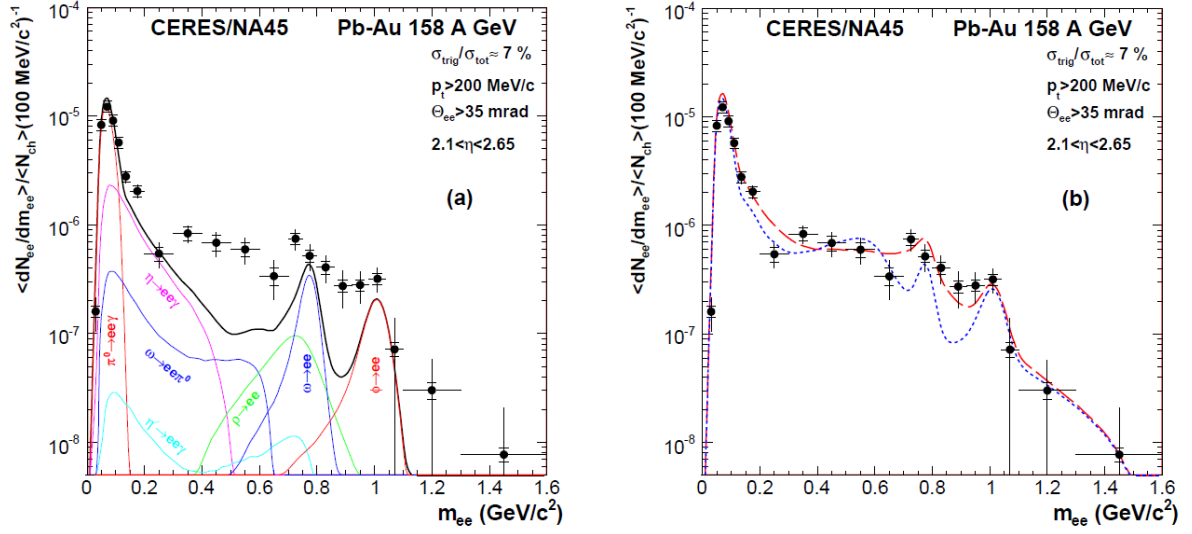


Figure 1.15: Dielectron data measured by the CERES experiment in Pb+Au collisions at 158 A GeV. The data are compared to a vacuum dielectron cocktail (left side) and to two different in-medium modification scenarios (right side).

### Strangeness

In the 1-2A GeV energy regime strangeness is produced below or close to its elementary production threshold, resulting in a steep excitation function. The elementary production thresholds for the lightest mesons carrying strangeness, the kaons vary significantly from positive and neutral to negative electric charge due to their quark content. While the  $K^+$  mesons contain an antistrange quark and can be produced together with a hyperon (Y) in the channel  $NN \rightarrow NYK^+$  at kinetic beam energies of  $1.6A$  GeV, such a mechanism is not possible for the  $K^-$  due to its strange quark content. Hence its production threshold in elementary collisions corresponds to a kinetic beam energy of  $2.5A$  GeV in the channel  $NN \rightarrow NNK^+K^-$ . As a further consequence of the quark content the scattering amplitude on nucleons of the two charged kaon species differ strongly as only the negative kaons can be resonantly absorbed. If the low density approximation is valid, the resulting mean free path in the medium is then also significantly different. Moreover, theoretical calculations predict a slightly repulsive kaon nucleon potential for the  $K^+$  and an attractive one for the  $K^-$ , increasing in strength as a function of the density [JSM97]. Therefore the behavior of the two charged kaon species is expected to be strongly different at these energies.

The production of charged kaons has been investigated by the KaoS experiment at the Helmholtzzentrum für Schwerionenforschung (GSI) in Darmstadt. Due to the subthreshold production the obtained kaon yield depends strongly on the accumulation of energy in the evolution of the HIC. The higher the achieved density the higher the production yields. Comparing the yields of positive charged kaons from C+C and Au+Au collisions to transport models, conclusions about the stiffness of the equation of state of nuclear matter could be drawn [eaKC01]; neglecting however the contribution from the symmetry energy.

Furthermore, systematics on the different behavior of positive and negative charged kaons were collected. While the inverse slope of the energy spectra are systematically 10-20 MeV lower for  $K^-$  (see Fig. 1.16), the ratio of the yields stays constant as a function of centrality (see Fig. 1.17). This is

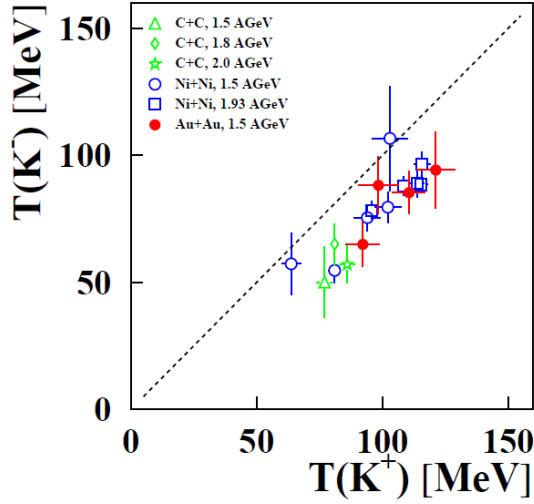


Figure 1.16: Comparison of inverse slope parameters of charged kaons obtained from Boltzman fits to the energy spectra. The obtained values are systematically lower for negative charged kaons [eaKC07].

surprising in the context of the different elementary production threshold.

The latter one points to an associated production of strangeness, which is a natural assumption since the conservation of strangeness is realized on the quark level. The lower inverse slope of the  $K^-$  was interpreted as a sign for a later freeze out, due to the smaller mean free path inside the medium leading to constant absorption and release of the  $K^-$ .

By comparing to transport models these observations could be nicely connected to the predicted kaon nucleon potentials, resulting in an effective increase/decrease of the meson masses: The strangeness exchange mechanism, e.g.  $\pi^0 + \Lambda \rightarrow p + K^-$  was identified as the dominant process for  $K^-$  production. This process is endothermal in vacuum. By lowering the mass of the  $K^-$  ( $\approx 200 \text{ MeV}/c^2$ ), the process becomes exothermal and more likely to process. In addition, the in this way modeled  $K^-$  shows a lower inverse slope parameter and leaves the reaction zone later compared to the  $K^+$ . For a review on the results obtained by the KaoS collaboration see [eaKC07].

While already data of the FOPI experiment gave hints for a sizeable contribution of  $K^-$  originating from a decay of  $\phi$  mesons [ea03], HADES data showed that in Ar+KCl collisions at 1.76A GeV at least 10% of the  $K^-$  originate from a  $\phi$  decay and not from the strangeness exchange channel [eaHC09c]. For more details and further implications of this observation, see chapter 6.

The data on strangeness production at these energies are completed by data of the FOPI experiment on  $K_s^0$  mesons and  $\Lambda$  hyperons [ea07].

For reviews on strangeness production in this energy regime see [Fuc06, CHA].

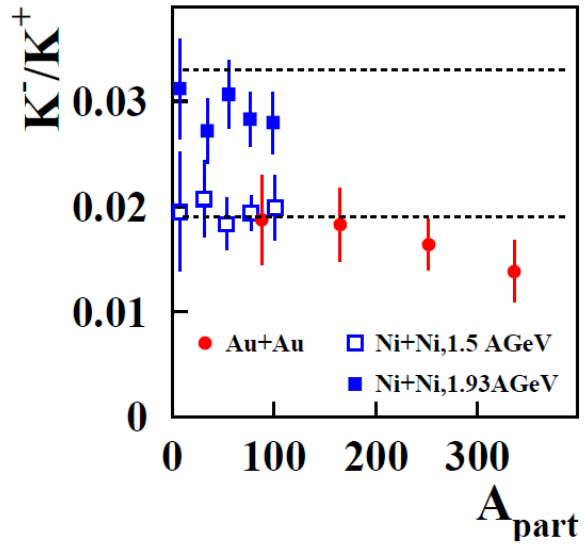
As already in the cold nuclear matter section, many of the drawn conclusions are based on the validity of the low density approximation, which is even more questionable in HIC. For example, it was shown in [EOT86] that already for pion absorption on the nucleus only 50% of the reactions proceed via a two body process.

## 1.4 Structure and goal of the thesis

In this thesis data taken in two measuring runs of the HADES spectrometer located at the GSI in Darmstadt are analyzed.

For the Ar+KCl data at 1.76A GeV, recorded in September 2005, a refinement of the simulated en-

Figure 1.17: Ratio of charged kaons as a function of the centrality. Within errors the observed ratio shows a flat behavior and is in accordance with a statistical hadronization model calculation indicated by the dashed lines[eaKC07].



ergy loss distributions followed by an efficiency correction based on this improved simulation for the charged kaons analyzed in [Lor08] is performed. Furthermore the dielectron identification, based for the first time on a neural network developed in [Lan08], is improved. The hadron yields, obtained in several analysis campaigns and theses, are compared to SHM fit and discussed with respect to the amount of thermalization of the system and the strong deviations observed for double strange particles.

The main part of this work deals with the analysis of dielectron radiation from p+Nb reactions at 3.5 GeV recorded in September 2008. The technical challenges were to adapt the multivariate analysis to the low multiplicity environment and to do a careful comparison to the standard electron identification method in order to reduce systematic uncertainties and to learn more about the advantages and disadvantages of both methods. The focus on the interpretation of the data is clearly put on the modification of the vector meson line shape by comparing the p+Nb dielectron spectra to data from elementary p+p collisions. Furthermore emphasis is put on the trivial effects for a nuclear modification of the cross section like particle production in secondary reactions.

The thesis is structured as follows: after an introduction and recapitulation of the status of the field in chapter 1, the subdetectors of the HADES setup are introduced and their particle identification capabilities are discussed in chapter 2. In chapter 3 the analysis of the p+Nb data is explained, while the results are presented and discussed in chapter 4. In the chapters 5 and 6 the Ar+KCl data analysis and interpretation are presented. At the end, in chapter 7, the obtained results from cold nuclear matter and heavy ion collisions are summarized and brought in context to each other, and, finally, an outlook to the future plans of the HADES collaboration is given. Moreover a summary in German is given in chapter 8.

## Chapter 2

# The HADES detector system

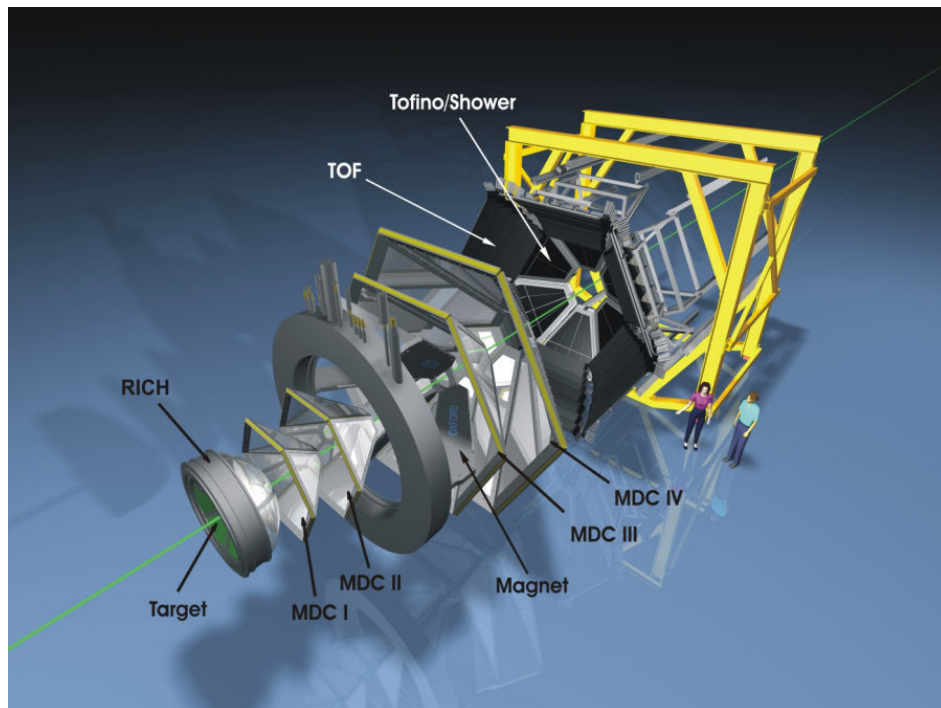


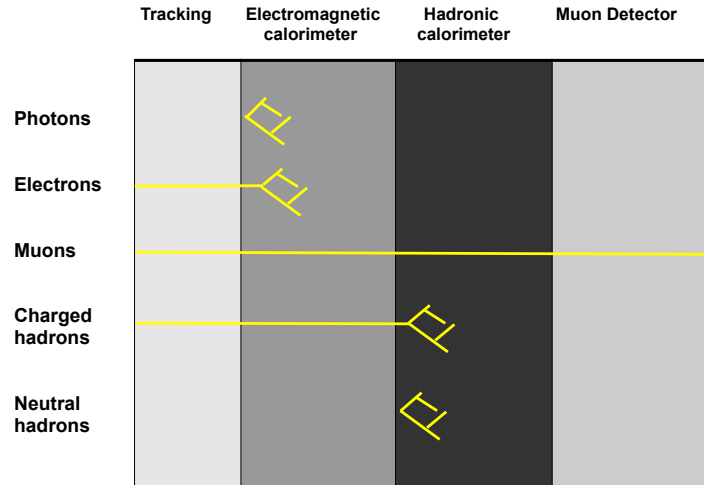
Figure 2.1: The HADES detector with its subcomponents in an elongated view. In measuring position the diameter of the whole apparatus is about 3 meters. Downstream of the target a **R**ing **I**maging **C**herenkov (RICH), followed by two layers of **M**ulti-**W**ire-**D**riftchambers (MDCs) in front of and behind a magnetic field are placed. The setup is completed by the 2 scintillator time of flight walls (TOF and TOFino) and an electromagnetic shower detector (Pre-SHOWER) at the end of the apparatus.

### 2.1 Physics goal and detector requirements

The detection of particles is based on the interactions between the detector material and the particles themselves. Obviously these interactions depend not only on the detector material but also on the particle properties. Therefore modern particle detectors are complex instruments consisting of several specialized subdetectors for different purposes like position measurements and measurements (track-

ing) used for momentum determination in a magnetic field and identification of different particles via e.g. energy loss or time of flight (PID), as illustrated in fig. 2.2.

Figure 2.2: Modern particle detectors consist of several layers of subdetector systems, specialized for the identification of different types of particles [Han11]. Often used are for example threshold detectors like Cherenkov or Transition Radiation Detectors (TRD) which are blind to heavy (slow) particles.



The **High-Acceptance Dielectron Spectrometer** HADES is located at the accelerator facility Helmholtzzentrum für Schwerionenforschung (GSI) in Darmstadt and was developed to reconstruct in particular dielectron pairs from decays of the light vector mesons  $\rho$  and  $\omega$  at ion beam energies of 1-2 A GeV. This physics goal puts specific constraints on the apparatus:

- **High geometrical acceptance:** to enhance the coverage of the rare dielectron pairs from low mass ( $\leq 1$  GeV) vector meson decays, which in addition have typically large opening angles between their legs
- **Fast detectors for high rates:** since the decay of vector mesons is twice electromagnetically suppressed one has to collect high statistics of events
- **High momentum resolution:** in order to have sufficient resolution in the invariant mass spectra for identification of e.g. a clear  $\omega$  signal ( $\Gamma=8.5\text{MeV}$ ,  $M_\omega=783$  MeV)
- **Low mass budget:** to reduce background from conversion of real photons into a dielectron pair inside the detector
- **Hadron discrimination:** to provide a clean electron/positron sample

### 2.1.1 Configuration

The setup of the HADES detector is shown in fig. 2.1 in an elongated view. The above requirements are realized by a geometrical coverage of the whole azimuthal angle, in six identical sectors. The polar angle is covered from  $15^\circ$  to  $85^\circ$ . The resulting acceptance of low mass vector meson pairs is of the order of  $\approx 40\%$  for beam energies between 1-2 GeV. All detectors can be read out with rates of 10-50 kHz depending on the particle multiplicity.

The high momentum resolution is achieved by double layers of **Multi-Wire-Driftchambers** (MDCs) placed in front of and behind a toroidal magnetic field. The mass budget of all detectors is kept as low

as possible in order to minimize conversion inside the detector. Finally, electrons and positrons can be separated from hadrons using the information from a **Ring Imaging Cherenkov detector (RICH)** surrounding the target and an electromagnetic shower detector (**Pre-SHOWER**) at the end of the apparatus. The system is completed by scintillator time of flight walls (**TOF** and **TOFino**) as well as 2 diamond strip detectors, placed directly in front of and behind the target (**START** and **VETO**) in case of heavy ion collisions. A cross section view of the apparatus is shown in fig. 2.3. In the following the subdetectors and the data acquisition (DAQ) will be presented, a detailed description can be found in [eaHC09b].

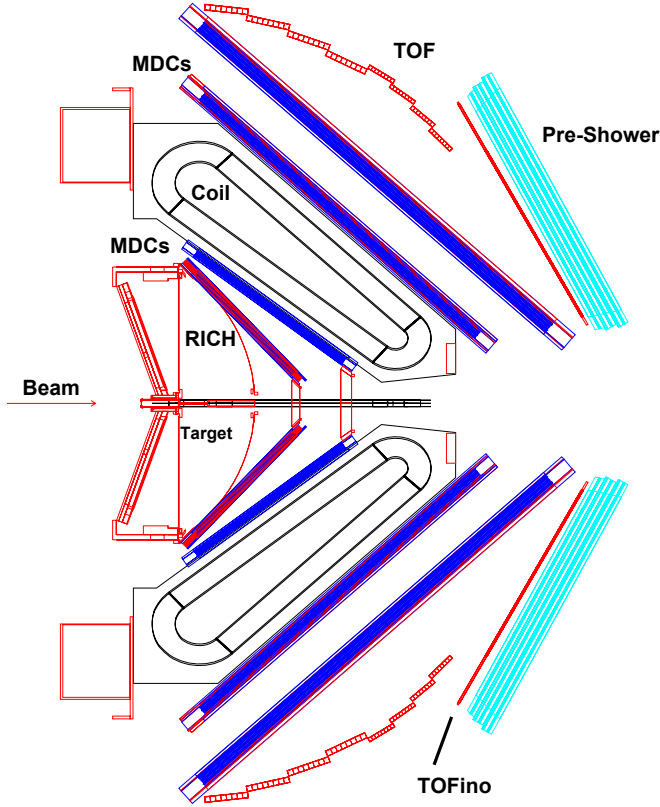


Figure 2.3: Cross section of the HADES detector. The beam impinges on a segmented target which is surrounded by a RICH detector for electron/positron identification. The magnet spectrometer consists of two double layers of drift chambers in front of and behind a toroidal magnetic field. The field geometry is chosen in order to provide field free regions for the detectors. At the end of the apparatus two scintillator time of flight walls and at low polar angles an electromagnetic pre-shower detector are placed.

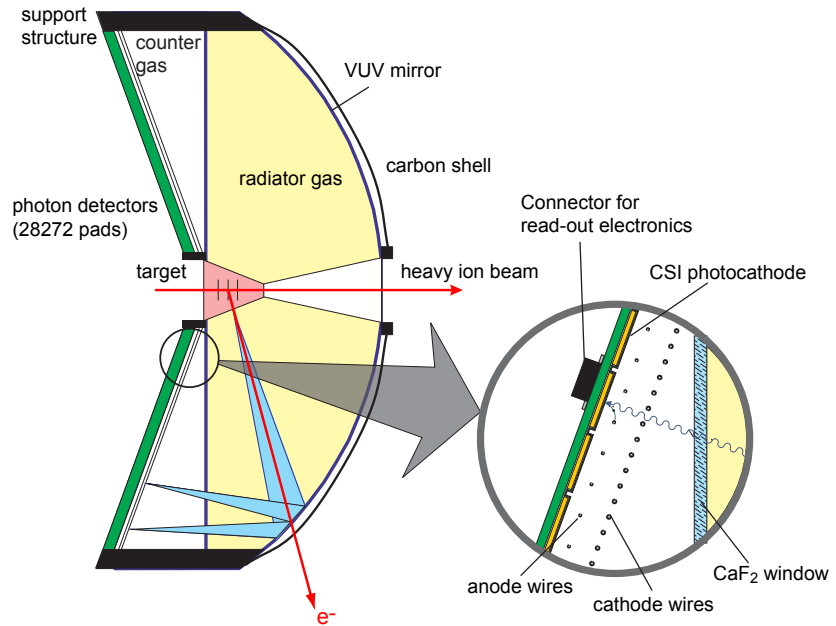
## 2.2 Ring Imaging Cherenkov detector (RICH)

The RICH detector is a gas detector used for the identification of electrons and positrons. Particles crossing the detector with a velocity higher than the speed of light inside the detector medium ( $c' = \frac{c}{n}$  with  $n > 1$  being the refractivity) generate a light cone under the emission angle:

$$\Theta = \arccos\left(\frac{c}{v \cdot n}\right). \quad (2.1)$$

The threshold for light emission is then given by the ratio  $\frac{v}{c} \geq \frac{1}{n}$  which can be converted to a Lorentz factor  $\gamma_{th} = \sqrt{\frac{1}{1 - \frac{1}{n^2}}}$ . The used radiator gas  $C_4F_{10}$  is chosen in the way that  $\gamma_{th} > 18$  which is sufficient to separate electrons and positrons from muons and pions for momenta smaller than 1.8 GeV/c. Since the light emission must be detected by the ring finder algorithm, see section 2.2.1, the separation is possible up to momenta of  $\approx 2.0 \text{ GeV}/c$ , due to the asymptotic ring diameter (see eq.2.1).

Figure 2.4: Schematic view of the RICH detector: An electron emitted from the target (red line) generates a light cone (blue) which is reflected by a spherical mirror to a photon detector placed on a level at backward angles (blue).



In order to avoid conversion and deflection of the particle tracks the material budget was kept as low as possible.

The schematic view of the detector is shown in fig. 2.4. Electrons emitted from the target, placed at the center of the detector, generate a light cone which is reflected by a spherical mirror to a photon detector placed at backward angles. For the photon detection wire chambers with a segmented cathode layer and a vacuum-metallized CsI photo converter are used. The number of emitted photons per electron track varies as a function of the angle by a factor 2, due to the different path lengths of the electrons inside the radiator gas, which affects also the quality of the ring reconstruction [Ebe04].

### 2.2.1 Ring reconstruction and quality assessment

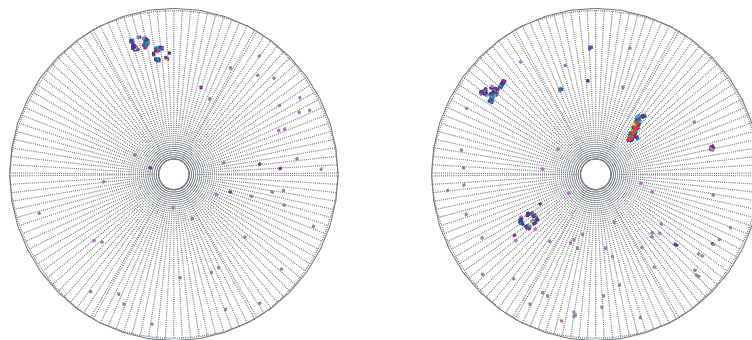


Figure 2.5: RICH read out for two events from the C+C beam time at 2A GeV with several ring candidates [Ebe04]

Fig. 2.5 shows the pad plane for two events from a C+C run at 2A GeV with several ring candi-

dates. Note that the pad plane is bent backwards and only approximately planar due to the large polar angular range. Based on the geometrical characteristics of rings, like symmetry, several algorithms are used for pattern recognition. Using the center of gravity of reconstructed rings and under the assumption that the particle is originating from the target the azimuthal and polar angle of the particle trajectory are calculated.

In order to suppress misidentified rings due to detector noise and charged particle tracks which fly through the photon detector and generate signals by ionizing the gas, selections on two quality parameters can be used to enhance the purity: The number of fired pads contributing to a ring and the ring centroid which gives the difference between the geometrical center and the charge center of the ring. The higher this value, the stronger the distortion of the ring, which points to a misidentified ring. For rings which are only partly inside the acceptance, the value for the ring centroid is set to -1. Fig. 2.6 shows the quality parameter for lepton signal and lepton background. The background is generated by particles not following the geometrical rules of matching by the RICH optics and thus can be reduced further.

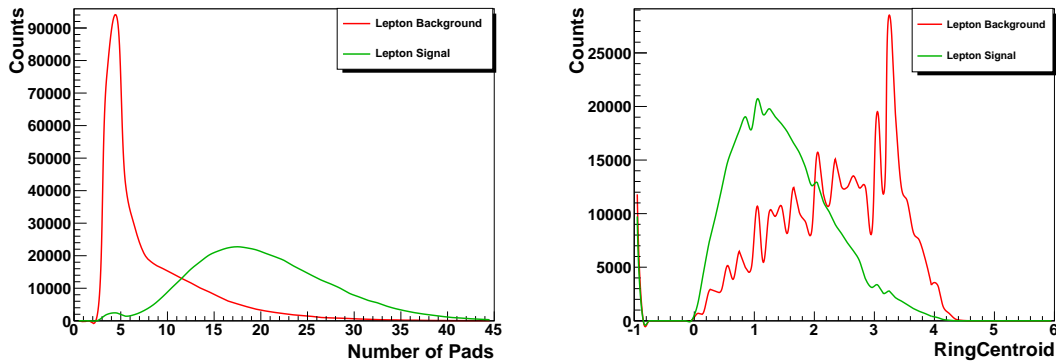


Figure 2.6: RICH ring quality parameters: number of fired pads (left) and ring centroid (right) for leptons (green) and lepton background (red).

## 2.3 Tracking system

The design of the tracking system was imposed by the required ability for high resolution spectroscopy (mass resolution  $\approx 1-2\%$ ) of light vector mesons via their dielectron decay channel.

More precisely, the momentum resolution for electrons and positrons must be around 2% since the mass resolution of reconstructed vector mesons is proportional to the momentum resolution<sup>1</sup>.

The read out of the detectors must be able to cope with the highest rate of heavy ions that can be provided by the accelerator in order to obtain a sufficient number of these rare events. Finally, again the mass budget must be as low as possible to minimize the background from conversion.

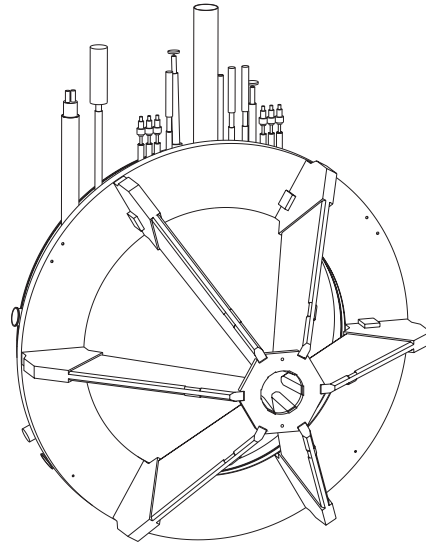
Consequently the HADES tracking system consists of 24 multiwire driftchambers arranged symmetrically in 2 layers in front of and behind a superconducting toroidal magnet.

<sup>1</sup>Only at low momenta the angular resolution becomes important as well.

### 2.3.1 Magnet

The field is generated by a liquid helium-cooled superconducting magnet consisting of 6 coils surrounding the beam axis and a circular support structure. Cooling is achieved via single phase He at 2.8 bar and at  $T=4.7\text{K}$ . The magnetic field strength inside the coils corresponds to  $B \approx 3.5\text{ T}$  and stays below  $B=0.9\text{ T}$  between the coils. The corresponding maximum current amounts to  $I \approx 3500\text{ A}$ . Superconducting coils are necessary to keep the construction compact, although the field strength is rather low. In addition, the operating costs are lower compared to a setup with conducting coils [eaHC09b].

Figure 2.7: The superconducting magnet consisting of 6 coils, surrounding the beam axis and a circular support structure. Cooling is achieved via single phase He at 2.8 bar and at  $T=4.7\text{K}$ . On the ceiling the power and gas supplies are connected. The magnetic field strength inside the coils corresponds to  $B \approx 3.7\text{ T}$  and stays below  $B=0.9\text{ T}$  between the coils.



### 2.3.2 Multiwire Driftchambers (MDCs)

The smallest sensitive unit of a drift chamber is the drift cell which consist of 2 cathode layers, 2 potential wires on both sides of a sense wire, see fig. 2.8. Each chamber is composed of 6 layers of these drift cells which are orientated in six different angles with respect to each other ( $40^\circ, -20^\circ, 0^\circ, 0^\circ, 20^\circ, 40^\circ$ ), in order to optimize the spatial resolution in the direction of the momentum kick.

The chambers are filled with gas (argon-isobutane). Charged particles flying through the chamber ionize the gas and electrons and ions start drifting, due to the potential between the field and cathode wires. On their way they ionize other atoms and an avalanche is generated close to the sense wire which is read out. In order to avoid a permanent discharge caused by photoemission one operates the chambers with a gas mixture consisting of an easily ionizing counting gas and a moderator gas which reabsorbs the free UV photons.

The spatial resolution was determined to be  $60\text{-}100\mu\text{m}$  in polar direction and  $120\text{-}200\mu\text{m}$  in azimuthal direction [Mar05]. In order to achieve this resolution it is essential to know the position of the chambers and the wires in the chambers with high precision. This is achieved by using a photometric alignment method, for details see [Sch08, eaHC09b].

#### PID using the energy loss in the drift chambers

Although the amplitude of the signal is not read out, with the current electronics it is possible to extract the energy loss of the particle using the width of the signal (time over threshold, ToT). Fig. 2.9

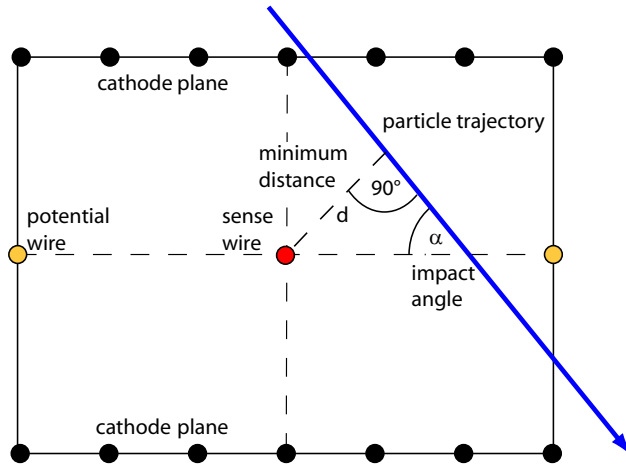


Figure 2.8: Schematic drawing of a MDC drift cell hit by a particle track (blue). The sense wire is surrounded by two potential wires and two layers of cathode wires.

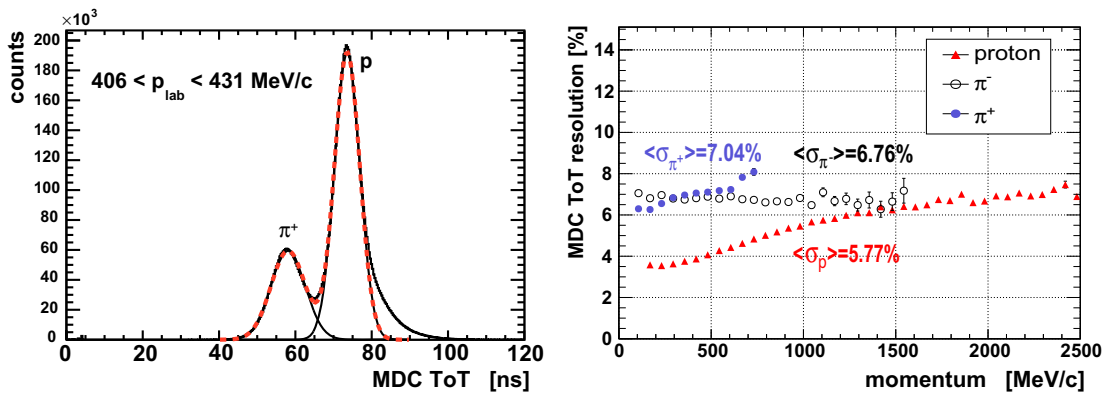


Figure 2.9: Left side: Time over threshold distribution for a given momentum range fitted with two gaussian functions. Right side: Resolution of the time over threshold distribution as a function of the momentum for different particles.

shows the ToT distribution for a given momentum slice and the estimated resolution as a function of momentum for different particles. The resolution depends strongly on the number of hit points in the MDCs and is in general a bit worse for minimum ionizing particles [eaHC09b].

The ToT information can be transformed into an energy loss information, given by the Bethe-Bloch formula which describes the energy loss of relativistic particles in matter, via a non linear transforma-

tion.

$$-\frac{dE}{dx} = 4\pi N_A r_e^2 m_e c^2 z^2 \frac{Z}{A} \frac{1}{\beta^2} \left[ \frac{1}{2} \ln \left( \frac{2m_e c^2 \beta^2 \gamma^2 T_{max}}{I^2} \right) - \beta^2 - \frac{\delta}{2} \right] \quad (2.2)$$

$z$  - charge of the incoming particle

$Z, A$  - proton and atomic number of the gas

$m_e$  - electron mass

$r_e$  - electron radius (2.3)

$N_A$  - avogadro number

$I$  - characteristic ionization constant of the gas

$\delta$  - density correction term

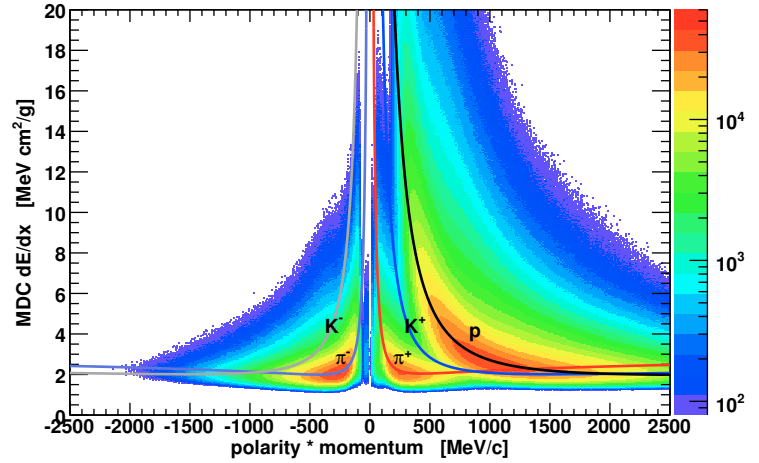
$T_{max}$  is the maximum kinetic energy, passed to one electron in a single collision:

$$T_{max} = \frac{2m_e c^2 \beta^2 \gamma^2}{1 + 2\gamma m_e/M + (m_e/M)^2} \quad (2.4)$$

$M$  - mass of colliding particle

This allows for a comparison with the theoretical energy loss of different particle species, see fig. 2.10. While pions are clearly separated from protons up to momenta of around 800 MeV/c, for the selection of kaon candidates one has to rely on the theoretical lines [Lor08, Sch08], see fig. 2.10. More information on the calibration of the drift chambers can be found in [Sch08, Mar05, eaHC09b].

Figure 2.10: MDC-dE/dx distribution as a function of the momentum, with lines of the theoretically calculated energy loss for different particles using the Bethe-Bloch formula, eq. 2.2.



### 2.3.3 Track reconstruction and momentum determination

The track reconstruction is only based on the hit points in 4 drift chambers, which makes the position and momentum determination challenging. In order to achieve the needed precision of 2-4% several steps of a careful track reconstruction are performed:

In order to obtain the spatial correlation of fired drift cells, in a first step the *track candidate* search, the area of fired drift cells is projected onto a common plane and a search for wire clusters on this plane is

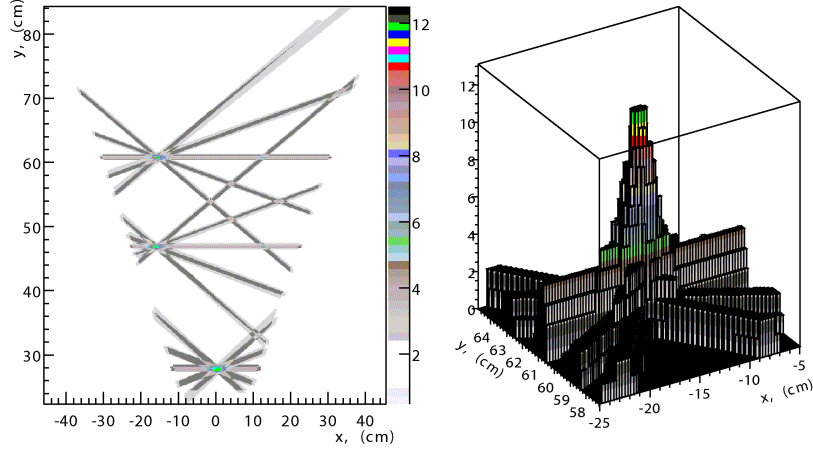


Figure 2.11: x-y coordinate projection used in the cluster finding procedure (left side). 3 dimensional histogram showing such a wire cluster, by incrementing the histogram along all fired wires (right side).

performed, as illustrated in fig. 2.11. Taking the location of the determined maximum and the known target position a *track segment* is defined afterwards. Finally the *track candidates* are generated by matching of track segments in the inner and outer drift chambers within one sector. In order to improve the spatial resolution the corresponding space positions of the track candidates are corrected using a model function with takes the drift time information of the different cells into account [eaHC09b].

The particle momentum is determined by a serial of 3 algorithms from the lowest to the highest precision level, making use of the knowledge of the bending of the trajectories of charged particles inside the magnetic field, which is described by a 3 dimensional field map. At every point inside the field with a given flux density  $\vec{B}$  the Lorentz force  $\vec{F}$  acts perpendicular to the direction of the particle momentum  $\vec{p}$ . Along the trajectory with the path  $s$  the total deflection of the momentum  $\vec{p}_{tot}$  is then given by:

$$\Delta\vec{p}_{tot} = \vec{p}_{out} - \vec{p}_{in} = \int d\vec{p} = \int \vec{F} dt = \int q[\vec{v} \times \vec{B}] dt = -q \int \vec{B} \times d\vec{s}. \quad (2.5)$$

With  $\vec{p}_{in}$  and  $\vec{p}_{out}$  being the momentum vectors of the in- and outgoing particles. Since eq.2.5 has no explicit dependence on the momentum itself,  $\Delta\vec{p}_{tot}$  is independent of the momentum at first order. The deflection angle  $\Delta\Theta$  between the vectors  $\vec{p}_{in}$  and  $\vec{p}_{out}$  is given as:

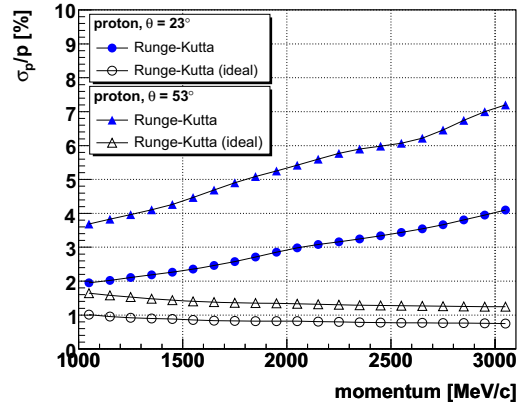
$$\sin\left(\frac{\Delta\Theta}{2}\right) = \frac{|\Delta\vec{p}_{tot}|}{2|\vec{p}|}, \quad (2.6)$$

At the highest precision level the momentum is determined using a *Runge-Kutta* algorithm which solves the equation of motion numerically. The procedure is repeated iteratively and at the end a  $\chi^2$  value is attributed to the reconstructed trajectory as a quality parameter. Currently the algorithm does not take into account the energy loss of the particle as well as its multiple scattering, which was justified by the low material budget which stays usually below 0.5% [eaHC09b]. However this results in a momentum dependence of the mean value of hadron signals in the mass spectra.

The momentum resolution has been estimated to  $\approx 4\%$  using elastic proton-proton collisions at 3.5 GeV [eaHC09b].

In order reproduce this values using a full-featured GEANT [App93] simulation, the errors on the time resolution in the drift chambers determined from GARFIELD [GAR00] calculations have to be scaled up by a factor of 4, as it is shown in fig. 2.19 for protons as a function of the momentum [eaHC09b].

Figure 2.12: Simulated momentum resolution, in order to match the resolution obtained from data the errors of the time resolution had to be scaled up (blue triangles and points).



## 2.4 Time of flight measurement

The time of flight measurement is done using a diamond counter in front of the target giving the start signal and two scintillator walls, TOF at high polar angles and TOFino at low polar angles, at the end of the setup.

For high intensity proton beams problems with the stable operation of the diamond counters occurred, resulting in a lack of the start time for those beam times. Meanwhile the problems have been solved and a stable operation of the diamond counters will be possible in future proton and pion induced measurements [JPC10].

### 2.4.1 Diamond counter

Figure 2.13: The schematic view of start and veto counter relative to the four segmented target used in the Ar+KCl beam time.

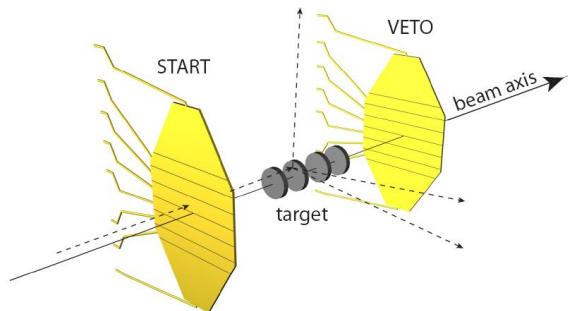


Fig. 2.13 shows a schematic view of the position of start and veto counters relative to the four-fold segmented target used in the Ar+KCl beam time. The start detector was placed inside the beam pipe, while the veto detector was installed behind the RICH detector. The detectors consist of polycrystalline layers and are kept as thin as possible to avoid strong diffusion of the beam. While the signal of the start detector is used as a reference for the signals in the time of flight walls, the signal of the

veto detector is used to suppress reactions without interaction in the target. Various shapes of the counters are used in experiment to optimize the position resolution for the different target geometries.

### 2.4.2 Scintillator time of flight wall (TOF)

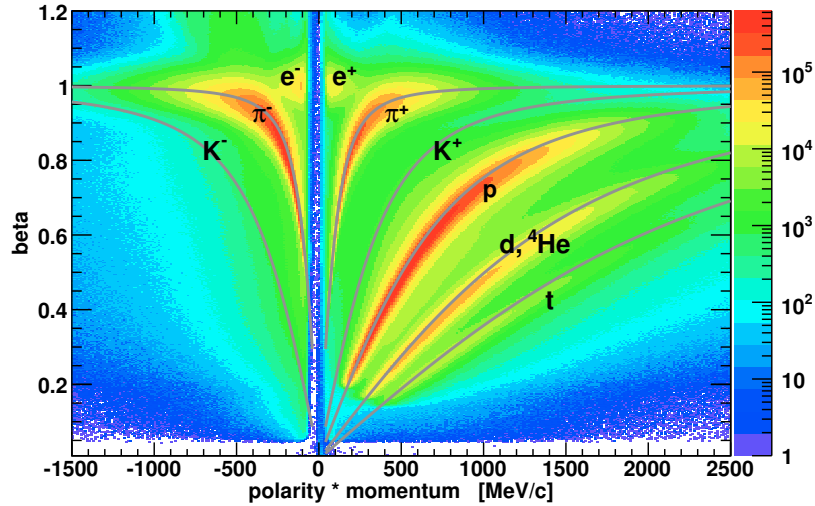


Figure 2.14: Beta vs. momentum distribution in TOF region

The scintillator time of flight wall (TOF) covers the polar angles between  $44^\circ$  and  $85^\circ$ . It consists of 8 strips of plastic scintillators per sector.

By passing through the detector material charged particles generate excited states, which fall back to their ground state by light emission. Inside the strip the light travels to photomultiplier tubes at both ends of the strip where the light pulses are converted to electronic signals and read out [Lan08].

Since the width and the amplitude of the generated signal, which is directly proportional to the energy loss of the particle, are detected, both the time of flight and the energy loss of the particle can be used for PID. The measured beta vs. momentum distribution is shown in fig. 2.14. The time resolution corresponds to  $\sigma_{TOF} \approx 190$  ps in coincidence with the start signal and to an intrinsic resolution of  $\sigma_{TOF_{int}} \approx 150$  ps and the spatial resolution is roughly three cm [eaHC09b]. The distribution of the energy loss vs. momentum is shown on the left side of fig. 2.15. The mean resolution for non minimum ionizing particles is about  $\sigma_{TOFdE/dx} \approx 4\%$  [Sch12b]. The theoretical energy loss curves for different particle species calculated using the Bethe-Bloch formula and the region used for kaon selection are shown [Lor08, Sch08].

### 2.4.3 Scintillator time of flight wall (TOFino)

For time of flight measurements at low polar angles between  $18^\circ$  and  $45^\circ$  a low granularity scintillator time of flight wall (TOFino), consisting of four scintillator strips per sector which are only read out from one side, is used. In combination with a hit point from the Pre-SHOWER located directly behind the TOFino it is possible to define the hit point of a particle trajectory on the strip and to correct for the different signal propagation times. The low granularity also increases the probability of two hits in one strip. Already in the medium sized collision system Ar+KCl the double hit probability was

higher than 50%.

The time of flight resolution corresponds to  $\sigma_{TOFino} \approx 420$  ps [eaHC09b] and the mean energy loss resolution for non minimum ionizing particles to  $\sigma_{TOFino} dE/dx \approx 8\%$  [Sch12b]. As one can see from the left side of fig. 2.15 pions and protons can only be separated for momenta lower than 700 MeV/c using the energy loss information.

The detector was replaced by high granularity resistive plate chambers (RPCs) in 2010, in preparation of the future runs with heavy systems, e.g. Au+Au, see 7 and [Fon01].

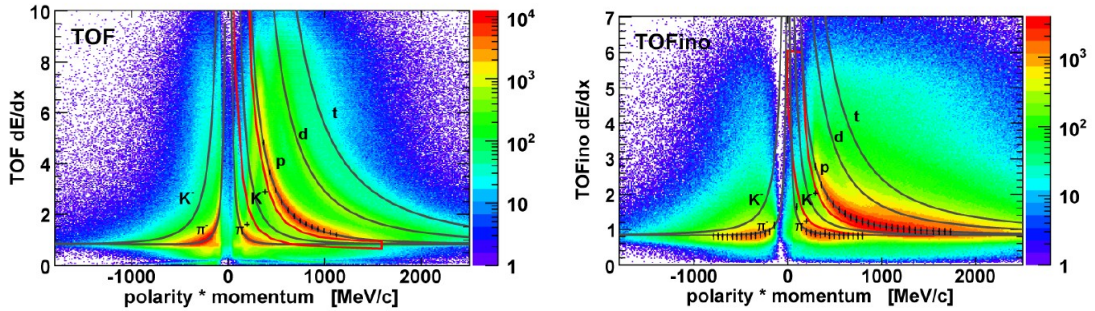
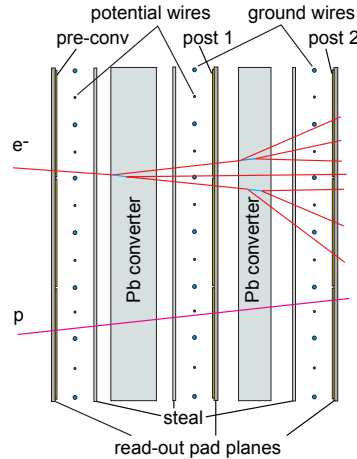


Figure 2.15: Energyloss vs. momentum distributions of the TOF detectors

## 2.5 Pre-SHOWER detector

Figure 2.16: Cross section of a Pre-SHOWER cell consisting of 3 wire chambers and 2 Pb converters. While electrons generate a shower, the effect is suppressed for hadrons due to their high masses.



At low polar angles behind the TOFino detector, where electrons and hadrons have similar momenta and time of flight distributions, a Pre-SHOWER detector, consisting of one module per sector with 1024 pads is used to improve the electron identification. Electrons passing through matter generate an electromagnetic shower by bremsstrahlung and pair production. On the other hand due to their higher masses shower generation of hadrons is strongly suppressed. The shower particles are detected in wire chambers placed between the two Pb converters, as illustrated in fig. 2.16.

For electron identification, the hit points of particle trajectories are identified and the collected charge

around the hit point is integrated. In case of a real electromagnetic shower, the integrated charge increases from chamber to chamber. Therefore a shower quantity sensitive to particle ID is defined in the following way:

$$shower_{sig} = integral_1 + integral_2 - integral_0 \quad (2.7)$$

$$(2.8)$$

The shower signal is plotted as a function of momentum for lepton and hadron candidates in fig. 2.17.

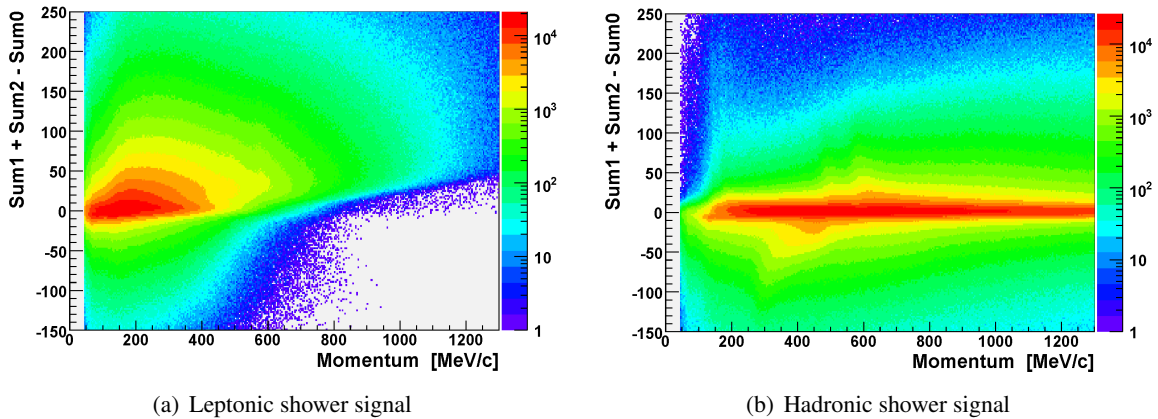


Figure 2.17: The shower signal as a function of the momentum for lepton candidates (left side) and lepton background (right side) [Lan08].

## 2.6 Trigger and data acquisition

HADES is using a two-stage trigger system in order to minimize the dead time of the data taking system by enhancing the data with events of interest.

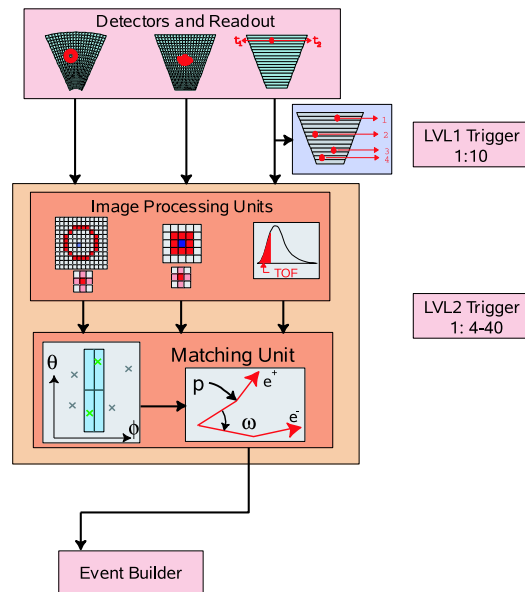
The first level trigger (LVL1) is a simple charged-particle multiplicity selection. Only events with a certain multiplicity in the TOF and TOFino detectors are selected. The usual time for the evaluation is less than 50 ns plus traveling times from/to the detectors of 200ns [Lan08].

The second level trigger (LVL2) is used to enhance the data sample with rare lepton events and is consisting of 2 steps: Fast **image processing units** (IPUs), one for each detector, are searching for electron signatures like RICH-rings, time of flights close to the speed of light and electromagnetic showers. In the second step the **matching unit** (MU) is correlating the signatures from the different detectors and giving a trigger decision, as shown in fig. 2.18.

If the decision is positive, the data of all detectors are read from intermediate storage pipes and combined by the event builder into one event and are written in the **hades list data** format (HLD) to data tape for further analysis. Additionally to the LVL2 events also LVL1 events are written to tape with a given, downscaled rate for hadron analysis, trigger efficiency studies, etc.

In order to be able to cope with the requirements of Au+Au collisions and enhance the statistics for the reconstruction of rare hadronic and leptonic probes a major upgrade of the data acquisition system was started after the beam time in September 2008, for details see 7 and [Miced].

Figure 2.18: Block diagram of the trigger system: The first level trigger is a multiplicity trigger followed by a second level trigger algorithm, firstly searching for electron signatures and secondly correlating them.



## 2.7 Analysis framework

The data analysis is realized within the HYDRA (**H**ades system for **d**ata **r**eduction and **a**nalysis) framework [HYD04], developed by the collaboration. It is entirely based on the C++ package ROOT [ROO04] developed and maintained by CERN, which is nowadays accepted as the standard tool in high energy and nuclear physics. This allows for an easy and consistent use of all features of the ROOT package. The detector parameters are initialized from an Oracle data base [ORA], where the full version management is available.

Real and simulated data are processed in the same way. For the simulation the detector description and simulation tool HGEANT [HGE04] is used, which is based on the package GEANT3 [App93]. The full geometry, correct material budget and an accurate magnetic field map, as well as a digitization part which uses detector response functions to generate realistic signal patterns, are implemented in the simulation.

In addition a ROOT-based decay generator Pluto++ [PLU04] was developed for fast physics studies as well as an input source for the described GEANT simulations.

The frameworks can be run on various versions of the Linux operating system.

### 2.7.1 Toolkit for Multivariate Data Analysis with ROOT

Multivariate classifiers have strongly evolved in the past years due to their broad application area ranging from arts and engineering to medical and life science and are meanwhile commonly used in high energy and nuclear physics especially for the detection of rare probes.

The **T**oolkit for **M**ulti**V**ariate **D**ata **A**nalysis (TMVA) [TMV] provides a ROOT integrated suite of 11 different multivariate analysis algorithms. All algorithms have to be trained with signal and background tracks, to determine the unique characteristics of the different event samples in order to be able to classify events of a whole data sample later on.

For the identification of electrons a multivariate analysis is implemented into the HADES analysis framework [Lan08]. The concept of such a multivariate analysis is, instead of applying a set of

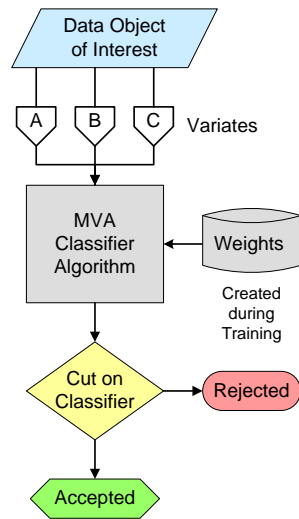


Figure 2.19: Concept of the multivariate analysis: instead of applying a set of boolean cuts sequentially to the data (hard cut), all cut criteria are fed into an algorithm which derives a single scalar response value, used as an input to the final digital decision [Lan08].

boolean cuts sequentially to the data (hard cut), feeding all cut criteria into an algorithm which derives a single scalar response value, used as input to the only cut. The advantage is that correlations between the different cut criteria are taken into account by the algorithm and that fluctuations in single cut criteria do not automatically lead to the complete rejection of the track, resulting in higher efficiencies.

The challenge in using such algorithms are:

- how to get pure signal and background samples for training?
- Which variates to use? Within which range?
- Which algorithm and settings should be used?

All algorithms were evaluated for the identification of electrons using the Ar+KCl data at 1.76 A GeV and a neural network<sup>2</sup> performed best. Figure 2.20 illustrates the coupling of the neurons of the input layer (0), the two hidden layers (1,2) and the output layer (3) for the neural network used to analyze the Ar+KCl data in the region of the TOFinno detector.

In the following different sets of variates in diverse ranges were tested. The final setup showed a strong improvement in efficiency, compared to the methods of hard cuts in the low momenta region but significant losses in the high momenta region.

These inefficiencies are corrected within this work by selecting a different set, described in chapter 5. Furthermore the multivariate analysis is adjusted to the low multiplicity environment of p+Nb collisions and to the lack of a measured start time, due to unstable operation of the diamond start counter, see chapter 3.

<sup>2</sup>Neural networks, or to be more precise artificial neural networks, emulate the reaction of a human brain by interconnecting neurons. Since real biological nervous systems are extremely complex and can not yet be matched by artificial emulations, the information processing must be simplified focusing on the specific assignment.

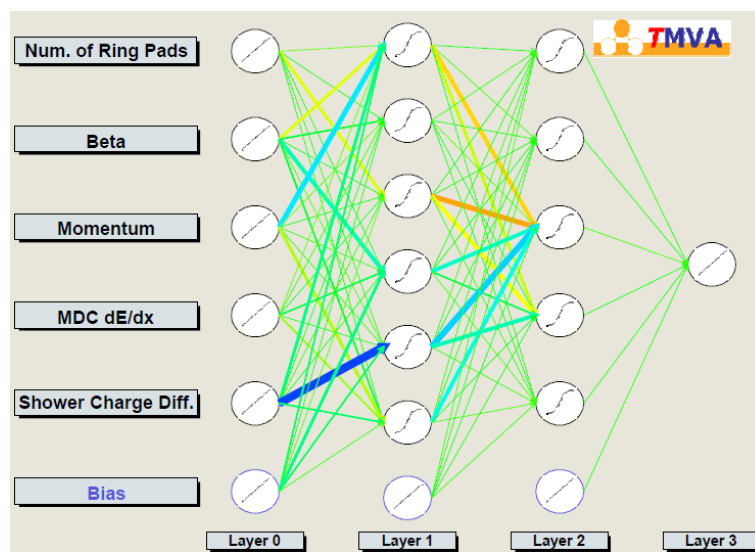


Figure 2.20: Architecture of the neural network used in for the Ar+KCl data in the region of the TOFINO detector. Shown are couplings between the neurons of the input layer (0), the two hidden layers (1,2) and the output layer (3) [Lan08].

## Chapter 3

# Analysis of the p+Nb data

### 3.1 Choice of the collision system

Although from the physics point of view a pion beam would be clearly preferable to a proton beam due to the lower relative momentum of the newly produced particles to the surrounding medium as well as better resolvability of calculations of the relevant processes from the theory side [WSC96], the selection of the beam particle was defined by accelerator operating issues. Pions have to be produced in particle collisions first and focused to a secondary beam. This procedure reduces the available luminosity by orders of magnitude. The resulting lower event rate has to be compensated by a longer run, in order to collect sufficient statistics of events containing the rare vector mesons, which was not possible. Moreover the beam can be only poorly focused on the target and consequently the background in the RICH photo detector would increase substantially. Therefore a proton beam was used.

For the target selection, three aspects were considered:

- the total vector meson production cross section,
- the fraction of vector meson decays inside the medium,
- the combinatorial background (CB) due to  $\gamma$  conversion inside the target.

To investigate these effects detailed simulations have been performed using the transport code HSD [HSD] and the HADES response and acceptance filter HAFT [HAF]. Niobium was found to be a good compromise between maximizing the production cross section and the fraction of decays inside the medium on the one hand and minimizing the CB due to  $\gamma$  conversion inside the target on the other hand. For targets of higher masses the percentage of inside decays and the cross section only slightly increases, while the conversion increases by a factor 2-3 when going from a Nb to Pb nucleus [Bea]. Another advantage of the Niobium target is, that the CBELSA-TAPS collaboration measured  $\omega$  production in photon induced reactions on this target [eaCC10a], which allows for a better comparison of the results.

The chosen beam energy is the highest possible energy for proton beams which can be achieved in stable operation by the SIS18 accelerator, in order to enhance vector meson production as strongly as possible.

<b>beam energy</b>	$E_{kin}=3.5$ GeV
<b>beam particle</b>	proton
<b>beam intensity</b>	$1.5 - 2.5 \cdot 10^6$ particles/s
<b>target</b>	$^{93}\text{Nb}$
<b>target diameter</b>	d=2.5 mm
<b>target geometry</b>	12 segments
<b>distance between segments</b>	$\Delta z = 4.5$ mm
<b>thickness of segment</b>	t=0.45 mm
<b>interaction probability</b>	P=2.8 %

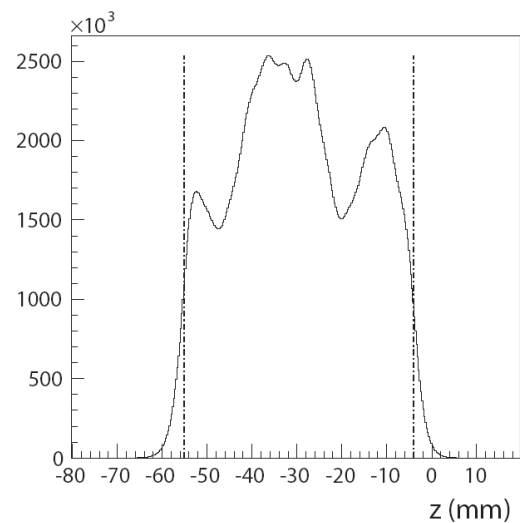
Table 3.1: Beam and target specifications.

### 3.2 Specifications of the p+Nb run

The experiment was performed in September 2008. A proton beam with intensities of  $(1.5 - 2.5) \cdot 10^6$  particles/s and a kinetic beam energy of 3.5 GeV was incident on a 12-fold segmented Niobium target. The distance between the different target segments of 4.5 mm was again optimized to minimize conversion. The total interaction probability in the target amounted to 2.8%, see Tab. 5.1.

In the data analysis the interaction vertex is reconstructed using the track coordinates of all reconstructed charged particles [APr09, Web11]. The vertex distribution is shown in Fig. 3.1 in beam direction. It can be seen, that an emission from the central segments of the target is favored as well as some accumulation at the edges of the target region, giving a hint for missing or misaligned segments. Therefore the target was inspected optically and by X-rays after the experiment. While missing segments could be excluded, several segments showed a slight misalignment [Web11].

Figure 3.1: Z-coordinate of the reconstructed vertex [Web11]. The dashed-dotted lines show the nominal edges of the target. It can be seen that an emission is favored from the central segments of the target with some accumulations at the edges of the target region, giving a hint for misaligned segments.



As mentioned in section 2.4, due the comparably high intensity of the proton beam, saturation

<b>LVL1 rate</b>	6-8 kHz
<b>LVL2 rate</b>	1-2 kHz
<b>LVL1 events</b>	$9.2 \cdot 10^9$
<b>LVL2 events</b>	$1.6 \cdot 10^9$
<b>down scaling factor</b>	3
<b>data volume on tape</b>	13.6 TB

Table 3.2: Specifications of the data taking [Web11].

effects hindered a stable operation of the diamond detectors, resulting in a missing of the start time for this experiment. In addition, sector 3 was equipped with one outer drift chamber, only.

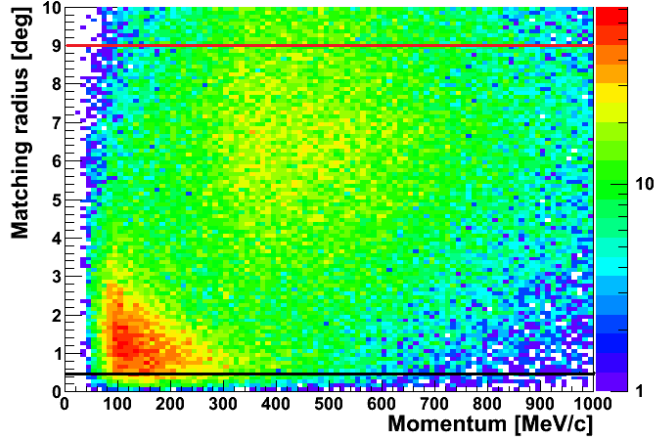
The read-out was started with a level-1 trigger (LVL1) demanding a multiplicity in the time of flight walls and the Pre-SHOWER detector of at least 3. It was followed by a second level trigger (LVL2) demanding a recognized ring in the RICH detector. All events with a positive LVL2 trigger decision and events with a positive LVL1 trigger with a down scaling factor of 3 were written to data tape. The average event rate written to data tape was 2.2 kHz and resulted in 13.6 TB data volume stored in total. Tab. 3.2 summarizes the relevant parameters of the data taking. All files have been validated for stable running conditions by the subdetector groups before the production of the **Data Summary Tapes (DST)**, which contain physical relevant information like particle momenta, energy loss etc. and are used as an input for the further analysis. For the dielectron analysis only events with positive LVL2 decision are used.

### 3.3 Electron identification

The identification of electrons and positrons is done using two different methods: The method of hardcuts (HCA), boolean selections applied consecutively to the data, described in detail in [Web11] for the pNb experiment as well as a multivariate algorithm (MVA) included in the analysis frame developed in [Lan08]. In order to do a step-by-step comparison of the two methods, the analysis of hard cuts is implemented into the analysis frame work used for the MVA. The results are discussed in chapter 3.6. The settings of the MVA are adjusted to the run conditions of the p+*Nb* experiment, like lower charged particle multiplicity, resulting in less combinatorics in the track reconstruction and to the lack of a start time measurement, due to unstable operation of the diamond start counter.

For the identification of pairs in the vector meson mass region the selection criterium of capital importance is the matching between rings in the RICH detector and the trajectories reconstructed in the drift chambers. In this low multiplicity environment the sequence of applied selections is not of importance unlike in heavy-ion collisions where the probability that several reconstructed particle trajectories point accidentally to one ring is much higher. Therefore the sequence of applied selections is matched with the analysis of hard cuts in order to ease a step by step comparison of the methods, especially the two different PID methods.

Figure 3.2: Matching radius between RICH and tracking detectors as a function of the momentum. The solid black line corresponds to the sharp cut at  $0.5^\circ$  used for the generation of the pure signal sample while the red line corresponds to a cut at  $9^\circ$  for the background sample.



### 3.3.1 MVA PID

For the identification of electrons a multivariate analysis based on a neural network algorithm is used [Lan08]. The concept of such a multivariate analysis is, instead of applying a set of boolean cuts consecutively to the data (hard cuts), feeding all cut criteria into an algorithm which presents one scalar response value, used as an input to a single decisive cut. Compared to the method of hard cuts, correlations between the different variables are taken into account by the algorithm and fluctuations in single variables do not automatically lead to the complete rejection of the track, which results in higher reconstruction efficiencies.

#### Training

The algorithm has to be trained with signal and background events, to determine the unique characteristics of the different event samples in order to be able to classify events of the whole data sample later on.

The challenges in training the neural network to obtain the optimal response are the creation of pure signal and background samples and the choice of the variables with the highest separation power between hadron and lepton tracks, in an optimized range of the variable space.

The signal and background samples are generated from real data, using a strong cut on the RICH track matching, which has sufficiently large separation power to generate a pure electron sample. Since the cut is used to define the training samples, it can not be included into the neural network and has to be applied in addition to the cut on the response value from the neural network in the data analysis later on. The matching radius between the RICH detector and the tracking detectors  $c_{radius}$  is defined as

$$c_{radius} = \sqrt{\Delta\phi^2 + \Delta\theta^2}, \quad (3.1)$$

with  $\Delta\phi = \phi_{RICH} - \phi_{RK}$  being the differences between the azimuthal and  $\Delta\theta = \theta_{RICH} - \theta_{RK}$  being the difference between the polar angle reconstructed using the RICH detector and a reconstructed track in the drift chambers using the Runge-Kutta algorithm. Since this is done globally for all sectors, the RICH detector has to be aligned to the tracking detectors [Sch08] first.

Fig. 3.2 shows the correlation (matching radius) as a function of the reconstructed track momentum. All tracks with values smaller than  $0.5^\circ$  are used as signal tracks, while all tracks with values higher

Variate	lower limit	upper limit
Momentum	45 MeV/c	2000 MeV/c
MDC dEdx	-	30 MeV cm <sup>2</sup> /g
TOF dEdx		10 [a.u.]
Shower Sum	-150 [a.u.]	250 [a.u.]
$\Delta \phi$	-10 [deg]	10 [deg]
$\Delta \theta$	-13 [deg]	13 [deg]

Table 3.3: Allowed ranges for variates and additional restrictions.

than  $9.0^\circ$  are marked as background. Although the average matching radius of correctly assigned rings to electron tracks is decreasing as a function of the momentum, due to the increasing momentum resolution, the signal identification cut is done at a constant value in order to enhance the statistics for high momentum tracks. The background identification cut value is chosen such that the low momentum tail of true electrons is still outside the cut region.

In the next step the variables with the highest separation power between electrons and hadrons of each subdetector system are identified and fed into the neural network. The variate ranges are restricted to meaningful regions, cutting away the tail of the distributions, which are mainly due to detector noise. Tab. 3.3 summarizes the allowed range for variables (variates) with additional restrictions.

The training is done separately for tracks traversing the TOF and the TOFino regions due to the additional information from the SHOWER detector, which is strongly momentum dependent and therefore requires an inclusion of the momentum, in the latter one. Although some of the variates in the TOF region are also momentum dependent an inclusion of the momentum causes several problems which are discussed in chapter 5, therefore it was not used as a variate in this region.

Several versions of separate training for electrons and positrons were investigated, in order to increase the purity of the positron sample especially in the TOF region, see section 3.11. The favored training scenario, using a pure signal sample containing only electrons and a background sample generated only from positive background tracks, was finally discarded due to the different acceptances of low momenta electrons and positrons. Furthermore the sensitivity to background originating from pions was reduced, as the background sample was dominated by protons. Instead the training is done for electrons and positrons together.

The integrated variables (variates) are listed and described below for each subdetector system:

- **RICH:** Compared to the settings for the Ar+KCl data from 2005 [Lan08] not only the **number of fired pads** (mainly a measure for the strength of the ring signal) contributing to a ring, but also the **ring centroid**, which is the difference between the center of gravity of charge deduced from the pulse heights and the geometrical center of the reconstructed ring, giving a measure to what extent the pads used in the ring fitting are distributed evenly, is used. This information is of importance to suppress rings from noisy regions of the detector. The upper part of the figures 3.3 and 3.4 show the corresponding distributions for the signal (green) and background sample (red) in the TOF and TOFino region, respectively. As can be seen from the pictures the distributions of the number of fired pads are more strongly separated compared to the ones of the ring centroid.

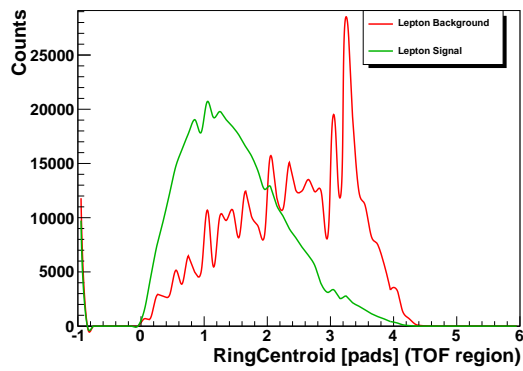
- **MDCs:** The average **energy loss** information of all four layers of drift chambers is included only in the TOF region. The corresponding distributions are shown in figure 3.3c). The energy loss for all charged particles as a function of the momentum is shown in section 2.10. While electrons are already at low momenta minimum ionizing and their energy loss rises gently with increasing momenta, pions and mainly protons, decrease their energy loss with rising momentum and cross the minimum ionizing region, as well as the region of the relativistic rise. This results in a crossing of the signal and background distribution, but since the momentum is not included in the TOF region the network can not consider this effect. Nevertheless the energy loss is included in the TOF region in order to suppress proton contamination. In the TOFino region proton contamination can be sufficiently suppressed with the help of the Shower quantity and the energy loss information of the drift chambers is not needed.
- **TOF wall:** The **energy loss** in the time-of-flight walls. The same argumentation as for the energy loss in the drift chambers is also true for the time of flight walls, although the relativistic rise of the electrons is not as strongly pronounced due to the different detector material. The energy loss for all charged particles as a function of the momentum is shown in section 2.15 in chapter 2. The corresponding distributions for the signal and background samples are shown in Fig. 3.3d) and Fig. 3.4d).
- **Shower:** The Shower quantity is defined as the collected charge in the second and third layer minus the collected charge of the first layer:

$$shower_{sum} = integral_1 + integral_2 - integral_0. \quad (3.2)$$

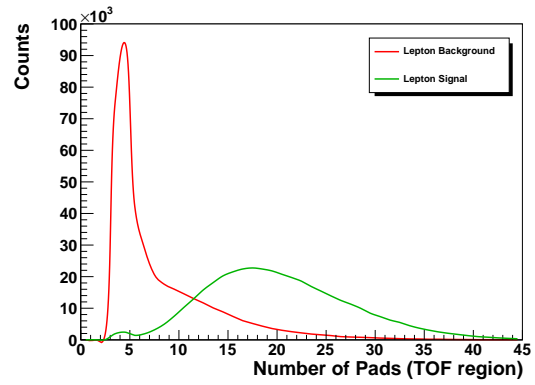
$$(3.3)$$

Since electrons create electromagnetic showers, this quantity is positive for real electrons. The corresponding distributions are shown in Fig. 3.4e). Since the quantity is momentum dependent the **momentum** is also included in the TOFino region, see Fig. 3.4d). The step in the background distribution of the momentum is due to protons, which only reach the outer drift chambers if their momenta are larger than 400 MeV/c. The momentum dependence for signal and background tracks are shown in 2.17 in chapter 2.

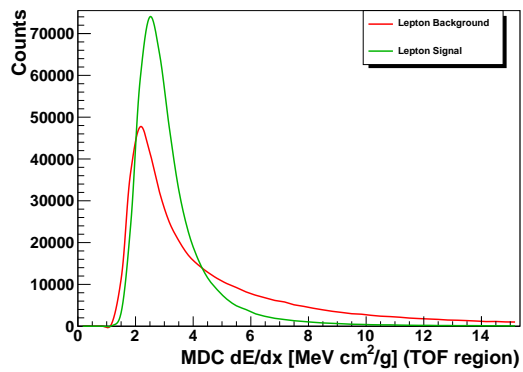
As already mentioned before some of the variates are correlated. The neural network takes this correlation into account via linear coefficients. These coefficients are plotted for the signal and background sample for both regions in the figures 3.5 and 3.6. In case of the signal sample the strongest correlation occurs between the RICH observables and the momentum dependence of the shower sum. For the background the energy loss distributions show the strongest correlation.



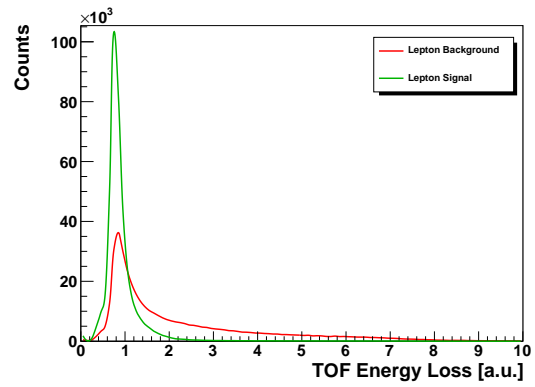
(a) RingCentroid (TOF region)



(b) Number of fired RICH pads (TOF region)

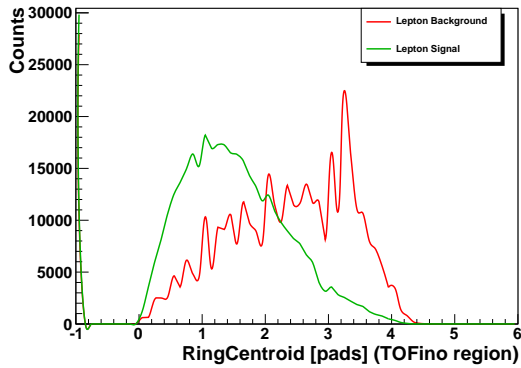


(c) MDC dEdx (TOF region)

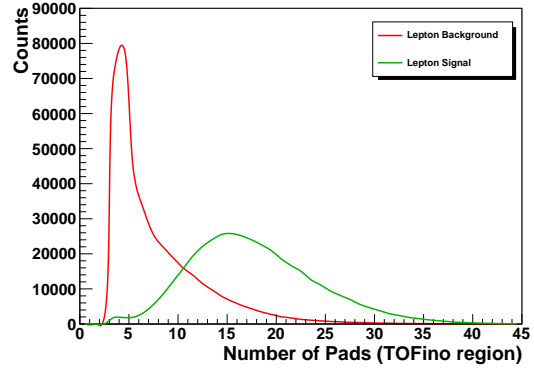


(d) TOF dEdx

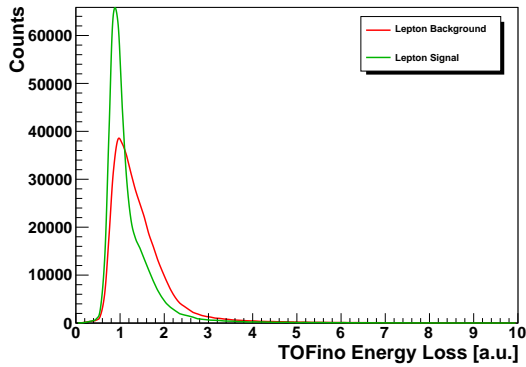
Figure 3.3: Shown are in green the distributions for the lepton tracks and in red for the background tracks starting with the RICH observables (top) and the energy loss in the drift chambers and the time of flight wall (bottom) for the TOF region.



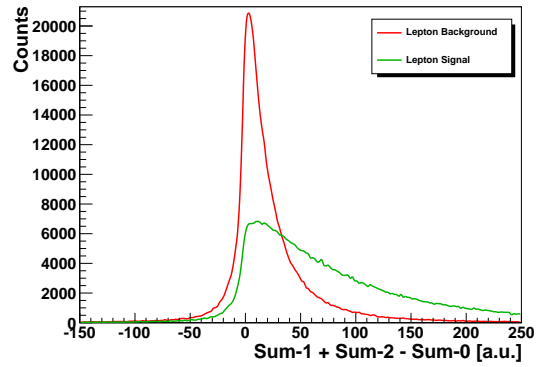
(a) RingCentroid (TOFin region)



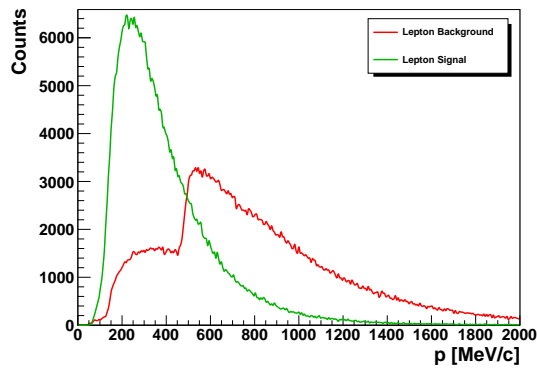
(b) Number of fired RICH pads (TOFin region)



(c) TOFin dEdx



(d) Shower Sum



(e) Momentum

Figure 3.4: Shown are in green the distributions for the lepton tracks and in red for the background tracks starting with the RICH observables (top) and the energy loss in the drift chambers and the time of flight wall (middle). In addition also the ShowerSum and the momentum is included in the TOFin region. The step in the momentum background distribution is due to protons.

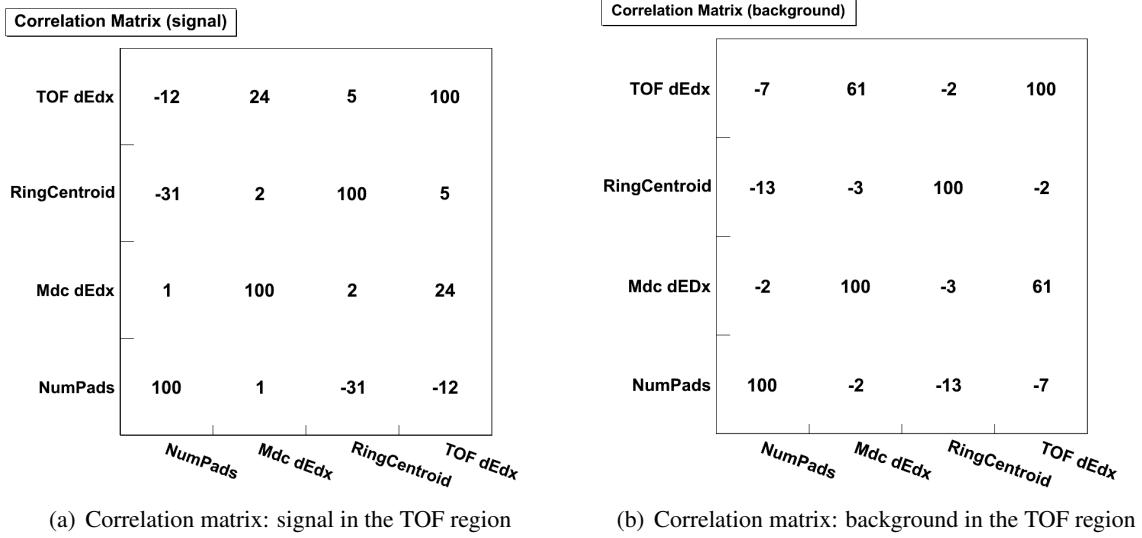


Figure 3.5: Linear correlation coefficients of the training sample in % for signal (left) and background (tracks) in the TOF region.

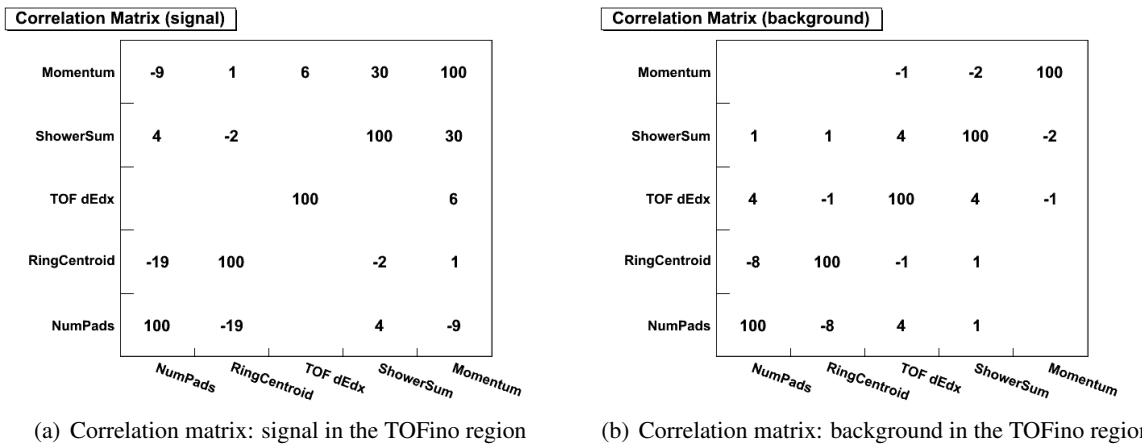


Figure 3.6: Linear correlation coefficients of the training sample in % for signal (left) and background tracks (right) in the TOFino region. Empty fields indicate no correlation.

## Data

The trained algorithm applied to the data returns a single scalar response value called classifier. Values close to 0 stand for probable background tracks while values around 1 for true electron tracks. The classifier distributions for the TOF and TOFino region are shown in fig. 3.7. In the further analysis for both systems return values smaller than 0.3 have been discarded in order to optimize the data sample for efficiency. The effect of the cut on the classifier is illustrated in fig. 3.8 where the matching radius

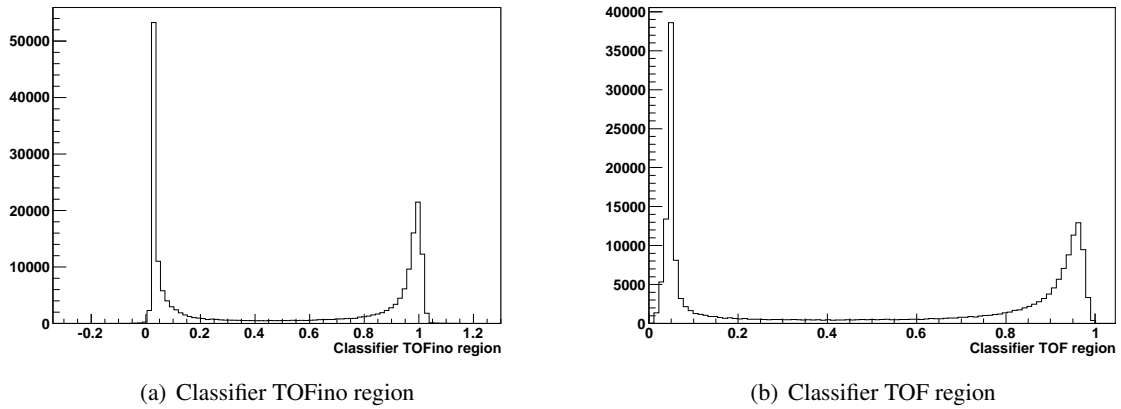


Figure 3.7: Return value of the neural network for the TOFino region (left side) and the TOF region (right side). Values around 1 indicate probable electrons, values close to 0 probable background tracks. In the further analysis for both systems return values smaller 0.3 have been discarded.

is shown, as a function of momentum before (left) and after the MVA PID (right). Electron tracks cluster at small values of the matching radius, compare section 3.3.1.

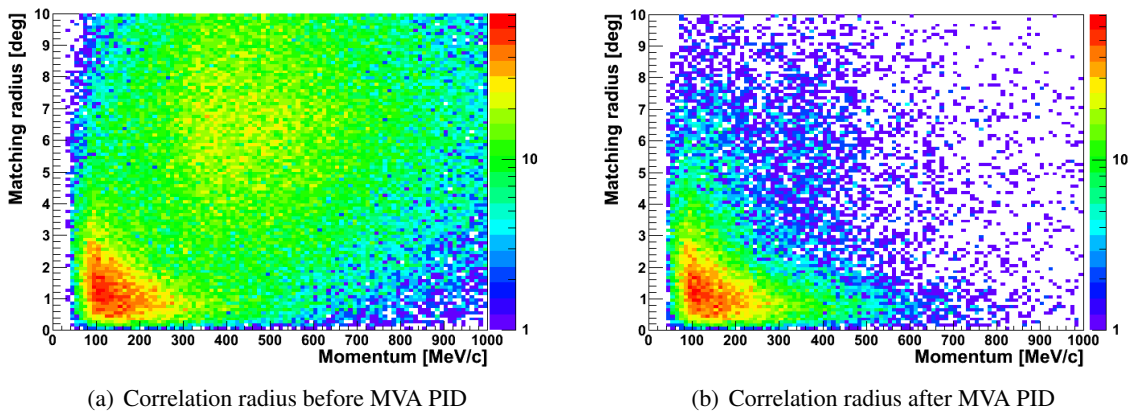


Figure 3.8: Illustration of the effect of the MVA PID on single tracks. Correlation radius as a function of momentum before MVA PID (left side) and after (right side). Electron tracks agglomerate at small values of the correlation radius.

### 3.3.2 RICH-Track matching

In order to ease the comparison with the method of hard cuts [Web11], the same ring track matching was used. The difference of the polar and azimuthal angles,  $\Delta\phi = \phi_{RICH} - \phi_{RK}$  and  $\Delta\theta = \theta_{RICH} - \theta_{RK}$  between the reconstructed tracks from the RICH and the tracking detectors using the RungeKutta method, were adapted with a 2-dimensional gaussian function, corresponding to ellipses in the polar and azimuthal angle space, see fig. 3.9. Since the RICH coordinate system is not perfectly aligned to the tracking detectors and since the width of the distribution is decreasing with increasing momentum due to less multiple scattering, the adaption is done for each sector separately and for several momentum regions. In order to describe the remaining background under the signal a straight (uncorrelated background) and a broad gaussian distribution (correlated background due to wrongly matched double rings) are also included in the fit [Web11, MWw09].

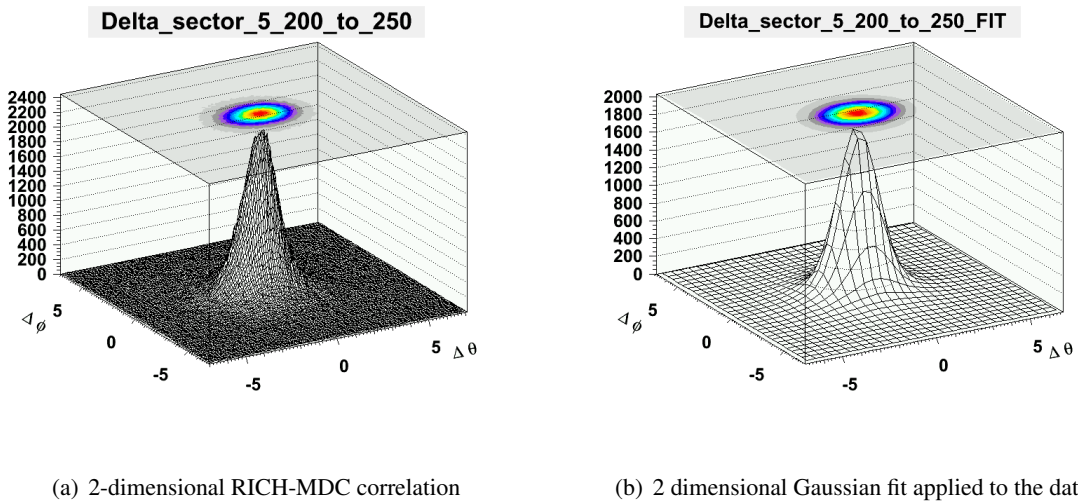


Figure 3.9: 2-dimensional correlation between the RICH detector and tracking detectors as a function of the difference of the polar and azimuthal angles measured with both detectors for a given momentum range of 0.2 to 0.25 GeV/c (right side). The distribution is matched with a Gaussian function in several momentum ranges (left side) [Web11, MWw09].

### 3.3.3 Track sorting

Since the reconstruction of particle trajectories is based on measurements in the drift chambers, it is possible that several tracks share one or more track segments. Several scenarios enhance the probability for such effects, each of them requiring an adapted treatment:

- Close to a real track the probability for creating so-called ghost tracks due to noise in one cell or several cells of the detector is increased. A reconstructed ghost track, might then consist of only a few noisy cells, combined with cells fired nearby. A procedure is needed, which suppresses the ghost track but maintains the associated real track.
- Photons which convert inside the detector into electron pairs, produce tracks with typically small opening angles due to the low Q value of their decay and therefore often share cells in the inner chambers due to the limited detector resolution. When traversing the magnetic field the

conversion pairs are bent in opposite directions and can be distinguished as individual tracks in the outer drift chambers. In such cases the pair can be identified as a conversion pair and both tracks should be discarded.

In order to reduce the amount of ghost tracks and to analyze only unique tracks, a sorting of the tracks according to the quality of the reconstruction, the product of the RungeKutta  $\chi^2$  and the MetaMatch quality, is performed. At the end only the best track is kept.

The selection is only performed for hit points in the outer chambers, in order to be able to clean the sample from conversion pairs, later on in the pair analysis using an opening angle restriction, see section 3.4. It is also important at which state of the analysis the sorting is done, since electrons are minimum ionizing and therefore have on average less recognized hits compared to hadron tracks, resulting in lower average quality of their reconstructed trajectories compared to hadrons. However in the low multiplicity environment of p+Nb collisions with average track densities of smaller than 1 per sector the sorting can be done at the beginning of the single track analysis. This is in contrast to high multiplicity Au+Au collisions, where one might lose the majority of lepton candidates if one applies the sorting without further selections to enhance the purity of true electrons.

### 3.3.4 Overview of the selections and purity estimation

In the processing of the data the selection criteria are applied in the following order:

- on the event level, only events with a positive LVL2 decision are analyzed.
- The first selection on the track level is the track sorting, followed by the ring matching and the cut on the response from the neural network (PID).
- Finally only events with more than one lepton candidate are processed further to the dielectron analysis.

The strongest selection criterion is the matching between rings in the RICH detector and the trajectories reconstructed in the drift chambers, which discards almost 67% of all candidates. In addition only 22% of all finally selected single tracks belong to events which can be processed to the pair analysis. Tab. 3.4 summarizes all applied selections, the corresponding number of entries in the analysis sample and the percentage of accepted entries of the single selections. Since the purity of the sample increases with every selection the percentage of accepted entries for each selection is only valid if the selections are applied in the same order.

#### Topology of the track samples

The topology of the sample after the different selections gives a good quality assessment for the performance of the software and hardware in general, see fig. 3.10. Without any condition applied the distributions are smooth and a clear enhancement in the sector equipped with only 3 chambers, due to an increased number of ghost tracks, is visible. If in addition a wide correlation with a RICH ring is asked for, hot spots due to noisy regions of the RICH become visible. If the track survives also the track sorting, the variates selection, the ring matching and the PID, there are still noisy regions visible. Only the tracks which finally pass the selection on the pair level, see section 3.4, show again a smooth behavior without noisy regions.

<b>event level</b>	<b>entries</b>	<b>accepted by selection</b>	<b>efficiency</b>
all	$9 \cdot 10^8$		
LVL2	$2.1 \cdot 10^8$	65%	96%
<b>single track level</b>	<b>lepton candidates</b>	<b>accepted by selection</b>	<b>efficiency</b>
input	$3.5 \cdot 10^8$		
track sorting	$2.5 \cdot 10^8$	71%	$\approx 80\%$
ring matching	$9.8 \cdot 10^7$	39%	$\approx 80\%$
PID (classifier > 0.3)	$9.4 \cdot 10^7$	95%	$\approx 95\%$
at least two tracks	$2.1 \cdot 10^7$	23%	

Table 3.4: Overview of selections applied on the event and single track level. The efficiency of the second level trigger was estimated by comparing the dielectron yield in level 1 and level 2 events. The strongest selection criteria is the matching between rings in the RICH detector and the trajectories reconstructed in the drift chambers, which discards almost 67% of all candidates. In addition only 22% of all finally selected single tracks belong to events which can be processed to the pair analysis. The efficiencies estimated for simulated single tracks averaged over the whole momentum range are listed in the fourth column, for details see section 3.5. Additionally a selection on the closest reconstructed tracks and a fitted segment in the inner drift chambers is applied in the dielectron analysis, see section 3.4, with an approximate efficiency of 93%.

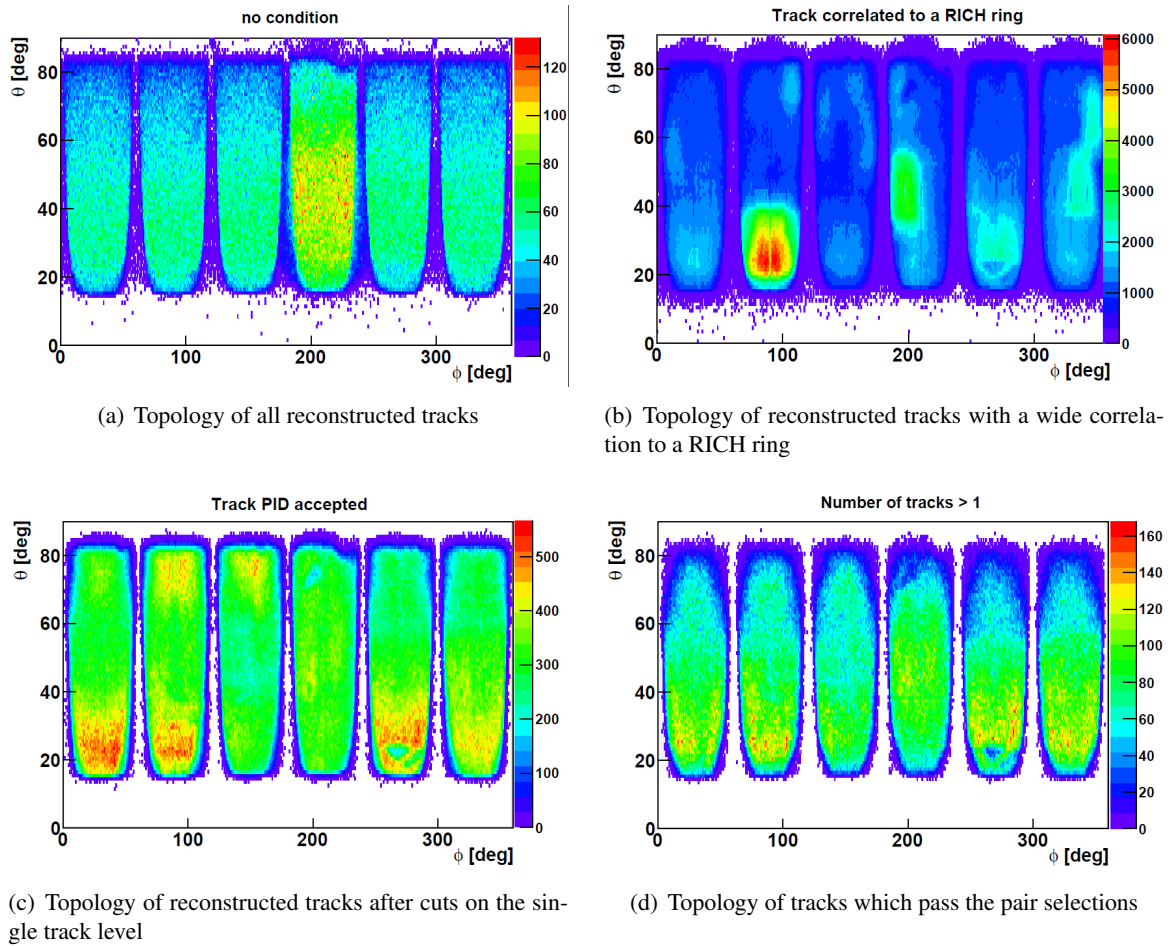


Figure 3.10: The topology of the sample: a) All reconstructed tracks. In the fourth sector equipped with only three chambers, more tracks (increased number of ghost tracks) are reconstructed on average. b) All tracks which have a wide correlation to a RICH ring, hot spots are visible due to noisy regions of the RICH. c) Only those tracks which survive the track sorting, the variates selection, the ring matching and the PID, still noisy regions are visible. d) Those tracks which finally pass the pair selections, the distribution shows again a smooth behavior.

### Purity estimation

The purity of the single track sample is estimated by a rotation of the RICH detector by one sector with respect to the rest of the detector. By definition, only uncorrelated rings and tracks are then matched. Applying the discussed selections in addition reduces the probability for a matched ring accordingly. The ratio of reconstructed rings in the rotated sample  $N_{rot}$  to the rings in the real sample  $N_{unrot}$  corresponds then to the purity  $P = (N_{nonrot} - N_{rot})/N_{rot}$ . Fig. 3.11 shows the purity for electrons and positrons in the TOF and TOFino region as a function of the track momentum.

While the purity is very high for electrons in both systems for all momenta, for positrons the purity decreases for momenta larger 600 MeV/c. The effect is much more pronounced in the TOF region since the information from the SHOWER detector is missing. Although the effect is dramatic in the high momenta region, the impact on the final spectra is overrated because of the falling rates with rising momentum. Restriction of the maximum allowed momenta in the training sample and in the following analysis could enhance the purity by increasing the separation power of momentum dependent variates like the energy loss in the drift chambers and the time of flight walls, in the future.

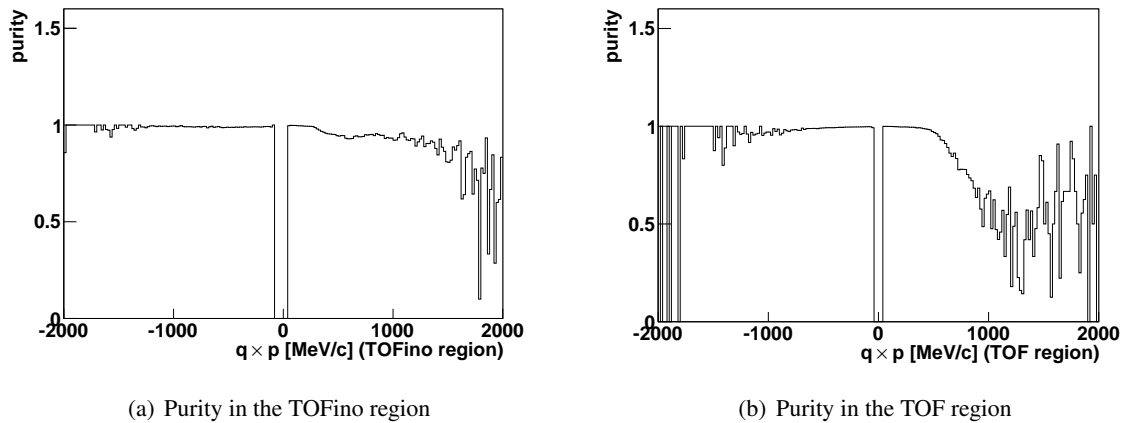


Figure 3.11: Purity of single lepton tracks as a function of the momentum in the TOFino (right side) and the TOF (left side). The purity is estimated by rotating the RICH detector by one sector around the beam axis before tracking.

## 3.4 Di-electron analysis

After the identification of single electrons and positrons the properties of the mother (virtual) photon can be calculated making use of the 4-momentum conservation.

However, besides the misidentified electrons and positrons due to hadron contamination, a sizeable fraction of the reconstructed electrons and positrons originate from  $\gamma$  conversion inside the detector and target material, introducing additional combinatorial background (CB). On top of this, there are also physical background sources, which are discussed in the following, as well as several ways to suppress and to describe the remaining combinatorial background below the physical signal.

### 3.4.1 Physical combinatorial background sources

Besides the background due to  $\gamma$  conversion or misidentification also physical sources contribute to the combinatorial background. One may distinguish between correlated and uncorrelated background. However the definition of correlations is not straight forward, therefore I define all leptons which can be traced back to the same electromagnetic vertex as correlated and everything else as uncorrelated. An example for uncorrelated background is then the combination of a dielectron pair from two single tracks originating from two different  $\pi^0$  Dalitz decays or a  $\Delta^+$  Dalitz decay, as illustrated in the left part of Fig. 3.12. However if one correlates two single tracks from one  $\pi^0$  Dalitz decay but originating from a different (virtual) photon, like it is shown on the right side of Fig. 3.12, both single tracks are correlated due to energy conservation in the decay of the primordial pion.

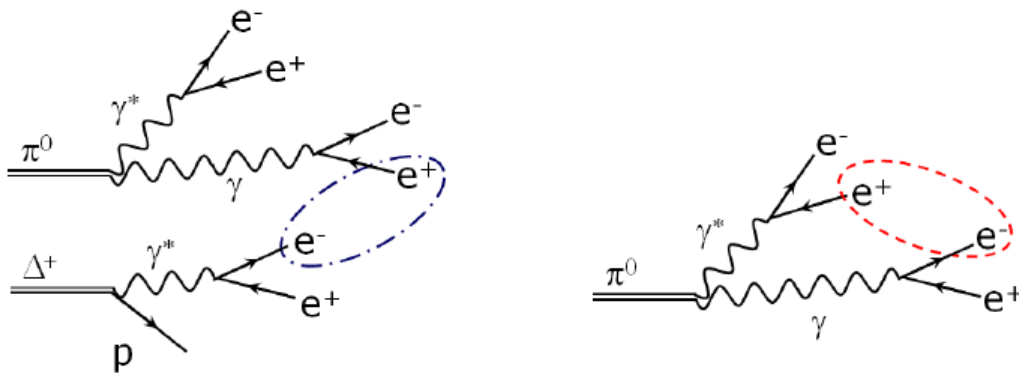


Figure 3.12: Example for uncorrelated (left) and correlated background (right) sources.

#### Combinatorial background rejection

Most of the conversion pairs can be suppressed making use of their decay kinematics: due to their low  $Q$  value the average opening angle between the two legs of such a pair is small and are rejected by asking for pair **opening angles** larger  $9^\circ$ . The value is chosen as a compromise between sufficient conversion rejection without losing too many pairs originating from  $\pi^0$  Dalitz decays, since sufficient statistics in the  $\pi^0$  region is important for the normalization later on.

The opening angle cut is applied such that, if a pair fails this cut both its legs are not used any more in the further pairing.

Finally two selections are applied which are actually single track selections: Related to the opening angle rejection is the cut on the **close neighbor trajectory**, also at values of  $9^\circ$ , in order to reject conversion reactions where one leg is bent out of the acceptance before hitting the outer drift chambers. Finally the range of the allowed **single momentum** is restricted to values larger than 100 MeV/c and smaller than 2000 MeV/c. The upper value is the edge up to which the RICH detector can separate electrons from myons and pions, while the lower value is the lower edge of the region where the efficiencies of the tracking procedure are well understood.

Same event like-sign background

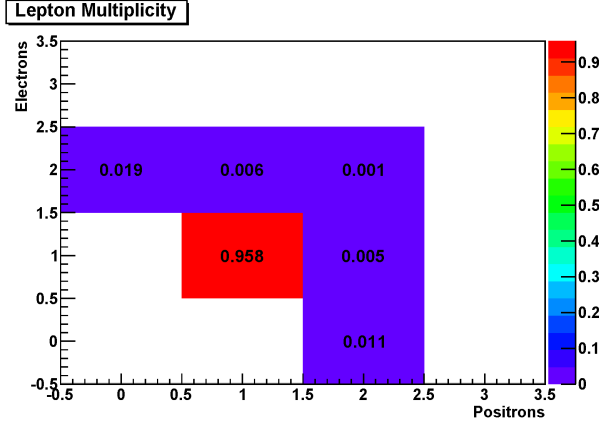
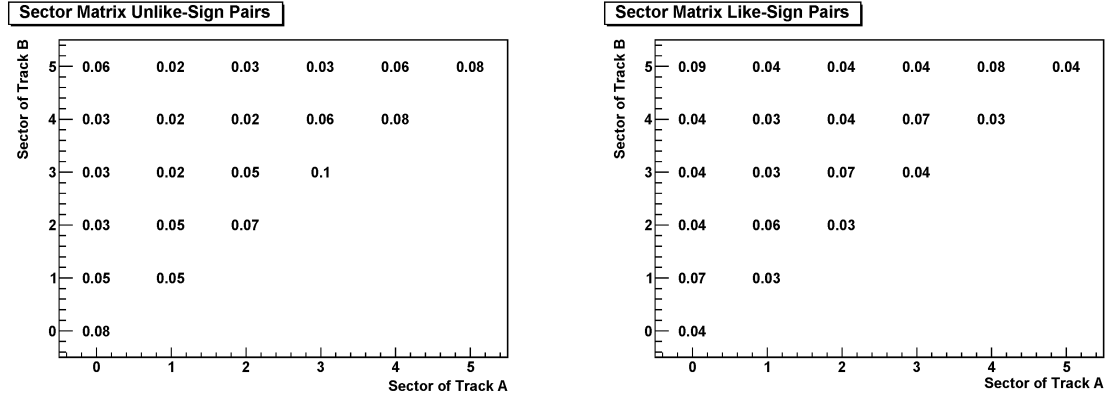


Figure 3.13: Relative rates of electrons and positrons in percentage before the selections on the pair level are applied. Only events which have at least two lepton tracks are listed.



(a) Distribution of unlike-sign track pairs over the 6 sectors      (b) Distribution of like-sign track pairs over the 6 sectors

Figure 3.14: Dispersion of unlike-sign track pairs (left side) and like sign track pairs (right side) over the 6 different sectors.

The remaining combinatorial background can be described by a combination of same event like sign pairs ( $e^+e^+, e^-e^-$ ), in order to take both correlated and uncorrelated background sources into account.

If the probability to have  $N_{e^+/e^-}$  per event follows the Poisson statistics the background can be described by the geometrical mean:

$$N_{+-}(CB) = 2 \cdot \sqrt{N_{++} \cdot N_{--}}. \tag{3.4}$$

Taking the acceptance into account, the probability to reconstruct more than 2 lepton tracks per event is negligible, see also Fig. 3.13. Therefore in order to describe the background the arithmetic mean given as

$$N_{+-}(CB) = N_{++} + N_{--}, \tag{3.5}$$

is used as an approximation [Sai07] rather than formula 3.4, in order not to underestimate the background contribution due to the low statistics.

As a quality assessment for the background description method one can compare the distribution of like sign and unlike sign pairs over the six different sectors. As can be seen from Fig. 3.14 the dispersion does not vary strongly between the two types of pairs, which assures that neither the background nor the signal contribution is dominated by noise arising from a specific part of the detector. A detailed description on methods for the background subtraction focused on heavy-ion reactions can be found in [GG01].

### Uncorrected invariant mass spectra

If the 4-momentum vectors of two particles are known, the invariant mass of the mother particle can be calculated making use of energy and momentum conservation. It is given as:

$$M_{1,2} = \sqrt{(E_1 + E_2)^2 - (\vec{p}_1 + \vec{p}_2)^2}. \quad (3.6)$$

For electrons and positrons the rest mass is small compared to the momentum and can be neglected, Eq. 3.6 can then be written as:

$$M_{ee} \approx 2\sqrt{p_{e^-} + p_{e^+}} \cdot \sin(\alpha_{ee}/2), \quad (3.7)$$

with  $\alpha_{ee}$  being the opening angle between the particle trajectories. The resulting  $e^+e^-$  invariant mass spectra (black points), together with the  $e^+e^+$  (red triangles),  $e^-e^-$  (blue triangles) and the total CB (green points) are shown in Fig. 3.15.

In the low invariant mass region below  $0.15 \text{ GeV}/c^2$  the spectra are dominated by Dalitz decays of neutral pions, note the presence of the peak structure also in the CB due to correlated background as described in the previous section. The intermediate part of the spectra from  $0.15 \text{ GeV}/c^2$  to  $0.47 \text{ GeV}/c^2$  is dominated by Dalitz decays of  $\eta$  mesons and baryonic resonances. The region between  $0.47 \text{ GeV}/c^2$  and  $0.7 \text{ GeV}/c^2$  is dominated by direct  $\rho$  decays and/or Dalitz decays of baryonic resonances, and in the high invariant mass region above  $0.7 \text{ GeV}/c^2$ , sharp peak structures of the direct decays of the light vector mesons  $\omega$  and  $\phi$  dominate over a continuum due to still contributing Dalitz decays of baryonic resonances and direct  $\rho$  decays, appear. While the peak structure around the  $\omega$  pole mass is clearly visible, the peak structure around the  $\phi$  pole mass suffers from low statistics. The ratio of the signal to background contribution, which is important to judge on how strong the signal might be affected by systematic errors of the background subtraction, is shown in Fig. 3.16. While the signal to background ratio reaches very high values close to 100 in the low invariant mass region, it drops to average values of 2 in the intermediate region and rises again in the vector meson region to values above 10.

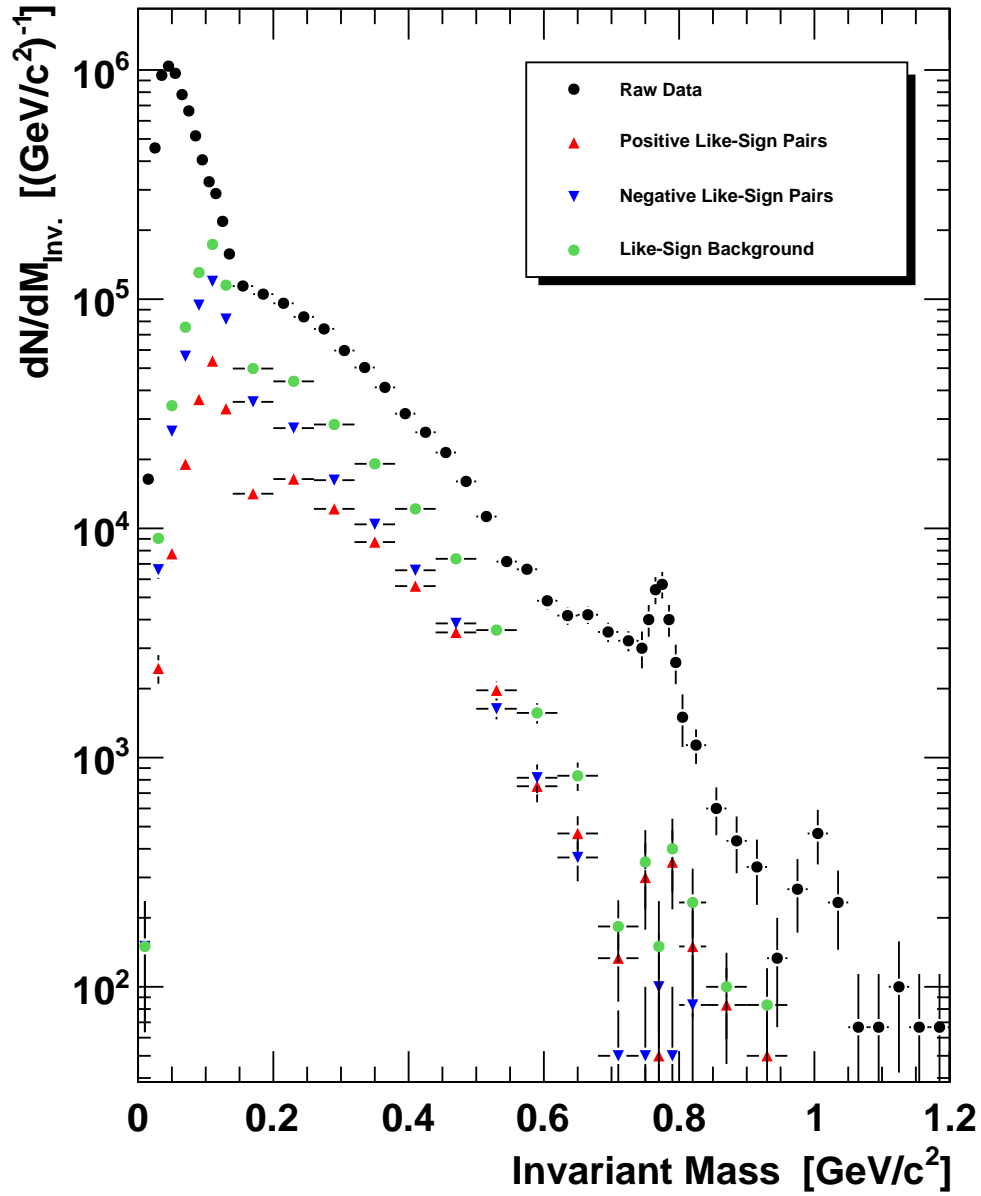
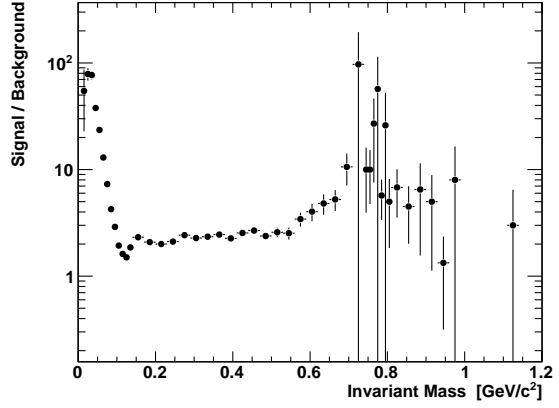


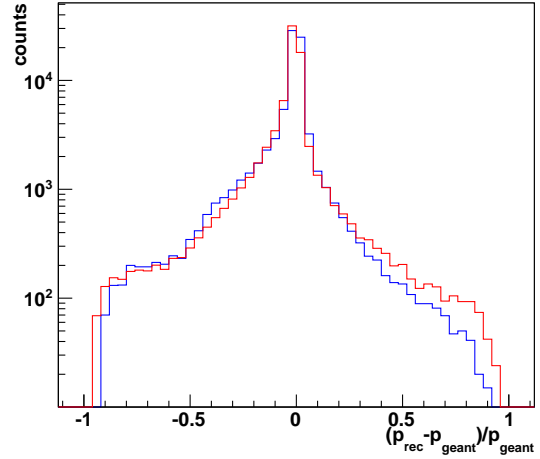
Figure 3.15: Uncorrected invariant mass spectra after all cuts. Shown are the distributions for unlike sign pairs (black) and for both like sign pair species as well as their sum. Due to correlated and uncorrelated background sources, see Fig. 3.12, the background contribution given by all like sign pairs (green) must be subtracted, see text for details.

Figure 3.16: The signal to background ratio as a function of the invariant mass. While the ratio has very high values in the low invariant mass region, it drops to average values of 2 in the intermediate region and rises again in the vector meson region to values higher than 10.



### 3.5 Efficiency corrections

Figure 3.17: The relative dispersion between the initial momentum at the target position and the reconstructed value estimated via simulation (blue: electrons, red: positrons). Besides the momentum resolution of the spectrometer also the energy loss of the electrons and positrons affects the distribution resulting in lower reconstructed momenta on average.



In order to get physical relevant information and to be able to compare the results with theoretical models the data have to be corrected for the detector and selection efficiencies.

The efficiency of a single selection is defined as

$$\epsilon_{Sel} = \frac{N_{aSel}}{N_{bSel}}, \quad (3.8)$$

with  $N_{aSel}$  being the number of tracks after application of the selection, while  $N_{bSel}$  is the number of tracks before applying the selection. If the selections are independent of each other, which is approximately fulfilled, the total efficiency factorizes.

The pair efficiency is therefore calculated as the product of single electron and positron efficiencies,

$$\epsilon_{e^+e^-} = \epsilon_{e^+} \cdot \epsilon_{e^-}, \quad (3.9)$$

which are estimated as a function of the momentum ( $p$ ), the polar angle ( $\Theta$ ) and the azimuthal angle ( $\Phi$ ) based on simulations. The assumption that both efficiencies are independent of each other holds

true for all tracks, except for those which are reconstructed in the same sector. For such pairs an additional correction has to be applied, see section 3.5.1 .

The efficiency correction is done in the following steps:

- Positrons and electrons are generated with a flat momentum distribution using the ROOT-based decay generator Pluto++ [PLU04]. In order to obtain realistic vertex distributions experimentally reconstructed distributions are used.
- The detector response is modeled using the simulation tool HGEANT [HGE04], which is based on the package GEANT3 [App93]. The digitization parameters are adapted for each experimental campaign.
- The simulated information is embedded into real events and DST files are produced, containing real and simulated tracks. For the latter one, all relevant informations from the HGEANT simulation are transported.
- Finally, the data are processed through the analysis and all selections are applied. The 3-dimensional single track efficiency matrix is defined as a function of the reconstructed momentum  $p_{rec}$ , the polar angle  $\Theta$  and the azimuthal angle  $\Phi$  in the numerator:

$$\epsilon(p, \Theta, \Phi) = \frac{N_{reconstructed}(p_{rec}, \Theta, \Phi)}{N_{accepted}(p_{smear}, \Theta, \Phi)}. \quad (3.10)$$

For the denominator self consistency studies, see [Wit, MWi10] and section 3.5.1, showed that the best results are obtained if the initial momentum value at the target is smeared according to the difference between the initial value and the reconstructed value. Note that in this way, besides the smearing due to track reconstruction also the energy loss of the tracks inside the detector is taken into account, resulting in lower reconstructed momenta on average. While the effect of using smeared values is of the order of 10% in the estimated efficiency for the momentum the smearing effect on the angles can be neglected.<sup>1</sup>

The resulting single track efficiency matrices for electrons and positrons are plotted in Fig. 3.18 for momenta between 210 and 230 MeV/c. In order to give a clear presentation of the reconstruction efficiencies, making use of the azimuthal symmetry of the apparatus, it is worth to project the efficiencies to the momentum axis. Fig. 3.19 shows the efficiencies as a function of the momentum for both detector systems for electrons (blue) and positrons (red).

---

<sup>1</sup>Technically the smearing is done using a matrix of histograms in 20 momentum regions and 8 polar angle regions, in order to cover up the polar angle dependence of the tracking and the energy loss as well as the more obvious momentum dependence. In order to better parameterize the smearing function for the HAFT filter version 3.9, the spread between the momenta is normalized to the initial momenta. The resulting contribution is shown in Fig. 3.17 for a given momentum and azimuthal angle region.

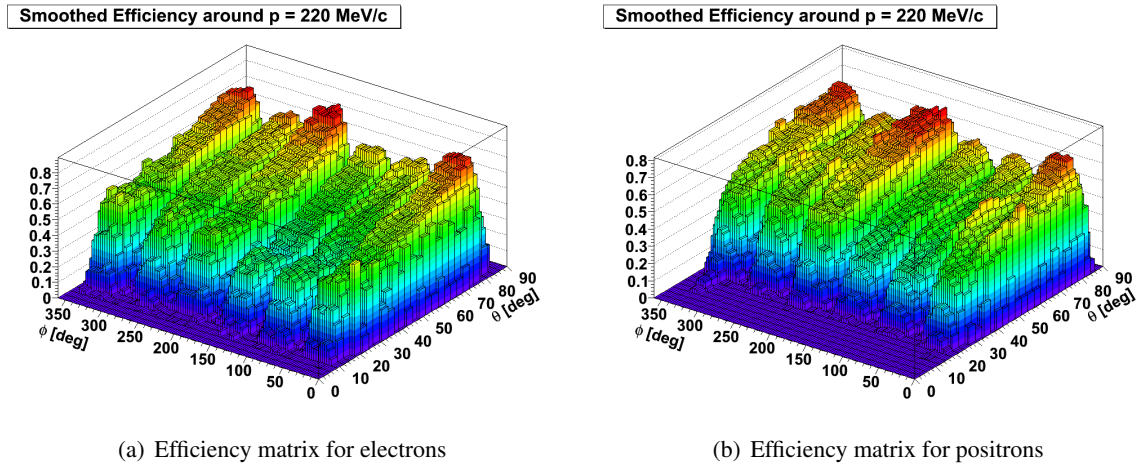


Figure 3.18: Efficiency matrix for electrons (left) and for positrons (right) for momenta around between 210 and 230 MeV/c.

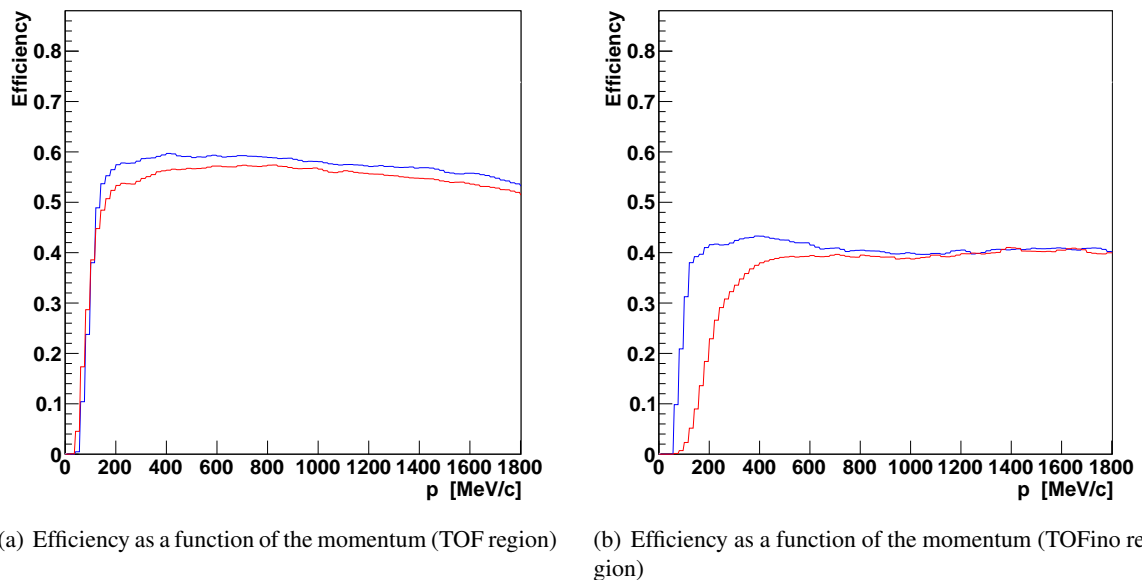


Figure 3.19: Efficiency as a function of the single track momentum for the TOF (left) and the TOFino region (right). The positron efficiency is shown in red, while the one for electrons is drawn in blue.

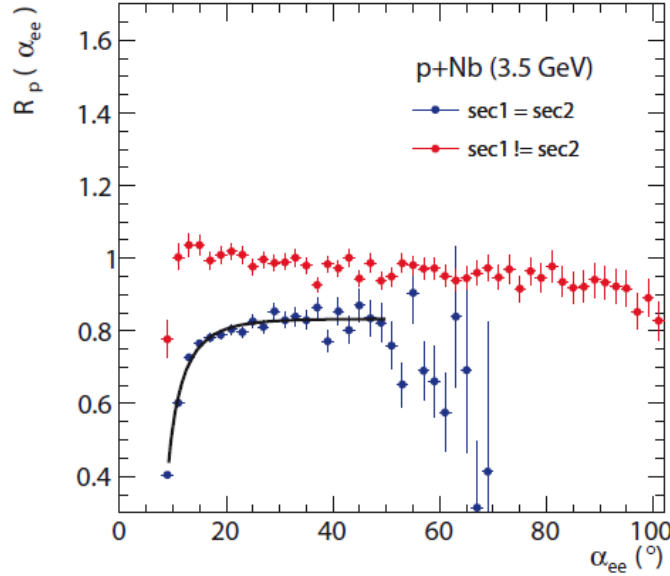
### 3.5.1 Self consistency check and opening angle correction

To check the validity of the efficiency correction method and to estimate its systematic uncertainty a self consistency check is performed. Several physical dielectron sources (Dalitz decays of  $\pi^0, \eta, \Delta^+$  and direct decays of  $\omega$ ) are generated and boosted using the event generator Pluto according to the phase space of a 3.5 GeV proton on proton collision. Similar to the white electron and positron distributions used for the generation of the efficiency matrix, the decay products are tracked through the HGEANT simulation, embedded into real events and processed through the whole analysis chain including the efficiency correction. The resulting physical pair observables like invariant mass  $M_{ee}$ , rapidity  $Y_{ee}$ , transverse momentum  $P_t$  and total momentum  $P_{ee}$  are compared to the initial distributions filtered by the HADES acceptance and smeared with previously used smearing functions in order to model the detector response.

As mentioned earlier, the assumption of independent efficiencies of both pair legs holds only true for pairs which are not reconstructed in the same sector of the detector, therefore an additional correction factor depending on the **opening angle**  $\alpha_{ee}$  between both legs is applied. The same correction function  $F(\alpha_{ee})$  as used in [Web11] is applied:

$$F(\alpha_{ee}) = 0.83 \cdot (1 - \exp^{-6.3 \cdot (\alpha_{ee} - 7.9)^{6.8}}). \quad (3.11)$$

The function was obtained by a fit to the relative reconstruction efficiency  $R_p(\alpha_{ee})$  for pairs origi-



(a) Opening angle distribution for dielectron pairs

Figure 3.20: Relative reconstruction efficiency for dielectron pairs originating from  $\eta$  Dalitz decays. If both legs are reconstructed in different sectors (red) no additional correction is needed. For pairs with both legs in the same sector (blue points) the correction function 3.11 plotted in black is applied [Web11].

nating from  $\eta$  Dalitz decays reconstructed in the same sector, shown in Fig. 3.20. It is observed that the opening angle distribution varies in the order of 10% depending on the physical source used as input [MWi10], probably due to different Q-values, resulting in different momentum dispersion of the

electron and positron tracks.

The ratio of both contributions for the different pair observables is shown in Fig. 3.21 for dielectrons originating from direct decays of  $\omega$  mesons as this mass region will be in the focus of the interpretation of the data. The average difference for all observables is at the order of 10% and is accounted for in the systematic errors, see section 3.8.

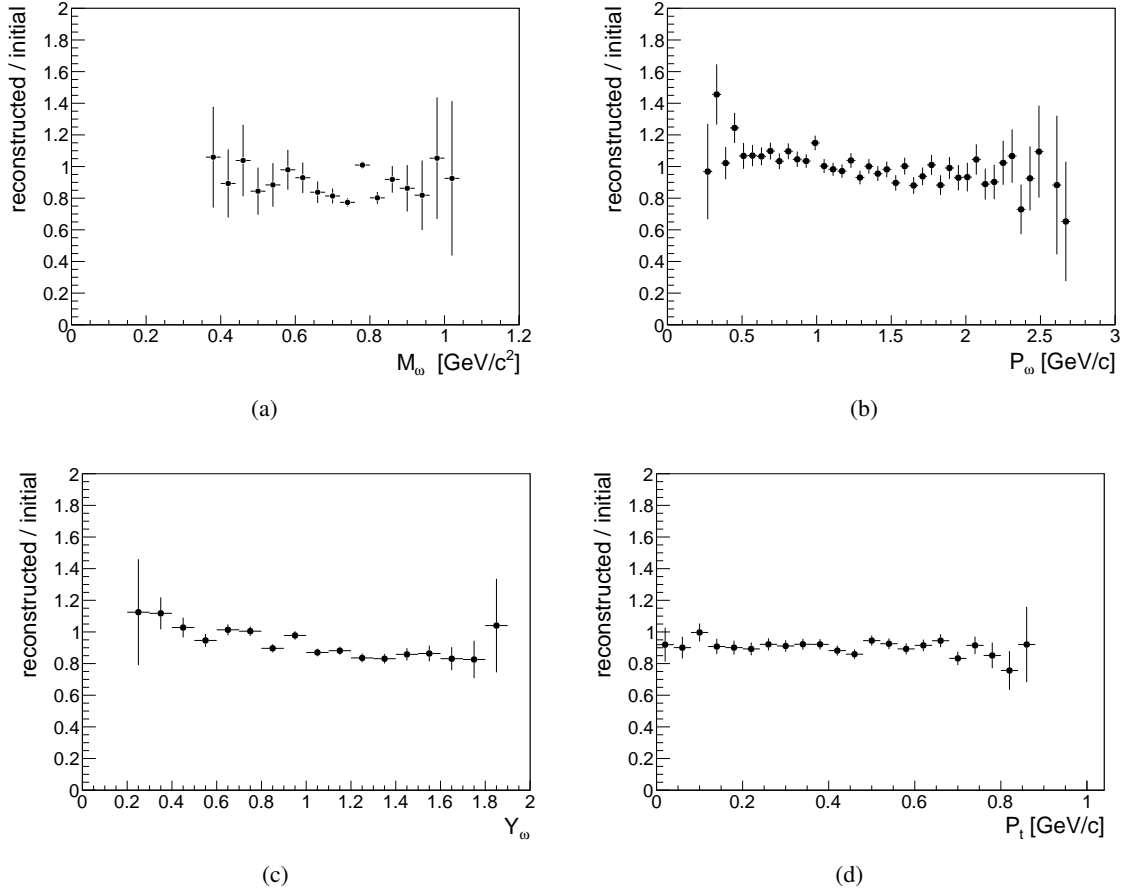


Figure 3.21: Self consistency of dielectrons originating from direct  $\omega$  decays. The average difference for all observables is of the order of 10%.

### 3.6 Comparison between MVA and HCA

After the implementation of the analysis of hard cuts (HCA) into the analysis frame work developed in [Lan08] a step by step comparison to the HADES standard analysis procedure was done to check that both procedures deliver identical results. In particular this allows for a detailed comparison between the two PID methods with respect to efficiency and the signal to background ratio. Moreover systematic errors due to the particle identification method can be estimated by comparing both results on the final pair observables.

While the signal to background ratio is nearly identical for both methods, compare Fig. 3.22, the single electron and positron efficiencies are about 20%-30% higher for MVA, depending on the detector

region, see Fig.8.4. With the purity staying constant but higher statistics due to the higher efficiency the significance ( $Sig = Signal / (\sqrt{Signal + Background})$ ) of the sample has higher values in case of the MVA. Whether this harvest is worth the extra effort and moreover if the MVA method is a valid option for the future heavy ion beam times, is discussed in chapter 7.

As mentioned earlier, the comparison of the final pair observables obtained with both methods gives

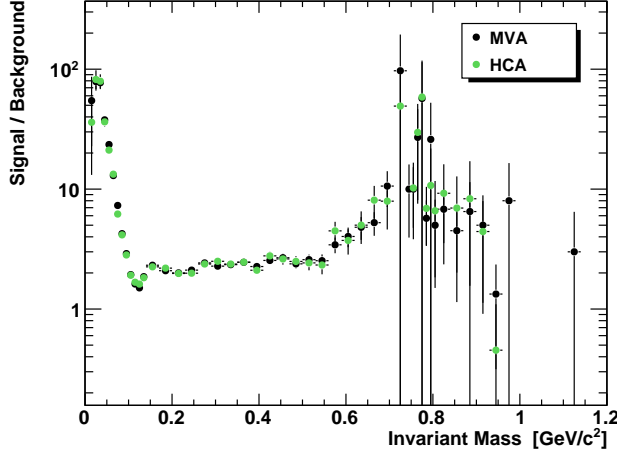
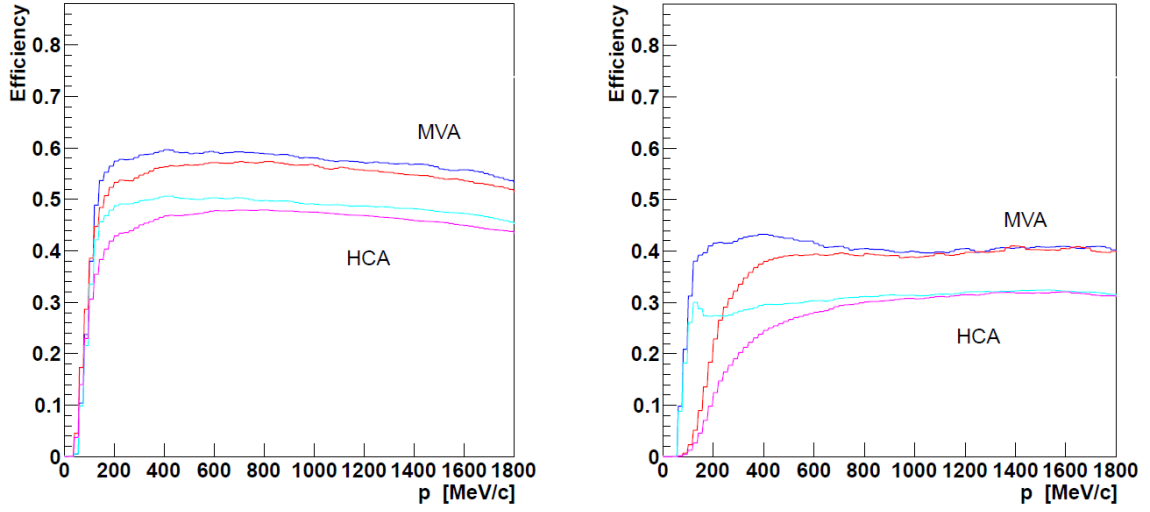


Figure 3.22: Comparison of the signal to background ratio as a function of the invariant mass for MVA (black dots) and HCA (green dots). The ratio is within error bars identical for both methods.

a handle on the systematic uncertainties due to the PID. In order to do these evaluations as accurately as possible, the comparison is done for all pair observables ( $M_{ee}$ ,  $P_{ee}$ ,  $Y_{ee}$  and  $P_t$ ) in the same differential invariant mass and momentum regions, which are later used for the physical interpretation of the data, see chapter 4. Namely these regions are pairs with momenta  $P_{ee} < 0.8 \text{ GeV}/c$ ,  $P_{ee} > 0.8 \text{ GeV}/c$  and no restriction on the momentum in case of the invariant mass spectrum. For the kinematical observables the 4 invariant mass regions introduced in section 3.4.1 are used:

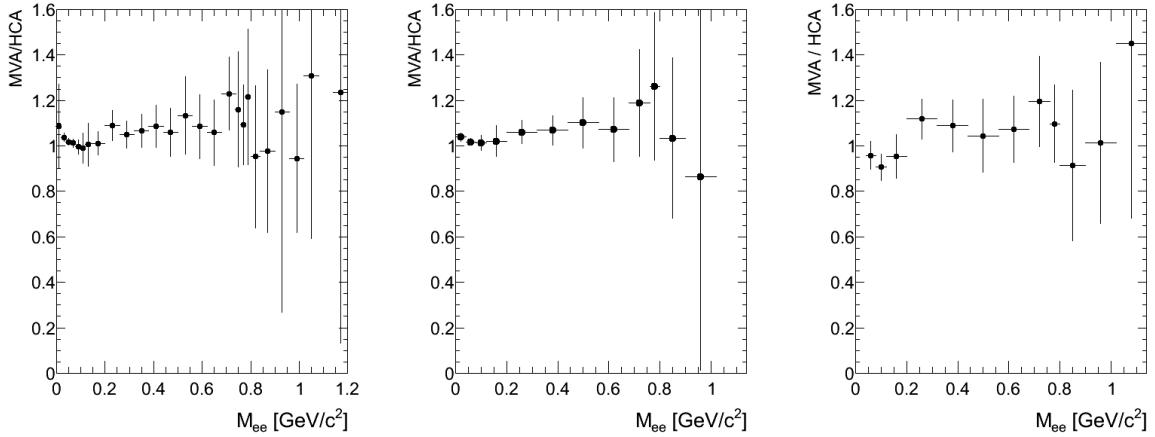
- $0-0.15 \text{ GeV}/c^2$ , dominated by Dalitz decays of neutral pions,
- $0.150-0.47 \text{ GeV}/c^2$  dominated by Dalitz decays of the  $\eta$  mesons,
- $0.47-0.7 \text{ GeV}/c^2$  dominated by direct  $\rho$  decays and/or Dalitz decays of baryonic resonances
- larger  $0.7 \text{ GeV}/c^2$  dominated by direct decays of the light vector mesons  $\omega$  and  $\phi$ .

The differences between the two analysis strategies after efficiency corrections were found to amount to 10% at most in all observables and regions see Fig. 3.24 and Fig. 3.25. It is accounted for in the systematical uncertainties, see section 3.8.



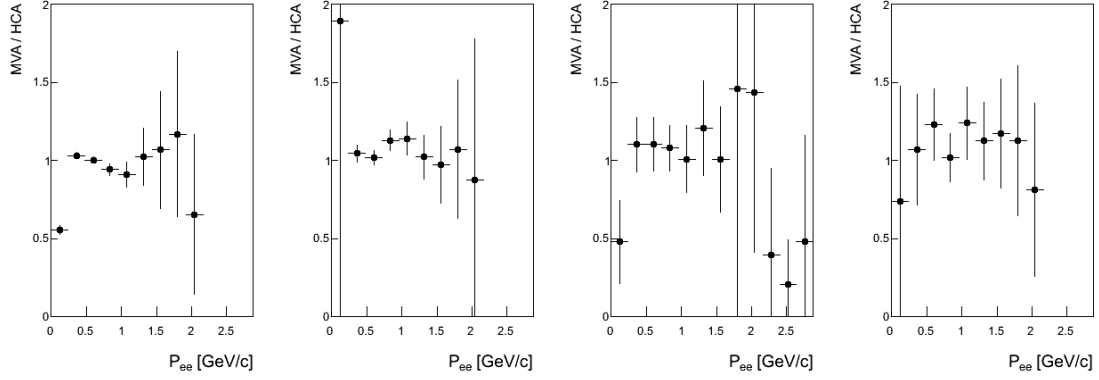
(a) Efficiency as a function of the momentum (TOF region) (b) Efficiency as a function of the momentum (TOFino region)

Figure 3.23: Comparison of the efficiencies as a function of the single track momentum for the TOF (left) and the TOFino region (right). The MVA efficiencies are shown in red (positrons) and in blue (electrons) while the ones for the HCA are shown in magenta (positrons) and light blue (electrons). Compared to the HCA the MVA gains around 20% in efficiency in the TOF region and about 30% in the TOFino region.

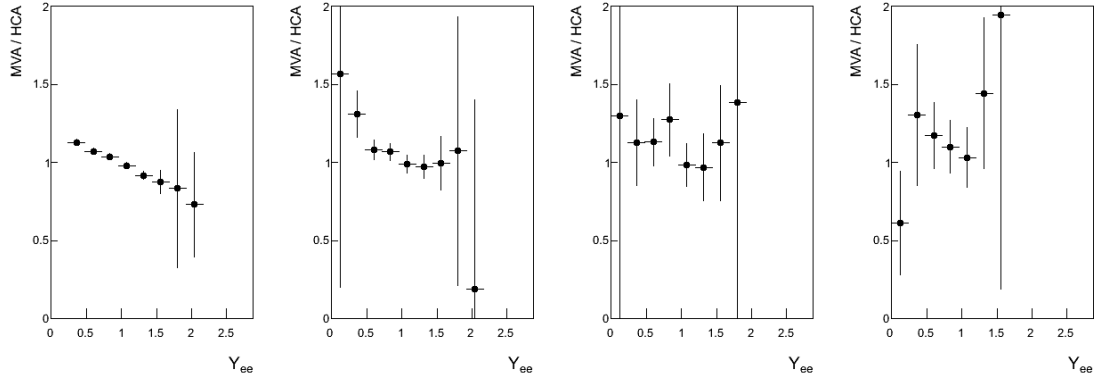


(a) Invariant mass (b) Invariant mass for slow pairs (c) Invariant mass for fast pairs

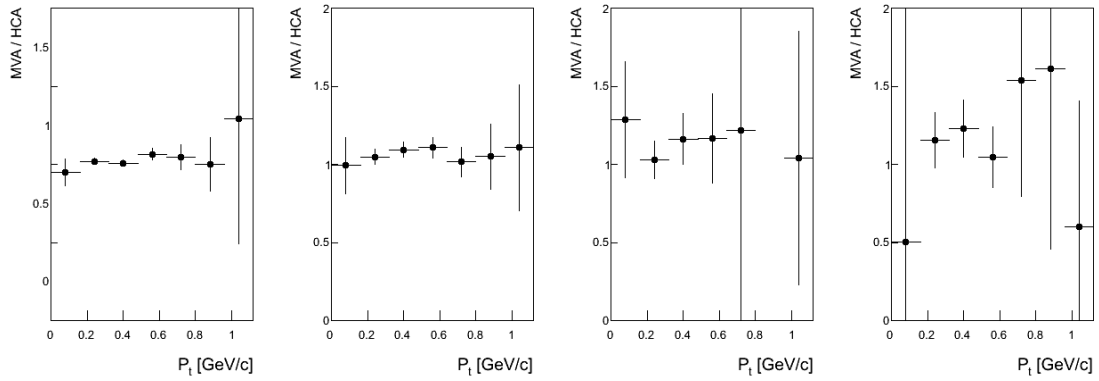
Figure 3.24: Ratio of the MVA and HCA real data invariant mass spectra after efficiency corrections, with no condition on the pair momenta (left), for momenta  $P_{ee} < 800$  MeV/c (middle) and for momenta  $P_{ee} > 800$  MeV/c (right) after efficiency correction.



(a) Momentum



(b) Rapidity



(c) Transverse momentum

Figure 3.25: Ratio of the MVA and HCA kinematical observables for the four defined mass regions after efficiency corrections. From left to right  $\pi^-$ ,  $\eta^-$ ,  $\rho/\Delta^-$  and the vector meson region, see text for details. Upper row:  $P_{ee}$ , middle row:  $Y_{ee}$  and lower row:  $P_t$ .

### 3.7 Normalization

In case of isospin symmetric heavy ion collisions (HIC) the HADES data are normalized to the number of neutral pions [Sud07, Pac08] estimated from the average of the charged pion multiplicities measured simultaneously. For elementary reactions [Gal09] the data are normalized to the known cross section of elastic reactions. For the p+Nb collision system the normalization procedure is more complicated.

In a first step the number of reconstructed dielectron pairs has to be corrected for the two level trigger system. During data taking every positive LVL2 event was written, while in addition every third LVL1 event was also written to tape. Therefore the total number of events seen by the detector is given as:

$$N_{LVL1total} = N_{LVL1recorded} \cdot F_{downscal} = 9.2 \cdot 10^9. \quad (3.12)$$

$N_{LVL1recorded}$  is the number of recorded LVL1 events,  $F_{downscal}$  is the down scaling factor of three. In order to estimate the total production cross section we make use of the systematics of the negative pion cross section in proton induced reactions on nuclei measured recently by the HARP-CDP collaboration [eaHCC09a, eaHCC09b, eaHCC09c, eaHCC09d]. Although the p+Nb collision system was not measured by the HARP-CDP collaboration, their systematics allow for an interpolation in beam energy and system size.

Technically this is done in the following way: negative pions are identified via their energy loss in the time of flight walls and corrected for efficiencies, acceptance and the trigger bias.

The corrected pion spectra are normalized in several  $\theta$  and  $p_{\perp}$  regions to the corresponding spectra of HARP-CDP experiment in the  $P_t$  region larger  $0.3 \text{ GeV}/c$ . The obtained scaling factor

$$\sigma_R = \frac{\sigma_{\pi^-}(HARP)}{M_{\pi^-}(HADES)}, \quad (3.13)$$

corresponds to the total reaction cross section of p+Nb reactions at 3.5 GeV. The best value corresponds to a reaction cross section of  $\sigma_R = (848 \pm 127) \text{ mb}$ . The error is estimated due to the uncertainty of the pion analysis and the uncertainties from the comparison with the HARP-CDP data. To get the total normalization factor for the dielectron spectrum one has again to correct for the difference in multiplicity between LVL1 events and minimum bias events this time for  $e^+e^-$ . The correction factor

$$F_{trigger}(e^+e^-) = \frac{N_{mb}}{N_{LVL1}} = 0.924, \quad (3.14)$$

is estimated based on a simulation with the transport model UrQMD [UrQ04].

The total normalization factor for the dielectron spectrum is then given as:

$$F_{NORM} = \frac{\sigma_R}{N_{LVL1total} \cdot F_{Trigger} \cdot \epsilon_{LVL2}} = (9.3 \pm 1.95) \cdot 10^{-8}, \quad (3.15)$$

with  $\epsilon_{LVL2}$  is the efficiency of the LVL2 trigger, which is estimated to be 0.96 by comparing the numbers of reconstructed pairs in LVL1 events and LVL2 events. A detailed discussion of the pion analysis and the normalization via the HARP-CDP data can be found in [Web11, pav10]. In order to be able to normalize to neutral pion multiplicity one has to rely on phenomenological models. Using again UrQMD to estimate the neutral pion multiplicity per event we get  $M_{\pi^0} = 0.661$ . [Tan11]. The neutral pion cross section is then given as:

$$\sigma_{\pi^0} = \sigma_R \cdot M_{\pi^0} = 559.7 \text{ mb}. \quad (3.16)$$

### 3.8 Error estimation

Several possible sources of errors are hidden in the analysis and have to be estimated in order to assign realistic systematic errors to the measured data.

As discussed in section 3.4.1 the obtained spectrum contains combinatorial background which must be subtracted. This combinatorial background is partially due to misidentified hadrons and mainly due to correlated and uncorrelated physical sources. The estimation of the background contains several systematic uncertainties, which are difficult to evaluate, since one does not know the contribution of this background with high precision. However since the signal to background ratio is above two in the continuum region of the spectrum and above ten in peak regions, the uncertainty to the background subtraction can be neglected.

The next cause of systematic errors is due to the efficiency correction. Here one distinguishes between errors due to the method itself and uncertainties due the digitization of the detector response. The first one is appraised by the self consistency checks in section 3.5.1 to 10%. The second one can be estimated by changing the PID selection criteria, either by varying the cut values in the HCA or by the comparison of the two PID methods, see section 3.6. Since the latter one accesses two different analysis frames it also covers coding errors. Both methods give uncertainties again at the order of 10%.

In addition the normalization of the spectrum causes uncertainties. Here errors from the pion analysis (13%) and the comparison to HARP-CDP data (5%) contribute. They are added quadratically to an total error of 15% due to the normalization.

#### 3.8.1 Total error of the measurement

Under the assumption that the different systematic errors are in first approximation uncorrelated, their quadratic sum gives the total systematic error of:

$$\sigma_{total} = \sqrt{\sigma_{selfcon}^2 + \sigma_{PID}^2 + \sigma_{norm}^2} = 0.21, \quad (3.17)$$

which is assigned to the measured data.

### 3.9 The HADES acceptance filter

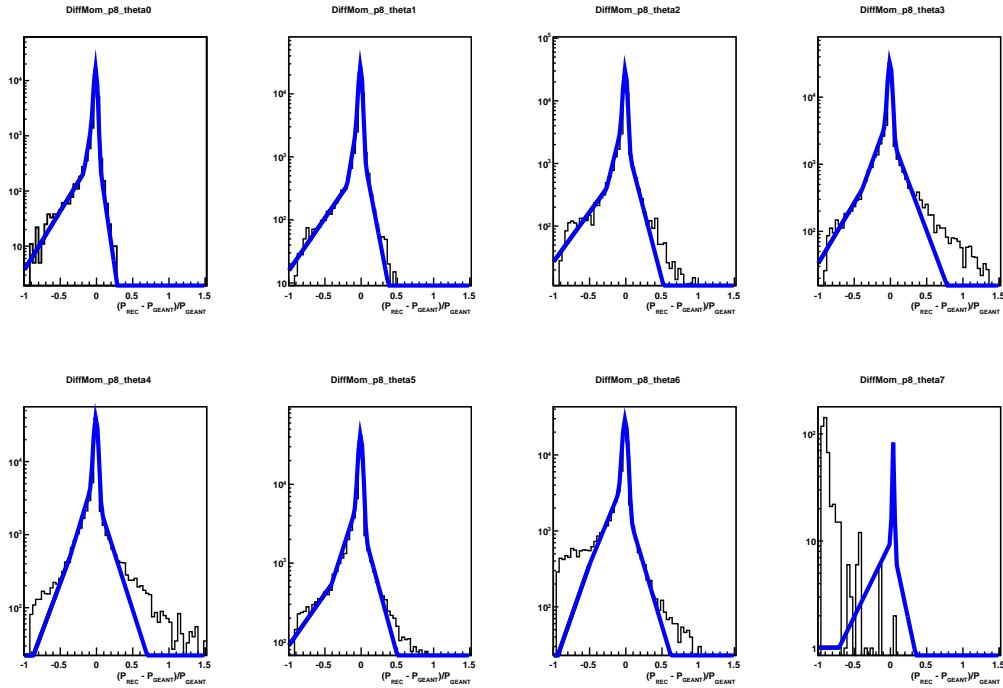
In order to be able to finally compare the data to phenomenological models either the data has to be corrected for acceptance or the models have to be filtered by an acceptance filter. Although the first method is much more convenient, since one has to correct the data once and can then compare it to any model, the second option is used by the HADES collaboration for dielectron data since any acceptance correction is model dependent in itself and therefore biased. Note that several sources contribute to the dielectron cocktail, some of them only poorly known, which would increase the uncertainties due to the model dependence of the acceptance correction.

Therefore the **HADES Filter for Theoreticians (HAFT)** [HAF] provides an acceptance filter for electron and positron tracks as well as for dielectron pairs. It includes also a realistic detector response concerning the energy loss and the momentum smearing. Further severe effects which have to be considered are multiple scattering and the treatment of Bremsstrahlung.

With the p+p and p+Nb experiments high statistic data in the region around the  $\omega$  pole mass are collected for the first time. Therefore the included response function has to be able to describe tails of the  $\omega$  contribution in the invariant mass spectra properly.

In order to achieve this goal, the difference between the initial momentum value at the target and the reconstructed value in the detector <sup>2</sup>, is adapted with a sum of three exponential and one gaussian function. To assure smooth transitions the first two exponential functions are connected to the gaussian two  $\sigma$  left and right of the mean value. The third exp. function is used to describe the additional tail on the left side of the contribution and is connected to the other exp. function at 0.1 of its initial value. In this way besides the smearing due to track reconstruction also the energy loss of the tracks inside the detector is taken into account, resulting in lower reconstructed momenta on average.

The adaption is done in several regions of the momentum and the polar angle to cover up the momentum and polar angle dependence of the track reconstruction as well as the different energy loss in the different polar angle regions, due to different path lengths in the active detector material. Fig. 3.26 illustrates the spread between the initial momentum and the reconstructed one for momenta from 800-900  $MeV/c^2$  and the eight polar angle regions <sup>3</sup>. The adapted functions are implemented via a parametrization into the HAFT code [Rom11] in order to save computing time.



(a)

Figure 3.26: Spread between the initial momentum at the target position and the reconstructed value for electrons, normalized to the initial momentum according to a HGEANT simulation. Besides the momentum resolution of the spectrometer also the energy loss is included in the distribution resulting in on average lower reconstructed momenta. The distribution is adapted with a sum of three exponential and one gaussian function (blue). Note the logarithmic scale.

<sup>2</sup>Note that the simulated detector response can only be accurate to a certain amount of precision!

<sup>3</sup>Note that the last polar angle region is nearly completely out of acceptance.

## Chapter 4

# Discussion of the p+ $\text{Nb}$ data compared to the p+p reference

In the following the reconstruction efficiency corrected p+ $\text{Nb}$  data are investigated in order to search for the predicted modifications of the light vector mesons  $\rho$  and  $\omega$ , like broadening or a shift of the mass due to the surrounding medium as discussed in chapter 1. In order to do so, one first needs to establish a valid reference spectrum on top of which one can extract additional effects.

The elementary p+p data taken at the same beam energy give a natural reference, if a proper scaling to p+ $\text{Nb}$  collisions can be obtained. Making use of the extracted cross section of the long-lived sources, like the neutral pions and a geometrical overlap model, a scaling factor is obtained and additional effects in the p $\text{Nb}$  data on top of this reference can be discussed.

### 4.1 Establishing a reference cocktail for p+ $\text{Nb}$

#### 4.1.1 The p+p dielectron spectrum

One distinguishes between two subcategories of hadron decays in the dielectron spectrum, two-body and multi-body (Dalitz) decays. In the low invariant mass region below  $0.15 \text{ GeV}/c^2$  of the spectrum mainly Dalitz decays of neutral pions contribute. The intermediate part of the spectrum from  $0.15 \text{ GeV}/c^2$  to  $0.47 \text{ GeV}/c^2$  is dominated by Dalitz decays of  $\eta$  mesons and weaker contributions of baryonic resonances. In the region between  $0.47 \text{ GeV}/c^2$  and  $0.7 \text{ GeV}/c^2$  direct  $\rho$  decays and Dalitz decays of baryonic resonances contribute, while the region above  $0.7 \text{ GeV}/c^2$ , is dominated by direct decays of vector mesons.

Several phenomenological microscopic models, like HSD [HSD], UrQMD [UrQ04] and GiBUU [eab], model the evolution and the particle emission of such collisions. It should be stated here that, after some parameter optimizations, all of the models describe the overall yield and shape in the spectrum with fair agreement, however the relative contributions of the various sources do vary. Deviations in the overall yield and shape of the spectrum are only present in the invariant mass region above  $0.5 \text{ GeV}/c^2$ , which is the crucial part of the spectrum in terms of medium modifications.

In the following, the focus will be put on two specific models: a tuned version of the high energy event generator PYTHIA [pyt] as well as a "resonance decay" version of the GiBUU which delivers the most satisfactory description of the data so far. The dielectron cocktail will be discussed differentiating between long-lived and short-lived sources. Although PYTHIA is usually used to describe particle production in the high energy regime ( $\sqrt{s} \approx 200 \text{ GeV}$ ) and generates particles according to

a quark and antiquark string fragmentation model (Lund), it was shown in [JWM11] that by a parameter adjustment a satisfactory description of p+p reactions at 3.5 GeV can be achieved. The decay of hadrons contributing to the dielectron spectrum is modeled by the PLUTO event generator [PLU04].

#### 4.1.2 Long-lived sources

The cross sections of the long-lived sources, the Dalitz decays of  $\pi^0$  and  $\eta$  mesons as well as the direct decay of  $\omega$  mesons, are estimated by fitting the simulated contributions to the measured yield in the corresponding regions, where the respective sources dominate the dielectron spectrum. The contribution from the  $\omega$  Dalitz decay is fixed by its known branching ratio and the defined cross section of its direct decay channel. The decay of the pseudoscalar ( $\pi^0, \eta$ ) and vector meson Dalitz decays are adopted according to [Lan85] including electromagnetic transition form factors. The transition form factors used for the direct vector mesons decays are based on the vector meson dominance model (VMD) [GQLS96].

#### 4.1.3 Short-lived sources

The contributions of short-lived sources like the  $\rho$  and  $\Delta$  are much more difficult to constrain. The dielectron yield originating from  $\Delta$  Dalitz decays can only be roughly constrained by the invariant mass distribution at the shoulder of the  $\eta$  contribution around  $0.5 \text{ GeV}/c^2$  and on the right side of the peak structure of the direct  $\omega$  decay at masses larger than  $0.85 \text{ GeV}/c^2$ . The dielectron yield of the direct decays of the  $\rho$  meson can be constrained on both sides of the  $\omega$  peak, which complicates the situation since also  $\Delta$  Dalitz decays contribute in both regions. Additional constraints, especially in case of the  $\Delta$  can be gained from the momentum distributions, which differ strongly for the different sources.

Following this discussion, it is clear that for fixing at the same time several overlapping broad contributions at different points in the spectrum a solid knowledge of their shape is of eminent importance. Unfortunately the knowledge on the pattern of dielectron emission from broad resonances is very limited and has to be guessed to some extent. It depends on several parameters, most of them can only be approximately constrained by data or theory up to now:

- **Mass dependent width and branching ratio:** The masses of the  $\Delta$  and  $\rho$  are generated according to relativistic Breit-Wigner distributions including a mass dependent total width  $\Gamma_{tot}(m)$ . In case of the  $\Delta$  the mass dependence is calculated by its dominant decay channel to  $\pi+N$  according to:

$$\Gamma_{tot}(m) \simeq \Gamma_{\Delta \rightarrow \pi N} = \Gamma_{pole} \frac{m_{pole}}{m} \left( \frac{q}{q_{pole}} \right)^{2L+1} \cdot F_{cutoff}, \quad (4.1)$$

with  $\Gamma_{pole}$ ,  $m_{pole}$  and  $q_{pole}$  representing the  $\Delta$  width, mass and the pion momentum in the  $\Delta$  rest frame at the resonance pole, while  $L=1$  is the quantum number of the orbital momentum and  $F_{cutoff}$ , the cut off parameter which will be discussed in the next item. The momentum term reflects the decrease of the decay probability towards small momenta, due to the fact that the pion must be generated at increasingly large distance from the nucleon in order to conserve the angular momentum.

The mass dependent branching ratio  $\frac{\Gamma_{\Delta \rightarrow \pi N}}{m}$ <sup>1</sup> is taken according to [KF02] and was found to deliver more favorable results compared to other parametrization [Bea08].

<sup>1</sup>Note that the branching ratio values listed by the PDG are always validated around the pole mass and are expected to

- **Cut off function:** For the mass states far above the resonance pole it is quite natural to assume that the probability to populate these states decreases asymptotically to 0. In literature several cut off parameterizations can be found. All of them are in good agreement in the region around the pole which is well constrained by photo absorption and  $\pi^+$ +p elastic scattering experiments. The asymptotic behavior however can only be guessed.<sup>2</sup> As cut-off the parametrization from [MS92]

$$F_{cutoff} \propto \frac{1}{q^2 + \delta^2}, \quad (4.2)$$

with  $\delta^2 = 0.04 \text{ GeV}^2$  is used. The asymptotic resonance width is then proportional to the pion momentum  $q$ , which seems to be reasonable since it reflects phase space.

- **Electromagnetic transition form factors:** Depending on the 4-momentum transfer  $q^2 = (\Delta E)^2 - (\Delta p)^2$  one defines the virtual photon to be space like or time like. If  $q^2 > 0$  the photon mainly transfers energy and is called time like, while for  $q^2 < 0$  mainly momentum is transferred and the photon is called space like. While in the space like region the electromagnetic transition form factors of the N- $\Delta$  transition are well constrained by data, no data and no solid theoretical parametrization exists for the time-like region. Therefore the magnetic form factor is approximated by its value at the photon point<sup>3</sup>, while the electric and Coulomb form factor terms are much smaller and neglected, like it is proposed in [KF02]. The transition form factors used for the direct vector meson decays, in particular the  $\rho$ , are based on the vector meson dominance model (VMD) [GQLS96] which on the other hand is based on the pion transition form factors.

The resulting dielectron cocktail compared to the data is shown in Fig. 4.1. The cocktail describes the spectrum with fair agreement apart from the region between the  $\eta$  shoulder and the direct  $\omega$  decay peak structure from  $\approx 0.5 \text{ GeV}/c^2$  to  $\approx 0.7 \text{ GeV}/c^2$ . The strength of the  $\Delta$  contribution is mainly constrained by the transverse momentum  $P_t$  of the dielectron [eaHC11c].

For more details on the procedure and the modeling of the particle decays see [eaHC11c] and [ea10b].

A better description may be achieved by changing either the shape of the  $\rho$  or the  $\Delta$  contribution e.g. by coupling the  $\rho$  to the  $\Delta$  resonance using a different parametrization of the transition form factor or by introducing higher lying resonance which couple via the  $\rho$  (VMD) to the virtual photon (see the diagram in Fig. 4.2)<sup>4</sup>. Indeed the best description of the data ( $M_{ee}$ , as well as  $P_t$  and  $Y_{ee}$ ) is achieved by using a version of the GiBUU which includes this coupling of the  $\rho$  to higher lying resonances [eaa]. The resulting spectrum shows a good agreement with the measured data due to a strong modification of the shape of the  $\rho$  meson. This modification can be understood first of all by the underlying reaction which changed from

$$NN \rightarrow NN\rho \quad (4.3)$$

to

$$NN \rightarrow NR \rightarrow NN\rho. \quad (4.4)$$

change as a function of the mass. The effect can easily be illustrated by moving away from the pole mass below the threshold of the dominant decay channel at the pole, where the branching ratio will clearly change strongly. Moreover, the branching ratio, the widths and the lifetime of a particle are entangled on the quantum level, which might cause unpredictable effects.

<sup>2</sup>The question becomes even philosophic if one moves so far away from the pole that the actual mass value already agrees with the pole mass of the next higher lying resonance with equal quantum numbers, e.g.  $\Delta(1232)$  and  $\Delta(1600)$ .

<sup>3</sup>real photon with  $m=0$

<sup>4</sup>It should be stated here that this graph is exactly the cut second part of the diagram of two pion annihilation used to explain the excess at low mass dilepton excess observed in HIC at higher energies, as discussed in chapter 1.

Figure 4.1: Comparison of p+p data to a calculated PYTHIA/PLUTO dielectron cocktail. The different sources are displayed on the upper right side of the figure. While the description is in good agreement with the data in most parts of the spectrum, the strong deviations in the invariant mass region from 0.5 to 0.7  $\text{GeV}/c^2$  are visible.

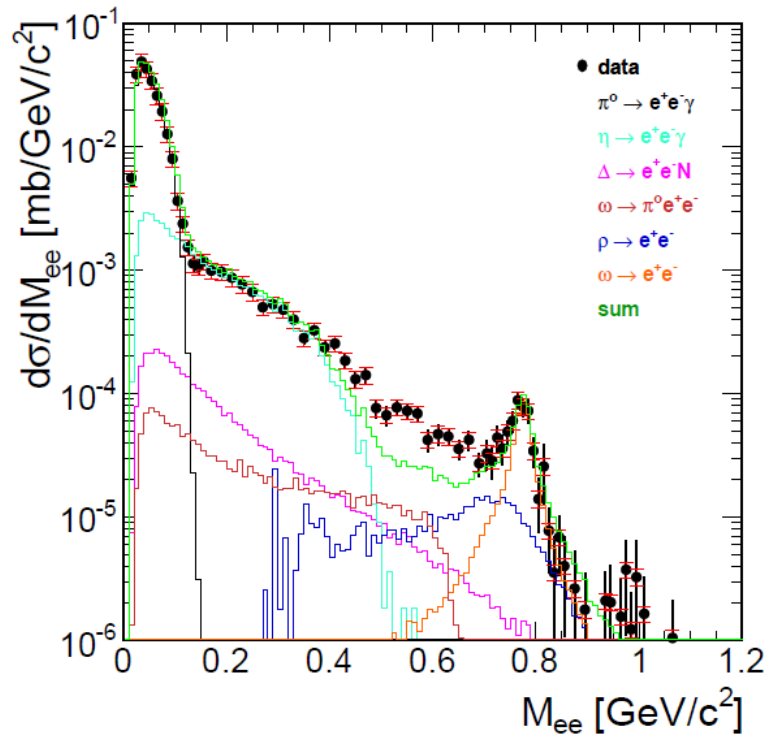
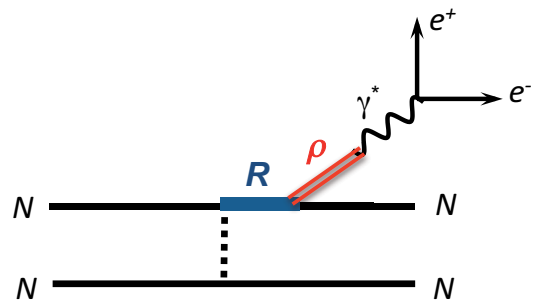


Figure 4.2: Diagram for a nucleon nucleon interaction and a subsequent resonance decay. The resonance decays via an intermediate  $\rho$  meson to a virtual photon, which irradiates an  $e^+e^-$  pair.



In the latter one the available phase space for the  $\rho$  meson is smaller, thus the low mass part of the  $\rho$  is populated more strongly. Secondly, this effect is enhanced by contributing resonances like the  $D_{13}(1520)$  with pole masses below the  $N+\rho$  threshold which favorably populate the low mass part of the  $\rho$ . The resulting dielectron yield is compared to the data in Fig. 4.3.

However the question arises whether it makes then sense anymore to distinguish between the  $\rho$  and baryonic resonance contributions as they are strongly coupled anyhow.

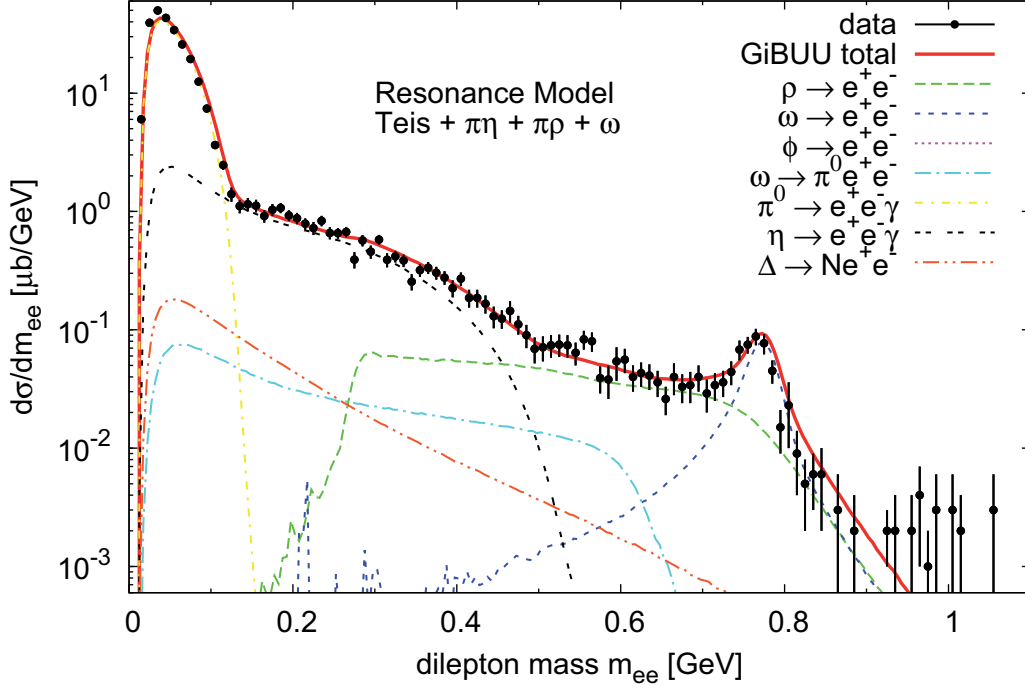


Figure 4.3: Comparison of p+p invariant mass to GiBUU (including resonances) [eaa]. The resulting spectrum shows a good agreement with the measured data due to a strong modification of the  $\rho$  meson shape, compared to the PHYTHIA/PLUTO calculation shown in Fig. 4.1, see text for details.

#### 4.1.4 Bremstrahlung

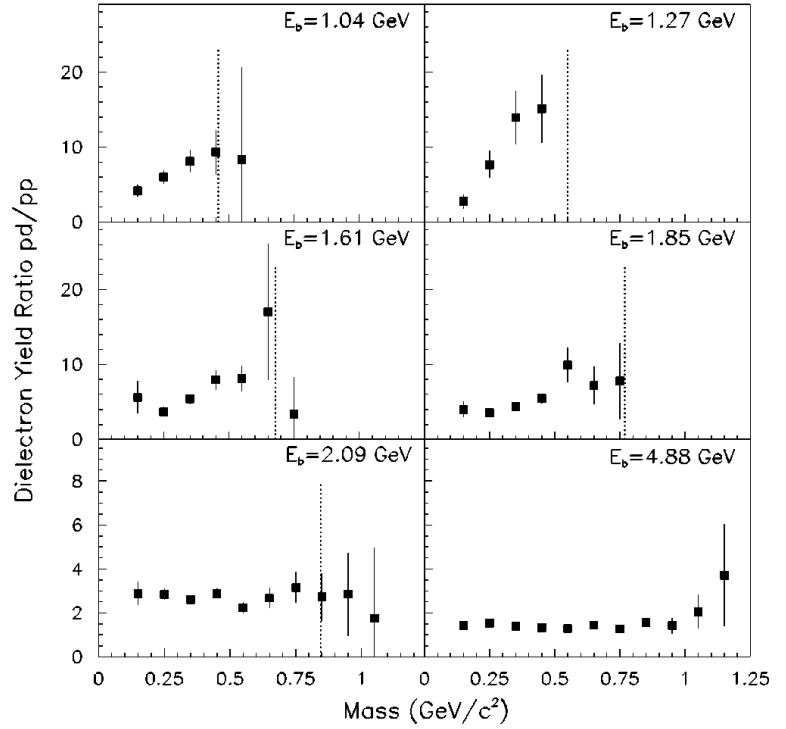
A big issue in heavy-ion and cold nuclear matter experiments are isospin effects resulting in different radiation of Bremstrahlung in p+p and n+p collisions. It is experimentally challenging to prepare elementary reactions with neutral particles and therefore data are often compared only to p+p data, which might then lead to misinterpretations. For example, in [eaHC10c] it could be shown that the longstanding excess in dielectron emission from C+C collisions at 1A GeV, above a theoretical

hadronic cocktail could be explained by a simple superposition of p+p and n+p data at a comparable energy.

Besides the HADES data on n+p at 1.25 GeV the DLS collaboration measured systematically dielectron emission in p+p and p+d for various energies [eaDC98]. While at kinetic beam energies from 1-1.9 GeV the ratio (p+d)/(p+p) shows a strong enhancement above the trivial factor of two due to isospin coefficients, rising with increasing invariant masses, at a beam energy of 2.09 GeV the ratio shows a flat behavior approaching the expected factor at 4.88 GeV where the ratio saturates, compare Fig. 4.4.

From the DLS systematics, it is save to conclude that at 3.5 GeV any difference between p+p and p+Nb due to Bremsstrahlung can be neglected for first chance collisions at least. Note that, since the secondary collisions proceed at on average lower energies  $\sqrt{s}$ , the effective beam energy for these collisions decreases and radiation of Bremsstrahlung can still be important for these collisions.

Figure 4.4: Energy dependence of dielectron emission from p+p and p+d collisions for beam energies between 1 and 5 GeV obtained by the DLS collaboration [eaDC98]. Displayed is the ratio (p+d)/(p+p) as a function of the invariant mass. While at low energies strong deviations from the trivial factor two obtained from the isospin coefficients are observed, at higher energies the values saturate around the factor two.



#### 4.1.5 Reaction kinematics and particle threshold

It is worth to recall the reaction kinematics of a free nucleon nucleon collision and what distortion one expects in proton induced reactions on heavy nuclei, before comparing the p+Nb data to the reference. An important kinematical parameter is the particle momentum in the laboratory system  $P$ , from which one can derive the transverse momentum  $P_t$  orthogonal to the beam direction and the rapidity  $Y$ . The latter one is defined as:

$$Y_{Beam} = \frac{1}{2} \ln \left( \frac{E + (p_{\parallel} \cdot c)}{E - (p_{\parallel} \cdot c)} \right), \quad (4.5)$$

being an indicator of the longitudinal momentum parallel to the beam direction. In symmetric collision systems, mid-rapidity ( $Y_{cm}$ ), around which particles are emitted symmetrically in the center of mass

frame of the collision, is defined as

$$\frac{Y_{Beam}}{2} = Y_{cm} = 1.1, \quad (4.6)$$

for  $E_{Beam} = 3.5$  GeV. In p+A collisions one expects that longitudinal energy will be stronger transformed into transversal modes compared to a p+p collision and hence lower average values in rapidity and slightly higher values in transverse momentum. Moreover a fraction of the energy might be additionally distributed in secondary particle production inside the nucleus. The available energy in the center of mass system  $\sqrt{s}$  is given as

$$\sqrt{s} = \sqrt{(m_P \cdot c^2)^2 + (m_T \cdot c^2)^2 + (E_{proj} + (m_P \cdot c^2)) \cdot 2 \cdot m_P \cdot c^2} = 3.18 \text{ GeV}, \quad (4.7)$$

with  $E_{proj}$  being the energy of the projectile, while  $m_P$  and  $m_T$  being the projectile and target masses, which are equal in the p+p collision system. The production threshold for a given final state is given as the sum over all particle masses in the final state

$$\sqrt{s_{th}} = \sum (m_i \cdot c^2). \quad (4.8)$$

The elementary production thresholds for various mesons and baryonic resonances, with respect to the available energy in the center-of-mass system are listed in Tab. 4.1. Note that for short-lived particle states like the  $\Delta$  or the  $\rho$ , no sharp threshold is defined, the value given corresponds to the pole mass. Furthermore, the production of the  $\phi$  meson is additionally suppressed by the OZI rule, as will be discussed in chapter 6, due to its strange quark content. For the p+Nb system the thresholds are washed out due to the Fermi motion of the nucleons inside the nucleus. On top of this, secondary reactions inside the nucleus proceed on average at lower available energy  $\sqrt{s}$ , contributing to the final yield.

## 4.2 The p+Nb data

The efficiency corrected and normalized invariant mass distributions of  $e^+e^-$  pairs are shown in Fig. 4.5 for both collision systems. The colored horizontal bars represent the systematic uncertainties, which result from the quadratic sum of errors estimated from the different particle identification (PID) methods (10%), from consistency checks of the efficiency correction (10%) including the uncertainty due to CB subtraction as well as the the uncertainty from the normalization (15%) as discussed in section 3.8. The total systematic error amounts to 21% in case of the p+Nb data while for the p+p data the systematic uncertainty reach 20%.

### 4.2.1 Scaling of the p+p data

A proper scaling of the spectra in order to be able to compare the line shape and strength can be obtained by normalizing both spectra to the number of neutral pions as described in chapter 3 or to the number of participants estimated with the help of a geometrical overlap model and the known cross sections (nuclear modification factor  $R_{pA}$ ). The latter one is defined as

$$R_{pA} = \frac{d\sigma/dp^{pNb}}{d\sigma/dp^{pp}} \cdot \frac{A_{part}^{pp}}{A_{part}^{pNb}} \cdot \frac{\sigma_{reaction}^{pp}}{\sigma_{reaction}^{pNb}}. \quad (4.9)$$

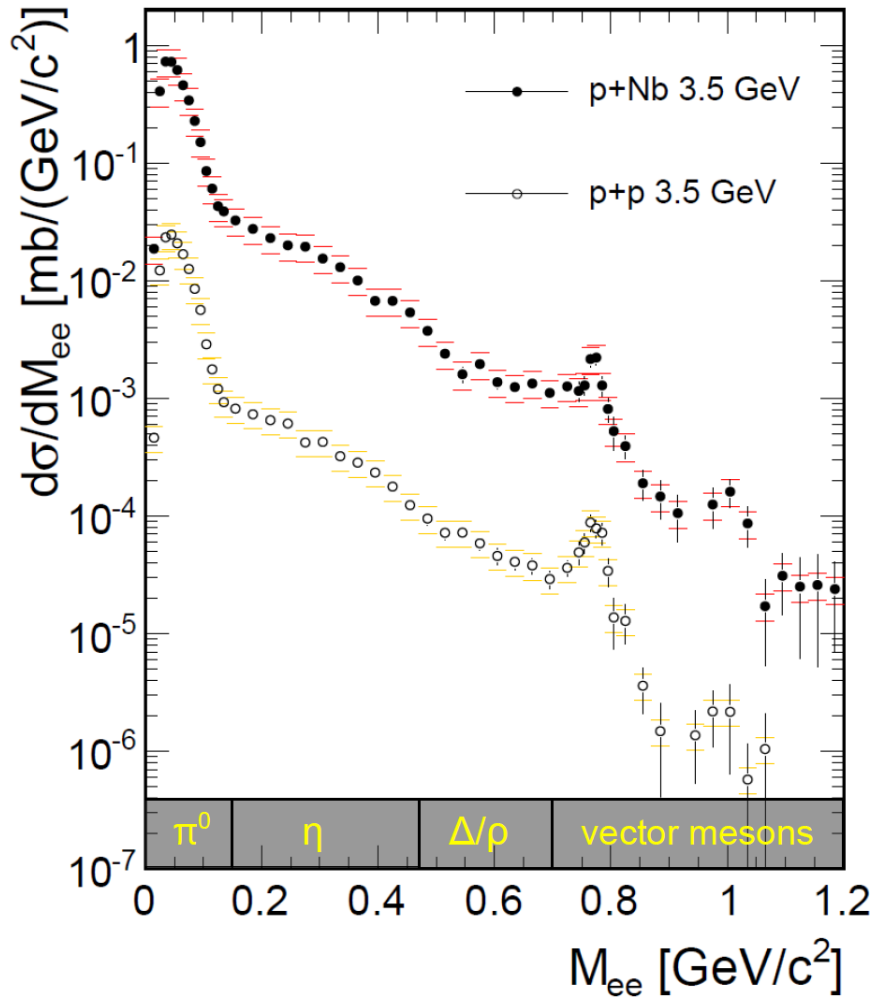


Figure 4.5: Comparison of dielectron cross sections as a function of the invariant mass. The p+Nb data are displayed with full circles and red lines indicating the systematical errors, while the p+p data are displayed with open circles and yellow lines.

particle	$\sqrt{s_{th}}$ [GeV]	$\sqrt{s} - \sqrt{s_{th}}$ [GeV]
$\pi^0$	2.01	1.17
$\eta$	2.42	0.76
$\rho$	2.65	0.53
$\omega$	2.66	0.52
$\phi$	2.90	0.28
$\Delta(1232)$	2.17	1.01
$\Delta(1600)$	2.54	0.64
N(1440)	2.36	0.82
N(1520)	2.45	0.73
N(1600)	2.54	0.64

Table 4.1: The elementary production threshold for various mesons and baryonic resonances with respect to the available energy in the center of mass system ( $\sqrt{s} = 3.2$  GeV at  $E_{Beam} = 3.5$  GeV).

While  $A_{part}^{pp}$  is equal to 2, the number  $A_{part}^{pNb} = 2.8$  is estimated using the overlap model (Glauber) [dar]. The total production cross section for the p+Nb  $\sigma_{reaction}^{pNb} = 848 \pm 127$  mb is derived in chapter 3 and the value for  $\sigma_{reaction}^{pp} = 43.4$  mb is taken from [ABM98].

The resulting normalization factor

$$f_{RpA} = \frac{A_{part}^{pNb}}{A_{part}^{pp}} \cdot \frac{\sigma_{reaction}^{pNb}}{\sigma_{reaction}^{pp}} = 27.3, \quad (4.10)$$

agrees within the errors with the one obtained for the normalization to the neutral pion yield per reaction in  $4\pi$

$$f_{Rpp} = \frac{\sigma_{\pi^0}^{pNb}}{\sigma_{\pi^0}^{pp}} = 31 \pm 6.5, \quad (4.11)$$

showing that the production of pion scales approximately like the number of participants, in agreement with data from other experiments [eaKC07]. The cross section for neutral pion production in p+p collisions  $\sigma_{\pi^0}^{pp} = (18 \pm 2.7)$  mb is taken from [eaHC11c], while the one for p+Nb collisions  $\sigma_{\pi^0}^{pNb} = 560 \pm 84$  is deduced in chapter 3. The spectra normalized to  $\pi^0$  production are displayed in Fig. 4.6. Within errors no significant difference in the spectral shape is visible.

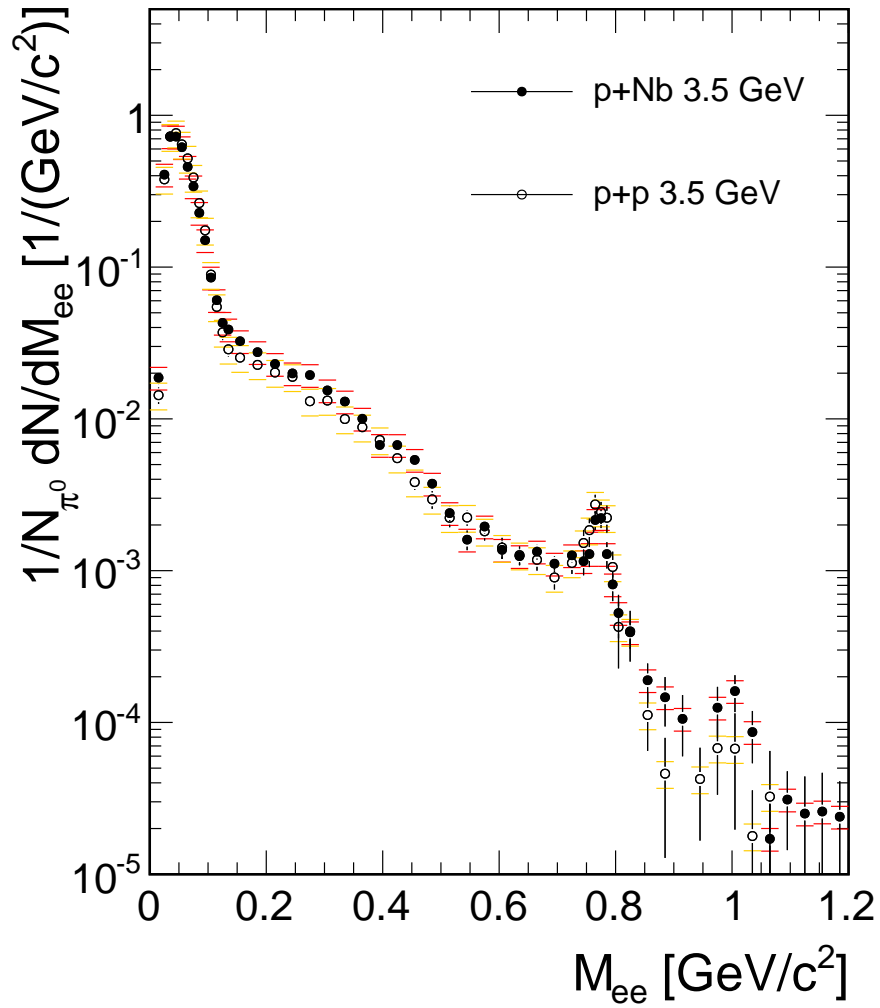


Figure 4.6: Comparison of the dielectron invariant mass spectra normalized to the neutral pion cross section. Again, the  $p+\text{Nb}$  data are displayed with full circles and red horizontal bars indicating the systematical errors, while the  $p+p$  data are displayed with open circles and yellow bars. No significant difference in the shape is visible.

### 4.2.2 Differential analysis

In order to learn more about the different evolution of the two collision types, one may compare kinematical observables like  $P_t$  and  $Y_{ee}$ . In general one expects in p+Nb reactions a stronger transformation of longitudinal energy to transverse energy, which would result in a shift of rapidity  $Y_{ee}$  to smaller values and higher values for the transverse momentum  $P_t$ . The resulting spectra normalized to the neutral pion cross section, are compared in Fig. 4.7 and Fig. 4.8 for the four different invariant mass regions, which are also displayed at the bottom of Fig. 4.5:

- 0-0.15  $GeV/c^2$ , Dalitz decays of neutral pions,
- 0.15-0.47  $GeV/c^2$ , Dalitz decays of the  $\eta$  mesons,
- 0.47-0.7  $GeV/c^2$ , direct  $\rho$  decays and/or Dalitz decays of baryonic resonances,
- larger than 0.7  $GeV/c^2$ , direct decays of the light vector mesons  $\omega$  and  $\phi$ .

Indeed a shift to lower values in case of the p+Nb data in rapidity  $Y_{ee}$  is visible. The shift in transverse momentum  $P_t$  becomes more clearly visible by comparing the mean values of the distributions, which are listed in Tab. 4.2. Concerning the particle production, this shift points to a significant production of particles in secondary collisions, e.g.  $N1N2 \rightarrow N1N2X1 \rightarrow X1N3 \rightarrow N3X2$ .

invariant mass region	$\pi^0$	$\eta$	$\Delta, \rho$	vector meson
$\langle Y \rangle$ (pNb)	0.88	0.92	0.91	0.90
$\langle Y \rangle$ (pp)	0.97	1.04	1.04	1.06
$\langle p_t \rangle$ (pNb) [ $MeV/c^2$ ]	0.29	0.26	0.32	0.4
$\langle p_t \rangle$ (pp) [ $MeV/c^2$ ]	0.28	0.30	0.30	0.34

Table 4.2: Comparison of the mean values of the kinematical observables  $P_t$  and  $Y$ . While the mean values of the rapidity distributions have in all cases lower values in p+Nb compared to p+p, the trend of the mean values of the transverse momentum is to higher values with the exception of the  $\eta$  region.

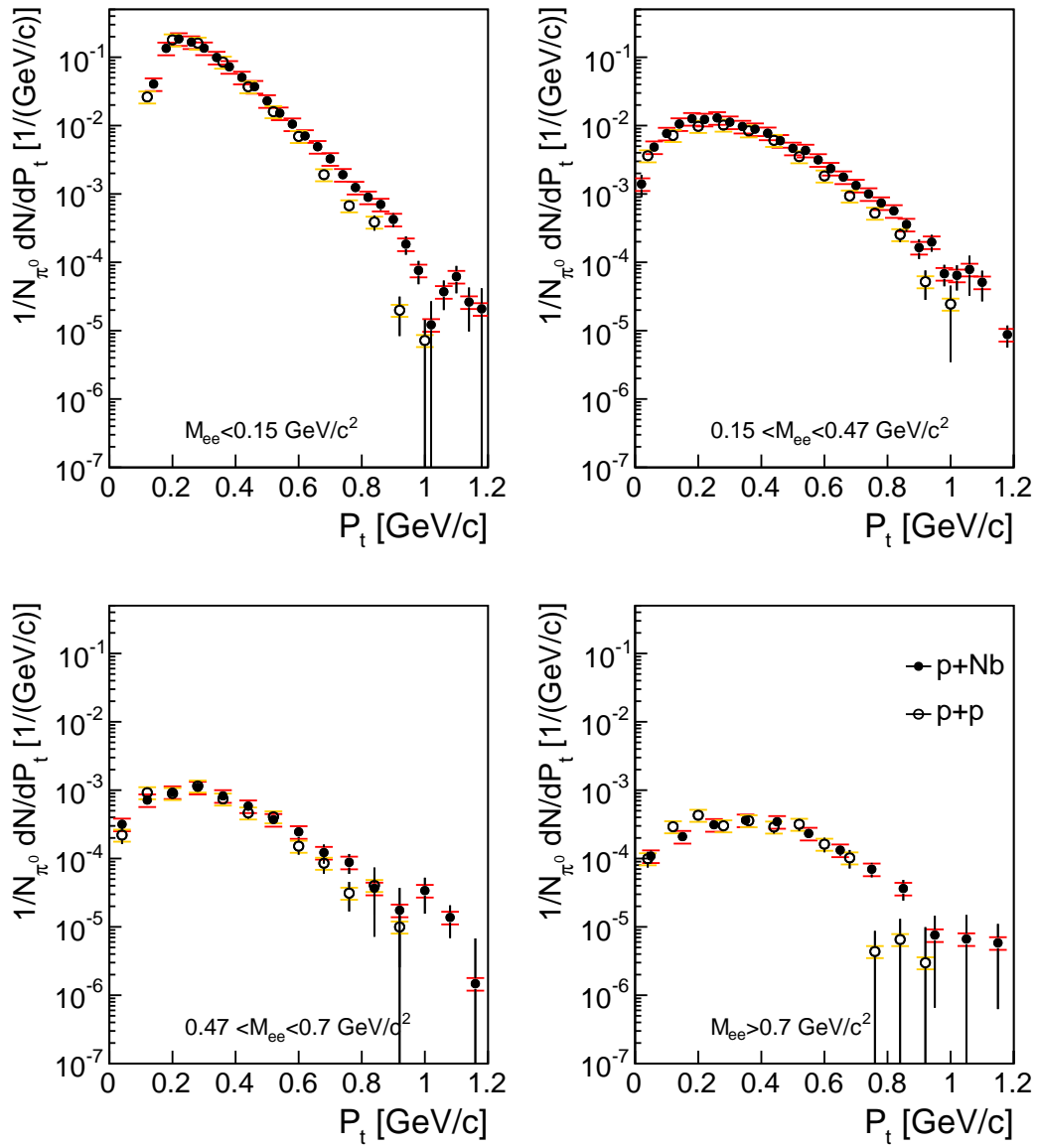


Figure 4.7: Comparison of transverse momentum, the horizontal bars indicate the systematic errors.

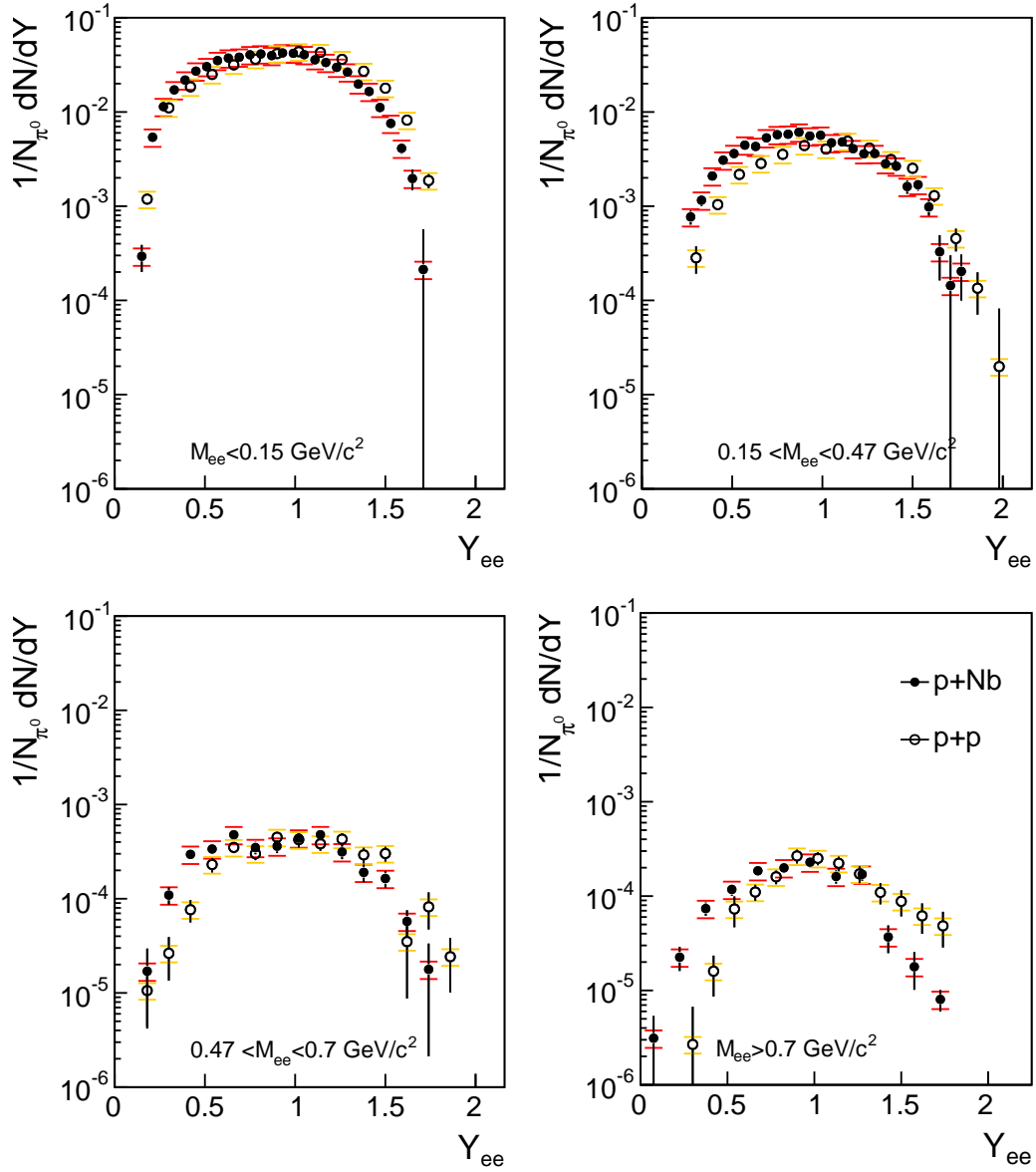


Figure 4.8: Comparison of rapidity, the horizontal bars indicate the systematic errors. A clear shift to smaller values in rapidity in the p+Nb data, compared to the p+p data, is visible in all 4 invariant mass ranges.

### 4.2.3 Momentum dependent comparison of the spectral shape

As discussed in chapter 1, in order to see a modification of the spectral shape, it is necessary for the particle to decay inside the medium. As shown in Fig. 4.9 by an HSD simulation taken from the original experiment proposal [Bea], the fraction of  $\omega$  meson decays inside the medium can be strongly enhanced by applying a selection on the pair momentum  $P_{ee}$ . Note that the fraction of  $\rho$  decays inside the medium is not significantly enhanced due to the short life time of this meson. However the modification of the  $\rho$  spectral function extracted from the  $\rho$  coupling to resonance-hole excitations is expected to be most pronounced at low relative momenta to the surrounding medium, as discussed in chapter 1. Therefore one expects the effects to be more pronounced for both vector mesons at low momenta.

The advantage of the HADES setup, compared to previous dielectron spectroscopy experiments

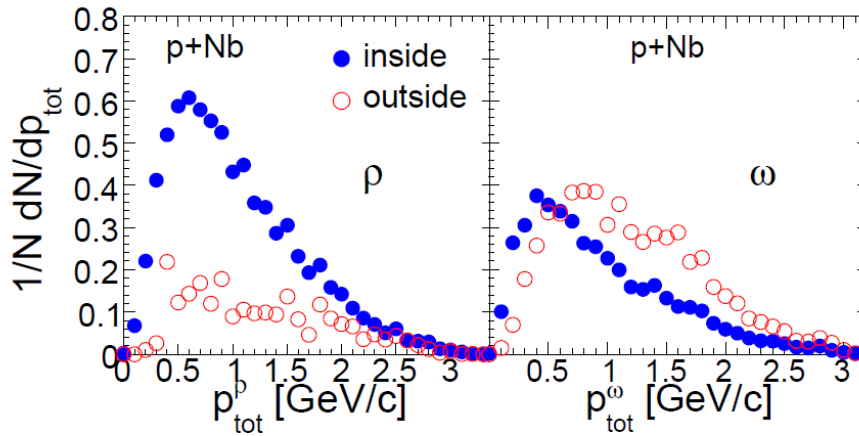


Figure 4.9: Fraction of inside to outside the nuclear medium decays as a function of the particle momentum in the laboratory frame according to an HSD calculation taken from [Bea]. While the majority of  $\rho$  mesons decays inside the medium for all momenta, the high momentum  $\omega$  mesons (above 0.8 GeV/c) decay predominantly outside the nucleus.

on cold nuclear matter like KEK E325 and Clas [eaCC07, eaEC06], is the good coverage for low momenta pairs (compare also the review of data on cold nuclear matter experiments in chapter 1). In particular the collected statistics allow to divide the data sample into two regions smaller and larger than  $P_{ee}=0.8$  GeV/c. The correlation between momentum and invariant mass is displayed in Fig. 4.10. The resulting invariant mass spectra for fast and slow dielectrons compared to the corresponding p+p data are displayed in Fig. 4.11 and Fig. 4.12. For fast pairs the dielectron yield from p+Nb is systematically lower compared to the p+p data pointing to absorption inside the nucleus and subsequently release of the energy in secondary particle production. These secondarily produced particles have on average smaller momenta and therefore contribute to the slow dielectron sample. Concerning the shape of the spectrum within the errors no difference compared to the elementary reference is visible. Especially in the vector meson region where the peak shapes of the  $\omega$  are in fine agreement with each other, compare the linear zoom into the vector meson region in the insert in Fig.4.11.

The situation changes completely for low momentum pairs. Here one observes a strong effect, as can be seen in the right panel of Fig. 4.12. Although the overall strength in the  $\omega$  peak is not reduced, the line shape strength of  $\omega$  mesons is lowered and an additional broad contribution is adding yield in the

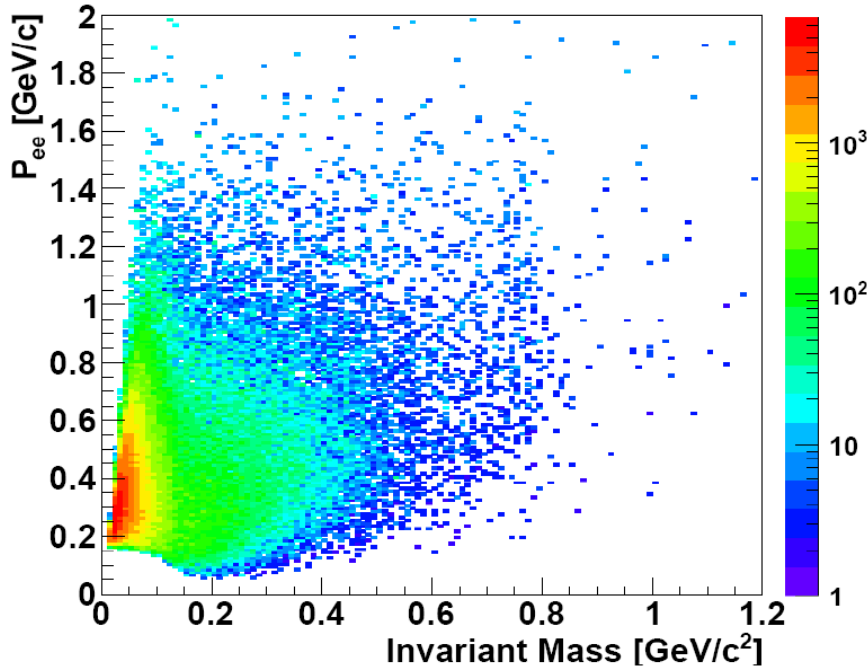


Figure 4.10: Pair momentum in the laboratory for di-electron pairs as a function of their invariant mass. The collected statistics allows to divide the data sample into two regions, below and above momenta  $P_{ee}$  of 0.8 GeV/c, as motivated by the hadronic model calculations discussed in chapter 1.

vector meson region.

Experimentally one can assume that the  $\rho$  contribution shows a smooth behavior under the  $\omega$  peak structure. Furthermore in the CBELSA-TAPS data, reconstructed in the decay channel  $\omega \rightarrow \pi^0\gamma$ , where the  $\rho$  meson is not contributing (branching ratio= $6 \cdot 10^{-4}$ ), no strongly enhanced tails are observed [eaCTC08]. Thus, the enhancement below the  $\omega$  peak can not be interpreted as a broad  $\omega$  contribution<sup>5</sup>.

Moreover apart from the neutral pion region, an enhancement in the p+Nb yield is visible over the whole range of the spectrum, probably due to the above mentioned secondary collisions.

<sup>5</sup>If they have the strong final state interaction of the decay products under control.

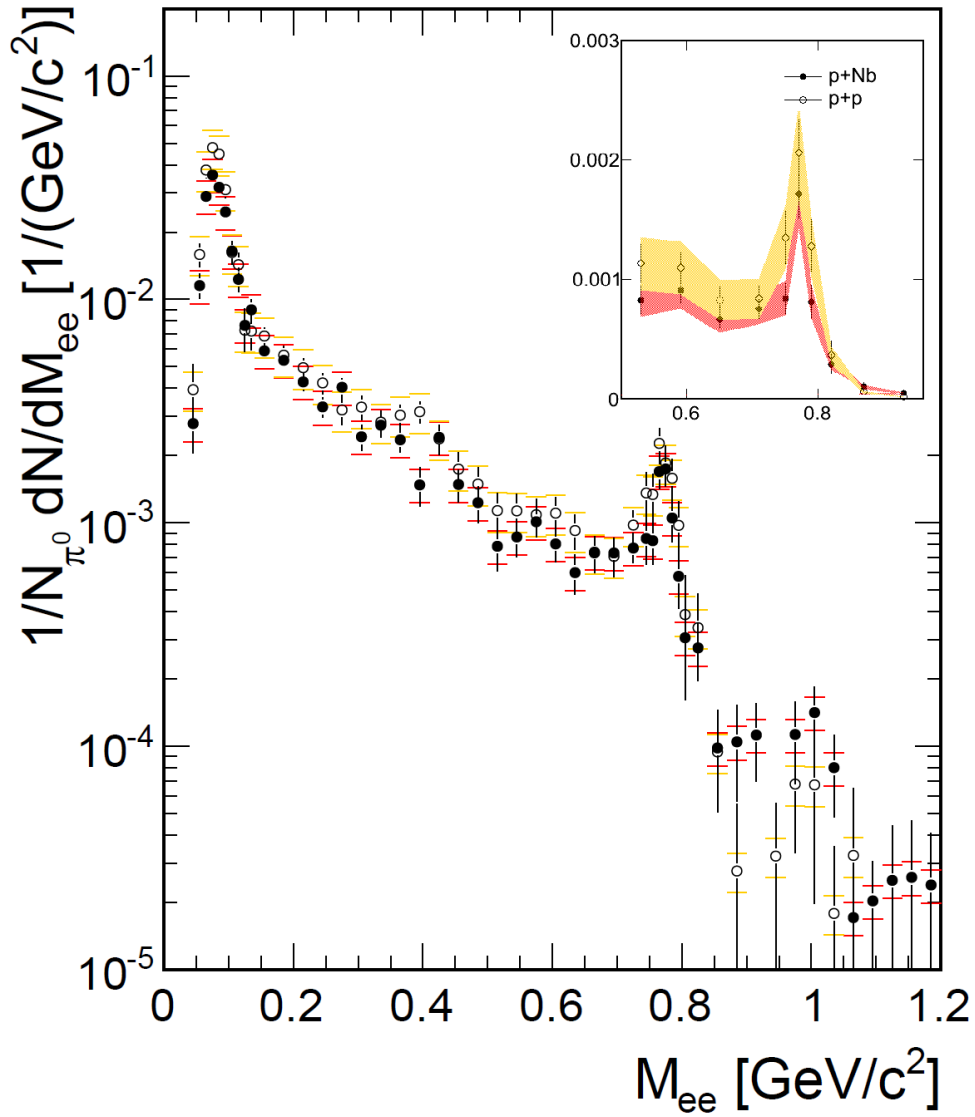


Figure 4.11: Comparison of the dielectron invariant mass spectra normalized to the neutral pion yields for fast pairs ( $P_{ee} > 0.8 \text{ GeV}/c$ ). Within the errors the two spectra agree with each other.

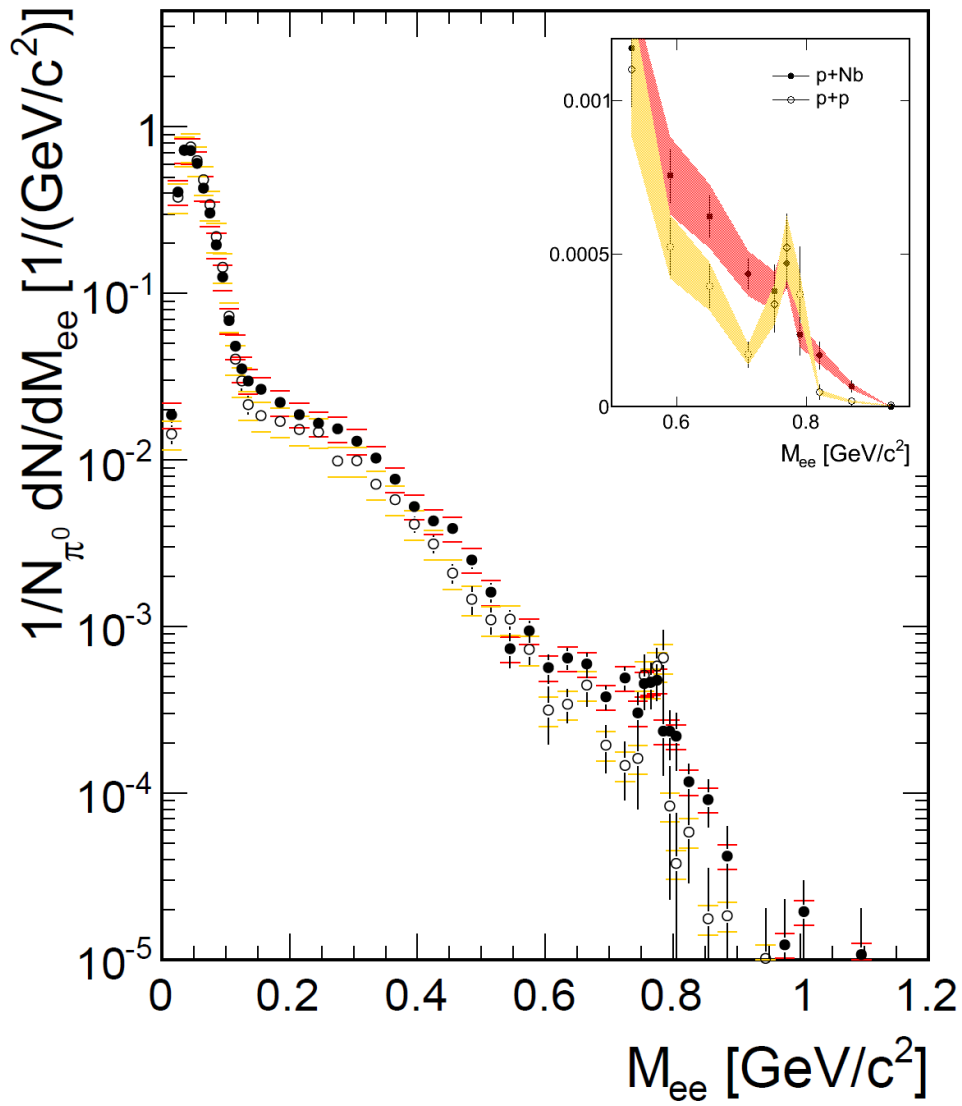


Figure 4.12: Comparison of the dielectron invariant mass spectra normalized to the neutral pion yields for slow pairs ( $P_{ee} < 0.8 \text{ GeV}/c$ ). The shape of the spectra in the vector meson region (linear insert) changes strongly.

#### 4.2.4 Momentum dependence of the nuclear modification

Before going deeper into the interpretation of the different line shapes, it is worth turning again to observables on the reaction kinematics in order to get a general view and better handle on the secondary reactions.

Fig. 4.13 shows the nuclear modification factor  $R_{pA}$ , as a function of the pair momentum in the laboratory  $P_{ee}$  for the four different invariant mass regions. In addition it is depicted for  $\omega$  mesons identified by adapting a Gaussian plus a polynomial function to the peak structure, under the assumption that the background shows a smooth behavior. The identification is done for both the p+p and p+Nb data sets, for the two pair momentum  $P_{ee}$  regions, ranging from 0-0.8 and 0.8-2.0 GeV/c, respectively. Dielectrons resulting from a decay of a strongly broadened  $\omega$  will not be counted by this method.

While for momenta larger than 1.0 GeV/c all values saturate slightly below one, for smaller momenta the value rises for all regions, the higher the mass region the more pronounced is this effect. This can be understood as a consequence of the strong contributions from secondary reactions already indicated by the rapidity distributions discussed in section 4.2.2. The ratio of identified  $\omega$  mesons nicely follows the trend of all the four invariant mass regions for high momenta, see Fig. 4.13. In the low momentum region, however, the ratio seems to be decreasing in contrast to all other contributions, which show a strong rise. This is especially remarkable since the strongest rise is observed for the invariant mass region above  $0.7 \text{ GeV}/c^2$ , which is dominated by direct decays of vector mesons. Consequently the yield of the  $\omega$  meson seems not to be fed by secondary collisions, compared to the other dominating source in this region, the  $\rho$  meson.

This observation is in accordance with a recent finding of the CBELSA-TAPS collaboration [PCN11], which the authors explain with simple phase space restrictions. The latter argument fails however to explain the presented HADES data.

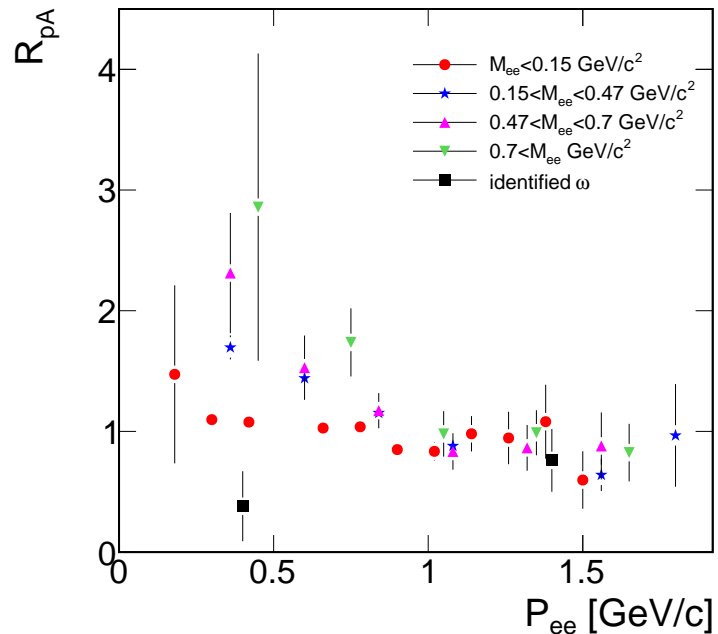


Figure 4.13: Nuclear modification factor  $R_{pA}$  as a function of the pair momentum for different invariant mass regions and the identified  $\omega$ . While the value rises with falling momentum in all regions, the values for the identified  $\omega$  mesons stays flat (see text for details).

### 4.2.5 Modification of ..

Since the  $\omega$  and the  $\rho$  mesons have comparable pole masses and the same quantum numbers apart from their isospin I and their G-parity, they can only be distinguished in dilepton spectroscopy based on probabilistic methods. The situation becomes even more complicated, if these mesons are broadened inside the medium: How to distinguish between a broadened  $\omega$  and a vacuum  $\rho$ ?

If discussing in-medium properties of vector mesons two effects have to be considered: the shape and also the suppression of the line strength. In cold matter the dielectron rate  $N_{e^+e^-}$  originating from a particular direct meson decay is proportional to the lifetime of the meson according to

$$N_{e^+e^-} \propto \Gamma_{e^+e^-} \cdot \tau_{meson} \propto \frac{\Gamma_{e^+e^-}}{\Gamma_{tot}} \quad (4.12)$$

with  $\Gamma_{e^+e^-}$  being the partial decay width to  $e^+e^-$  and  $\Gamma_{tot}$  being the total decay width. The latter one is given inside a medium as the vacuum width  $\Gamma_{vac}$  plus an additional term  $\Gamma_{coll}$  due to collisions inside the medium:

$$\Gamma_{tot} = \Gamma_{vac} + \Gamma_{coll}. \quad (4.13)$$

As a consequence, the partial decay rates are reduced resulting in less observed yield. The medium term  $\Gamma_{coll}$  is related to the imaginary part of the medium self-energy of the meson according to

$$\Gamma_{coll} = -\frac{1}{E_{meson}} \cdot Im\Pi_{med} \approx \rho_d \sigma v^6 \quad (4.14)$$

where  $E_{meson}$  stands for the energy of the meson [SL10]. Applying the so called low density approximation valid for a dilute gas:

$$\lambda = \frac{1}{\rho_d \cdot \sigma}, \quad (4.15)$$

which assumes that the mean free path  $\lambda$  of a particle inside a medium is the inverse of the density  $\rho_d$  times its cross section  $\sigma$ , the right side of Eq. 4.14 is approximately the product of the particle cross section  $\sigma$ , its velocity  $v$  and the density  $\rho_d$  of the surrounding medium.

As a consequence of Eq. 4.13 and Eq. 4.14 the medium term of the width,  $\Gamma_{coll}$ , can be deduced from the nuclear modification factor  $R_{pA}$  for the  $\omega$  meson<sup>7</sup>.

Following this approach, a comparison of  $\omega$  production cross sections on different nuclei, in photo production experiments by the CBELSA-TAPS, with several phenomenological models indicate a broadening of the  $\omega$  meson inside the medium by a factor of  $\approx 16$  [eaCTC08]. The disadvantage of these indirect measurements is clearly its model dependence, e. g. the recent analysis of [RAN11] led to a significantly different width of the  $\omega$  meson inside the medium as extracted in [eaCTC08].

As the  $R_{pA}$  of the  $\omega$  meson stays systematically below one, which is in strong contrast to the rising ratio in the vector meson region (green triangles in Fig. 4.13) it indicates an overall absorption of  $\omega$  mesons and seems to support the above scenario of a strong broadening inside the medium, as any yield due to secondary collisions will not contribute sizeably and/or not being identified as  $\omega$ . Furthermore in the GiBUU model a comparable in medium  $\omega$  width parametrization, as used to reproduce the measurements of the CBELSA-TAPS, must be included in order to reproduce the strength of the  $\omega$  contribution in the HADES data [Jan11].

A severe difference, which helps to understand the diverging trends for the  $\omega$  and the  $\rho$ -like contributions is given by their widths. The  $\rho$  is already broad in vacuum, hence any additional broadening

<sup>6</sup>For better readability  $\hbar$  and  $c$  have been set to 1.

<sup>7</sup>In the given reference it is not referred to the nuclear modification factor but rather to the so called transparency ratio  $T_A$ .

inside the medium is not as strongly reflected in a suppression of the partial decay branch, resulting in less suppression of the observed yield. Furthermore, the  $\rho$  is known to couple strongly to baryonic resonances, while for the  $\omega$  no strong coupling has been observed [SL10, PDG]. This would be of special importance if secondary reactions proceed dominantly via intermediate baryonic resonances and then consequently, feed only those contributions to which they are coupling.

However, again the question arises to what extent it makes sense to distinguish between strongly coupled short lived particle states, like the  $\rho$  and baryonic resonances inside a medium. In this way a much more natural explanation for our observations would be a suppression of line strength of particle states in favour of additional bulk radiation inside the medium.

### The additional $\rho$ -like contribution

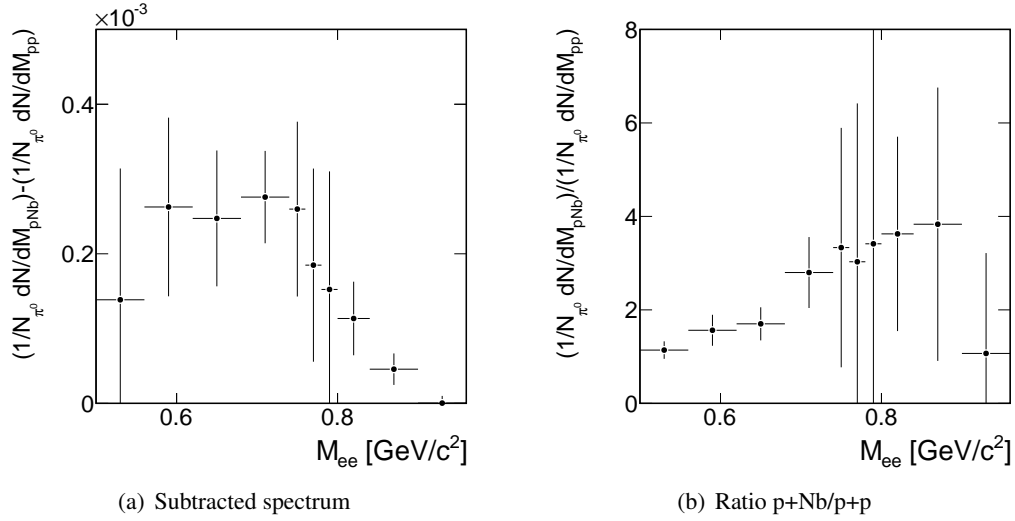


Figure 4.14: Right side: Additional yield in the vector meson region in p+Nb compared to p+p normalized to the neutral pion yield after subtracting the  $\omega$  contribution in both spectra for slow pairs (see text for details) ( $P_{ee} < 0.8 GeV/c$ ). Left side: Corresponding ratio p+Nb/p+p.

As can be seen from the shape of the dielectron yield in the invariant mass spectra for slow pairs and from the nuclear modification factor  $R_p A$  the yield of  $\rho$ -like contributions is strongly enhanced for low momenta pairs.

After subtracting the  $\omega$  in both the p+p and p+Nb data set, one is left with only  $\rho$ -like contributions in the invariant mass region from 0.55 to 0.9  $GeV/c^2$ . In the next step one can subtract the remaining p+p contribution from the p+Nb data. The resulting spectrum hence corresponds to the additional yield from p+Nb and is shown on the left side of Fig. 4.14 in the vector meson region for slow pairs. The corresponding ratio of p+Nb/p+p is shown on the right side of Fig. 4.14.

The theoretical treatment of the  $\rho$  in hadronic models is more straightforward compared to the  $\omega$  due to its coupling to resonances. Experimentally this coupling complicates the identification of the  $\rho$  meson, since its Breit-Wigner shape is distorted, compare e.g. its shape in the GiBUU calculation for p+p shown in Fig. 4.3 with the direct  $\rho$  decay in Fig. 4.1. As a consequence of this deformation the mean value of the  $\rho$  contribution moves to lower values. In addition this effect might also result in an measured effective broadening of the structure. These effects must be under control before addressing

an additional broadening and/or mass shift due to the surrounding medium and hence a solid theoretical treatment is needed.

#### 4.2.6 Comparison to other experiments

Making use of the measured total cross sections, one can nicely compare the obtained systematics to the initially discussed data from other experiments to gain a general view.

Note that photon induced reactions illuminate the nucleus equally, while proton induced reactions proceed on or near the surface. In terms of medium modifications the latter one is a clear advantage, since the produced particles dives deeper into the medium and consequently has higher probabilities to decay inside the nucleus. Therefore the comparison to photon induced reactions has to be done with some care.

The nuclear suppression is reflected in the scaling factor  $\alpha$  with the nuclear mass number  $A$ :  $\sigma_A \sim \sigma_0 \cdot A^\alpha$ . From the nuclear modification factor of the  $\omega$  a  $\alpha$  value of  $0.58 \pm 0.10$  could be extracted over the whole momentum region. This result is in agreement with the CBELSA-TAPS result [eaCTC08], where in  $\gamma$  induced reactions, but a different decay channel  $\alpha$  values between 0.54-0.74 depending on the meson momentum are found. Moreover this value is in agreement with proton induced reactions at higher beam energies from the KEK-PS E325 experiment [ea06], where  $\alpha = 0.710 \pm 0.021(stat) \pm 0.037(syst)$  is extracted measured as HADES in the  $e^+e^-$  decay channel but has been restricted to higher average momenta. The same holds true for the CLAS experiment which reported on a stronger absorption compared to the CBELSA-TAPS result [eaCC10b], which they attribute to  $\omega$ - $\rho$  interference effects. The latter one should however be also present in the HADES data.

The modification of the line shape in the vector meson region for slow pairs, represents the first measurement of its kind as the CLAS and KEK-E325 collaborations have no acceptance in this momentum region. In context of the in chapter 1 restricted modifications to momenta smaller 0.8 GeV/c as deduced from hadronic models [MPM04], it is not surprising that the CLAS result [eaCC07] is consistent with trivial many body effects,. The reported shift of the  $\rho$  pole mass by the KEK-E325 experiment [eaEC06], however is puzzling in this context and might be due to underestimated systematics.

### 4.3 Summary and conclusion

The best theoretical description of the p+p data is achieved in the GiBUU model by introducing a coupling of the  $\rho$  to higher lying nucleon resonances like  $N^*(1520)$ .

Comparing the line shape of the p+p with the p+Nb invariant mass spectra normalized to the number of neutral pions no significant difference is visible. The situation changes significantly if one applies a selection on the pair momenta. While for pair momenta larger than 0.8 GeV/c the spectra still agree, for smaller momenta a strong modification in the vector meson region, where modification due to the nuclear medium are predicted by hadronic models, is observed.

The nuclear modification factor  $R_{pA}$  shows a rise for all four distinguished regions of the invariant mass for small momenta, indicating strong contribution from secondary reactions already consistent with the observed shift in rapidity. The value for identified  $\omega$  stays flat over the whole region, pointing to no strong contribution from secondary reactions to the  $\omega$  yield. These strongly diverging trends

for the  $\omega$  and  $\rho$ -like contributions in low momentum region of the nuclear modification ratio might be explained by the different coupling to baryonic resonances and absorption of particle like states inside the medium.

After subtracting the  $\omega$  contribution for slow pairs, the ratio of the two data sets in the vector meson region rises for values of the invariant mass larger than  $\omega/\rho$  pole mass, indicating additional broadening of the  $\rho$  meson, apart from the expected effects due to its coupling to resonances.

Comparing the presented results to other experiments we find good agreement on the nuclear suppression of  $\omega$  mesons. The hints for a flat behavior of these modifications as a function of the momentum, reported recently by the CBELSA-TAPS collaboration can be confirmed.

### 4.3.1 ... and what about chiral symmetry?

The relation between chiral condensates and hadronic spectral functions is not trivial, since the condensates are only related to the integral of the latter one. Therefore the spectral functions are constrained but not determined and one still needs hadronic models for predictions on specific hadron properties. In order to claim a (partial) restoration of chiral symmetry one would need to show that broadening of the spectral shape goes beyond trivial effects due to e.g. production via resonances etc. Comparing the modification of different particles one might be able to get more control on the various effects. In this context the presented data are the first measurement sensitive to predicted changes in the spectral function of vector mesons, as all predictions are calculated for particles at rest or small relative momenta.

## Chapter 5

# Finalizing the Ar+KCl data

### 5.1 Specifications of the Ar+KCl run and status of the data analysis

In September and October 2005 the HADES collaboration took data of the collision system Ar+KCl at 1.76A GeV beam energy. The detector read out was started with a LVL1 multiplicity trigger demanding a multiplicity larger than 16 in the META detector, accomplished by a LVL2 trigger asking for electron candidates in the RICH and META detectors. During the five weeks of operation about nine TB of data were collected. The beam and target specifications are summarized in Tab. 5.1. Since

<b>beam energy <math>E_{kin}</math></b>	1.76A GeV
<b>beam particle</b>	${}_{18}^{40}Ar$
<b>beam intensity</b>	$1.5 - 2.5 \cdot 10^6$ particles/s
<b>target</b>	${}_{19}^{39.1}K{}_{17}^{35.5}Cl$
<b>target diameter <math>d</math></b>	3 mm
<b>target geometry</b>	4 segments
<b>distance between segments <math>\Delta z</math></b>	9 mm
<b>thickness of segment <math>t</math></b>	1.25 mm
<b>total interaction probability <math>P</math></b>	3.3 %

Table 5.1: Beam and target specifications

then both lepton and hadron data were analyzed within several thesis and analysis campaigns. A summary of the activities and the corresponding publications are given in Tab. 5.2. Within this work the efficiency correction for charged kaons, which was done in [Lor08] based only on the experimental data, is cross checked using a HGEANT simulation and the multivariate electron analysis (MVA) developed in [Lan08], which showed some inefficiencies in the TOF part of the detector, is improved. Furthermore the complete set of reconstructed particle yields is compared to a statistical hadronization model and interpreted. This part of the thesis is organized as follows, in section 5.2 the correction for the charged kaons is explained, in section 5.3 the improvement of the MVA is presented, while

Analyzed particle	Thesis	Published Reference
$e^+e^-$	[Lan08, Kri08, Jur10]	[eaHC11a]
$\Lambda, K_s^0, \phi, p, \pi^-$	[Sch08]	[eaHC09c, eaHC10a, eaHC11b]
$K^\pm$	[Lor08]	[eaHC09c]
$\pi^\pm$	-	[eaHC]
$\Xi^-$	-	[eaHC09a]
interferometry	[Wen09]	[eaHC10b, eaHC11d]
$d, t, He^3$	[Sch12b]	not yet
$t_\Lambda$	[Sch12a]	not yet
$\Sigma(1385)^\pm$	[Reh11]	not yet

Table 5.2: Overview of analyzed particle species. Listed are also the corresponding thesis and publications.

the discussion and interpretation of the data, as well as the comparison to the statistical hadronization model is presented in chapter 6.

## 5.2 Efficiency correction for charged kaons

The energy loss information of the time of flight walls and the drift chambers are beside the time of flight information the crucial information for the identification of charged kaons. The energy loss vs. momentum distributions are displayed in chapter 2.

The effect of the inclusion of the different information is illustrated in the mass spectrum in Fig. 5.1. The blue mass spectrum corresponds to the raw information of all tracks which are selected by the track sorting procedure<sup>1</sup>. Without additional identification power no significant  $K^\pm$  signal is visible. For the green spectra the energy loss information of the TOF detector and selections on the quality of the track reconstruction, optimized for kaons, are applied. Finally, for the red spectrum also the energy loss information of the drift chambers, again optimized for charged kaons, is included. After all selection criteria are applied significant peak structures are visible for both charged kaon species. Technically the energy loss information is included by a graphical selection ("banana cuts") in the energy loss vs. momentum distribution. In order to estimate the efficiencies of such a selection either the energy loss distribution including its momentum dependence must be well reproduced by the digitizer used in the HGEANT detector simulation or the efficiencies have to be estimated relying on data only.

For the latter one a method was developed in [Lor08]. It could be shown that the efficiencies of both energy loss distributions are independent from each other, therefore the efficiency of one cut can be estimated using both cuts for the sample in the denominator and only one cut for the sample in the

<sup>1</sup>Tracks which share one or more common detector hit(s) are sorted due to the quality of their reconstruction, only the best ones are kept.

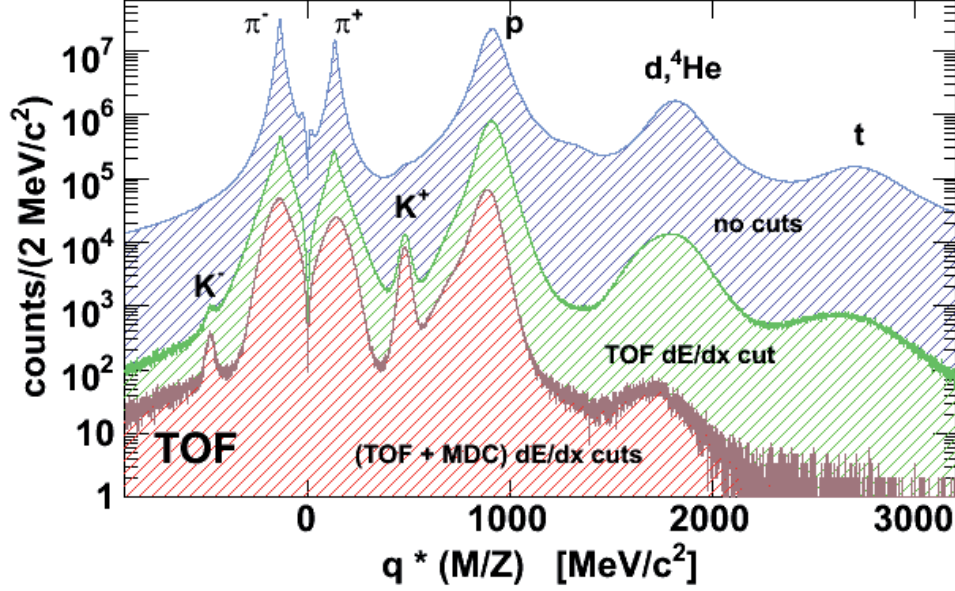


Figure 5.1: Mass spectra in the TOF region. Blue spectrum: All tracks which have been selected by the track sorting procedure. Green spectrum: Cuts on track quality and the energy loss information of the TOF wall are included. Red spectrum: In addition the energy loss information of the drift chambers is included [eaHC09c].

nominator. The corresponding efficiencies are then given as:

$$\epsilon_{dEdxTOF} = \frac{N_{trackquality+dEdxTOFMDC}}{N_{trackquality+dEdxMDC}}, \quad (5.1)$$

$$\epsilon_{dEdxMDC} = \frac{N_{trackquality+dEdxTOFMDC}}{N_{trackquality+dEdxTOF}}. \quad (5.2)$$

In this way one is able to reconstruct clean  $K^+$  signals in both data samples. Since the cuts for the  $K^-$  identification are identical to the  $K^+$  cuts, asking in contrast only for a track with negative polarity, the efficiencies obtained with the positive kaon sample are also used for the negatively charged kaons. Unfortunately this method does not work in the whole phase space covered by the detector, since applying only one of the cuts does not give sufficient identification power for the extraction of a clear signal in the high momentum regions. Therefore the efficiency is assumed to be constant in those regions. This assumption introduces a systematical bias on the high transverse mass region of the spectra close to mid rapidity. Therefore the efficiencies were also estimated based on simulation and

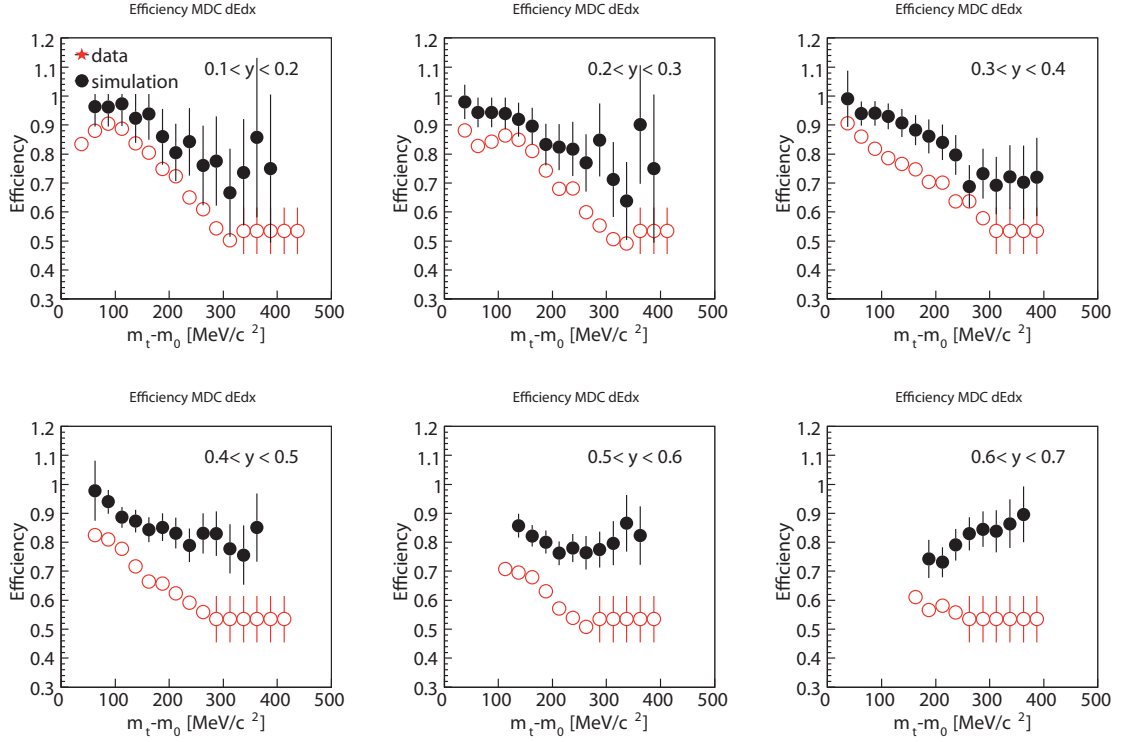


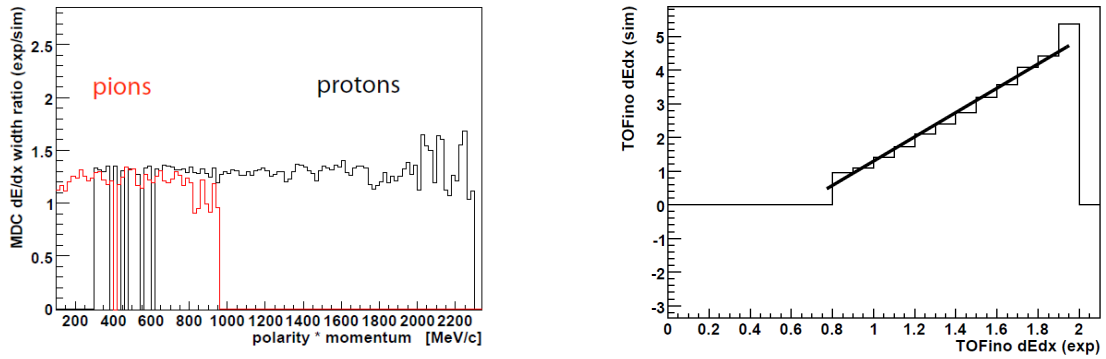
Figure 5.2: Efficiencies of the cut in the energy loss vs. momentum plane for the drift chambers estimated from data (red) and simulation (black). The results show large discrepancies, see text for details.

the standard embedding method. Fig. 5.2 shows a comparison of the efficiencies obtained with both methods for the selection in the MDC energy loss vs. momentum plane, as a function of the corrected transverse mass  $m_t - m_K$  in different regions of rapidity. Besides the expected difference in the high momenta regions the efficiencies obtained by simulation are systematically higher pointing to too small widths of the simulated energy loss distribution. Indeed a comparison between the two distributions shows, that the experimental distribution is about 20% broader for pions as well as for protons than the simulated one, see Fig. 5.3. Technically this is done by selecting pions and protons, making use of the time of flight information only and adapt their energy loss distribution in various momentum regions using gaussian- or landau-like functions.

The easiest way to correct this effect is by adapting the width of the graphical cut applied to the simulated data using the obtained scaling factor. This method has become a standard procedure within the HADES collaboration and has been used since then in various thesis [Sch12b, Sie10, Epp09, Tei11], including various refinements.

For the energy loss of the TOF detector the method is used analogously. In addition a constant offset between the mean values of the experimental and simulated distributions has to be corrected.

In the TOFino detector a more sophisticated method has to be used, since the offset is not constant but shows a linear dependence of the relative positions to each other, see Fig. 5.3. Since charged kaons are only identified in the TOF region this is not part of this work. For details on the adaption in the



(a) Ratio of the MDC energy loss distribution widths

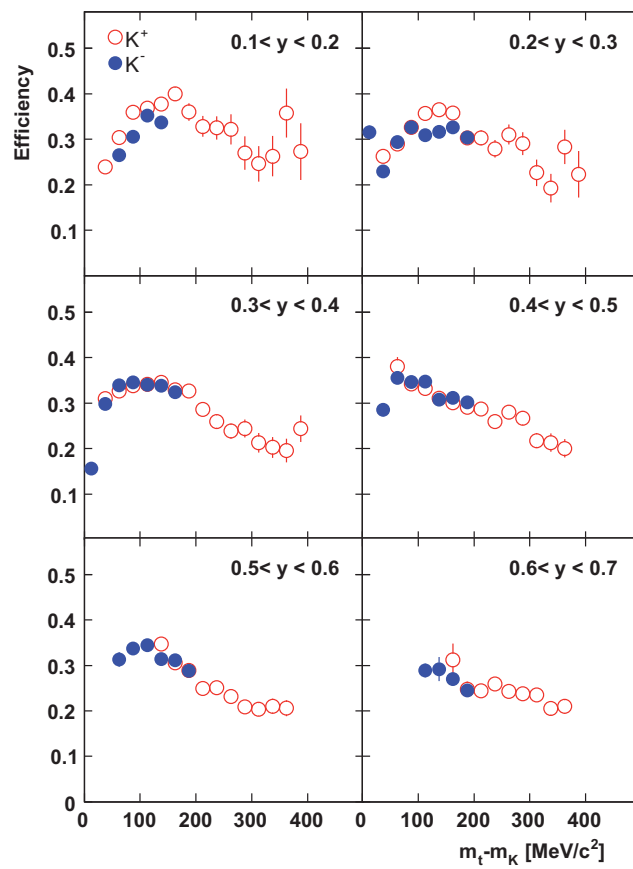
(b) Simulated energy loss (TOFino) as a function of the experimental observed energy loss (TOFino)

Figure 5.3: Left side: Ratio of the MDC energy loss distribution widths (experiment/simulation) for pions (red) and protons (black). For both particle species the real experimental distribution is about 20% broader. Right side: Dependence of simulated and real energy loss distributions in the TOFino, see text for details.

TOFino region, see for example [Sch12b]. The corrected simulated efficiencies for both energy loss distributions are again compared to the one obtained only from data in Fig.5.5. Besides the already discussed and expected differences in the high momenta regions the values agree well with each other. Fig. 5.4 shows the total efficiency of the kaon identification, including besides the cuts on the energy loss the detector response, tracking+tracking cuts as well as the efficiency of the count rate estimation in the mass spectra. They are again plotted as a function of the transverse mass for various regions in rapidity.

In addition the acceptance of the HADES spectrometer is estimated from simulation, using thermal distributions, for each transverse mass and rapidity region and takes values between 20 – 40% for most of the regions.

Figure 5.4: The total efficiency including the cuts on the energy loss, the detector response, tracking as well as cuts on the quality of the track reconstruction and the efficiency of the count rate estimation in the mass spectra for  $K^+$  (open red circles) and  $K^-$  (blue full circles) in various rapidity regions.



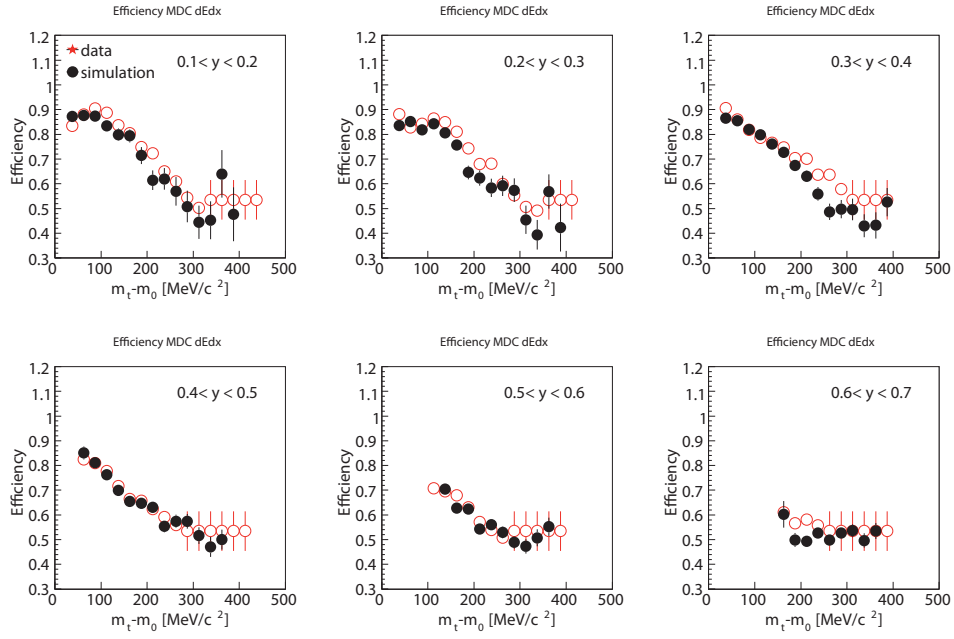
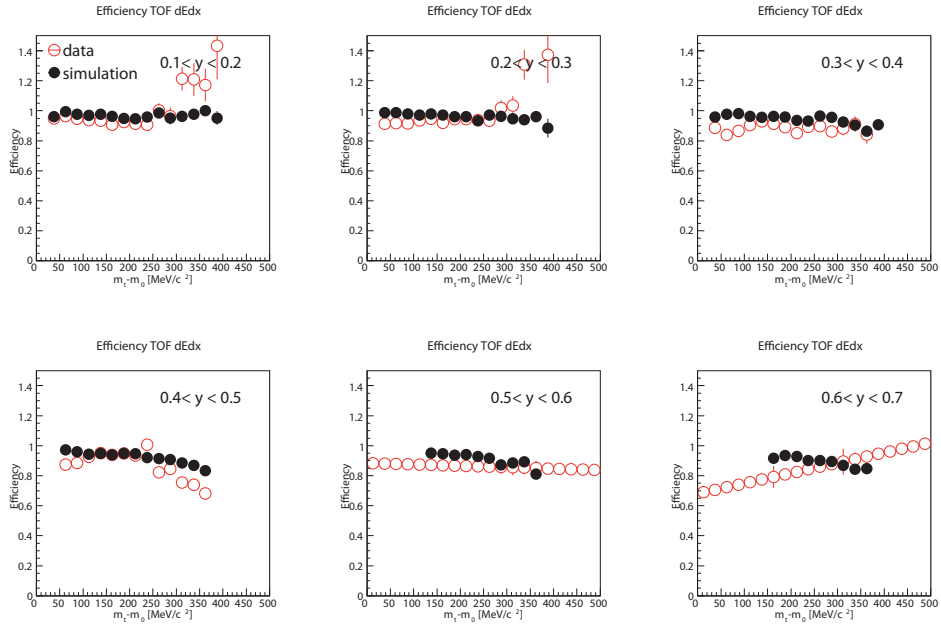
(a) Corrected simulated efficiencies compared to the ones obtained from data for MDC  $dE/dx$ (b) Corrected simulated efficiencies compared to the ones obtained from data for TOF  $dE/dx$ 

Figure 5.5: Corrected simulated efficiencies (black) compared to the ones obtained from data (red) for MDC  $dE/dx$  (top) and for TOF  $dE/dx$  (bottom). Besides the expected deviations in the high momenta regions the values are well in agreement with each other.

### 5.2.1 Transverse mass spectra and total production yields

The efficiency and acceptance corrected, normalized  $(m_t - m_0)$  spectra are shown in Fig. 5.6 for both kaon species. For the  $K^+$  a rapidity region of  $-0.85 \leq y_{cm} \leq -0.15$  and for the  $K^-$  a region of  $-0.75 \leq y_{cm} \leq -0.25$  is covered. The momentum distribution of particles emitted from a thermal source is described by a Boltzmann distribution

$$\frac{1}{m_t^2} \frac{d^2 N}{d(m_t - m_0) dy_{cm}} = A \cdot \exp \frac{-(m_t - m_0)}{T_B} \quad (5.3)$$

for a given interval in rapidity, which is approximately fulfilled in heavy ion collisions. Both parameters, the integration constant  $A$  and the inverse slope parameter  $T_B$  are rapidity dependent. The adapted Boltzmann distribution describes the shape of the spectra well and are used to extrapolate to the unmeasured part of the phase space. The resulting distribution of the inverse slope parameter

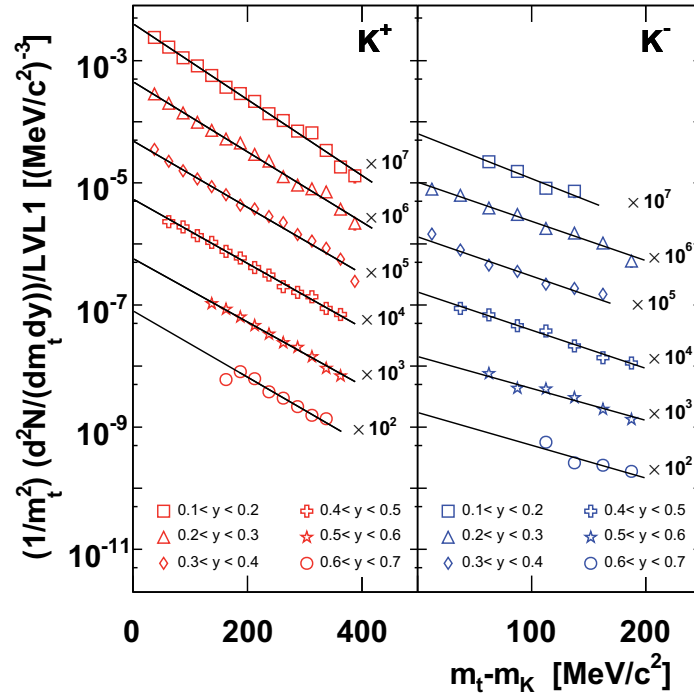


Figure 5.6: Transverse mass spectra of  $K^+$  (right) and  $K^-$  (left) for different rapidity regions. For better separation the spectra are scaled with different power of ten factors.

$T_B$  as a function of the center of mass rapidity  $y_{cm}$ <sup>2</sup> is shown in Fig. 5.7. For an isotropically emitting thermal source the inverse slope parameter  $T_B$  is the temperature of the system  $T_{eff}$  and shows a simple dependence from  $y_{cm}$ :

$$T_B = \frac{T_{eff}}{\cosh y_{cm}}. \quad (5.4)$$

The effective slopes of the  $K^-$  are systematically 10-15 MeV lower compared to the ones of  $K^+$ . The reason for this observation will be discussed in chapter 6.

<sup>2</sup>The distribution is centered around mid-rapidity ( $y_{midrapidity} = 0.86$ ).

In order to estimate the total kaon yield per event, the data points are integrated and the Boltzmann fit is used to extrapolate to the uncovered phase space. The resulting yield per rapidity region  $dN/dy_{cm}$  is shown in Fig. 5.7. Again in order to extrapolate the yield to uncovered phase space, the distribution is adapted with a simple gaussian function<sup>3</sup>. For a pure thermal source the width of the gaussian would be

$$\sigma_y = \sqrt{\frac{T_{eff}}{m_K c^2}} \quad (5.5)$$

shown in red in Fig. 5.7. The experimentally observed distribution deviates about 30% for  $K^+$  and about 20% for  $K^-$  from the one of a pure thermal source. A reason for this could be development of radial flow or a coupling of kaons to not fully stopped baryons.

The yield of the  $K^+$  is about two orders of magnitude higher, as one expects from associated strangeness production as discussed in chapter 1.

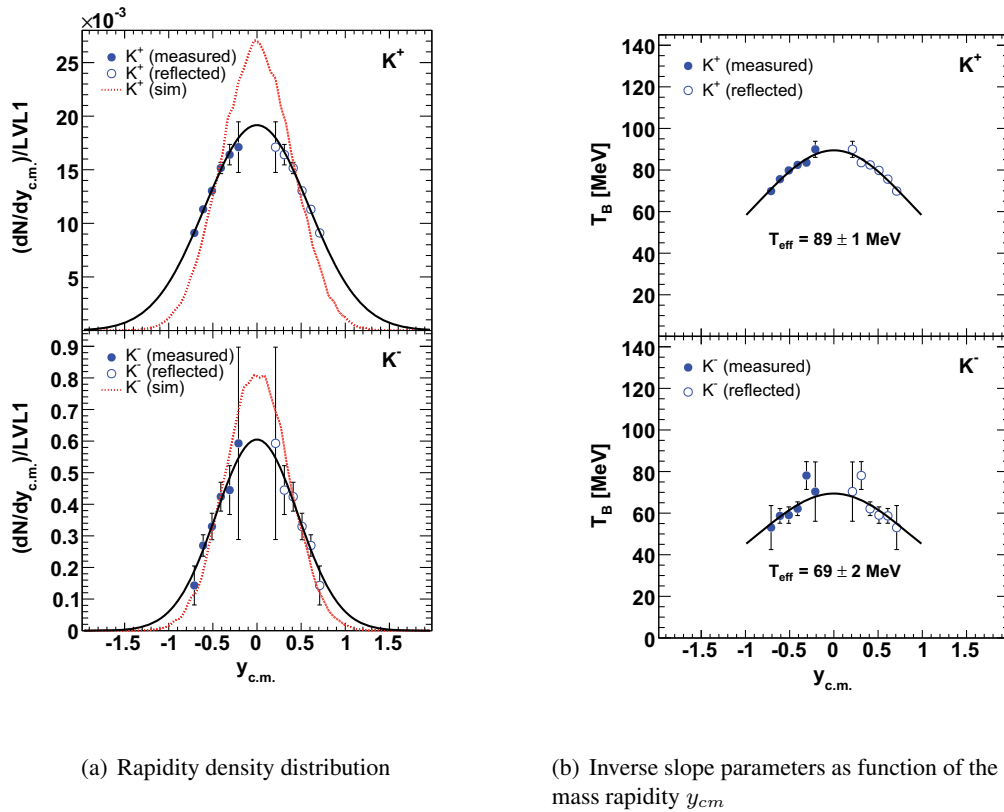
The inverse slope parameters, production yields and width of the rapidity distributions are summarized in Tab. 5.3. The first error following the multiplicity value indicates the statistical error. The systematical errors are estimated by varying the graphical cuts on the MDC and TOF  $dE/dx$  distributions within 30%.

For the total production yield in order to check the sensitivity to the assumed parametrization using a gaussian distribution for the extrapolation, also a sum of two gaussian functions is used as introduced in [eaNC08]. The resulting uncertainty is reflected in the third error on the total production yield in Tab. 5.3.

particle	$K^+$	$K^-$
multiplicity/LVL1	$(2.8 \pm 0.2 \pm 0.1 \pm 0.1) \cdot 10^{-2}$	$(7.1 \pm 1.5 \pm 0.3 \pm 0.1) \cdot 10^{-2}$
$\sigma_{exp}$	$0.59 \pm 0.02$	$0.47 \pm 0.06$
$\sigma_{therm}$	0.43	0.37
$T_{eff}$	$89 \pm 1 \pm 2 \text{ MeV}$	$69 \pm 2 \pm 4 \text{ MeV}$

Table 5.3: Overview of the results for charged kaons.

<sup>3</sup>The extrapolation to the forward rapidity hemisphere is possible due to the nearly perfect symmetry of the Ar+KCl collision system.



(a) Rapidity density distribution

(b) Inverse slope parameters as function of the center of mass rapidity  $y_{cm}$ 

Figure 5.7: Left side: Rapidity density distributions for  $K^+$  (top) and  $K^-$  (bottom) compared to pure thermal distributions (red). Right side: Inverse slope parameters obtained from the Boltzmann fits to the transverse mass spectra for  $K^+$  (top) and  $K^-$  (bottom) as a function of the center of mass rapidity  $y_{cm}$ . The full lines represent a fit according to formula 5.4.

Since the ratio of charged kaons is nearly independent from the participating nucleons  $A_{part}$  as mentioned in chapter 1 and observed in [eaKC07], it can be directly compared to the systematics obtained by the KaoS collaboration as a function of the beam energy, see Fig. 5.8. As can be seen from the figure, the HADES data point agrees nicely with previously observed systematics.

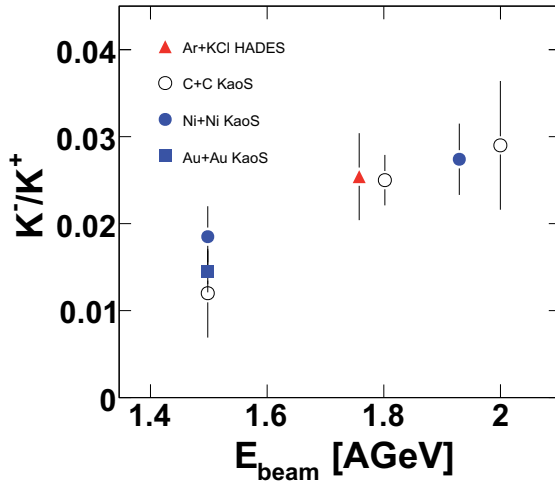


Figure 5.8:  $K^-/K^+$  ratio as a function of the beam energy. Since the ratio is almost independent of  $A_{part}$  the HADES data point can be directly compared to the systematics obtained by the KaoS collaboration [eaKC07].

### 5.3 Refinement of the MVA settings

The electron and positron identification for the Ar+KCl experiment was performed making use of a neural network for the first time. The concept of such a multivariate analysis is presented in chapter 2, section 2.7.1, while details on the realization within the HADES analysis are described in chapter 3, section 3.3.1 and in [Lan08].

Compared to the analysis of hard cuts (HCA) [Kri08], the original setting of the MVA [Lan08] shows a break down of efficiency in the high momentum region, while the efficiency of the HCA stays constant. The trend of the electron efficiency<sup>4</sup> for both methods is plotted as a function of the momentum in Fig. 5.9.

Unfortunately, the electron momentum is directly correlated with the invariant dilepton mass  $M_{ee}$ ,

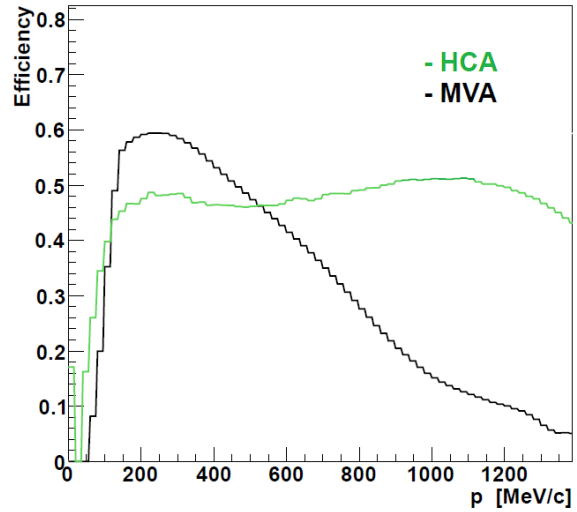
$$M_{ee} \approx 2\sqrt{p_{e^-} + p_{e^+}} \cdot \sin(\alpha_{ee}/2) \quad (5.6)$$

with  $\alpha_{ee}$  being the opening angle between the particle trajectories. On average the higher the momenta of the pair legs are, the higher the invariant mass is. Therefore, in order to collect sufficient statistics in the vector meson region which was one of the goals of the Ar+KCl beam time, this inefficiency has to be removed. Note that at this beam energy the  $\omega$  meson is produced below its free nucleon nucleon threshold<sup>5</sup> and in addition the decay branch to  $e^+e^-$  is electromagnetically suppressed. Taking the acceptance and reconstruction efficiency into account, nearly 30 million events have to be seen by the detector in order to reconstruct a single  $\omega$  meson. Reflecting these numbers it is clear that one can not

<sup>4</sup>Note that the efficiency matrix used to correct the Ar+KCl data is defined different compared to the one used for p+Nb. While for the latter one, a smeared initial momentum value is used in the denominator, for the Ar+KCl data the initial momentum value is used. This results in  $\approx 20\%$  difference in the pair yield, which translates to  $\approx 10\%$  differences in the single electron efficiencies.

<sup>5</sup> $\sqrt{s} - \sqrt{s_\omega} = -50$  MeV

Figure 5.9: Comparison of electron reconstruction efficiency as a function of the momentum for the original MVA of S. Lang (black) and the HCA (green). Although in the low momenta region the MVA has higher efficiency values, a strong drop with rising momentum is observed, while the efficiency of the HCA stays rather constant.



afford to lose any statistics due to an insufficient particle identification method.

First investigations of adapting the track sorting algorithm and matching between the reconstructed trajectories in the tracking detectors and rings in the RICH detector to the one used in the HCA showed no improvement. For this reason the main origin of the inefficiencies had to be hidden in the multivariate analysis. A comparison of the MVA efficiencies in the TOFinio and the TOF regions showed much stronger dropping of the efficiency with rising momentum in the latter one, compare Fig 5.10. On that account the studies were focussed on the TOF region.

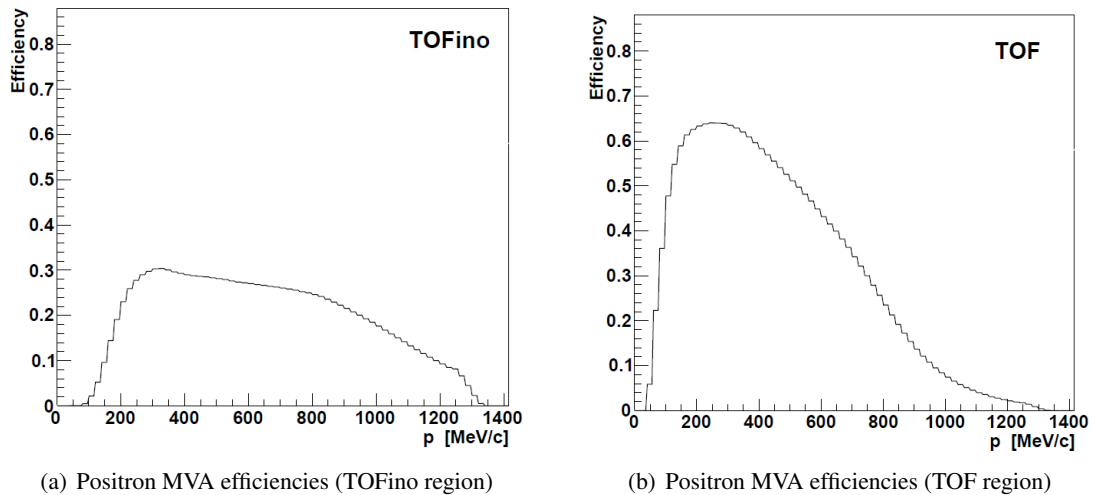


Figure 5.10: Efficiencies of positrons obtained for the MVA as a function of the momentum in the TOFinio region (left) and the TOF region (right). The dropping with rising momentum is much more pronounced in the TOF region of the detector.

### 5.3.1 Choice of variates

An alternation of the included variates used as input for the algorithm is the native regulator to improve the performance of a neural network. Consequently possible changes of the included variates are investigated.

As variates in the original setup [Lan08] the detector variables with the highest separation power between electrons and hadrons of each subdetector system are used. In addition the momentum was included in order to take the momentum dependence of some of the variables into account. The following detector parameters are used as variates in the TOF region:

- RICH: number of fired pads
- MDC: energy loss, momentum
- TOF wall: energy loss, time of flight

and in the TOFino region:

- RICH: number of fired pads
- MDC: energy loss, momentum
- TOFino wall: time of flight
- SHOWER: pre/post shower charge ratios.

The variates distributions for the signal and background samples obtained by a strong cut on the RICH-MDC matching (for details see chapter 2, section 2.7.1) are presented in Fig. 5.11.

Neither an exclusion of the energy loss of the TOF wall motivated by the overlapping energy loss distributions of electrons and hadrons in the minimum ionizing high momentum region nor a separate training for electrons and positrons suggested by the different physical background (protons), led to a significant improvement. For the latter one a gain in efficiencies for negative charged tracks was counterbalanced by a decrease for positive charged tracks.

The inclusion of the polar angle  $\Theta$  in order to cover up their polar angle dependency besides the momentum dependence of the variates, shows no improvement either, but gives some notion of a possible exclusion of the momentum.

Like the polar angle the momentum is included for its correlations with nearly all used variates, for example the abundantly discussed dependence of the particle energy loss of the momentum. As hadrons have on average higher momentum than electrons, resulting in a strong shift of the background momentum distribution towards higher values compared to the signal momentum, which are used to train the network, see Fig. 5.11. Therefore high momentum tracks are discarded with a much higher probability by the algorithm since they are more likely to be hadrons. Unfortunately the network is not fed with any pair information, especially the strong interest on vector meson decays, whose single legs have on average higher momenta than the much more abundant legs from neutral pion Dalitz decays. A good solution would be training with a sample of single legs originating from vector meson decays. Another long term solution would be a training based on simulation only but so far this has never been successfully used in any heavy-ion experiment. The future plans of the TMVA [TMV] developer provide the definition of spectator variates which only take correlations into account and do not contribute directly to the final decision of the network, which should improve the situation.

For now the momentum in the TOF region is simply discarded and the impact on single efficiencies and signal as well as background counts in the vector meson region of the final pair spectra is investigated.

### 5.3.2 Impact of the refinement

The effect of the exclusion of the momentum on the efficiency in the TOF region is dramatic. Fig. 5.12 shows a comparison of the efficiencies for electrons obtained with the old setting and the one after the improvements. The new efficiency shows only a slight decrease with rising momentum and stays for the whole momentum region above 0.6.

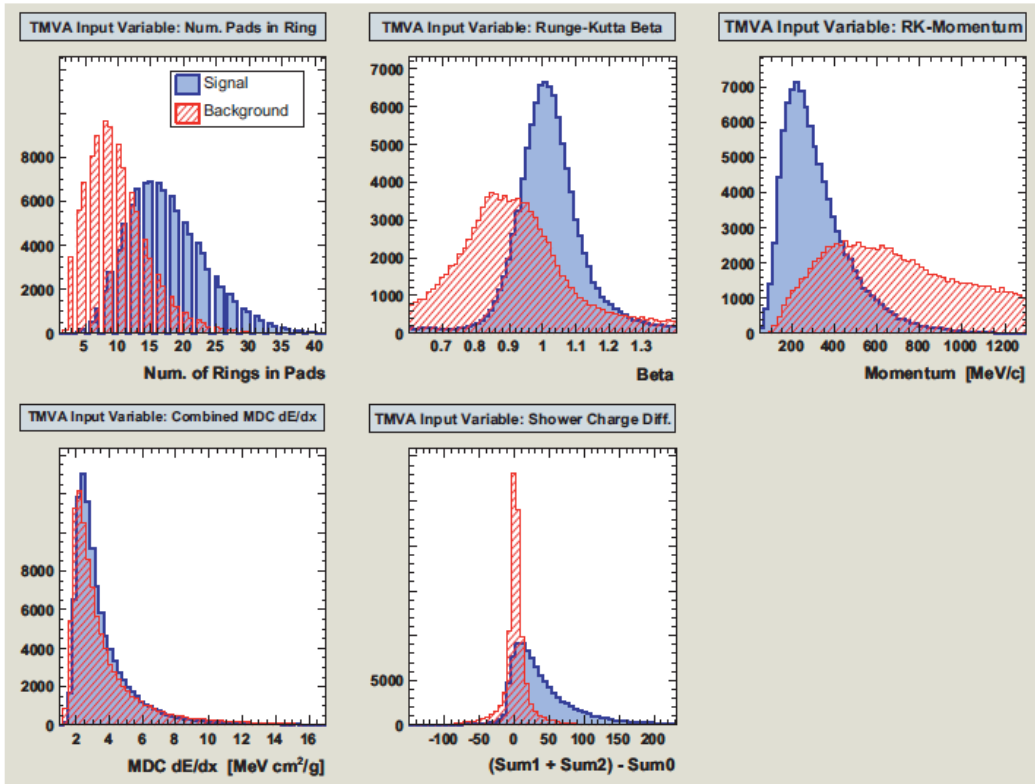
Although the total number of reconstructed pairs decreases on the order of a few percent, due to a small decrease in the low momentum region where most of the statistics of electrons and positrons are located, the number of reconstructed pairs in the pole mass region of the  $\omega$  meson increases by 40% from 20 to 33. In order to estimate the effect on the purity one can compare the signal to background ratio and the corresponding significance <sup>6</sup> of the reconstructed pairs. While the signal to background ratio stays constant within the errors the significance in the vector meson region increases.

Unfortunately, the exclusion of the momentum from the used variates is only possible in the TOF region, due to the strong momentum dependence of the SHOWER quantity in the TOFino region.

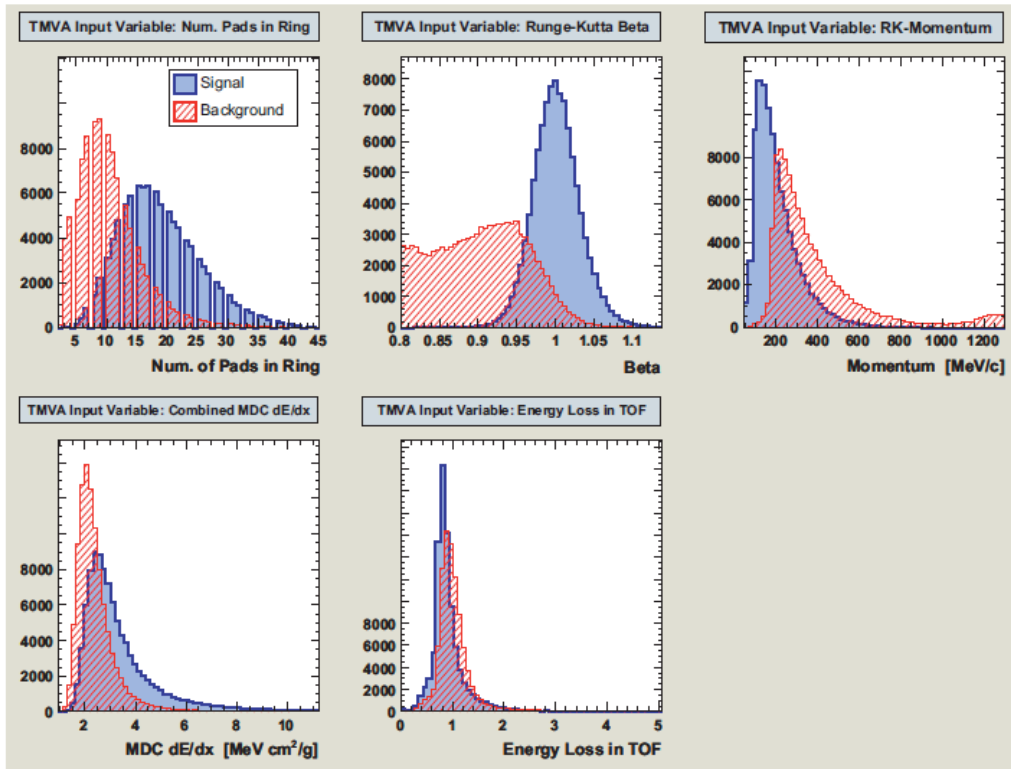
A new comparison between the improved MVA and the HCA efficiencies for electrons over the whole detector region is shown in Fig. 5.13. The efficiency of the MVA is about 15% higher in the low momentum region and decreases only gently with rising momentum. At around  $900 \text{ MeV}/c^2$  both lines cross and the hard cut analysis has higher efficiencies. The efficiencies for positrons are slightly below the ones for electrons for both analysis.

---

<sup>6</sup> $Sig = Signal/\sqrt{Signal + Background}$



(a) TOFino region



(b) TOF region

Figure 5.11: Distribution of the variates obtained from the signal (blue) and background (red) sample in the TOFino region (top) and the TOF region (bottom).[Lan08]

Figure 5.12: Comparison of the improved MVA setting efficiency for electrons (magenta) to the original one (black) as a function of the momentum, in the TOF region.

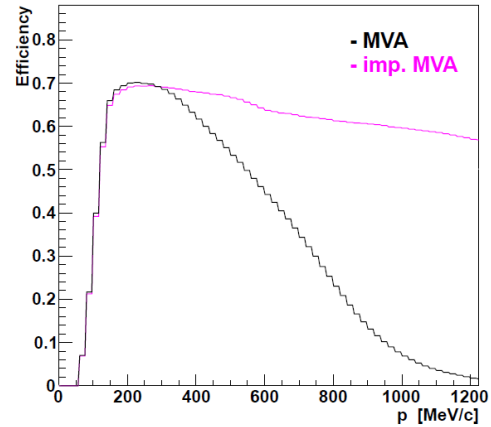
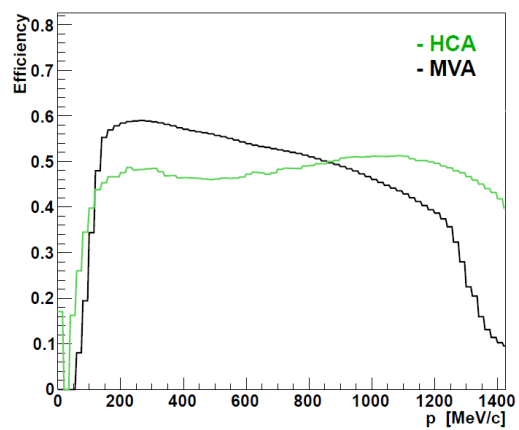


Figure 5.13: Comparison of the improved MVA setting efficiency for electrons (black) to the original one of the HCA (green) as a function of the momentum, over the whole detector region.



### 5.3.3 $\omega$ yield

In order to investigate systematics due to the particle identification three different analysis, the MVA, the HCA [Kri08] and a Bayesian approach [Jur10], were used. All three led to consistent results, remaining differences are taken care of as systematic errors. For the publication an average spectra of the different analysis is used [eaHC11a].

Fig. 5.14 shows a linear zoom into the  $\omega$  region, showing a clear peak structure.

The  $\omega$  yield is extracted by adapting a gaussian plus an exponential function to the spectra assuming continuous behavior of the background. The fit values correspond to a peak position of  $M_\omega = (0.770 \pm 0.01) \text{ GeV}/c^2$ , a width of  $\sigma_\omega = (0.022 \pm 0.01) \text{ GeV}/c^2$  and an integral value of  $N_\omega = (3.9 \pm 1.7) \cdot 10^{-8}$  per event. The small down shift of the peak position is well within expectations for the effect of the energy loss of the single legs in the detector estimated from HGEANT simulations. The width is dominated by the statistics and the HADES mass resolution of 3% in the vector meson region, giving no hint for broadening due to possible medium effects. The branching ratio and acceptance corrected (assuming a thermal source of  $T_{eff} = 84 \text{ MeV}$  as measured for the  $\phi$  mesons [eaHC09c]) integral value gives a normalized yield of  $N_\omega/N_{\pi^0}$  which translates into a total production yield per LVL1<sup>7</sup> event of  $N_\omega = (6.7 \pm 2.8) \cdot 10^{-3}$ .

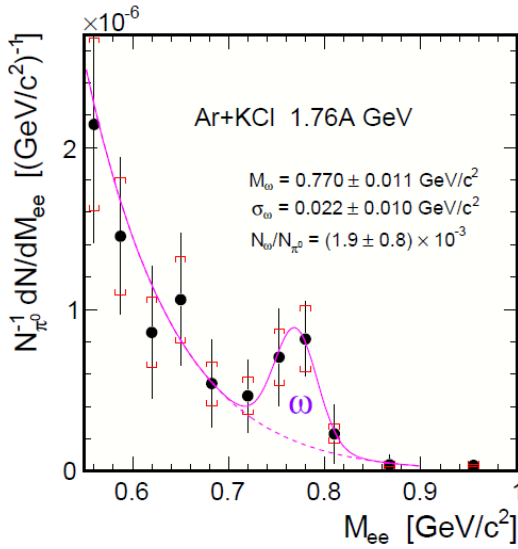


Figure 5.14: Efficiency corrected and normalized invariant mass of dielectrons in the vector meson region. The  $\omega$  signal is adapted using a gaussian plus an exponential function assuming continuous behavior of the background.

<sup>7</sup>The level one trigger (LVL1) selected the 35% most central collisions



## Chapter 6

# Interpretation of the Ar+KCl data

### 6.1 Particle yields

From the Ar+KCl data an up to now unmatched set of different particle species in the 1-2A GeV energy regime has been reconstructed, offering new possibilities of comparison to systematics obtained in elementary reactions or at higher energies, as well as unique possibilities to test phenomenological models. Table 6.1 summarizes all particle yields extrapolated to full phase space, the corresponding inverse slope parameters from fits to the particle  $m_t - m_0$  spectra and the references.

#### 6.1.1 Strangeness balance

The strong interaction conserves strangeness, i.e. the numbers of  $s$  and  $\bar{s}$  quarks produced in a heavy ion reaction must be equal. As those quarks are ultimately bound in hadrons the multiplicities of strange particles fulfill a balance equation which can be written at SIS energies as:

$$K^+ + K^0 = \Sigma^{0\pm} + \Lambda + K^- + \bar{K}^0 + 2\Xi^{0,-} \quad (6.1)$$

where, for simplicity, the symbols denoting the particles stand for their respective yields at the time of production. Note that this equation takes care of the strong decay of heavier strange resonances via the counting of their decay products, namely kaons and  $\Lambda$ s. Using the HADES detector setup, the  $\Sigma^0$  can not be separated from the  $\Lambda$ , thus this contribution is to be counted explicitly together with  $\Lambda$ s. Analogously, according to the analysis procedure, most  $\Xi^{-,0}$  decay products feed the  $\Lambda$  channel and are counted as  $\Lambda$ s, therefore the factor in Eq. (6.1) in front of the  $\Xi^{-,0}$  is two instead of four. (Note that anyhow the  $\Xi^{-,0}$  contributions are small.) In case of the neutral kaons, in fact the yield of the  $K_s^0$  is measured, which obeys the equality  $K_s^0 = (K^0 + \bar{K}^0)/2$ . Assuming isospin symmetry the yield of the  $\bar{K}^0$  should be contributing here at the same order as the  $K^-$  yield. Eq. (6.1) can then be rewritten using the measured yields. Hence the unobserved  $\Sigma^\pm$  hyperon yield can be estimated as:

$$\Sigma^+ + \Sigma^- = K^+ + 2K_s^0 - (\Sigma^0 + \Lambda) - 2\Xi^- - 3K^- \quad (6.2)$$

Still heavier multi-strange particles, e.g.  $\Omega$  hyperons, have significantly higher production thresholds and should not contribute sizeably at SIS energies. From Eq. (6.2) a total multiplicity of charged  $\Sigma$  hyperons of  $(7.5 \pm 6.5) \times 10^{-3}$  is deduced when using the values of the multiplicities listed in Table 6.1. The error is the quadratic sum of the statistical and systematic error of the different yields. If one assumes isospin symmetry for the  $\Sigma^{\pm,0}$  yields one can subtract the  $\Sigma^0$  contribution from the  $\Lambda$

Table 6.1: Multiplicities (i.e. yield/LVL1 event) and effective temperatures of particles produced in Ar+KCl reactions at 1.76A GeV. Depending on the analysis method several systematical errors are given, see references for details. The error on the  $\Sigma$  and  $\Xi^-$  yield is the quadratically added statistical and systematic error.

Particle	Multiplicity	$T_{eff}$ [MeV]	Reference
$\pi^-$	$3.9 \pm 0.1 \pm 0.1$	$82.4 \pm 0.1_{-4.6}^{+9.1}$	[eaHC10a]
$\Lambda + \Sigma^0$	$(4.09 \pm 0.1 \pm 0.17_{-0.37}^{+0.17}) \times 10^{-2}$	$95.5 \pm 0.7 + 2.2$	[eaHC11b]
$K^+$	$(2.8 \pm 0.2 \pm 0.1 \pm 0.1) \times 10^{-2}$	$89 \pm 1 \pm 2$	[eaHC09c]
$K_S^0$	$(1.15 \pm 0.05 \pm 0.09) \times 10^{-2}$	$92 \pm 2$	[eaHC10a]
$K^-$	$(7.1 \pm 1.5 \pm 0.3 \pm 0.1) \times 10^{-4}$	$69 \pm 2 \pm 4$	[eaHC09c]
$\omega$	$(6.7 \pm 2.8) \times 10^{-3}$	$131 \pm 26$	[eaHC11a]
$\phi$	$(2.6 \pm 0.7 \pm 0.1 - 0.3) \times 10^{-4}$	$84 \pm 8$	[eaHC09c]
$\Xi^-$	$(2.3 \pm 0.9) \times 10^{-4}$	-	[eaHC09a]
$A_{part}$	$38.5 \pm 4$	based on UrQMD simulation	[eaHC11b]
$\Sigma^+ + \Sigma^-$	$(0.75 \pm 0.65) \times 10^{-2}$	estimated via strangeness balance	[eaHC11b]
$p$	$22.11 \pm 2.4$	$142.5 \pm 5$	[Sch08]

yield and finds the ratio  $\Sigma^{\pm,0}/\Lambda$  to be  $0.3 \pm 0.26$  although the difference in mass is only 10%. Note that the difference in yield is nearly 70%, even after correcting the  $\Lambda$  yield for its  $\Sigma^0$  contribution (assuming isospin symmetry for the  $\Sigma^{\pm,0}$  yields). This might be related to a threshold effect, as the  $\Lambda$  is produced here slightly above, while the  $\Sigma$  is produced slightly below their respective free NN thresholds. The only other published multiplicity of charged  $\Sigma$  hyperons in heavy ion collisions, based on a similar analysis of strangeness yields measured with the FOPI detector at GSI in Ni+Ni reactions at 1.93A GeV, is  $(7 \pm 8 + 32 - 17) \times 10^{-3}$  [eaFC07a]. Differences with respect to the HADES data are: (1) a higher beam energy (1.93 vs. 1.76A GeV), (2) a larger reaction system (58+58 vs. 40+37), and (3) a different centrality selection ( $\langle A_{part} \rangle = 71$  vs. 38.5) resulting in a higher  $\Lambda$  yield ( $0.137 \pm 0.005 + 0.007 - 0.008$ ) and inverse slope parameter ( $119 \pm 1 + 9 - 7$ ). In view of the higher bombarding energy and larger system size, one would expect a larger charged  $\Sigma$  contribution. The resulting  $\Sigma^{\pm,0}/\Lambda$  ratio is  $0.08 \pm 0.09 + 0.33 - 0.18$ . Unfortunately, the large uncertainties do not allow to draw a firm conclusion on the behavior of the respective cross sections with energy.

## 6.2 Comparison with statistical hadronization

### 6.2.1 Ensemble theory and particle production in heavy-ion collisions

Statistical mechanics describes physical systems using the ensemble theory, based on the Ergodic hypothesis. The Ergodic hypothesis assumes that the average over time  $A_t$  is equal to the average over various ensembles  $\langle A \rangle$ :

$$A_t = \langle A \rangle . \quad (6.3)$$

One distinguishes between 3 different ensembles.

- The **micro canonical ensemble (E,V,N)** which is consistent with a closed system of given energy **E**, given volume **V** and given number of particles **N**. All micro states of such a closed system are occupied with equal probability.
- In the **canonical ensemble (T,V,N)** the energy of the system is no longer constant. Instead the average energy over various ensembles is kept constant by a temperature **T**. The probability  $p_i$  for finding a particle in a given micro state is then proportional to

$$p_i \propto \exp\left(\frac{-E_i}{kT}\right) \quad (6.4)$$

with  $k$  being the Boltzmann constant.

- Finally in the **grand canonical ensemble (T,V, $\mu$ )** also the number of particles is conserved only on average by the chemical potential  $\mu$ . The probability  $p_{i,q}$  for finding a particle in a given micro state and given quantum number  $q$  is then proportional to

$$p_{i,q} \propto \exp\left(\frac{-E_i + \mu q}{kT}\right) . \quad (6.5)$$

For the description of HIC yields, the grand canonical ensemble and in case of rare particles (abundance  $\ll 1$ ) the canonical ensemble is used. Besides the temperature  $T$  and the volume  $V$  of the system, one introduces usually three chemical potentials,  $\mu_Q$ ,  $\mu_B$  and  $\mu_S$ , conserving the charge  $Q$ , the baryon number  $B$ , and the strangeness  $S$ . The particle number density  $\rho_{i,q}$  using the grand canonical ensemble is proportional to:

$$\rho_{i,q} \propto \int_0^\infty p^2 dp \exp\left(\frac{-E_i + \vec{\mu}\vec{q}_i}{kT}\right), \quad (6.6)$$

with  $\vec{\mu} = (\mu_Q, \mu_B, \mu_S)$  and  $\vec{q}_i$  being the corresponding quantum numbers.

Statistical hadronization models (SHM) have been successful in fitting particle yields or yield ratios from relativistic and ultrarelativistic heavy-ion collisions by assuming a sudden freeze-out in chemical equilibrium [RAS03, FBS04, PBMS03, JCW06]. With the help of SHM fits it has been possible to systematically map out a unique chemical freeze-out line in the  $T - \mu_b$  plane of the phase diagram of strongly interacting matter, with  $T$  denoting temperature and  $\mu_b$  the baryochemical potential (see e.g. [JCW06, ea10a]). At higher energies the chemical freeze-out line is believed to mark the phase boundary between the hadronic gas phase and the phase of free quarks and gluons, called the quark gluon plasma. At moderate and low energies the line has recently been proposed, to be the boundary between the hadronic gas and an hypothetic phase of still confined but overlapping hadrons, which allows the quarks to percolate between the different hadrons, resulting in a quasi free sea of quarks, called quarkyonic matter [ea10a].

However, while the various SHM approaches agree fairly well at high bombarding energies, discrepancies appear in the low-energy regime. At beam energies of a few GeV, however, the validity of the SHM models is not firmly established. Indeed, a mechanism providing fast enough equilibration has not yet been uniquely identified. The situation is further complicated by the need for strangeness suppression which is indeed handled differently in the various implementations of the SHM. Furthermore, at SIS energies, only pions are produced abundantly. Heavier and especially strange particles are rare, and their yields were mostly poorly known. Hence in the past only few particle yields with small statistical errors were available as input to the fit procedure. In the following 13 particle yields obtained from the Ar+KCl run are fitted with a statistical hadronization model (SHM). Note that a similar fit, with less particles included, was already performed in [eaHC11b] for the same system.

## 6.2.2 SHM fit to Ar+KCl yields

The freely available THERMUS code [WC09] is chosen as SHM, using the mixed canonical ensemble, where strangeness is exactly conserved while all other quantum numbers are calculated grand canonically. Additional strangeness suppression is introduced by a strangeness correlation radius  $R_c$ , within which strangeness has to be exactly conserved; as discussed in [IKW07].

All particle yields listed in Table 6.1 are fitted simultaneously, except for the  $\Sigma^\pm$  yield which is estimated using the multiplicities of the other particle yields containing strangeness. The model takes the infinite resonance width into account, which enhances particle production from resonances, as well as quantum statistics. The charge chemical potential  $\mu_Q$  is constrained by the ratio of the baryon and the charge numbers of the collision system, resulting in 4 free parameters.

We find the chemical freeze-out at a temperature of  $T_{chem} = (73 \pm 3)$  MeV and at a baryochemical potential of  $\mu_b = (785 \pm 21)$  MeV. The strangeness correlation radius comes out as  $R_c = (2.5 \pm 0.5)$  fm, which corresponds to about half the fitted radius  $R = (4.7 \pm 0.7)$  fm of the whole fireball, while the  $\chi^2$  per degree of freedom (d.o.f.) value of the fit corresponds to 20/8.

Fig. 6.1 shows the resulting freeze-out point together with a compilation of similar points [AAS06,

JCW06, eaFC07b] in the  $T - \mu_b$  plane. Our result, as well as the FOPI result from the collision system Al+Al at 1.9A GeV, differ from the regularity of freeze-out points following the fixed energy per particle condition  $\langle E \rangle / \langle N \rangle \approx 1$  GeV, which is one of the commonly proposed freeze-out criteria [JCW06]. This might be due to the light collision systems, since small systems have the tendency to show higher freeze-out temperatures [ea99].

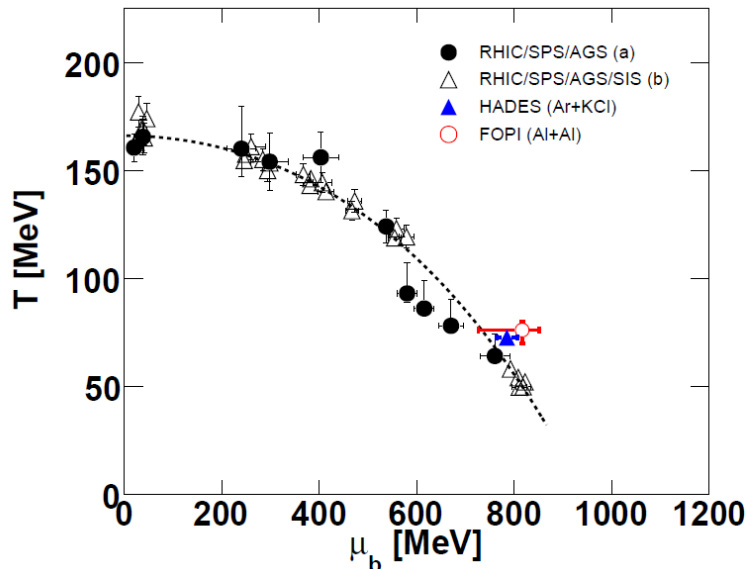


Figure 6.1: Chemical freeze-out points in the  $T - \mu_b$  plane. The filled black circles (a) are taken from [AAS06], the black open triangles (b) are taken from [JCW06]. The red circle is taken from [eaFC07b]. The THERMUS fit to our Ar+KCl data is shown as blue triangle. The dashed line corresponds to a fixed energy per nucleon of 1 GeV, calculated according to [JCW06].

A detailed comparison of the data with the statistical model fit is shown in the upper part of Fig. 6.2, while the lower part of this figure depicts the ratio of data and fit. All measured particle yields except for the  $\Xi^-$  and the  $\eta$  are described with remarkably good agreement considering the facts that semi central collisions of a medium sized collision system are used as input.

The yield of the  $\eta$  meson is not measured by HADES but extrapolated from TAPS measurements at 1.5 and 2.0A GeV [RAS03] and not included in the fit. The quite abundantly produced  $\eta$  meson seems to follow different freeze out criteria compared to the rest of the more abundant particles, compare also the parametrization of  $T$  and  $\mu_B$  obtained in [RAS03] using mainly neutral pion and  $\eta$  yields as input to the statistical model fit. The resulting values are systematically higher than the parameterizations of [JCW06, ea10a].

### 6.2.3 The $\phi$ meson and OZI suppression

A particularly interesting case is the  $\phi$  meson. The  $\phi$  is treated as a strangeness neutral object in the  $R_c$  formalism and is therefore not suppressed at all. Its yield is well described by the SHM. This means that the  $\phi$  yield is compatible with the assumption that it takes part in the equilibration of the more abundant hadrons. This is quite different from the situation at higher bombarding energies, where the  $\phi$  requires indeed an effective strangeness between 1 and 2 to have the appropriate suppression in the SHM and to reproduce the data [IKW07]. For an understanding of  $\phi$  production, one may have a look at the  $\phi/K^-$  ratio which, according to the SHM with  $R_c$ , should rise at low beam energy. Indeed over a wide range in HIC from  $\sqrt{s} = 8$  GeV to  $\sqrt{s} = 200$  GeV the  $\phi/K^-$  ratio stays rather constant at a value of  $\approx 0.1$ . Only below  $\sqrt{s} = 3$  GeV the ratio is predicted to rise depending on the ratio of the strangeness correlation radius to the radius of the whole fireball  $R_c/R$ . Indeed such a rising is

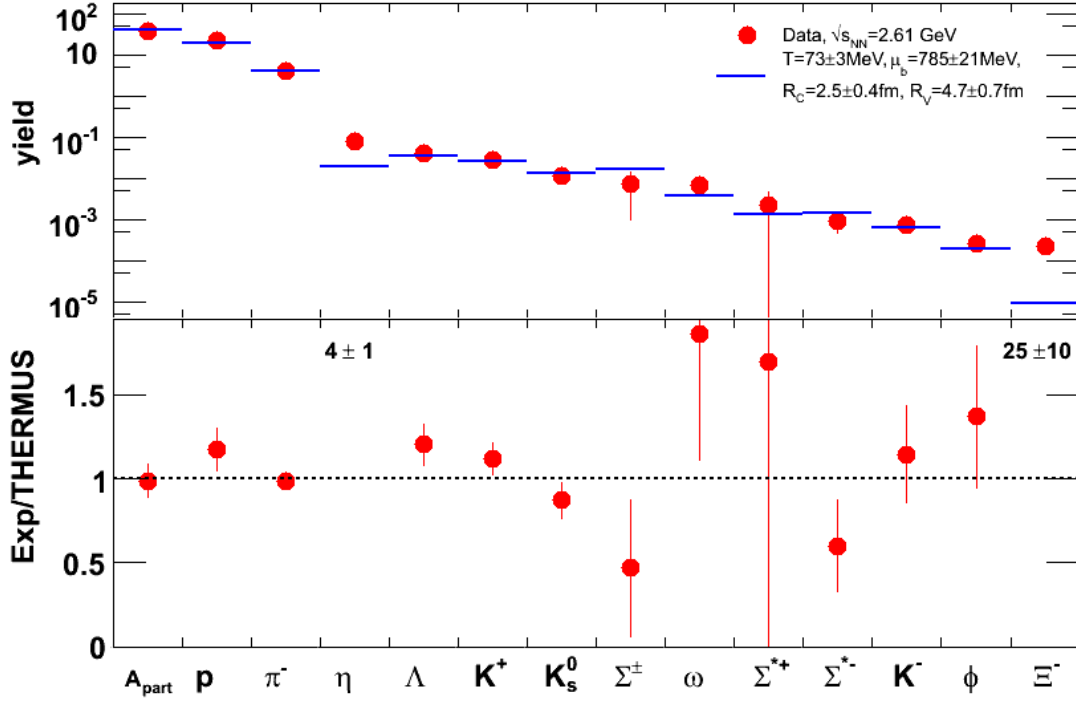


Figure 6.2: The upper plot shows the yields of hadrons in Ar+KCl reactions (filled red circles) and the corresponding THERMUS fit (blue bars). The lower plot shows the ratio of the experimental value and the SHM value. For the  $\Xi^-$  and the  $\eta$  the ratio numbers are quoted instead of a point.

supported by the HADES data, as discussed in [eaHC09c], and the ratio seems to approach the value seen in elementary NN reactions [eaAC08].

The opposite extreme to full thermalization is the elementary  $\phi$  production, where the cross section should be suppressed according to the Okubo-Zweig-Iizuka (OZI) rule [Oku63, Zwe64, Iiz66]. Due to the spin and parity assignments of the  $\phi$  meson ( $J^{PC} = 1^{--}$ ) the  $s\bar{s}$  quark pair creation can only proceed by exchanging an odd number of gluons. Since the theory of strong interaction Quantum Chromo Dynamics (QCD) requires color neutrality, the lowest possible quark diagram graph is a three gluon exchange, which is strongly suppressed.

The  $\phi$  cross section is commonly normalized to the cross section of simultaneously measured  $\omega$  mesons given as the ratio R:

$$R_{\phi/\omega} = \frac{A + B \rightarrow \phi X}{A + B \rightarrow \omega X} = \tan^2(\delta\Theta_v) \cdot f = 4.2^{-3} \cdot f \quad (6.7)$$

where  $f$  is the ratio of the available phase space for both mesons while  $\delta\Theta_v$  is the deviation from an ideal singlet and octet mixing in the  $\phi$  wave function according to SU(3) flavor symmetry. Historically the ratio R has been discussed in terms of strangeness content of the nucleon.

Fig. 6.3 shows  $R_{\phi/\omega}$  obtained in the HADES data compared to the value obtained from the SHM fit together with results from elementary p+p [eaDC01, eaAC06] and pion induced  $\pi + N$  [ABM98] reactions, plotted as function of the corresponding  $\phi$  excess energy. Note that this demonstration varies from the common definition used in literature for elementary collisions where both the  $\phi$  and the  $\omega$  yield are compared at the same excess energy, corresponding hence to different bombarding

energies.

Technically this is done by dividing the measured  $\phi$  cross sections by an interpolation of the  $\omega$  cross sections based on the parameterizations proposed in [SC00].

While already in elementary reactions a deviation from the ideal OZI rule is observed, our data suggest that in heavy-ion reactions close to threshold the ratio is more than an order of magnitude larger than in p+p collisions and the suppression seems to be fully neutralized, being in agreement with the value of the SHM fit.

This strong effect on the observable could be explained in a simple picture by a vanishing of the suppression due to color neutrality inside the surrounding strongly interacting medium.

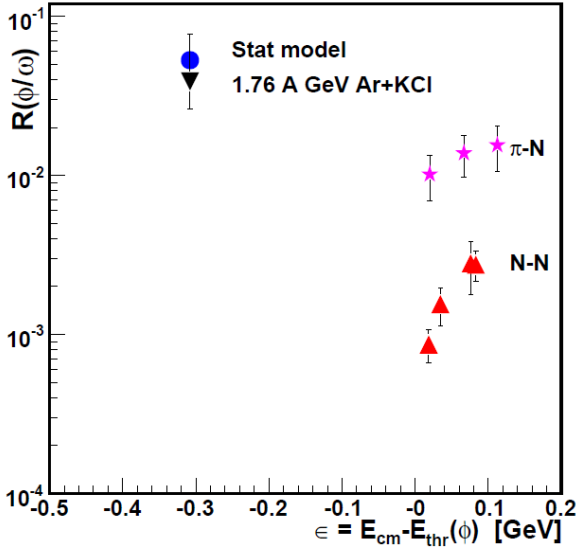


Figure 6.3: Comparison of the  $\phi$  to  $\omega$  ratio in Ar+KCl (black) with the value of the SHM fit (blue) and values obtained in elementary (red) and pion induced collisions (magenta) as a function of the  $\phi$  excess energy.

#### 6.2.4 The $\Xi^-$ hyperon and catalytic strangeness production

According to the strangeness suppression mechanism implemented in SHM, the double-strange  $\Xi^-$  ( $S=2$ ) should be suppressed strongly with respect to the  $\phi$  with its hidden strangeness ( $S=0$ ). Nevertheless, the measured  $\Xi^-$  yield is of the same magnitude as the one of the  $\phi$ , i.e. the data show no indication for any strangeness suppression. This is very surprising since the  $\Xi^-$  yields observed above threshold at RHIC [eaSC07], at SPS [eaNC04] and even at AGS [eaEC03] are consistent with statistical model fits. In fact the same secondary pion-hyperon process  $\pi + Y \rightarrow \phi + Y$ , which was invoked by Kolomeitsev and Tomasik [KT09] to explain the enhanced  $\phi$  yield, can here be the origin of the high  $\Xi^-$  production via the reaction  $\pi + Y \rightarrow \Xi + K$ . These catalytic processes are not suppressed by the OZI rule due to the presence of a strange quark in the initial state of the reaction.

To get a better understanding, one may have to move away from the SHM. The probability for the production of two  $s\bar{s}$  pairs in one collision  $P_{2s\bar{s}}$ , assuming that both pairs are independently created, is given as the square of the single-pair production probability  $P_{s\bar{s}}$ . Keeping associated production in mind,  $P_{s\bar{s}}$  can be estimated as the combined multiplicity of all particles that carry a strange quark, respectively the combined multiplicity of all anti-strange particles, i.e.  $K^+ + K^0 + \phi$ , yielding  $P_{s\bar{s}} \simeq 0.05$  and hence  $P_{2s\bar{s}} \simeq 0.0025$ . Considering that the observed  $\Xi^-$  yield is in fact only an order of magnitude smaller, we conclude that in 10% of these events both  $s$  quarks end up together in a  $\Xi^-$ , whereas from strangeness suppression in the SHM one obtains less than 1%. The question is why the probability that both  $s$  quarks end up in one particle is higher than the statistical expectation.

A possible scenario which could explain this observation is the formation of overlapping baryons and percolating quarks<sup>1</sup>. If such a system exists long enough the different quark flavors fill up potential wells, analog to protons and neutrons in a nucleus. In order to minimize the energy of the system the strange quark potential well will be filled up by transforming light quarks to strange quarks via the weak interaction. However since the life time of the system is only at magnitudes of the strong interaction a different process must drive the filling of the strange quark well. A candidate for such a process can be interactions of the constituent quarks with the surrounding meson cloud of virtual  $q\bar{q}$  pairs. A light constituent quark can then be blasted out of the system together forming a kaon with an  $\bar{s}$  quark, while the corresponding  $s$  quark falls into the strange quark potential well. If such bags become big enough this process is likely to happen more than once. If the system evolves further in time and cools down, it breaks apart. Under the assumption that this process is dominant for strangeness production, the probability for double strange particle production is enhanced over statistical production.

Note that a different realization of the SHM using the strangeness canonical ensemble and the multiplicative strangeness suppression factor  $\gamma_s$  for additional strangeness suppression delivers comparable freeze-out parameters, but fails to reproduce the  $\phi$  multiplicity by an order of magnitude due to its suppression with  $\gamma_s^2$ .

### 6.3 Chemical vs. kinetic freeze-out

Figure 6.4: Effective temperature  $T_{eff}$  of all measured particle species as a function of their mass. The horizontal line and error band show the chemical freeze-out temperature  $T_{chem}$  from the THERMUS fit (blue), whereas the red line shows a linear fit to the data points corresponding to non strange particles (red circles).

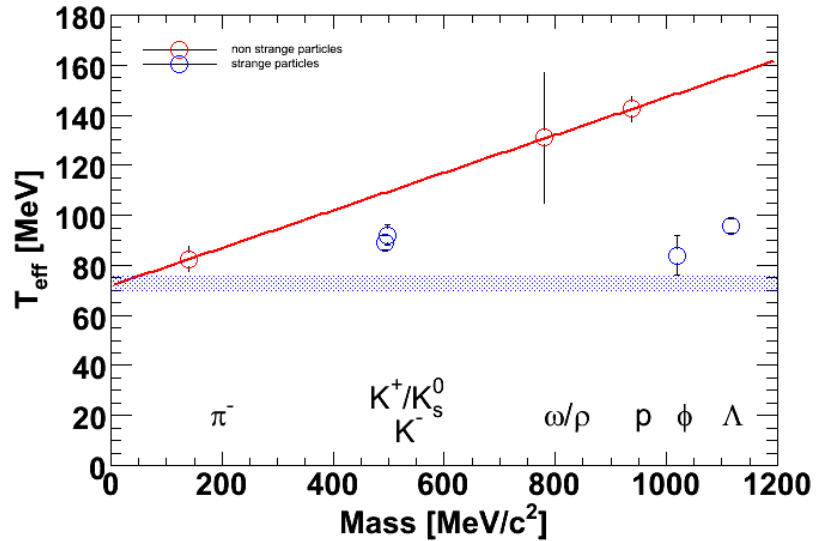


Fig. 6.4 compares the systematics of the inverse-slope parameter  $T_{eff}$  obtained from Boltzmann fits to the  $m_t - m_0$  spectra for the different particle species as a function of their masses to the temperature  $T_{chem}$  obtained for the chemical freeze-out using the SHM. Two trends are visible; while particles containing strangeness are showing a rather flat behavior with increasing mass, the non strange particles show a linear rise with increasing mass. The latter one can be parameterized as a kinetic freeze out temperature  $T_{kin}$  plus a linear term in particle mass which is related to the radial expansion according to:

$$T_{eff} \approx T_{kin} + \frac{1}{2}mc^2 \cdot \langle \beta \rangle^2 \quad (6.8)$$

<sup>1</sup>Note the similarity to the proposed phase of Quarkyonic matter discussed earlier.

The deduced value for the radial flow  $\langle \beta \rangle$  corresponds to  $\approx (0.39 \pm 0.1)$ .

The obtained kinetic freeze out temperature for non strange particles  $T_{kin} = 72 \pm 6$  MeV nicely agrees with the chemical freeze out temperature obtained from the SHM fit  $T_{chem} = 73 \pm 3$  MeV. Apart from the  $K^-$ , which will be discussed in more detail in section 6.3.1, the kinetic freeze out temperature of strange particles seems to be higher, reflecting the need for strangeness suppression in the SHM. The rather flat behavior with increasing mass indicates that strange particles do not participate in the radial expansion, due to their lower reaction cross sections, as discussed in [Oes09].

While at SPS energies, after the sudden drop in  $T_{eff}$  for masses larger than the proton mass, particles show a flat behavior, at RHIC energies a slight rise of  $T_{eff}$  after the drop is observed and interpreted as a sign for flow development in a partonic phase [Oes09]. However the observation of a sudden drop for masses again larger than the proton mass observed in the inverse slope of dimuon spectra is interpreted as a sign for radiation from a partonic phase described in [eaNc09].

### 6.3.1 The different freeze out criteria of charged kaons

A pure Boltzmann shape can be distorted by various effects, like collective motion or early vs. late particle decays. One example is apparent in the difference between the  $K^+/K_s^0$  and  $K^-$  slopes (see Fig. 6.4). The much lower value of  $T_{eff}$  of the  $K^-$  has often been interpreted as due to its much later freeze-out time [eaKC07] neglecting the admixture of soft  $K^-$  stemming from  $\phi$  decays.

Using the event generator PLUTO [PLU04] we generate a cocktail of  $K^-$  arising from the decay of thermal  $\phi$  mesons according to the measured inverse slope of  $T_\phi = 84 \pm 8$  MeV and a thermal source of  $T_{K^-} = T_{K^+} = 89 \pm 1 \pm 2$  MeV corresponding to the measured inverse slope for the positive kaons under the assumption that these two contributions are fully dominating the  $K^-$  spectra and yield. In order to get realistic particle ratios we normalize the rapidity density distributions of the thermal  $K^-$  and the ones resulting from a  $\phi$  decay according to the measured  $\phi/K^-$  ratio. The resulting distributions are shown in the left panel of Fig. 6.5. In the next step the transverse mass distributions around mid-rapidity are scaled in accordance to the rapidity density distributions. A Boltzmann fit according to

$$\frac{1}{m_t^2} \frac{d^2 N}{dm_t dy} = C(y) \exp\left(-\frac{(m_t - m_0)c^2}{T_B(y)}\right). \quad (6.9)$$

is applied in the HADES  $m_t - m_K$  acceptance range 0-200 MeV/c<sup>2</sup> for  $K^-$  in the same way as it was done for the HADES data. The thermal  $K^-$  spectrum, the spectrum of the  $K^-$  which stem from the  $\phi$  decay and the resulting cocktail spectrum are shown in the right panel of figure 6.5. The inverse slope parameter of the  $K^-$  cocktail is found to be  $T_{K^-} = 74$  MeV and agrees within errors with the experimentally obtained value of  $T_{K^-} = 69 \pm 2 \pm 4$  MeV, leaving little room for possible differences in slope due to different freeze-out conditions. For  $K^+$  the effect is negligible due to the much higher production yield, mainly from additional production channels as  $NN \rightarrow N\Delta K^+$ . This effect is similar to the one observed for pions where two different slopes can be extracted from the transverse mass distributions. Here it is generally accepted that the origin of the smaller slope is the decay of a  $\Delta$  resonance into  $N\pi$ .

## 6.4 Summary and conclusions

Applying a statistical model fit to the measured hadron yields, a fair agreement, except for the  $\Xi^-$ , in a strangeness-canonical approach is achieved, considering the facts that semi-central collisions of a medium-sized collision system are used as input. This underlines the assumption that a unique freeze

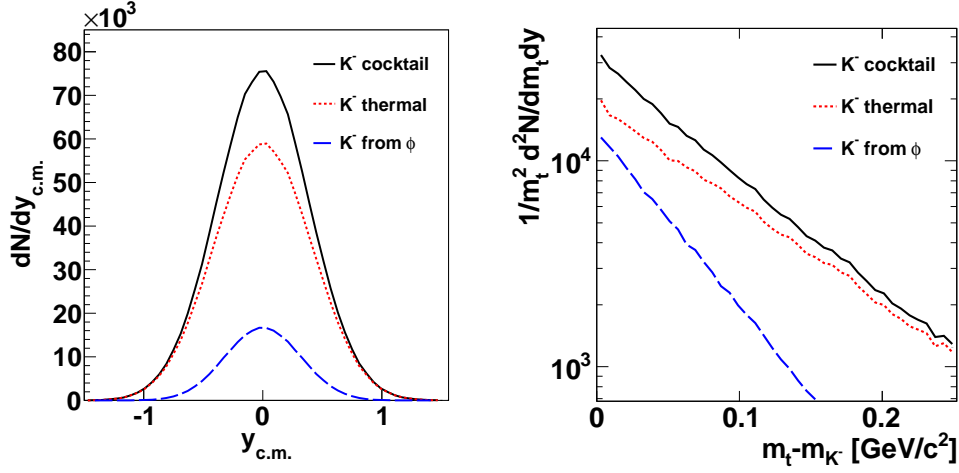


Figure 6.5: Left: According to the measured yields in [eaHC09c] normalized rapidity density distributions of the thermal  $K^-$  and the ones resulting of a  $\phi$ . The black solid line shows the sum of the two distributions. Right: Simulated transverse mass spectra for  $K^-$  coming from a thermal source with a temperature of 89 MeV and those which stem from a  $\phi$  decay. The resulting cocktail spectrum is shown as a black solid line.

out of all particles occurs to some extent.

Two observables show strong enhancements over the expectation values, indicating effects of the strongly interacting medium: Besides the  $\phi$  to  $\omega$  ratio, which shows no indication of any suppression due the OZI rule, the  $\Xi^-$  yield is one magnitude higher as expected from thermal production. The only present scenario which could explain this high yield requires overlapping hadrons and percolating quarks.

The linear dependence of the  $T_{eff}$  of non strange particles suggest a radial expansion velocity  $\langle \beta \rangle$  of  $0.39 \pm 0.1$ . The obtained kinetic freeze out temperature for non strange particles  $T_{kin} = 72 \pm 6$  MeV nicely agrees with the chemical freeze out temperature obtained from the SHM fit  $T_{chem} = 73 \pm 3$  MeV. The kinetic freeze out temperature of strange particles seems to be higher and shows a rather flat behavior with increasing mass indicating lower reaction cross sections of those particles. The difference between the slope of the  $K^-$  and  $K^+$  can be explained by feed-down from of  $\phi$  meson decays.

## Chapter 7

# Summary and outlook

For this thesis, data taken in two measuring campaigns of the HADES spectrometer located at the GSI in Darmstadt were analyzed.

In Ar+KCl collisions at 1.76A GeV an efficiency correction based on simulation was performed for the charged kaons. For their identification the energy loss information of the drift chambers and the time of flight wall are essential. Comparisons of the simulated and experimental distributions showed deviations in both, widths and positions, leading to wrongly estimated efficiencies. Therefore a method was developed to adjust the cuts applied in the simulation in order to make it act in the same way on simulated data as the corresponding cuts on real data. Comparisons with the efficiencies obtained only from data in [Lor08] show a fair agreement after this adjustment.

Furthermore, the dielectron identification in Ar+KCl is based for the first time on a neural network developed in [Lan08]. Comparisons to the standard method showed a low efficiency for electrons and positrons in the TOF region. By adjusting the input variates on which the algorithm bases its identification decision, the efficiencies could be improved by a factor larger than three for electron momenta  $>0.5$  GeV/c.

The hadron yields obtained in several analysis campaigns and thesis are compared to an SHM fit and discussed with respect to the amount of thermalization of the system and the strong deviation observed for double strange particles.

A fair agreement, except for the  $\Xi^-$ , in a strangeness-canonical approach is achieved, considering the facts that semi-central collisions of a medium sized collision system are used as input. This is consistent with the assumption that a unique freeze out of all particles occurs.

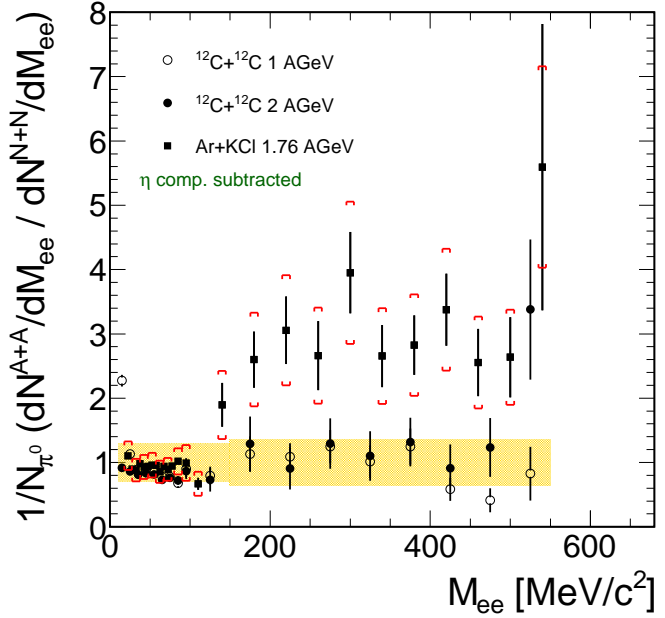
The linear dependence of the  $T_{eff}$  of non strange particles as a function of the particle mass suggests a radial expansion velocity  $\langle \beta \rangle$  of  $\approx 0.39 \pm 0.1$ . The obtained kinetic freeze out temperature for non strange particles  $T_{kin} = 72 \pm 6$  MeV nicely agrees with the chemical freeze out temperature obtained from the SHM fit  $T_{chem} = 73 \pm 3$  MeV. The kinetic freeze out temperature of strange particles seems to be higher and shows a rather flat behavior with increasing mass, which is interpreted as a sign for lower reaction cross sections of those particles in [HOX09]. This interpretation is however in strong contrast to the observation of strong broadening of the  $\phi$  meson inside the medium from cold nuclear matter experiments, as discussed in chapter 1. It was shown by a PLUTO simulation, that the difference between the slope of the  $K^-$  and  $K^+$  can be explained by correcting the spectra for the feed down of  $\phi$  meson decays.

In addition to the  $\phi$  to  $\omega$  ratio, which shows no indication of any suppression due to the OZI rule, and the  $\Xi^-$  yield which is one magnitude higher as expected from thermal production, an excess in the low mass dielectron pairs is observed [eaHC11a], indicating effects of the strongly interacting medium.

The latter one shall be discussed in more detail. As mentioned in chapter 1, the DLS collaboration published dielectron data in 1997, namely from C+C and Ca+Ca collisions at energies of 1-2A GeV [eaDC97]. The observed high yield in the low mass region could for a long time not be explained by transport models [BK99]. Only recently it could be shown by HADES that part of the unexplained excess, is resulting from an insufficient treatment of elementary p+n collisions in the models [eaHC10c]. The yield in the invariant mass region in elementary p+n reactions is much stronger compared to p+p reactions. Therefore a simple superposition of p+n and p+p dielectron data normalized to the neutral pion yield and after subtracting the  $\eta$  contribution from all data samples, is able to explain the C+C data at a kinetic energy of 1 GeV, see Fig. 7.1. Moreover also the C+C data at a kinetic beam energy of 2 GeV are close to this elementary reference. One can conclude, that this trivial excess has the same energy scaling like the production of pions. Comparing however dielectron radiation from Ar+KCl collisions at 1.76A GeV to the elementary reference, one observes a strong excess suggesting the onset of additional effects of the medium.

Further analysis campaigns of light clusters [Sch12b], in order to better characterize bulk observ-

Figure 7.1: Ratio of dielectron yields from C+C and Ar+KCl collisions to an elementary reference consisting of p+p and p+n collisions, normalized to the neutral pion yield and after subtracting the  $\eta$  contribution from all data samples. While the C+C data can be well explained by a superposition of elementary reactions, in case of Ar+KCl data a clear excess is observed.



ables of the collisions, as well as on the first excitations of hyperons [Reh11] and on exotic clusters containing strangeness [Sch12a] are ongoing.

The main part of this thesis deals however with the analysis of dielectron radiation from p+Nb reactions at 3.5 GeV recorded in September 2008. Technical challenges were to adapt the multivariate analysis to the low multiplicity environment and to do a careful comparison to the standard electron identification method in order to reduce systematic uncertainties and to learn more about the advantages and disadvantages of both methods. It could be clearly shown that already in the low multiplicity environment of p+Nb reactions the MVA has on average 20% higher efficiencies compared to the standard method of hard cuts, while the signal to background ratio in the final dielectron spectra showed no differences between the two methods. The focus on the interpretation of the data is put on the modification of the vector meson line shape by comparing the p+Nb dielectron spectra to data from elementary p+p collisions. Furthermore emphasis is put on the additional effects for a nuclear

modification of the cross section, like particle production in secondary reactions.

The best theoretical description of the p+p data is achieved by introducing a coupling of the  $\rho$  to baryonic resonances e.g.  $N^*(1520)$ , leading to modifications of the  $\rho$  meson line shape due to phase space restrictions of the resonance decays. These modifications already in elementary p+p collisions complicate the extraction of further modifications of the line shape in the p+Nb data due to the medium.

Comparing the line shape of the p+p with the p+Nb invariant mass spectra, normalized to the number of neutral pions, no significant difference is visible. The situation changes significantly if one applies a selection on the pair momenta. While for pair momenta larger than 0.8 GeV/c the spectra still agree, for smaller momenta a strong modification in the vector meson region, where modification due to the nuclear medium are predicted by hadronic models, is observed.

The nuclear modification factor  $R_{pA}$  shows a rise for all regions of the invariant mass for small momenta, pointing to a strong contribution from secondary reactions as also indicated by a shift in rapidity. The value for identified  $\omega$  stays flat over the whole region, pointing to no large contribution from secondary reactions to the  $\omega$  yield. This could be explained by an increase of its in-medium width resulting in a massively reduced partial branching ratio to dielectrons.

Comparing the presented results to other experiments we find good agreement on the nuclear suppression of  $\omega$  mesons. The hints for a flat behavior of this modifications as a function of the momentum, reported recently by the CBELSA-TAPS collaboration can be confirmed. Moreover the modification of the line shape in the vector meson region for slow pairs, represents the first measurement sensitive to the momentum region where the modification are expected to be most pronounced.

The relation between chiral condensates and hadronic spectral functions is not trivial, since the condensates are only related to the integral of the latter one. Therefore the spectral functions are constrained but not determined and one still needs hadronic models for predictions of specific hadron properties. In order to claim a (partial) restoration of chiral symmetry, one would need to show that the broadening of the spectral shape goes beyond trivial effects due to e.g. production via resonances etc.

Comparing the modification of different particles, one might be able to get more control on the various effects. At the moment several analysis of hadronic decay channels of the p+Nb data are proceeding. In [Kre10] it was shown that the reconstruction of  $\phi$  mesons is possible in the two charged kaon decay channel, although the start time is lacking for this experiment due to problems with the start detector. The reconstructed signal is shown in Fig. 7.2. The analysis will be refined and the data corrected for efficiency in [Wenon]. Furthermore, the analysis of the neutral kaons in p+p [CBon] and p+Nb collisions [Kir11] might give new insights to the kaon nucleon potential by comparing the energy spectra of both data samples, as well as on the general characteristics of the reaction kinematics.

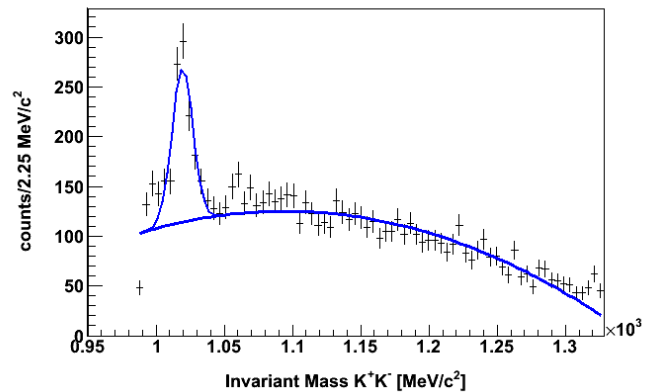
Combining the observation of the reversed OZI suppression, the high  $\Xi^-$  yield and the low mass dielectron excess in Ar+KCl collisions with the observation in cold nuclear matter of a strong modification of the spectral shape for slow dielectrons in the vector meson invariant mass region, we conclude on a very strong broadening of particle states inside the medium.

As a consequence radiation from a broadened  $\rho$  and baryonic resonances won't be distinguishable anymore <sup>1</sup>. Furthermore, the great extent of thermalization observed for the Ar+KCl system could then be driven by these broad states, which might also enhance the production of double strange particles as discussed in section 6.2.4.

---

<sup>1</sup>Probably, due to the strong coupling it does not make sense to distinguish between them in order to explain the enhancement, anyway.

Figure 7.2: Invariant mass spectra of negative and positive charged kaons from the p+Nb data set. Although no start time measurement is available a significant signal of the  $\phi$  meson is visible.



## 7.1 The upgraded HADES

In order to deliver excellent data on collision systems like Ag+Ag and Au+Au an extensive upgrade project of the HADES setup has been completed.

A major part of the project was the upgrade of the trigger and data acquisition system (DAQ) with the

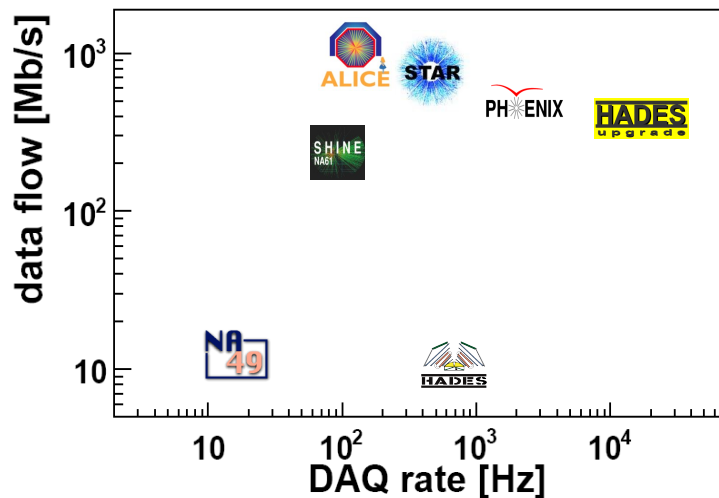


Figure 7.3: Comparison of the data flow as a function of the event rate written to the storage for different HIC experiments. For the upgraded HADES setup the design values are shown. A comparison of these values should be done with precaution due to different online trigger mechanisms used in the various experimental setups.

goal to increase the event rate capability by a factor of up to 20 to reach 100 kHz in elementary and 20 kHz in Au+Au, and to achieve a data rate written to the storage of 400 MByte/s. These values can be compared to other HIC experiments under some precautions due to different online trigger mechanism, see Fig. 7.3. In order to achieve the design goals, the complete read-out system was exchanged to FPGA-based platforms using optical communication and, for the data transport, a general-purpose real-time network protocol was developed. More than 500 FPGAs are included in the final setup of

the complete system. In order to detect and correct transmission errors due to electromagnetic noise environment and radiation damage, several detection and correction features are included [Miced]. Furthermore, the low granularity scintillator time of flight wall (TOFino) at low polar angles between  $18^\circ$  and  $45^\circ$  was replaced by high granularity resistive plate chambers (RPCs) in 2010 [Fon01]. The intrinsic time resolution of the detector is at the order of 80 ps. The charged kaon analysis, which has been restricted before to the TOF region at high polar angles only, will benefit most from the new RPCs.

A forward wall, in order to allow event plane reconstruction and to enable measurements of the flow parameter  $v_1$  and  $v_2$ , two other important observables to characterize a HIC, was also added to the setup [AuA].

In addition, the cluster finding and track reconstruction procedure had to be completely redeveloped in order to be able to handle the high multiplicity environment of a Au+Au reaction [AuA].

A test beam time with the upgraded setup done in August 2011 showed promising results. In total,



Figure 7.4: The top view of the planned facility for antiproton and ion research in Darmstadt, for details on the project see [Fai11]

for 64 hours, a Au beam with an intensity of  $1.3 \cdot 10^6$  ions per second was incident on a segmented Au target. The achieved trigger rate of 8 kHz and data rate of 200 Mbyte/s are already close to the design values. In total,  $0.84 \cdot 10^9$  events, corresponding to  $17 \cdot 10^{12}$  byte of data, were collected. The amount of collected data in these four days corresponds to half the data volume collected in all previous measuring campaigns added.

Concerning the validity of the creation of the training samples for MVA in the high multiplicity environments, preliminary analysis showed, that after applying selections on the track quality, the number of tracks corresponding to a RICH ring in a sharp matching radius is around 1-2 [Tan11]. Hence a generation of the training samples only from data seems to be also possible for Au+Au collisions.

For the future, from 2018 on, HADES will provide for the first time the opportunity to perform di-electron measurements at kinetic energies between 2-8A GeV at the planned SIS100 accelerator at the new **F**acility for **A**ntiproton and **I**on **R**esearch (FAIR) in Darmstadt, see Fig.7.4. For details on the HADES program at FAIR see [Fai] and for details on the facility [Fai11].



## Chapter 8

# Zusammenfassung

Die Entstehung von Masse ist eine der großen fundamentalen Fragen der modernen Physik. Nach unserem heutigen Kenntnisstand sind die kleinsten Bausteine der Kernmaterie sogenannte Quarks. Diese Quarks können auf Grund ihrer gegenseitigen starken Wechselwirkung, theoretisch beschrieben durch die Quanten Chromo Dynamik (QCD), nicht frei existieren. Sie sind eingesperrt in einem um das fünfzigfach schwereren "Beutel" aus Vakuumfluktuationen, mit dem sie zusammen das Nukleon formen.

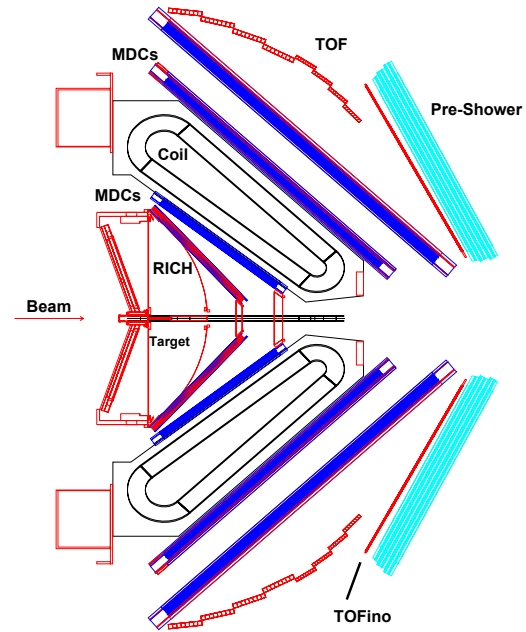
Die besonderen Eigenschaften der starken Wechselwirkung haben bis heute ein tieferes Verständnis über den Prozess dieser Massenerzeugung verhindert. Aufgrund theoretischer Überlegungen und Modelle erwartet man jedoch eine Veränderung dieses Prozesses für höhere Materiedichten und/oder Temperaturen. Man erwartet, dass diese am stärksten für Teilchen mit langsamen Relativgeschwindigkeiten zum umgebenden Medium ausgeprägt sind.

Experimentell lassen sich höhere Materiedichten und Temperaturen in relativistischen Kollisionen schwerer Ionen realisieren. Protonen, Photonen oder Pionen induzierte Reaktionen in schweren Kernen, sogenannte kalte Materie Experimente, bieten eine weitere Möglichkeit die Dichte bis zur nuklearen Grundzustandsdichte  $\rho_0$  zu erhöhen. Beide Methoden haben ihre Vor- und Nachteile. So erwartet man stärkere Effekte in Schwerion-Kollisionen, aufgrund der höheren Dichten und Temperaturen, die dort erreicht werden. Das generierte System durchläuft jedoch nach den ersten Nukleon-Nukleon Kollisionen verschiedene Phasen unterschiedlicher Dichten, in denen Teilchen emittiert werden. Signale stellen also immer eine Überlagerung der Signale aus den verschiedenen Phasen da, was die Isolierung von Effekten bestimmter Phasen erschwert.

Experimente mit kalter nuklearer Materie auf der anderen Seite haben den Vorteil, dass das System keine Dichteevolution durchläuft. In dieser Arbeit werden Daten zweier Messkampagnen, Ar+KCl und p+Nb Kollisionen, des an der GSI in Darmstadt installierten HADES Spektrometers analysiert und Ergebnisse der zwei zuvor beschriebenen unterschiedlichen experimentellen Zugängen zu Mediummodifikationen diskutiert.

Abbildung 8.1 zeigt den schematischen Aufbau des HADES-Spektrometers. Die Vieldrahtdriftkammern (**M**ulti-**w**ire **D**rift **C**hambers **M**DC) dienen zur Spurverfolgung der geladenen Teilchen und sind in sechs Sektoren in jeweils zwei Ebenen vor und hinter dem supraleitenden Magneten ILSE (**I**ron**L**ess **S**uperconducting **E**lectromagnet) angebracht. Der ringabbildende Cherenkov Detektor RICH (**R**ing **I**maging **C**herenkov) und der SHOWER Detektor dienen wesentlich der Leptonenidentifikation, während TOF und TOFino (**T**ime **O**f **F**light) die Flugzeit der Teilchen messen. Für Ar+KCl Kollisionen bei einer kinetischen Strahlenergie von 1.76A GeV werden Effizienzkorrekturen, basierend auf Simulationen, für geladene Kaonen durchgeführt. Um diese zu identifizieren ist die Energieverlustin-

Figure 8.1: Schematischer Aufbau des HADES-Spektrometers. Der Strahl wird auf ein segmentiertes Target gelenkt, das von einem RICH Detektor zur Elektron/Positron-Identifizierung umgeben ist. Das Magnet-Spektrometer besteht aus zwei Ebenen von Driftkammern, vor und hinter einem supraleitenden Magneten, dessen Feldgeometrie so gewählt wurde, dass die Detektoren sich in feldfreien Regionen befinden. Am Ende des Aufbaus sind Szintillatoren-Flugzeitwände und ein elektromagnetischer Pre-Shower Detektor angebracht.



formation in den Driftkammern und den Flugzeitwänden essentiell. Im Vergleich der simulierten mit den experimentell gemessenen Verteilungen zeigten sich jedoch Abweichungen, die eine Anpassung der für die Simulation verwendeten Auswahlsschnitte erforderten. Sie wurden derart angepasst, dass sie auf simulierte Daten genauso wirken, wie die entsprechenden Auswahlsschnitte auf echte Daten. Weiter wurde die Dielektronen-Identifizierung, die in dieser Strahlzeit zum ersten Mal auf einem neuronalen Netzwerk basierte [Lan08], in Bezug auf Effizienz verbessert. Durch Änderung der als Eingabe in das neuronale Netzwerk verwendeten Detektorinformationen konnte diese um mehr als einen Faktor drei in der TOF-Region des Detektors für Impulse größer als 0.5 GeV/c verbessert werden.

Aufgrund der Eingangs erwähnten verschiedenen Phasen, die eine Schwerionenkollision durchläuft, ist es wichtig diese anhand geeigneter Observablen möglichst genau klassifizieren zu können, um später die beobachteten Effekte möglichst genau den einzelnen Phasen zuordnen zu können. Charakteristisch für die Ausfrierphase sind die gemessenen Hadronen-Raten. Durch Anpassung dieser Raten mit einem statistischen Hadronisierungsmodell (SHM) kann man Rückschlüsse auf den Grad der erreichten Thermalisierung des Systems ziehen. In der Tat beschreibt ein SHM-Fit alle Teilchenraten, bis auf die des  $\Xi^-$  Hyperon, zufriedenstellend. Letztere zeigen eine deutliche Überhöhung über dem thermischen Erwartungswert. Der Vergleich der verschiedenen Raten mit den SHM Werten ist in Abbildung 8.2 dargestellt. Darüber hinaus lässt sich über diese Anpassung der sogenannte Ausfrierpunkt anhand der beiden Parameter  $T$  (Temperatur) und  $\mu_b$  (baryochemisches Potential) im Phasendiagramm der stark wechselwirkenden Materie bestimmen.

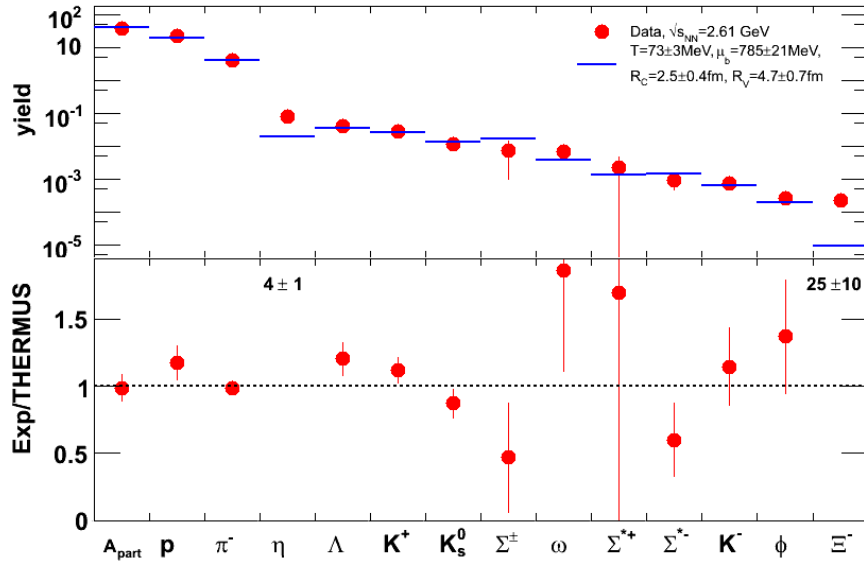


Figure 8.2: Im oberen Bereich ist der Vergleich der Hadron-Raten in Ar+KCl Kollisionen (rote Kreise) mit den entsprechenden Werten des statistischen Modell (SHM) Fits (blaue Balken) dargestellt, während die Verhältnisse der Werte im unteren Bereich gezeigt wird. Die Verhältnisse für  $\Xi^-$ -Hyperonen und für  $\eta$ -Mesonen sind als Zahlenwerte ausgewiesen.

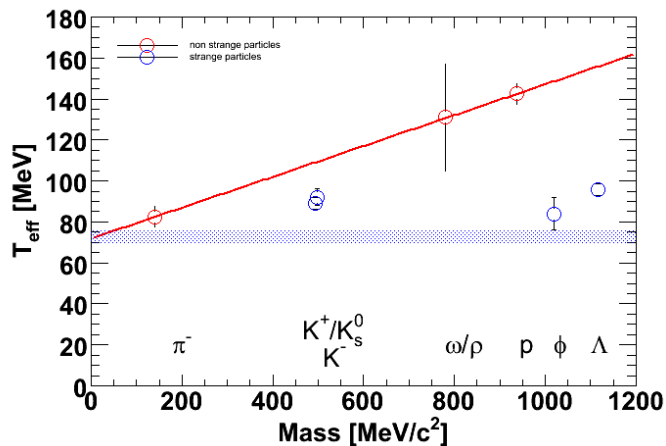


Figure 8.3: Effektive Temperaturen  $T_{eff}$  aller gemessenen Teilchenarten als Funktion ihrer Masse. Die horizontale Linie stellt die chemische Ausfrieretemperatur  $T_{chem}$  bestimmt mittels eines SHM Fits (blau) dar, während die rote Linie eine lineare Anpassung an die Datenpunkte der Teilchen ohne Strangeness-Inhalt darstellt, für Details siehe Text. Dies ist ein Maß für den radialen Fluß  $\langle \beta \rangle \approx 0.39 \pm 0.1$ .

Die lineare Abhängigkeit von  $T_{eff}$  von Teilchen ohne Strangeness-Inhalt deutet auf eine radiale Expansionsgeschwindigkeit von  $\langle \beta \rangle \approx 0.39 \pm 0.1$  hin. Die bestimmte kinetische Ausfrieretemperatur  $T_{kin} = 72 \pm 6$  MeV stimmt sehr gut mit der chemischen Ausfrieretemperatur von  $T_{chem} = 73 \pm 3$  MeV, bestimmt mittels des SHM-Fits, überein. Die kinetischen Ausfrieretemperaturen der Teilchen mit Strangeness-Inhalt zeigen keinen starken Anstieg zu höheren Massen, siehe Abbildung 8.3. Anhand einer PLUTO-Simulation konnte gezeigt werden, dass die beobachteten unterschiedlichen inversen Steigungsparameter der geladenen Kaonen durch Korrektur der Beiträge aus Zerfällen des  $\phi$  Mesons erklärt werden können, und nicht notwendigerweise auf einen späteren Ausfrierzeitpunkt, aufgrund des bisher als dominant für die  $K^-$  Produktion angesehenen Strangeness-Austausch-Prozess, hindeuten.

Zusätzlich zu der beobachteten Erhöhung in der Dileptonen-Rate, zeigt das  $\phi$  zu  $\omega$  Verhältnis keinerlei Anzeichen für eine Unterdrückung aufgrund der OZI-Regel, sowie die Rate der  $\Xi^-$  eine starke Überhöhung über der SHM Vorhersage. Alle drei Beobachtungen deuten auf Medium Effekte hin.

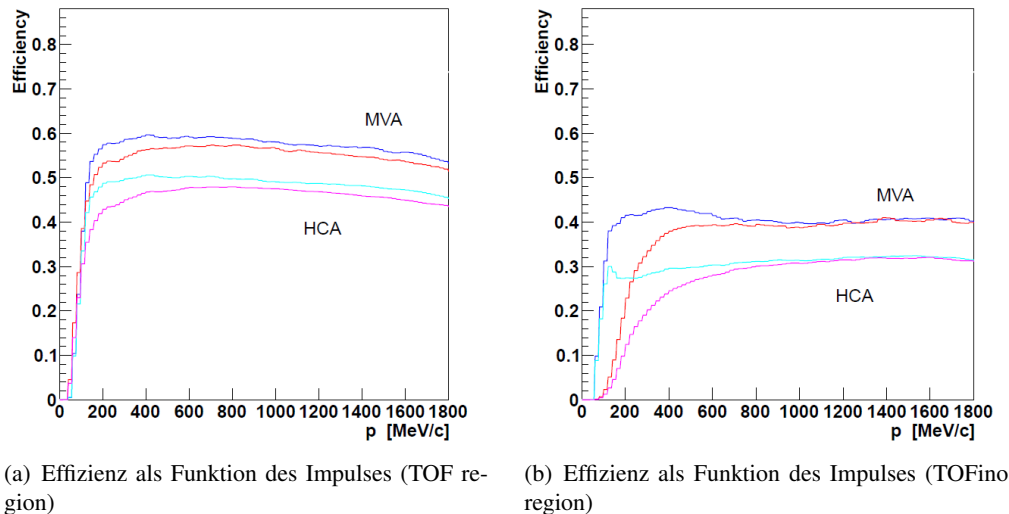


Figure 8.4: Vergleich der jeweiligen Effizienzen zur Elektronen- und Positronen-Rekonstruktion als Funktion des Impulses in der TOF- (linke Seite) und TOFino-Region (rechte Seite). Die Effizienzen der MVA Methode sind in rot (Positronen) und blau (Elektronen), während die der Standard-Methode (HCA) in pink und hellblau dargestellt sind.

Der Hauptteil der Arbeit behandelt die Analyse von Dielektronenstrahlung aus p+Nb Reaktionen bei einer kinetischen Strahlenergie von 3.5 GeV. Die technische Herausforderung bestand darin, die multivariate Analyse an die geringe Spurdichte der p+Nb Umgebung anzupassen. Weiter wurden systematische Vergleiche zur Standard-Elektronen-Identifizierung Methode mit dem Ziel mehr über die Eigenarten der beiden Methoden zu lernen und sie verbessern zu können, durchgeführt. Es konnte gezeigt werden, dass die multivariate Analyse eine um mehr als 20% bessere Effizienz für Elektronen und Positronen bei vergleichbarem Signal zu Untergrundverhältnis erzielt. Der Vergleich der jeweiligen Effizienzen der Elektronen- und Positronen-Rekonstruktion als Funktion des Impulses in der TOFino- und TOF-Region ist in Abbildung 8.4 dargestellt.

In der Interpretation der Daten wird der Fokus auf die Modifikation der Dielektronen-Linienform im Vergleich mit elementaren p+p Reaktionen gelegt. Darüber hinaus wird die nukleare Modifikation

der Raten diskutiert. Diese ist sensitiv auf eine mögliche Verbreiterung der Mesonen im Medium, da dadurch die partielle Verzweigung in den Dielektronenzerfallskanal verringert wird, und somit die gemessene Rate relativ zur elementaren Produktion reduziert wird.

Es zeigt sich, dass die theoretisch beste Beschreibung der p+p Daten erzielt wird, indem man eine Kopplung der  $\rho$  Mesonen an baryonische Resonanzen einführt. Als Konsequenz aus den Phasenraumbeschränkungen dieser Resonanzzerfälle wird allerdings die Linienform schon in elementaren Reaktionen verändert. Dieser Umstand kompliziert die Isolierung von Modifikationen der Linienform aufgrund weiterer Medium-Effekte in p+Nb Reaktionen.

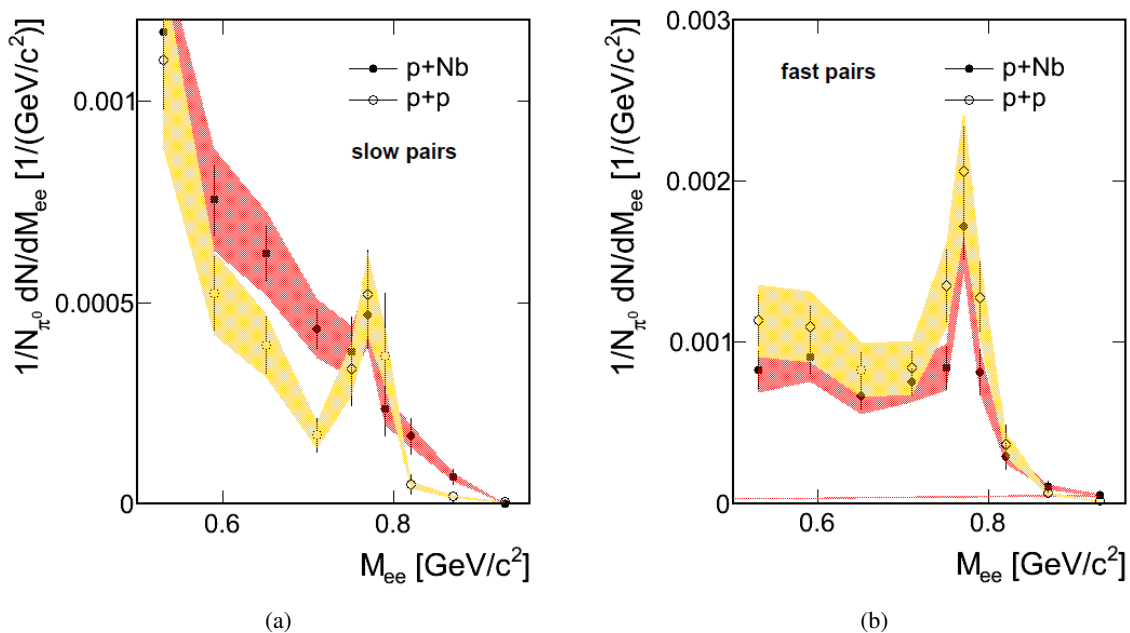
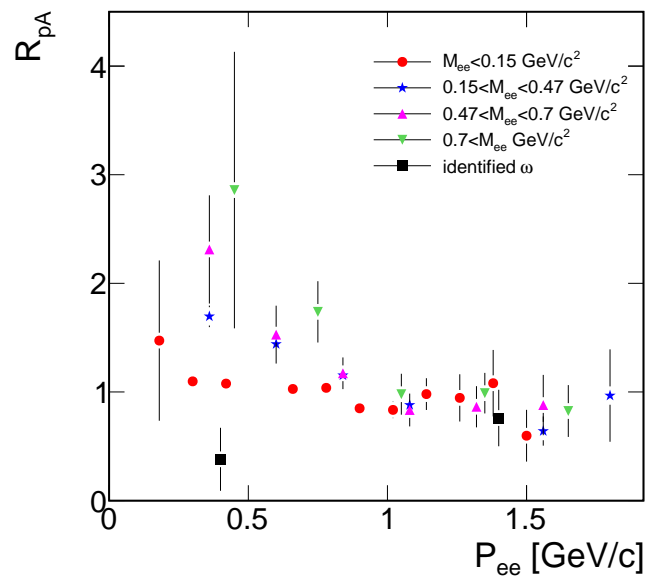


Figure 8.5: Vergleich der Linienform für langsame Paare ( $P_{ee} < 0.8$  GeV/c) in der Vektormeson-Massenregion (linke Seite) und für schnelle Paare ( $P_{ee} > 0.8$  GeV/c) (rechte Seite). Für langsame Paare zeigt sich eine starke Modifikation, während für schnelle Paare viel schwächere Abweichungen beobachtet werden.

Es zeigt sich im Vergleich der Linienform für langsame Paare in der Vektormeson-Massenregion eine starke Modifikation, während für schnelle Paare keine starken Abweichungen beobachtet werden, siehe Abbildung 8.5. Der nukleare Modifikationsfaktor  $R_{pA}$  zeigt einen Anstieg zu niedrigen Impulsen in allen Massenbereichen. Zusammen mit der beobachteten Verschiebung der Rapiditätsverteilungen deutet dies auf starke Beiträge von Teilchenproduktion in sekundären Reaktionen hin, siehe 8.6. Im Gegensatz zeigen die Werte für identifizierte  $\omega$ -Mesonen ein flaches Verhalten. Dies kann zum Beispiel durch eine starke Verbreiterung des  $\omega$ -Mesons im Medium und daraus resultierendem verringertem Verzweigungsverhältnis zu Dielektronen erklärt werden wie sie auch in Photon-induzierten Reaktionen gefunden wurde.

Darüber hinaus zeigen die Resultate zur nuklearen Modifikation von  $\omega$  Mesonen gute Übereinstimmungen mit anderen Experimenten.

Figure 8.6: Nukleare Modifikation  $R_{pA}$  als Funktion des Paarimpulses. In allen Massenbereichen ist ein Anstieg zu niedrigen Impulsen zu beobachten. Im Gegensatz zeigen die Werte für identifizierte  $\omega$ -Mesonen ein flaches Verhalten.



## Appendix A

# Abbreviations register

Abbreviation	Meaning	Explanation
<b>Experimental Facilities</b>		
GSI	Helmholtzzentrum für Schwerionenforschung	Darmstadt, Germany
FAIR	Facility for Antiproton and Ion Research	planned facility in Darmstadt, Germany
CERN	European Organization for Nuclear Research	near Geneva, Europe
BNL	Brookhaven National Laboratory	Brookhaven, USA
KEK	High Energy Accelerator Research Organization	Tsukuba, Japan
<b>Accelerators</b>		
SIS 18	Schwerionen Synchrotron	located at GSI, Germany
AGS	Alternating Gradient Synchrotron	located at BNL, USA
SPS	Super Proton Synchrotron	located at CERN, Europe
RHIC	Relativistic Heavy Ion Collider	located at BNL, USA
LHC	Large Hadron Collider	located at CERN, Europe

Table A.1

<b>Abbreviation</b>	<b>Meaning</b>	<b>Explanation</b>
<b>Analysis and Physics</b>		
HIC	Heavy-Ion Collision	
QCD	Quantum Chromo Dynamic	Theory of the strong interaction
SHM	Statistical Hadronization Model	
OZI	Okuba, Zweig, Iizuka rule	Decays with disconnected quark lines are suppressed
HCA	Hard Cut Analysis	Standard HADES dielectron analysis
MVA	Multivariate Analysis	All cut criteria are fed into one algorithm
PID	Particle Identification	
LVL1	HADES Level 1 Trigger	multiplicity selection
LVL2	HADES Level 2 Trigger	electron selection
<b>Nuclei and Molecules</b>		
Ar	Argon	A=40
KCl	Potassium Chloride	$A \approx 37$
Nb	Niobium	A=93
<b>HADES detectors</b>		
MDC	Multiwire Driftchambers	Main tracking detectors
RICH	Ring Imaging Cherenkov	Electron identification
TOF	Time of Flight Wall	High granularity scintillator detector, located at polar angles of 45-85°
TOFino	Time of Flight Wall (small)	Low granularity scintillator detector, located at polar angles of 18-45°

Table A.2

# Bibliography

- [AAS06] P. Braun-Munzinger A. Andronic and J. Stachel. Hadron production in central nucleus nucleus collisions at chemical freeze-out. *Nucl. Phys., A* 772(167), 2006. 121
- [ABea11] M. Cheng C. DeTar H. T. Ding S. Gottlieb R. Gupta A. Bazavov, T. Bhattacharya and P. Hegde et al. The chiral and deconfinement aspects of the QCD transition. arXiv:1111.1710 [hep-lat] 2011. 22
- [ABM98] W. G. Moorhead A Baldini, V. Flaminio and D. R. O. Morrison. *Landolt-Börnstein, New Series, Springer, I/12a*, 1998. 85, 122
- [APea11] Y. .T. Kiselev E. Y. .Paryev M. Buscher D. Chiladze S. Dymov A. Polyanskiy, M. Hartmann and A. Dzyuba et al. Measurement of the in-medium phi-meson width in proton-nucleus collisions. *Phys. Lett. B*, 695(74), [arXiv:1008.0232 [nucl-ex]] 2011. 20
- [App93] Geant - detector description and simulation tool, 1993. 40, 44, 67
- [APr09] A. Prehn, private communication, 2009. 48
- [AuA] Investigation of baryon rich dense nuclear matter by means of rare probes with HADES, beamtime proposal, HADES collaboration, 2010. 131
- [Bea] Vector meson production in  $pA$  and  $\pi A$  collisions, beamtime proposal, HADES collaboration, 2006. 47, 90
- [Bea08] Study of different expressions for Delta Dalitz decay dilepton mass spectra. HADES internal report, 2008. 78
- [Bel11] [http://en.wikipedia.org/wiki/Bell\\_test\\_experiments/](http://en.wikipedia.org/wiki/Bell_test_experiments/), 2011. 11
- [BK99] E. L. Bratkovskaya and C. M. Ko. Low-mass dileptons and dropping rho meson mass. *Phys. Lett. B*, 445(265), [arXiv:nucl-th/9809056] 1999. 26, 27, 128
- [BM88] V. Bernard and Ulf G. Meissner. *Nucl. Phys.*, A489, 1988. 14
- [BR91] G. E. Brown and M. Rho. Scaling effective lagrangians in a dense medium. *Phys. Rev. Lett.*, 66(2720), 1991. 14
- [CBon] C. Chen-Berger. Dissertation, Physik-Department der Technischen Universität München, Institut E12, in preparation. 129
- [CHA] Y. Leifels E. L. Bratkovskaya C. Hartnack, H. Oeschler and J. Aichelin. Strangeness production close to threshold in proton-nucleus and heavy-ion collisions. arXiv:1106.2083 [nucl-th]. 25, 29

- [DAea08] D. Antonczyk H. Appelshauser V. Belaga J. Bielcikova P. Braun-Munzinger D. Adamova, G. Agakichiev and O. Busch et al. Modification of the rho-meson detected by low-mass electron-positron pairs in central Pb-Au collisions at 158-A-GeV/c. *Phys. Lett. B*, 666(425), [nucl-ex/0611022] 2008. 27
- [dar] [www-linux.gsi.de/misko/overlap/](http://www-linux.gsi.de/misko/overlap/). 85
- [eaa] J. Weil et al. Dilepton production in proton-induced reactions at SIS energies with the GiBUU transport model. arXiv:1203.3557 [nucl-th]. 79, 81
- [eab] O. Buss et al. Transport-theoretical description of nuclear reactions. arXiv:1106.1344 [hep-ph]. 77
- [ea97] R. Rapp et al. *Nucl. Phys.*, A617, 1997. 14
- [ea99] J. Cleymans et al. *Phys. Rev. C* 59(1663), 1999. 121
- [ea03] A. Mangiarotti et al. Sub-threshold phi meson yield in central Ni-58 + Ni-58 collisions. *Nucl. Phys. A*, 714:89, 2003. 29
- [ea05] T. Ishikawa et al. Phi photo-production from Li, C, Al, and Cu nuclei at  $E(\gamma) = 1.5\text{-GeV} - 2.4\text{-gev}$ . *Phys. Lett. B*, 608(215), [arXiv:nucl-ex/0411016] 2005. 20
- [ea06] T. Tabaru et al. *Phys. Rev. C*, 025201, 2006. 20, 97
- [ea07] M. Merschmeyer et al. K0 and lambda production in Ni+Ni collisions near threshold. *Phys. Rev. C*, 76(024906), 2007. 29
- [ea10a] A. Andronic et al. Hadron Production in Ultra-relativistic Nuclear Collisions: Quarkyonic Matter and a Triple Point in the Phase Diagram of QCD. *Nucl. Phys.*, A 837(65), [arXiv:0911.4806 [hep-ph]] 2010. 23, 25, 120, 121
- [ea10b] I. Frohlich et al. A versatile method for simulating pp – pp e+ e- and dp – pn e+ e-p(spec) reactions. *Eur. Phys. J.*, A 45(401), [arXiv:0909.5373 [nucl-ex]] 2010. 79
- [eaAC06] M. Hartmann et al. (ANKE Collab.). *Phys. Rev. Lett.*, 96(242301), 2006. 122
- [eaAC08] Y. Maeda et al. [ANKE Collaboration]. Kaon pair production in proton–proton collisions. *Phys. Rev.*, C77(015204), 2008. 122
- [eaC10] A. Adare et al.(PHENIX Collaboration). Detailed measurement of the  $e^+e^-$  pair continuum in  $p + p$  and au+au collisions at  $\sqrt{s_{nn}} = 200$  gev and implications for direct photon production. *Phys. Rev.C*, 81(034911), [arXiv:0912.0244 [nucl-ex]] 2010. 27
- [eaCC07] R. Nasseripour et al. (CLAS Collaboration). *Phys. Rev. Lett.*, 99(262302), 2007. 15, 17, 19, 90, 97
- [eaCC10a] M. Nanova et al. [CBELSA/TAPS Collaboration]. In-medium omega mass from the  $\gamma + \text{Nb} \rightarrow \pi^0 \gamma + X$  reaction. *Phys. Rev.*, C 82(035209), [arXiv:1005.5694 [nucl-ex]]. 2010. 47
- [eaCC10b] M. H. Wood et al. (CLAS Collaboration). Absorption of the  $\omega$  and  $\phi$  mesons in nuclei. *Phys. Rev. Lett*, 105(112301), [arXiv:1006.3361 [nucl-ex]] 2010. 18, 20, 97

- [eaCTC08] M. Kotulla et al. (CBELSA-TAPS Collaboration). Modification of the  $\omega$ -meson lifetime in nuclear matter. *Phys. Rev. Lett.*, 100(192302), [arXiv:0802.0989 [nucl-ex]] 2008. 18, 20, 91, 95, 97
- [eaDC97] R. J. Porter et al. (DLS Collaboration). Dielectron cross section measurements in nucleus nucleus reactions at 1.0-A-GeV. *Phys. Rev. Lett.*, 79(1229), [arXiv:nucl-ex/9703001] 1997. 27, 128
- [eaDC98] W.K. Wilson et al. (DLS Collaboration). Inclusive dielectron cross-sections in p + p and p + d interactions at beam energies from 1.04-GeV to 4.88-GeV. *Phys. Rev.*, C57:1865–1878, [nucl-ex/9708002] 1998. 82
- [eaDC01] F. Balestra et al. (DISTO Collab.). *Phys. Rev. C*, 63(024004), 2001. 122
- [eaEC03] P. Chung et al. [E895 Collaboration]. Near-threshold production of the multi-strange Xi- hyperon. *Phys. Rev. Lett.*, 91(202301), [arXiv:nucl-ex/0302021] 2003. 123
- [eaEC06] M. Naruki et al. (E325 Collaboration). Experimental signature of the medium modification for rho and omega mesons in 12-GeV p + A reactions. *Phys. Rev. Lett.*, 96(092301), [arXiv:nucl-ex/0504016] 2006. 16, 90, 97
- [eaFC07a] M. Merschmeyer et al. (FOPI Collaboration). *Phys. Rev.*, C 76(024906), 2007. 119
- [eaFC07b] X. Lopez et al. [FOPI Collaboration]. Subthreshold production of Sigma(1385) baryons in Al+Al collisions at 1.9A GeV. *Phys. Rev.*, C 76(052203), [arXiv:0710.5007 [nucl-ex]] 2007. 121
- [eaFC10] W. Reisdorf et al. (FOPI Collaboration). Systematics of central heavy ion collisions in the 1A GeV regime. *Nucl. Phys. A*, 848:366, [arXiv:1005.3418 [nucl-ex]] 2010. 25
- [eaHC] P. Tlustý et al. [HADES Collaboration]. Charged pion production in C+C and Ar+KCl collisions measured with HADES. [arXiv:0906.2309 [nucl-ex]]. 100
- [eaHC09a] G. Agakishiev et al. [HADES Collaboration]. Deep sub-threshold Xi- production in Ar+KCl reactions at 1.76A-GeV. *Phys. Rev. Lett.*, 103(132301), [arXiv:0907.3582 [nucl-ex]]. 2009. 100, 118
- [eaHC09b] G. Agakishiev et al. [HADES Collaboration]. The High-Acceptance Dielectron Spectrometer HADES. *Eur. Phys. J.*, A 41(243), [arXiv:0902.3478 [nucl-ex]]. 2009. 33, 36, 37, 38, 39, 40, 41, 42
- [eaHC09c] G. Agakishiev et al. [HADES Collaboration]. Phi decay: A relevant source for K- production at SIS energies? *Phys. Rev.*, C 80(025209), [arXiv:0902.3487 [nucl-ex]]. 2009. 29, 100, 101, 115, 118, 122, 126
- [eaHC10a] G. Agakishiev et al. [HADES Collaboration]. In-Medium Effects on  $K^0$  Mesons in Relativistic Heavy-Ion Collisions. *Phys. Rev.*, C 82(044907), [arXiv:1004.3881 [nucl-ex]]. 2010. 100, 118
- [eaHC10b] G. Agakishiev et al. [HADES Collaboration]. Lambda-p femtoscopy in collisions of Ar+KCl at 1.76 AGeV. *Phys. Rev.*, C 82(021901), [arXiv:1004.2328 [nucl-ex]]. 2010. 100

- [eaHC10c] G. Agakishiev et al. (HADES Collaboration). Origin of the low-mass electron pair excess in light nucleus-nucleus collisions. *Phys. Lett. B*, 690:118, [arXiv:0910.5875 [nucl-ex]] 2010. 27, 81, 128
- [eaHC11a] G. Agakishiev et al. [HADES Collaboration]. Dielectron production in Ar+KCl collisions at 1.76A GeV. *Phys. Rev.*, C84(014902), [arXiv:1103.0876 [nucl-ex]]. 2011. III, 100, 115, 118, 127
- [eaHC11b] G. Agakishiev et al. [HADES Collaboration]. Hyperon production in Ar+KCl collisions at 1.76A GeV. *Eur. Phys. J.*, A 47(21), [arXiv:1010.1675 [nucl-ex]]. 2011. 100, 118, 120
- [eaHC11c] G. Agakishiev et al. (HADES Collaboration). Inclusive dielectron spectra in p+p collisions at 3.5 gev. arXiv:1112.3607 [nucl-ex] 2011. 79, 85
- [eaHC11d] G. Agakishiev et al. [HADES Collaboration]. p p and pi pi intensity interferometry in collisions of Ar + KCl at 1.76A-GeV. *Eur. Phys. J.*, A 47(63), 2011. 100
- [eaHCC09a] A. Bolshakova et al. (HARP-CDP Collaboration). *EPJ, C* 62:697–754, 2009. 74
- [eaHCC09b] A. Bolshakova et al. (HARP-CDP Collaboration). *EPJ, C* 63:549–609, 2009. 74
- [eaHCC09c] A. Bolshakova et al. (HARP-CDP Collaboration). *EPJ, C* 64:181–241, 2009. 74
- [eaHCC09d] A. Bolshakova et al. (HARP-CDP Collaboration). *EPJ, C* 66:57–117, 2009. 74
- [eaKC01] C. T. Sturm et al. (KAOS Collaboration). Evidence for a soft nuclear equation of state from kaon production in heavy ion collisions. *Phys. Rev. Lett.*, 86:39, [arXiv:nucl-ex/0011001] 2001. 28
- [eaKC07] A. Forster et al. (KaoS Collaboration). *Phys. Rev.*, C 75(024906):57–117, [nucl-ex/0701014] 2007. 29, 30, 85, 109, 125
- [eaKPEC07] R. Muto et al. (KEK-PS-E325 Collaboration). Evidence for in-medium modification of the phi meson at normal nuclear density. *Phys. Rev. Lett.*, 98(042501), [arXiv:nucl-ex/0511019] 2007. 15, 17
- [eaNC04] F. Antinori et al. [NA57 Collaboration]. Energy dependence of hyperon production in nucleus nucleus collisions at SPS. *Phys. Lett.*, B595(68), [arXiv:nucl-ex/0403022] 2004. 123
- [eaNC06] R. Arnaldi et al. (NA60 Collaboration). First measurement of the rho spectral function in high-energy nuclear collisions. *Phys. Rev. Lett.*, 96(162302), [arXiv:nucl-ex/0605007] 2006. 25, 26
- [eaNC08] C. Alt et al. (NA49 Collaboration). *Phys. Rev.*, C 78(044907), 2008. 107
- [eaNc09] R. Arnaldi et al. (NA60 collaboration). Na60 results on thermal dimuons. *Eur.Phys.J.*, C61:711–720, [arXiv:0812.3053 [nucl-ex]] 2009. 125
- [eaNC11] A. Uras et al. (NA60 Collaboration). Low mass dimuon production in p-A collisions at  $\sqrt{s} = 27.5$  GeV with NA60. *J. Phys. GG*, 38(124180):[arXiv:1108.0970 [hep-ex]], 2011. 20

- [eaSC] M. M. Aggarwal et al. (STAR Collaboration). An experimental exploration of the qcd phase diagram: The search for the critical point and the onset of de-confinement. arXiv:1007.2613 [nucl-ex]. 23
- [eaSC05] J. Adams et al. (STAR Collaboration). Experimental and theoretical challenges in the search for the quark gluon plasma: The star collaboration's critical assessment of the evidence from rhic collisions. *Nucl. Phys. A*, 757(102), [arXiv:nucl-ex/0501009] 2005. 23
- [eaSC07] J. Adams et al. [STAR Collaboration]. Scaling properties of Hyperon production in Au+Au collisions at  $\sqrt{s_{NN}} = 200$  GeV. *Phys. Rev. Lett.*, 98(062301), [arXiv:nucl-ex/0606014] 2007. 123
- [eaWC11] E. Komatsu et al. (WMAP Collaboration). Seven-year wilkinson microwave anisotropy probe (wmap) observations: Cosmological interpretation. *Astrophys. J. Suppl.*, 192(18), [arXiv:1001.4538 [astro-ph.CO]] 2011. 12
- [Ebe04] T. Eberl. *Untersuchung  $\pi^0$ -Mesonen induzierter  $e+e$ -Paare in C+C Stößen*. Dissertation, Technische Universität München, München, 2004. 34
- [EOT86] Y. Futami E. Oset and H. Toki. Pion absorption in the resonance region. *Nucl. Phys. A*, 448(597), 1986. 29
- [Epp09] E. Epple. The Lambda(1405) Resonance measured via its decay into Sigma0  $\pi^0$  in proton proton collisions with the HADES spectrometer. Diploma thesis, Physik-Department der Technischen Universität München, Institut E12, 2009. 102
- [Fai] Technical design report for hades-100, HADES collaboration, 2009. 131
- [Fai11] www.fair-center.de, 2011. 131
- [FBS04] A. Keranen J. Manninen F. Becattini, M. Gazdzicki and R. Stock. Study of chemical equilibrium in nucleus nucleus collisions at AGS and SPS energies. *Phys. Rev., C* 69(024905), [arXiv:hep-ph/0310049] 2004. 120
- [Fon01] P. Fonte. Development of large area and of position-sensitive timing RPCs. *Nucl. Instr. Methods*, A(478):170–175, 2001. 42, 131
- [Fuc06] C. Fuchs. Kaon production in heavy ion reactions at intermediate energies. *Prog. Part. Nucl. Phys.*, 56, [arXiv:nucl-th/0507017] 2006. 29
- [Gal09] T. Galatyuk. *Di-electron spectroscopy in HADES and CBM: from p+p and n+p collisions at GSI to Au+Au collisions at FAIR*. Dissertation, Institut für Kernphysik, Johann Wolfgang Goethe-Universität, Frankfurt am Main, 2009. 74
- [GAR00] GARFIELD 7.02. Simulation of gaseous detectors; <http://www.cern.ch/garfield>; Online User Guide, 2000. 40
- [GG01] M. Gazdzicki and M.I. Gorenstein. Charm estimate from the dilepton spectra. [arXiv:hep-ph/0003319v2], 2001. 64

- [GQLS96] G. E. Brown G. Q. Li, C. M. Ko and H. Sorge. Dilepton production in proton - nucleus and nucleus-nucleus collisions at SPS energies. *Nucl. Phys. A*, 611(539), [arXiv:nucl-th/9611037] 1996. 78, 79
- [Gre05] B. Greene, the fabric of the cosmos: Space, time, and the texture of reality, 2005. 12
- [HAF] HAFT: Hades acceptance filter for theorists, <http://hades-wiki.gsi.de/cgi-bin/view/simana/hadesacceptancefilter>. 47, 75
- [Han11] Hands on particle physics, 2011. [<http://www.physicsmasterclasses.org>]. 32
- [HGE04] HGEANT. HADES Simulation Package; <http://www-hades.gsi.de/>;, 2004. 44, 67
- [HL92a] T. Hatsuda and S. H. Lee. *Phys. Rev., C* 46, 1992. 14
- [HL92b] T. Hatsuda and S. H. Lee. Qcd sum rules for vector mesons in nuclear medium. *Phys. Rev. C*, 46(34), 1992. 14
- [HOX09] H. G. Ritter H. Oeschler and N. Xu. Hadron production in heavy ion collisions. arXiv:0908.1771 [nucl-ex] 2009. 127
- [HSD] The HSD transport approach. <http://th.physik.uni-frankfurt.de/brat/hsd.html>. 47, 77
- [HYD04] HYDRA. - HADES analysis package; <http://www-hades.gsi.de/>;, 2004. 44
- [Iiz66] J. Iizuka. Systematics and phenomenology of meson family. *Prog. Theor. Phys. Suppl.*, 37(21), 1966. 122
- [IKW07] H. Oeschler K. Redlich I. Kraus, J. Cleymans and S. Wheaton. Chemical Equilibrium in Collisions of Small Systems. *Phys. Rev., C*76(064903), 2007. 120, 121
- [Jan11] J. Weil, private communication, 2011. 95
- [JCW06] K. Redlich J. Cleymans, H. Oeschler and S. Wheaton. Comparison of chemical freeze-out criteria in heavy-ion collisions. *Phys. Rev., C* 73(034905), [arXiv:hep-ph/0511094] 2006. 25, 120, 121
- [JPC10] L. Fabbietti J. Pietraszko and W. Koenig [HADES Collaboration]. Diamonds as timing detectors for MIP: The HADES proton-beam monitor and start detectors. *Nucl. Instrum. Meth., A* 618(121), [arXiv:0911.0337 [nucl-ex]]. 2010. 40
- [JPea95] T. Rubehn A. Schuttauf A. Worner E. Zude M. Begemann-Blaich J. Pochodzalla, T. Mohlenkamp and T. .Blaich et al. Probing the nuclear liquid - gas phase transition. *Phys. Rev. Lett.*, 75(1040), 1995. 24
- [JSM97] J. Bondorf J. Schaffner and I. N. Mishustin. In-medium kaon production at the mean-field level. *Nucl. Phys. A*, 625(325), [arXiv:nucl-th/9607058] 1997. 28
- [Jur10] M. Jurkovic. *Spektroskopie virtueller Photonen in Ar+KCl Stößen bei  $E_{kin} = 1,76$  AGeV*. Dissertation, Technische Universität München, München, 2010. 100, 115
- [JWM11] K. Gallmeister J. Weil and U. Mosel. In-medium properties of vector mesons in a transport approach. arXiv:1105.0314 [nucl-th] 2011. 78

- [KF02] M. I. Krivoruchenko and A. Faessler. Comment on delta radiative and dalitz decays. *Phys. Rev. D*, 65(017502), [arXiv:nucl-th/0104045] 2002. 78, 79
- [Kir11] K. Laidus, Private communication, 2011. 129
- [Kre10] M. Krebs. Rekonstruktion der phi mesonen in p+Nb bei 3.5 GeV mit HADES. Bachelor thesis, Institut für Kernphysik, Johann Wolfgang Goethe-Universität, Frankfurt am Main, 2010. 129
- [Kri08] F. Krizek. *Study of inclusive electron-positron pair production in collisions of Ar+KCl at 1.756 A GeV*. Dissertation, NPI CAS, Rez, 2008. 100, 109, 115
- [KT09] E. E. Kolomeitsev and B. Tomasik. Catalytic phi meson production in heavy-ion collisions. *J. Phys.*, G36(095104), [arXiv:0903.4322 [nucl-th]] 2009. 123
- [Lan85] L. G. Landsberg. *Phys. Rep.* 128, 301, 1985. 78
- [Lan08] S. Lang. *Di-Leptonen Produktion in Ar+KCl Reationen bei 1.756 AGeV*. Dissertation, Institut für Kernphysik, Johann Wolfgang Goethe-Universität, Frankfurt am Main, 2008. III, V, 30, 41, 43, 44, 45, 46, 49, 50, 51, 70, 99, 100, 109, 111, 113, 127, 134
- [LMS09] K. Redlich L. McLerran and C. Sasaki. Quarkyonic matter and chiral symmetry breaking. *Nucl. Phys. A*, 824:86, [arXiv:0812.3585 [hep-ph]] 2009. 23
- [Lor08] M. Lorenz. Produktion geladener Kaonen in Ar+KCl Reaktionen bei 1.756 AGeV. Diplomarbeit, Institut für Kernphysik, Johann Wolfgang Goethe-Universität, Frankfurt am Main, 2008. 30, 38, 41, 99, 100, 127
- [Mar05] J. Markert. *Untersuchung zum Ansprechverhalten der Vieldraht-Driftkammern niedriger Massenbelegung des HADES Experimentes*. Dissertation, Institut für Kernphysik, Johann Wolfgang Goethe-Universität, Frankfurt am Main, 2005. 36, 38
- [Met11] V. Metag, Do hadron properties change inside the medium? Presentation given at the 42. Arbeitstreffen der Kernphysik in Schleching, 2011, 2011. 21
- [MGAW98] K. Rajagopal M. G. Alford and F. Wilczek. Qcd at finite baryon density: Nucleon droplets and color superconductivity. *Phys. Lett. B*, 422(247), [arXiv:hep-ph/9711395] 1998. 23
- [Miced] J. Michel. *Development and Implementation of a New Trigger and Data Acquisition System for the HADES Detector*. Dissertation, Institut für Kernphysik, Johann Wolfgang Goethe-Universität, Frankfurt am Main, to be published. 43, 131
- [MLW92] S. Klimt M. Lutz and W. Weise. *Nucl. Phys.*, A542(621), 1992. 13, 15
- [MPM04] S. Leupold M. Post and U. Mosel. Hadronic spectral functions in nuclear matter. *Nucl. Phys. A*, 741(81), [arXiv:nucl-th/0309085] 2004. 14, 16, 97
- [MS92] D. M. Manley and E. M. Saleski. Multichannel resonance parametrization of pi n scattering amplitudes. *Phys. Rev. D*, D 45(4002), 1992. 79
- [MWi10] Michael Weber, self consistency studies. HADES internal report, 2010. 67, 69

- [MWw09] Michael Weber. <http://hades-wiki.gsi.de/cgi-bin/view/SimAna/Sep08RingRKMMatching>, 2009. 57
- [Oes09] Helmut et al. Oeschler. Hadron production in heavy ion collisions. [arXiv:0908.1771 [nucl-ex]] 2009. 125
- [Oku63] S. Okubo. Phi meson and unitary symmetry model. *Phys. Lett.*, 5(165), 1963. 122
- [ORA] Oracle corporation. 500 Oracle Parkway, Redwood Shores, CA 94065, USA. 44
- [Pac08] Y. Pachmayer. *Dielektronenproduktion in 12C+12C Kollisionen bei 1GeV pro Nukleon*. Dissertation, Institut für Kernphysik, Johann Wolfgang Goethe-Universität, Frankfurt am Main, 2008. 74
- [pav10] P. Tlustý, M. Weber, P. Salabura (HADES Collaboration). GSI Scientific Report, 2010. 74
- [PBMS03] K. Redlich P. Braun-Munzinger and J. Stachel. Particle production in heavy ion collisions. [arXiv:nucl-th/0304013] 2003. 120
- [PCN11] M. Nanova, Private communication, 2011. 20, 22, 94
- [PDG] The particle data group. <http://pdg.lbl.gov/>. 96
- [PLU04] Pluto++, A Monte Carlo simulation tool for hadronic physics; <http://www-hades.gsi.de/>, 2004. 44, 67, 78, 125
- [pyt] <http://home.thep.lu.se/torbjorn/Pythia.html>. 77
- [qua] A. Manohar, Quark masses. <http://pdg.lbl.gov/2000/quarks/q000.pdf>. 12
- [RAN11] T.E. Rodrigues and J.D.T. Arruda-Neto. *Phys. Rev. Lett.*, C 84(021601), 2011. 20, 95
- [RAS03] V. Metag R. Auerbeck, R. Holzmann and R. S. Simon. Neutral pions and eta mesons as probes of the hadronic fireball in nucleus nucleus collisions around 1-A-GeV. *Phys. Rev.*, C 67(024903), [arXiv:nucl-ex/0012007] 2003. 120, 121
- [Reh11] L. Rehnisch. *Seltene Resonanzen in Ar+KCl-Reaktionen bei 1.756A GeV*. Master thesis, Institut für Kernphysik, Johann Wolfgang Goethe-Universität, Frankfurt am Main, 2011. 100, 128
- [Rom11] R. Holzmann, private communication,, 2011. 76
- [ROO04] ROOT - An Object Oriented Data Analysis Framework; <http://root.cern.ch/>, 2004. 44
- [Sai07] B. Sailer. *Inklusive  $e^+e^-$  Paarproduktion in pp-Reaktionen bei  $E_{kin} = 2, 2\text{GeV}$* . Dissertation, Technische Universität München, München, 2007. 63
- [SC00] A. Sibirtsev and W. Cassing. On the current status of ozi violation in pi n and p p reactions. *Eur. Phys. J.*, A7(407), 2000. 123
- [Sch08] A. Schmah. *Seltensamkeit Produktion in Ar+KCl Reationen bei 1.756 AGeV*. Dissertation, Fachbereich Physik, Technische Universität Darmstadt, Darmstadt, 2008. 36, 38, 41, 50, 100, 118

- [Sch12a] T. Scheib. Hypertriton Produktion in Ar+KCl-Reaktionen bei 1.756A GeV. Master thesis, Institut für Kernphysik, Johann Wolfgang Goethe-Universität, Frankfurt am Main, 2012. to be published. 100, 128
- [Sch12b] H. Schuldes. Produktion leichter Fragmente in Ar+KCl Reaktionen bei 1.756A GeV. Master thesis, Institut für Kernphysik, Johann Wolfgang Goethe-Universität, Frankfurt am Main, 2012. to be published. 41, 42, 100, 102, 103, 128
- [Sie10] J. Siebenson. Exclusive analysis of the Lambda(1405) resonance in the charged Sigma-pi decay channels in proton proton reactions with HADES. Diploma thesis, Physik-Department der Technischen Universität München, Institut E12, 2010. 102
- [SL10] U. Mosel S. Leupold, V. Metag. Hadrons in strongly interacting matter. *Int. J. Mod. Phys.*, E19:147–224, [arXiv:0907.2388 [nucl-th]] 2010. 18, 20, 95, 96
- [Sud07] M. Sudol. *Measurements of low-mass  $e^+e^-$  pair production in 2 AGeV C-C collisions with HADES*. Dissertation, Institut für Kernphysik, Johann Wolfgang Goethe-Universität, Frankfurt am Main, 2007. 74
- [Tan11] T. Galatyuk, private communication,, 2011. 74, 131
- [Tei11] K. Teilab. *The production of  $\eta$  and  $\omega$  mesons in 3.5 GeV p+p interaction in HADES*. Dissertation, Institut für Kernphysik, Johann Wolfgang Goethe-Universität, Frankfurt am Main, 2011. 102
- [TMV] TMVA - Toolkit for Multivariate Analysis v3.6 <http://tmva.sourceforge.net> or [arxiv:physics/0703039](http://arxiv.org/abs/physics/0703039). 44, 111
- [UrQ04] URQMD. The UrQMD Collaboration; <http://www.th.physik.uni-frankfurt.de/~urqmd/>;, 2004. 74, 77
- [vHR06] H. van Hees and R. Rapp. Comprehensive interpretation of thermal dileptons at the sps. *Phys. Rev. Lett.*, 97(102301), [arXiv:hep-ph/0603084] 2006. 27
- [WC09] S. Wheaton and J. Cleymans. THERMUS: A thermal model package for ROOT. *Comput. Phys. Commun.*, 180(84), 2009. 120
- [Web11] M. Weber. *Dielektronen Spektroskopie in kalter Kernmaterie*. Dissertation, Technische Universität München, München, 2011. 48, 49, 57, 69, 74
- [Wen09] C. Wendisch. Zweiteilchenkorrelationen von Protonen und geladenen Pionen in Schwereionenreaktionen von Ar+KCl bei 1,756 AGeV. Diploma thesis, Technische Universität Dresden, Dresden, 2009. 100
- [Wenon] C. Wendisch. Dissertation, Technische Universität Dresden, Dresden, in preparation. 129
- [Wil10] F. Wilzek, the lightness of being: Big questions, real answers, 2010. 12
- [Wit] Witek, Przygoda, private communication. 67
- [WSC96] W. König W. Schon, H. Bokemeyer and V. Metag (HADES Collaboration). Simulation of recoilless production of omega mesons. *Acta Phys. Polon. B*, 27(2959), 1996. 47

- [YAS06] S. D. Katz, Y. Aoki, Z. Fodor and K. K. Szabo. The qcd transition temperature: Results with physical masses in the continuum limit. *Phys. Lett. B*, 643:46, [arXiv:hep-lat/0609068] 2006. 22
- [Zwe64] G. Zweig. An SU(3) model for strong interaction symmetry and its breaking. *Cern*, 1964. 122

## **RECHTLICHES**

Die vorliegende Druckfassung enthält kleinere, inhaltlich nicht relevante Änderungen, gegenüber der dem Promotionsbüro vorgelegten Version.



## DANKE

Zunächst, möchte ich meinem Doktorvater Prof.Dr. Joachim Stroth für die Möglichkeit meine Doktorarbeit in seiner Arbeitsgruppe anfertigen zu können und seine fortlaufende Unterstützung sowie die vielen nützlichen Diskussionen danken. Ich konnte stark, von seinem strukturiertem Denken und seiner Fähigkeit komplizierte Sachverhalte anschaulich zu erklären profitieren und habe die Wahl meiner Arbeitsgruppe nicht besser treffen können.

Anschließend möchte ich meinen beiden Betreuern Dr. Jochen Markert und Dr. Holzmann danken. Ohne ihr enormes Wissen in technischen bzw. physikalischen Aspekten wäre diese Arbeit so nicht möglich gewesen. Darüber hinaus, haben beide ihren eigenen, sehr individuellen Humor, mit dem sie mich immer wieder aufgeheitert haben.

Großer Dank geht Dr. Wolfgang König, das Genie mit dem Herz am richtigen Fleck!

Ich danke Dr. Christian Müntz, der mir in den vergangenen Jahren immer Vertrauen entgegenbrachte, und an den ich mich stets mit allen möglichen soften Problemen wenden konnte.

Prof.Dr. Laura Fabbietti danke ich für ihr Vertrauen und ihre Unterstützung, sowie dafür, dass sie mich dazu brachte mich näher mit statistischen Modellen zu befassen, was zu einem großen Erfolg wurde.

Ich danke meinem langjährigen Mitstreiter in der p+nb Analyse, Deputy Young Members Representative und Freund Dr. Michael Weber für die angenehme Zusammenarbeit in allen Bereichen. In diesem Sinne ist mir besonders in Erinnerung geblieben, wie wir nach der HADES Sommer Schule 2009 stundenlang einen Grill geputzt haben.

Prof.Dr. Tetyana Galatyuk danke ich für ihre zahlreichen Tipps bzgl. Leptonen und ihre exzellenten Vorträge, aus denen ich mir viel abschauen konnte.

Meinem ehemaligen Betreuer und guten Freund Dr. Alexander Schmah danke ich für zahlreiche Diskussionen, durch die ich von seiner großen Analyse Expertise profitieren konnte. Es freut mich sehr, dass der Kontakt nie abgerissen ist.

Für das gute Arbeitsklima, dass er zu schaffen wusste, sowie zahlreiche wichtige Kommentare und Anregungen in Bezug auf meine Arbeit danke ich Prof.Dr. Piotr Salabura.

Prof.Dr. Volker Metag danke ich für seine zahlreichen exzellenten Hinweise besonders in Bezug auf kalte nukleare Materie.

Ebenfalls enorm profitiert habe ich von Prof.Dr. Herbert Stroebele's Schwerionenexpertise und seiner ihm eigenen Art, sich nie mit der einfachen Antwort zufrieden zu geben, vielen Dank.

Zu Dank verpflichtet bin ich Dr. Yvonne Leifles und Prof.Dr. Christoph Blume für ihre Unterstützung. Ein großer Dank, besonders im Hinblick auf die Publikationen und die Hadronenanalysen geht an Prof.Dr. Burkhard Kämpfer und Dr. Roland Kotte.

Ich danke den Mitgliedern der Arbeitsgruppe Dr. Jerzy Pietraszko, Dr. Michael Traxler, Dr. Ilse König, Dr. Gosia Gumberidze, Erwin Schwab, Dr. Burkhard Kolb, Dr. Olga und Vladimir Pechenov, Dr. Ingo Fröhlich, Dr. Christian Sturm und der HADES Kollaboartion, ich habe mich stets sehr wohl gefühlt.

Meinem Kommilitonen und Mitdoktoranden Jan Michel danke ich im Besonderen, es hat mir stets Spaß gemacht für dich Kabel verlegen zu dürfen in dich Bezug auf die DAQ Überwachung beraten zu dürfen (als Dummy User).

Ein ganz großer Dank geht an die Studenten die ich während meiner Promotion betreuen durfte bzw. mit denen ich zusammen gearbeitet habe. Auch wenn ihr manchmal genervt habt (gell Heidi ;-)), hat mir die Arbeit mit euch stets super viel Spass bereitet. Zusehen, wie ihr euch entwickelt habt war die größte Motivation für mich. Im einzelnen: Laura Rehnisch, Timo Scheib und Heidi Schuldes. Ferner Katharina Gill, Erik Krebs, Claudia Behnke und Patrick Sellheim.

Ebenfalls danken für das gute Klima und den vielen Spass den wir zusammen hatten, möchte ich meinen langjährigen Kollegen Samir, Khaled, Attilio, Christoph, Christine sowie der CBM Gruppe in Frankfurt.

Ein riesiges Dankeschön geht an Marianne Frey für ihre Unterstützung. Ihre organisatorischen Fähigkeiten machen sie zur wichtigsten Person im Institut. In diesem Bezug danke ich auch Lea Wunderlich und Sandra Schecker an der GSI.

Meinem Kommilitonen Dr. Jan Steinheimer danke ich für die vielen Gespräche beim Mittagessen, in denen er mir die Sicht eines Theoretikers zu vermitteln versuchte.

Dem HGS Hire Team danke ich für ihren Einsatz und ihre Unterstützung im Rahmen des Graduierten-Programms.

Gerade in Zeiten, in denen es nicht läuft, sind gute Freunde besonders wichtig. Ich danke Shih, Christian, Timo, Matthias und Cintia für ihr Verständnis, ihren Rückhalt und die Ablenkung, die sie mir gegeben haben; sowie Janis für wertvolle Anregungen aus Sicht des Germanisten.

Luise danke ich für ihre Begleitung über einen weiten Zeitraum meiner Promotion.

Meinen Eltern schulde ich großen Dank für ihr Vertrauen, ihre Unterstützung und ihren Rückhalt.

## Curriculum Vitae

Manuel Lorenz

Hörselbergstr. 7  
65929 Frankfurt



Date of birth  
Place of birth

08 October 1982  
Frankfurt Main

### EDUCATION

08/1990 – 06/1994 Lindenschule Kriftel

08/1994 – 06/1999 Elisabethenschule Hofheim

08/1999 – 06/2002 Konrad-Adenauer Schule Kriftel  
*“Abitur”(Ø 1.3)*

10/2003 – 03/2008 Goethe-University Frankfurt am Main  
*Diploma in Physics (Ø 1.0 with honour)*

08/2008 – present Goethe-University Frankfurt am Main  
*PhD Student, Institute of nuclear physics*

### DIPLOMA THESIS

*“Geladene Kaonen Produktion in Ar+KCl Reaktionen bei 1.76 AGeV” Supervisor Prof. J. Stroth*

### AWARDS

Philip Siedler Scientific Award 2008